DAHLGREN DIVISION
NAVAL SURFACE WARFARE CENTER
Dahlgren, Virginia 22448-5100

NSWCDD/TR-95/160

EXTENSION OF THE NSWCDD AEROPREDICTION CODE TO THE ROLL POSITION OF 45 DEGREES

BY FRANK MOORE ROY MCINVILLE

WEAPONS SYSTEMS DEPARTMENT

DECEMBER 1995

REPORT DOCUMENTATION PAGE

Form Approved
OMB No. 0704-0188

1. AGENCY USE ONLY (Leave blank)	2. REPORT DATE	3. REPORT TYPE AND DATES COVERED
	December 1995	Final

4. TITLE AND SUBTITLE
Extension of the NSWCDD Aeroprediction Code to the Roll Position of 45 Degrees

5. FUNDING NUMBERS

6. AUTHOR(s)

F. Moore, R. McInville

7. PERFORMING ORGANIZATION NAME(S) AND ADDRESS(ES)

Naval Surface Warfare Center
Dahlgren Division, G04
17320 Dahlgren Road
Dahlgren, VA 22448-5100

8. PERFORMING ORGANIZATION REPORT NUMBER

NSWCDD/TR-95/160

9. SPONSORING/MONITORING AGENCY NAME(S) AND ADDRESS(ES)

10. SPONSORING/MONITORING AGENCY REPORT NUMBER

11. SUPPLEMENTARY NOTES

12a. DISTRIBUTION/AVAILABILITY STATEMENT

Approved for public release; distribution is unlimited.

12b. DISTRIBUTION CODE

13. ABSTRACT (Maximum 200 words)

The NSWCDD Aeroprediction Code has been extended to the roll position of 45 degrees (or fins in cross or "x" orientation). New technology developed includes wing-body and body-wing interference factors for this roll orientation and to angles of attack of 90 degrees; new semi-empirical wing-tail interference models for both the fins in 0 and 45 degrees roll positions; and approximate methods to estimate wing-alone center of pressure shift at high angles of attack and 45 degrees roll position as well as "fin choking" at high mach number.

This new technology allows aerodynamics to be estimated with average accuracy levels of ±10 percent on normal and axial force coefficients and ±4 percent of body length on center of pressure. An exception to this is at subsonic mach number and high angle of attack where wind tunnel sting interference effects are present and at high Mach number and angle of attack where internal shock interactions from a forward fin onto an aft-mounted fin are present. Results are presented for several wing-body and wing-body-tail configurations at various Mach numbers and angles of attack to support this average accuracy level conclusion.

14. SUBJECT TERMS

body-wing interference, nonlinear, aerodynamics, center of pressure, linear theory, slender body theory, normal force, planform area, canard, axial force, Mach number, angle of attack, wind tunnel data, interference factor, vortex

15. NUMBER OF PAGES
155

16. PRICE CODE

17. SECURITY CLASSIFICATION OF REPORTS	18. SECURITY CLASSIFICATION OF THIS PAGE	19. SECURITYCLASSIFICATION OF ABSTRACT	20. LIMITATION OF ABSTRACT
UNCLASSIFIED	UNCLASSIFIED	UNCLASSIFIED	UL

FOREWORD

The 1995 version of the aeroprediction code (AP95) was capable of computing approximate aerodynamics on most tactical weapons over the range of angles of attack from 0 to 90 deg and at any Mach number they may fly. However, the aerodynamics were limited to the roll position of 0 deg, or the tail fins oriented in a plus (+) fin arrangement. The methodology described in this report extends the nonlinear AP95 code to the roll position of 45 deg, or the tail fins in a cross (x) arrangement. This new technology will be transitioned in a later version of the aeroprediction code, after additional new technology has been developed.

The work described in this report was supported through the Office of Naval Research (Mr. Dave Siegel) by the following programs: the Air Launched Weapons Program managed at the Naval Air Warfare Center, China Lake, CA, by Mr. Tom Loftus and Dr. Craig Porter, and the Surface Weapons Systems Technology Program managed at the Naval Surface Warfare Center, Dahlgren Division (NSWCDD) by Mr. Robin Staton and Mr. Gil Graff. Also, some support was provided in FY 94 by the Army Missile Command at Huntsville, AL, under Mr. Dave Washington and in FY 95 by the Marine Corps Weaponry Technology Program managed at NSWCDD by Mr. Bob Stiegler. The authors express appreciation for support received in this work. Appreciation is also given to Mr. Tom Hymer, who provided some data used in the validation process.

Approved by:

David S. Malyevac

DAVID S. MALYEVAC, Deputy Head
Weapons Systems Department

Accesion For	
NTIS CRA&I	☑
DTIC TAB	☐
Unannounced	☐
Justification	
By	
Distribution /	
Availability Codes	
Dist	Avail and / or Special
A-1	

CONTENTS

ILLUSTRATIONS

ILLUSTRATIONS (Continued)

ILLUSTRATIONS (Continued)

ILLUSTRATIONS (Continued)

ILLUSTRATIONS (Continued)

TABLES

1.0 INTRODUCTION

Many of the world's missiles fly in either the roll stabilized position of $\Phi = 0$ deg (or plus fin orientation) or $\Phi = 45$ deg (or cross fin orientation). Figure 1 illustrates these fin orientations for a cruciform missile looking from the missile nose toward the rear. As illustrated in the figure, the $\Phi = 0$ deg plane generally gives slightly more normal force and a slightly more stable configuration in pitch at a given angle of attack than does the missile rolled to $\Phi = 45$ deg (the physics of why this occurs will be discussed in the analysis section). On the other hand, a missile in the $\Phi = 45$ deg plane is in a roll-stable position, which means less energy is required to maintain a constant roll orientation. Also, all four fins can be deflected simultaneously, giving 30 to 50 percent more normal force from control deflection than only two fins deflected in the $\Phi = 0$ deg roll position.

The latest version[1] of the NSWCDD Aeroprediction Code (APC), AP95, calculates aerodynamics only in the $\Phi = 0$ deg plane. As such, aerodynamics at $\Phi = 45$ deg roll must be obtained from another aerodynamics code[2,3] or estimated from the AP95 $\Phi = 0$ deg results. It is the intent of this report to discuss the physical phenomena that occur at the $\Phi = 0$ and 45 deg roll orientations and to develop a semiempirical mathematical model that will allow the AP95 to be extended to the $\Phi = 45$ deg plane.

The AP95 is an approximate analytical Aeroprediction Code primarily designed to provide preliminary estimates of aerodynamics for use in particle ballistic models, trim aerodynamic models, or structures and heat transfer models. Static aerodynamics are generally estimated within ±10 percent and center of pressure within ±4 percent of the body length. To obtain aerodynamics estimation accuracy levels generally desired for full six-degree-of-freedom (6 DOF) simulations requires either a more accurate numerical code[4] or wind tunnel data or both. As such, the AP95 does not attempt to compute out-of-the-pitch-plane aerodynamics or coupling effects between the pitch and yaw planes. On the other hand, if one is interested in the $\Phi = 45$ deg plane, and control deflections are symmetric with respect to the pitch plane, then the AP95 code can be modified to allow aerodynamics for the $\Phi = 45$ deg plane. These modifications will be made in an analogous process to the nonlinear semiempirical methodology of Reference 1.

One may ask, why not use another engineering code such as that of Reference 2 or 3 to compute aerodynamics in the $\Phi = 45$ deg plane. There are several reasons for this. First of all, it is more convenient to have the capability for $\Phi = 0$ and 45 deg aerodynamics in a single code as opposed to two codes. Second, the codes of References 2 and 3 are more limited in angle of attack and Mach number than the AP95 code at $\Phi = 0$ deg. Third, along with other works,[5] Reference 1 has shown the AP95 to give more consistently accurate static aerodynamics in the $\Phi = 0$ deg roll orientation than either the Reference 2 or 3 code. It is believed this accuracy level can be extended to the $\Phi = 45$ deg roll orientation.

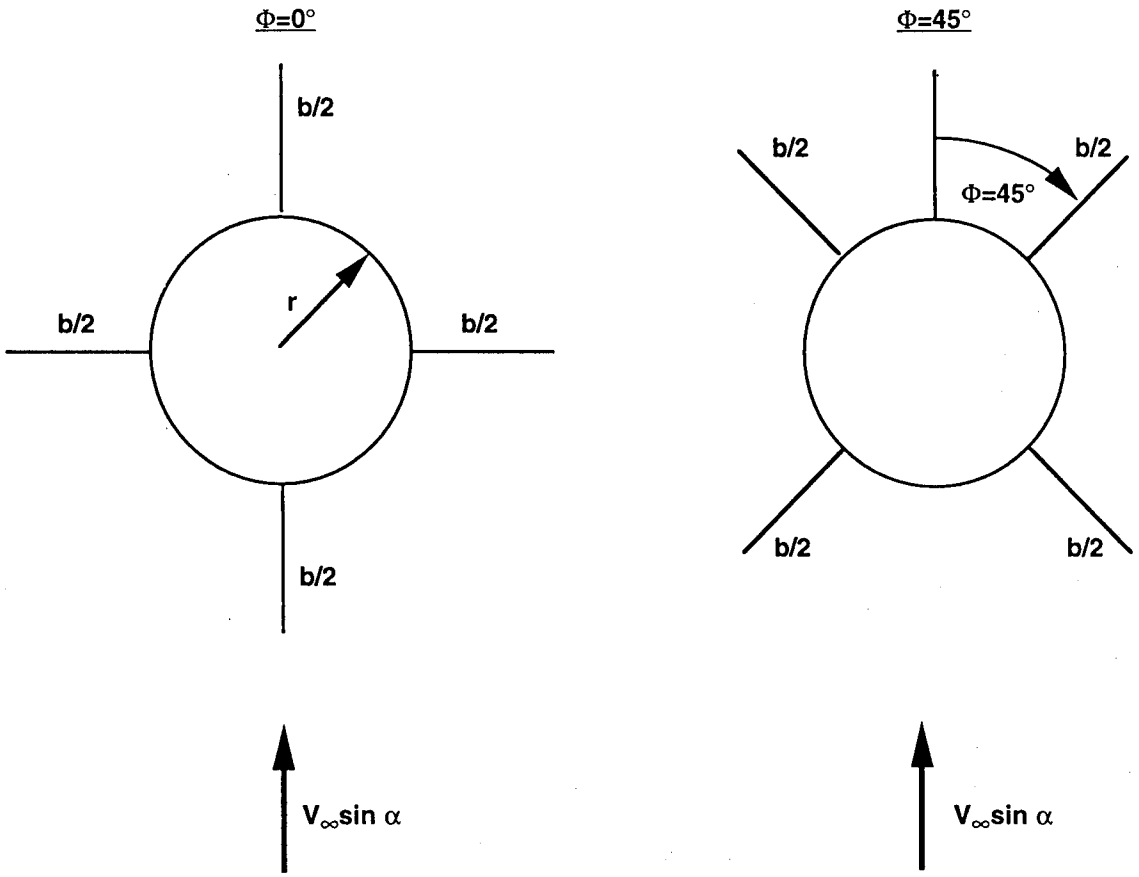

TYPICAL FORCE AND MOMENT COMPARISONS

Φ=0°

- **$(C_N)_{\Phi=0°}$ GENERALLY HIGHER THAN $(C_N)_{\Phi=45°}$ AT HIGHER α**
- **GENERALLY MORE STABLE IN PITCH AT Φ=0° vs Φ=45°**

Φ=45°

- **NATURALLY STABLE POSITION IN ROLL (LESS ENERGY TO MAINTAIN CONSTANT ROLL)**
- **MORE CONTROL AUTHORITY AT Φ=45° DUE TO FOUR FINS DEFLECTED vs TWO AT Φ=0°**

FIGURE 1. CRUCIFORM WING-BODY-TAIL MISSILE CONFIGURATION FLYING AT ROLL OF Φ = 0 AND 45 DEG

On the other hand, the methods of References 2 and 3 can compute aerodynamics at any roll orientation. Hence, if one wants to perform 6 DOF performance analysis and is willing to accept potentially large inaccuracy levels in the out-of-pitch-plane aerodynamics over a more limited range of angle of attack (AOA) and Mach number, then References 2 and 3 are the only engineering codes available in the United States for performing this analysis, to the authors' knowledge. The approach of the AP95 is to neglect the body vortex scale effects due to length and leave the body vortex effects in the fin aerodynamics. This eliminates the errors associated with applying a semiempirical theory to subtract out nonlinear body vortex effects on one configuration and then add them back in for a different configuration.

The body vortex effects are therefore inherently a part of the interference factors of the wing in conjunction with the body and the body in conjunction with the wing. Based on limited comparisons to date, the direct approach of AP95 of using data from wind tunnel results versus modeling data for the wing in conjunction with the body for body vortex effects appears to give better agreement with experiment on configurations outside the wind tunnel data base. It is also much more straightforward to apply and requires less computational time as well. Certainly, as one attempts to achieve angle-of-attack capability exceeding 20 deg, the errors associated with subtracting out body vortex effects with a semiempirical theory based on limited data become more and more questionable.

The overall approach to modify the AP95 code for nonlinear aerodynamics in the $\Phi = 45$ deg plane will thus be very similar to that for the $\Phi = 0$ deg plane. Linearized theories or slender body theory will be used for low angle of attack estimates and the data bases of References 6-9 will be used to develop empirical or semiempirical corrections to account for the nonlinearities that occur in normal force and center of pressure with increasing angle of attack.

2.0 ANALYSIS

As indicated in the introduction, the goal is to develop a nonlinear semiempirical model for cruciform missiles for the $\Phi = 45$ deg plane. It is envisioned that this model will be analogous to the $\Phi = 0$ deg plane methods in AP95, except the normal force and pitching moments due to the wing alone and interference aerodynamics will have to be derived for the $\Phi = 45$ deg roll orientation.

Referring to the total normal force coefficient equation for a wing-body-tail configuration as given by Reference 9 we have

$$C_N = C_{N_B} + \left[\left(K_{W(B)} + K_{B(W)}\right) \alpha + \left(k_{W(B)} + k_{B(W)}\right) \delta_W\right] \left(C_{N\alpha}\right)_W$$

$$+ \left[\left(K_{T(B)} + K_{B(T)}\right) \alpha + \left(k_{T(B)} + k_{B(T)}\right) \delta_T\right] \left(C_{N\alpha}\right)_T + C_{N_{T(V)}} + C_{N_{B(V)}} \qquad (1)$$

In the AP81,[10] all terms in Equation (1) were linear except for body-alone normal force. As a result, the AP81 gave increasingly erroneous results as the nonlinear aerodynamics associated with AOA became important. This typically meant 10 to 15 deg AOA as an upper limit. The AP93[11,12] developed nonlinear corrections for each of the terms in Equation (1) up to AOA 30 deg using wind tunnel component data bases[6-8]. A more consistently accurate Aeroprediction Code was obtained up to AOA 30 deg. Typical average accuracy boundaries of ±10 percent on axial and normal force and ±4 percent of body length for center of pressure could be obtained. The AP95[1] extended the AOA nonlinear corrections of Equation (1) to 90 deg AOA through extrapolation of the data bases of References 6-8 plus the more recent data base of Reference 9, along with engineering judgement. Jorgenson's[13] data were also used for improvements in body-alone aerodynamics. The accuracy levels of the AP93 code were maintained for the AP95 except in regions of strong internal shock interactions (high M, high AOA).

The way Equation (1) is implemented in both the AP93 and AP95 codes is by computing the nonlinearities of the body-alone term based on AOA only, but all the other nonlinear corrections to the interference factors and wing or tail aerodynamics are based on the total angle of attack, or $\propto + \delta$. This was done for ease of implementation into the operational AP81 code. Hence, even though the component nonlinear terms were derived from wind tunnel data bases from AOA data only, they were implemented in a total local AOA sense. The empirical nonlinear corrections were then fine-tuned based on comparisons to other configuration aerodynamics outside the data bases. The center of pressure of individual missile component aerodynamics were treated similarly to the AP81 except shifts in center of pressure based on data were derived. These shifts were implemented in tabular form as a function primarily of AOA and M_∞.

Also, the $C_{N_{B(V)}}$ term of Equation (1), which is the downwash normal force on the body due to the wing shed vortices, is neglected. This is because it is inherently included in the wind tunnel data bases and it is believed the errors in trying to analytically estimate the term, subtract it out on one configuration, and then add it back in later on a different configuration, are as large or larger than the errors from incorporating it into the $K_{B(W)}$ term.

Equation (1) can also be rewritten as

$$C_N = C_{N_B} + C_{N_{W(B)}} + C_{N_{B(W)}} + C_{N_{T(B)}} + C_{N_{B(T)}} + C_{N_{T(V)}} \qquad (2A)$$

where it is understood that $C_{N_{B(T)}}$ encompasses the $C_{N_{B(V)}}$ term. For ease of implementation into an existing code designed primarily for linear aerodynamics, most of the terms in Equation (2A) are separated into a linear and nonlinear contribution due to $\propto$ or δ. For example, the wing-body term is computed in the AP95 code as follows:

$$C_{N_{W(B)}} = \left[\left(C_{N\alpha}\right)_L + \left(C_{N\alpha}\right)_{NL}\right]_W \left\{\left[\left(K_{W(B)}\right)_{SBT} + \left(\Delta K_{W(B)}\right)_{NL}\right] \alpha \right.$$

$$\left. + \left(C_1\left[k_{W(B)}\right]_{SBT} + C_2\right) \delta_W\right\}\left(\frac{A_W}{A_{REF}}\right) \qquad (2B)$$

The linear or small angle of attack terms of Equation (2B) are estimated by linear theory (LT) or slender body theory (SBT). This gives the Aeroprediction Code a good fundamental basis for its aerodynamic estimates. The nonlinear corrections due to higher AOA or control deflection are each estimated directly from component wind tunnel data bases.[6-9] Each of the other terms in Equation (2A) is treated in a similar fashion to Equation (2B) in the actual implementation into the Aeroprediction Code.

In the context of Equation (2), we therefore seek the nonlinear definition of each of the terms in Equation (2). It is expected that the body-alone term [first term of Equation (2A)] will be independent of Φ. In reality, this is not necessarily the case for M<2 and high angle of attack because of the asymmetric shedding of vortices. The mechanism of this shedding is not clear, but it is suspected that slight imperfections in the flow or body shape, from uniform or axisymmetric, respectively, could contribute to this phenomenon. At present, the Aeroprediction Code does not account for out of plane aerodynamics, and therefore the side force created by the asymmetric shedding of body vortices is not predicted. Also, in the Reference 8 data, normal force varied by about 10 percent as a function of roll in the region of asymmetric vortex shedding. Instead of including this variation, it was averaged out.

Each of the remaining terms in Equation (2) will be predicted in an analogous fashion to the AP95 code developed for $\Phi = 0$ deg, except here the quantities will be for $\Phi = 45$ deg. As already mentioned, that approach was based on linear theory or slender body theory for small values of α and empirical data bases (References 6-9) to develop nonlinear corrections for large α. As such, it is instructive to examine the fundamental impact of roll orientation on linearized and slender body theory before proceeding to the nonlinear corrections, which are empirical in nature.

2.1 SLENDER BODY AND LINEAR THEORY RESULTS FOR ROLL-DEPENDENT AERODYNAMICS

References 14 and 15 were primary materials used for examining roll dependence implications from slender body and linearized theories. A somewhat detailed summary of these results is given for information purposes in Appendix A. The summary of the key findings in Appendix A, repeated here for convenience, are

a) For cruciform wings alone or a wing-body combination, the total normal force is independent of roll.

b) For a planar wing-body combination at roll, the loading on the windward plane panel is greater by an equal amount to that on the leeward plane panel. This means that if one were trying to design a code for lateral aerodynamics, roll dependence of each fin planform must be considered. On the other hand, if longitudinal aerodynamics are of primary interest, the total normal force on the entire wing planform can be considered.

c) For a cruciform wing-body-tail configuration at roll, eight vortices are shed in the wing-body region, which adversely affects the tail lift. This is as opposed to four vortices at $\Phi = 0$ deg.

d) The planar theory developed for wing-tail interference can be used to approximate the loss of lift on the tails at $\Phi = 45$ deg.

e) The aerodynamics of a cruciform wing-body-tail combination with zero control deflections are independent of roll position.

These findings for roll dependence from linearized or slender body theory are quite useful in helping plan how to develop a nonlinear APC for $\Phi = 45$ deg. While the conclusions of linear theory roll dependence may not translate to the nonlinear case, we will still use the findings to help guide the nonlinear code development. In particular, the item (a) conclusion implies use of the $\Phi = 0$ deg, wing alone data for $\Phi = 45$ deg. This is quite important because the available wing-alone data bases are all at $\Phi = 0$ deg. This means that any nonlinear wing-alone roll dependence will be included in the interference factors rather than the wing-alone solution, which is independent of Φ.

The second major result of the key slender body/linear theory roll dependence findings is that for cruciform missiles, we can use the same interference approaches as in the AP95, except the constants need to be changed because of a different roll angle. The combination of these two conclusions are quite important because they basically allow the direct usage of the AP95 code with different constants for the nonlinear interference terms at $\Phi = 45$ deg versus $\Phi = 0$ deg.

The third significant conclusion is that for small AOA, wing-body-tail aerodynamics are independent of roll position. This allows the usage of wing-tail interference methodology designed for planar computations for different roll orientations, so long as the proper number of vortices are considered. Again different nonlinear corrections are expected for the $\Phi = 45$ deg versus the $\Phi = 0$ deg roll position.

2.2 NONLINEAR AERODYNAMICS METHODS

This section will describe the methods used for computing the nonlinear corrections for each of the terms in Equation (2). These corrections, with the exception of the body alone, are all empirical in nature.

2.2.1 Wing-Alone Method

One of the primary reasons for analyzing the slender body and linear theory implications on component aerodynamics in Appendix A was to show that the wing-alone methodology developed for the $\Phi = 0$ deg plane could also be applied in the $\Phi = 45$ deg plane. This was at least true in the linear sense. It will also be assumed to be true in the nonlinear sense. Any nonlinearities not accounted for in using the $\Phi = 0$ deg methods for $\Phi = 45$ deg will therefore be included in the interference factors.

As a result of this approach, the methodology of Reference 16 can be used directly. This methodology uses a fourth order equation in angle-of-attack to estimate wing-alone lift, as opposed to the second order approach of Reference 11. The specific equations are defined by

$$C_{N_W} = a_1 \alpha_w + a_2 \alpha_w^2 + a_3 \alpha_w^3 + a_4 \alpha_w^4 \tag{3}$$

$$a_2 = 34.044 \left(C_N\right)_{\alpha=15^\circ} - 4.824 \left(C_N\right)_{\alpha=35^\circ} + 0.426 \left(C_N\right)_{\alpha=60^\circ} - 6.412 a_1 \tag{4}$$

$$a_3 = -88.240 \left(C_N\right)_{\alpha=15^\circ} + 23.032 \left(C_N\right)_{\alpha=35^\circ} - 2.322 \left(C_N\right)_{\alpha=60^\circ} + 11.464 a_1 \tag{5}$$

$$a_4 = 53.219 \left(C_N\right)_{\alpha=15^\circ} - 17.595 \left(C_N\right)_{\alpha=35^\circ} + 2.661 \left(C_N\right)_{\alpha=60^\circ} - 5.971 a_1 \tag{6}$$

The term a_1 of Equations (3)-(6) is the value of the wing-alone lift curve slope at $\alpha = 0$ given by linear theory. The terms $\left(C_N\right)_{\alpha=15^\circ}$, $\left(C_N\right)_{\alpha=35^\circ}$ and $\left(C_N\right)_{\alpha=60^\circ}$ are values of the wing-alone normal force coefficients at $\alpha = 15$, 35, and 60 deg, respectively, defined by the data bases of References 2, 6 and 7. Above α_W of 60 deg, extrapolation of the aerodynamics at α_W of 60 deg is used. For more details of the method, the reader is referred to Reference 16. As shown in Reference 16, the fourth-order method of Equations (3)-(6) improves the wing-alone prediction accuracy below $\alpha_W = 30$ deg over the second-order method used in the AP93, while allowing wing-alone aerodynamic estimation to 180 deg.

The value of C_{N_W} computed by Equation (3) includes the linear and nonlinear term. To include it into a term like Equation (2B), requires this term to be separated into a linear and nonlinear component. This is easily done, as the linear term is known; so the nonlinear term is simply the difference between the total wing-alone value and its linear counterpart. The secant slope is then formed for each of these terms by dividing the linear and nonlinear parts by the local AOA, $\alpha + \delta$. This approach was taken for ease of incorporation into an existing, operational, linearized code.

The center of pressure of wing-alone normal force is predicted the same way as the AP93. That approach used a second order method to move the center of pressure from the linear theory value at $\alpha = 0$ to the centroid of the planform area at $\alpha = 60$ deg.

2.2.2 Body-Alone Method

The body-alone methodology is the same as that of Reference 1, with one exception. The one exception from the Reference 1 work is a slight shift in the C_{d_c} "drag bucket" at low crossflow Mach numbers. Reference 1 was optimized to the Reference 8 data base, which seemed to show a critical crossflow Reynolds number (the point where the C_{d_c} curve dropped from a value of 1.2 to a lower value that was caused by the flow remaining laminar over a greater portion of the body) around R_N of 330,000. On the other hand, most other wind tunnel results seemed to imply the Reference 13 drag bucket to be more representative of most data than that assumed as the baseline for the Aeroprediction Code. As a result, this drag bucket was implemented into the Aeroprediction Code. The effect of this is that the code is more in line with most other data bases, but is no longer as accurate for the Reference 8 data base. The user still has the option of shifting the drag bucket, however. Also, it was found that when two sets of lifting surfaces were present, the body alone data upon which this "drag bucket" was based were no longer valid, and a C_{d_c} of 1.2 at low subsonic crossflow Mach numbers seemed to be more appropriate.

Reference 1 basically modified the Allen-Perkins[17] methodology somewhat by using $\sin \propto$ versus $\propto$ and including crossflow Reynolds number in the crossflow drag computation at low crossflow Mach numbers. The center of pressure estimation is the same as that used in the AP95. In that approach, the nonlinear normal force center of pressure was assumed to occur at the centroid of the planform area. The linear theory center of pressure was computed analytically in most cases. Finally, an empirical data base was used to approximate center of pressure shifts due to transonic and asymmetric vortex effects.

2.2.3 Wing-Body and Body-Wing Interference Due to AOA

The wing-body and body-wing interference factors were computed using a combination of the Reference 8 data base for $0.6 \leq M_\infty \leq 4.6$ and the Reference 9 data base at $M = 0.1$. Outside these Mach limits, extrapolations were made to allow the methodology to compute aerodynamics at all Mach numbers. These extrapolations were not as difficult as they may seem because normal forces and center of pressure have basically leveled out at $M = 4.6$ and further increases in Mach number produce fairly small changes in these parameters.

The wing-body interference factor is defined as

$$K_{W(B)} = \frac{C_{N_{W(B)}}}{C_{N_W}} \tag{7}$$

Here $C_{N_{W(B)}}$ was measured directly in the data base of Reference 8 by having the wing in close proximity to the body and measuring directly the load on the wing in the presence of the body. Since the normal force was measured normal to a single fin, to get the normal force on the wing in the presence of the body at $\Phi = 45$ deg from the data required the data to be multiplied by cos Φ. To reduce measurement errors, the data from all four fins were averaged. Hence, if subscripts 1 through 4 represent the loads on the individual fins, then

$$C_{N_{W(B)}} = \frac{\cos \Phi}{2} \left[| C_{N_1} | + | C_{N_2} | + | C_{N_3} | + | C_{N_4} | \right] \tag{8}$$

No attempt was made to correct for wind tunnel errors near zero AOA caused by flow misalignments. These errors can cause the normal force curve to be shifted as much as a degree. This means that the $C_{N_{W(B)}}$ accuracy could have some slight errors near zero AOA.

Based on the accuracy analysis of Reference 1, this should give fairly accurate values of $K_{W(B)}$ for all but the highest aspect ratio where the wing planform area was only about 2 percent of the body planform area in the crossflow plane. C_{N_W} of Equation (7) was arrived at from Reference 1, which in turn used the data bases of References 2, 6 and 7. Figure 2 shows the wing and wing-body configurations tested in References 6, 8, and 9, respectively.

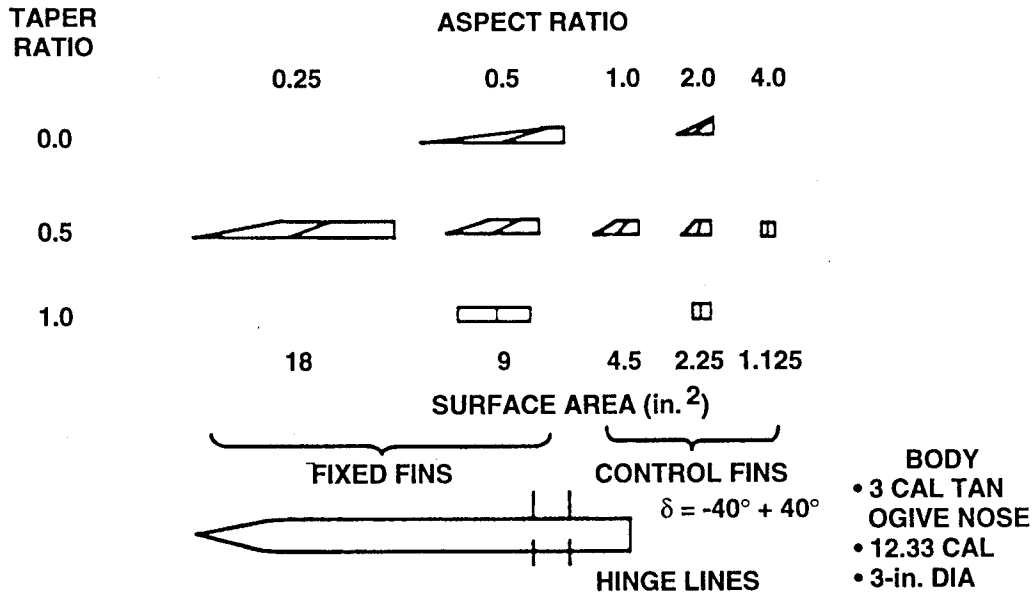

FIGURE 2A. MODELS USED IN LANGLEY[6] WING-BODY TESTS

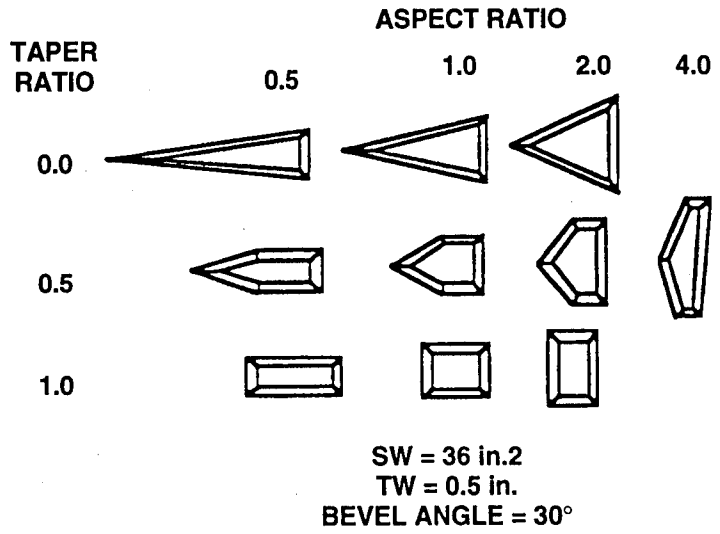

FIGURE 2B. MODELS USED IN STALLINGS AND LAMB[8] WING-ALONE TESTS

The body-wing interference factor is defined as

$$K_{B(W)} = \frac{C_{N_{B(W)}}}{C_{N_W}} \tag{9}$$

Unfortunately, $C_{N_{B(W)}}$ was not a quantity that was measured directly in Reference 6 but was computed from three other independent measurements of body alone, wing in conjunction with the body and total normal force. The computation for $C_{N_{B(W)}}$ was then made by

$$C_{N_{B(W)}} = C_N - C_{N_B} - C_{N_{W(B)}} \tag{10}$$

As shown in the Reference 1 error analysis, this process gave potential errors that were much higher than for $C_{N_{W(B)}}$, particularly for the smaller wings (AR ≥ 1.0) and higher Mach numbers (M ≥ 2.5), where the $C_{N_{B(W)}}$ term decreased to the point it was within the accuracy of the data. As a result, much more scatter in the data is expected for this term and more engineering judgement is required in the empirical model development.

Unlike Reference 8, Reference 9 had a fairly large wing planform area compared to the body planform area (approximately 60 percent). Moreover, $C_{N_{B(W)}}$ was apparently measured separately. Hence, $C_{N_{B(W)}}$ could be computed based on direct measurements as well as calculated similar to

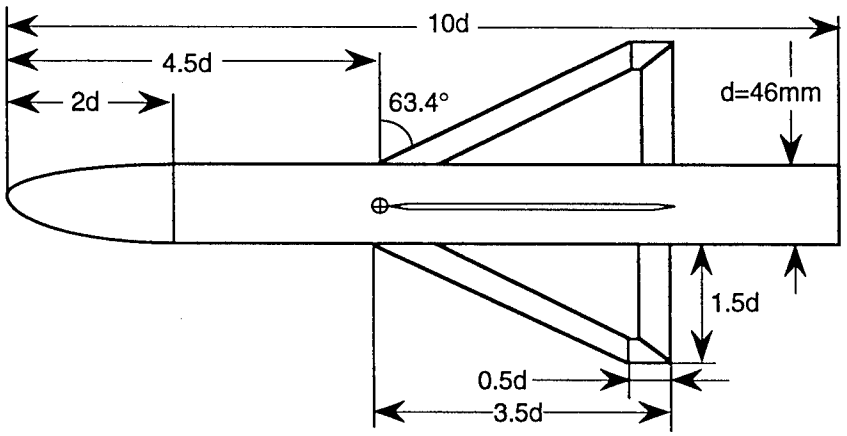

WING B - MID POSITION CONFIGURATION

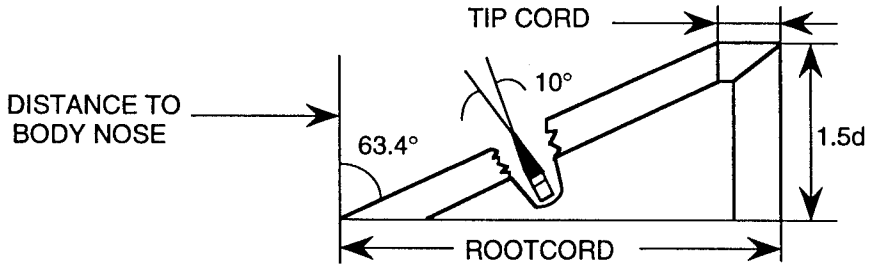

CONFIGURATION	DISTANCE TO NOSE	ROOT CHORD	TIP CHORD
WING A - MID POSITION	4.5d	3.0d	0.0d
WING B - FORE POSITION	2.4d	3.5d	0.5d
WING B - MID POSITION	4.5d	3.5d	0.5d
WING B - BACK POSITION	6.0d	3.5d	0.5d
WIND C - MID POSITION	4.5d	4.0d	1.0d

FIGURE 2C. MODELS USED IN MEYER'S[9] WING-BODY TESTS

Equation (10). Also, data were obtained all the way to $\propto = 90$ deg and at an r/s value of 0.25. As a result, more confidence is placed on the Reference 9 body-wing interference at high angle of attack than the Reference 8 data. Unfortunately, the Reference 9 data were taken only at $M_\infty = 0.1$, so it is hard to extrapolate it past about $M_\infty = 0.6$. Fortunately, it compliments the Mach number range of the larger Reference 8 data base quite nicely.

Figures 3-21 present the computed results for $K_{W(B)}$ and $K_{B(W)}$ for the various fin planforms at the various Mach numbers covered by the data bases of References 8 and 9 for $\Phi = 45$ deg. Also shown on the figures are the slender body theory or linear theory results for $K_{W(B)}$ and $K_{B(W)}$ along with approximations to the data that will be used in the empirical model. In examining the $\Phi = 45$ deg data of Figures 3-21, it is seen that the data follow the same general trends as the $\Phi = 0$ deg data of Reference 1. That is, $K_{W(B}$ decreases with increasing angle of attack until a minimum is reached. The Reference 9 data showed this minimum to be about 20 percent lower than the $\Phi = 0$ deg data. This difference in minimums could not be confirmed by the Reference 6 data because of a lack of data above $\propto = 25$ to 30 deg subsonically and 40 deg supersonically. In fact, at supersonic speeds, the Reference 6 data seemed to indicate a minimum value of $K_{W(B)}$ near one at high $\propto$, similar to the $\Phi = 0$ deg data. Also as seen in the figures, SBT gives a reasonable approximation to $K_{W(B)}$ at $\propto$ up to about 10 to 15 deg, but becomes increasingly inaccurate as $\propto$ increases.

The $K_{B(W)}$ data follow generally the same trends as that for $\Phi = 0$. However, it is seen that the magnitude of $K_{B(W)}$ is somewhat different at both subsonic and supersonic speeds. Take a couple of specific cases for example to illustrate this. One of these is the M = 0.8 data for AR = 0.5. The $\Phi = 0$ deg data increase with $\propto$ until a maximum is reached somewhere around 20 to 30 deg AOA, after which $K_{B(W)}$ starts decreasing. The maximum value is above that estimated by SBT.[1] Referring to Figure 5 for the $\Phi = 45$ deg data, it is seen that the $K_{B(W)}$ data start out near the SBT but decrease continually with angle of attack. The minimum value of 25 percent of SBT is assumed based on the Figure 3 high AOA data. This fairly large difference between the $\Phi = 0$ and $\Phi = 45$ deg data for $K_{B(W)}$ is the main reason missiles flying at the $\Phi = 45$ deg orientation have less lift and static stability than those flying at $\Phi = 0$ deg orientation at subsonic Mach numbers and $\propto > 10$ deg.

A second case is considered to compare $K_{B(W)}$ at $\Phi = 0$ and $\Phi = 45$ deg. Again, the aspect ratio 0.5 case is considered, but at $M_\infty = 3.0$ (see Figure 10). Reference 1 gave the $\Phi = 0$ deg $K_{B(W)}$ as close to the SBT value at $\propto = 0$, decreasing to 0.4 to 0.6 at $\propto = 25$ deg. Again Figure 10 shows a value of $K_{B(W)}$ of about half that at $\Phi = 0$ deg, again indicating a lower normal force and less stability from the body carryover term for $\Phi = 45$ deg versus $\Phi = 0$ deg roll.

All the data in Figures 3-21 for $K_{W(B)}$ and $K_{B(W)}$ can be generically represented by Figures 22 and 23. Referring to Figure 22 first, it is seen that there are six parameters needed to represent the $K_{W(B)}$ as a function of $\propto$, M, and fin planform. These are defined as follows:

$\left[\Delta K_{W(B)}\right]_{\propto=0}$ = difference between SBT and data at $\propto = 0$

$\propto_C$ = angle of attack where $K_{W(B)}$ starts decreasing

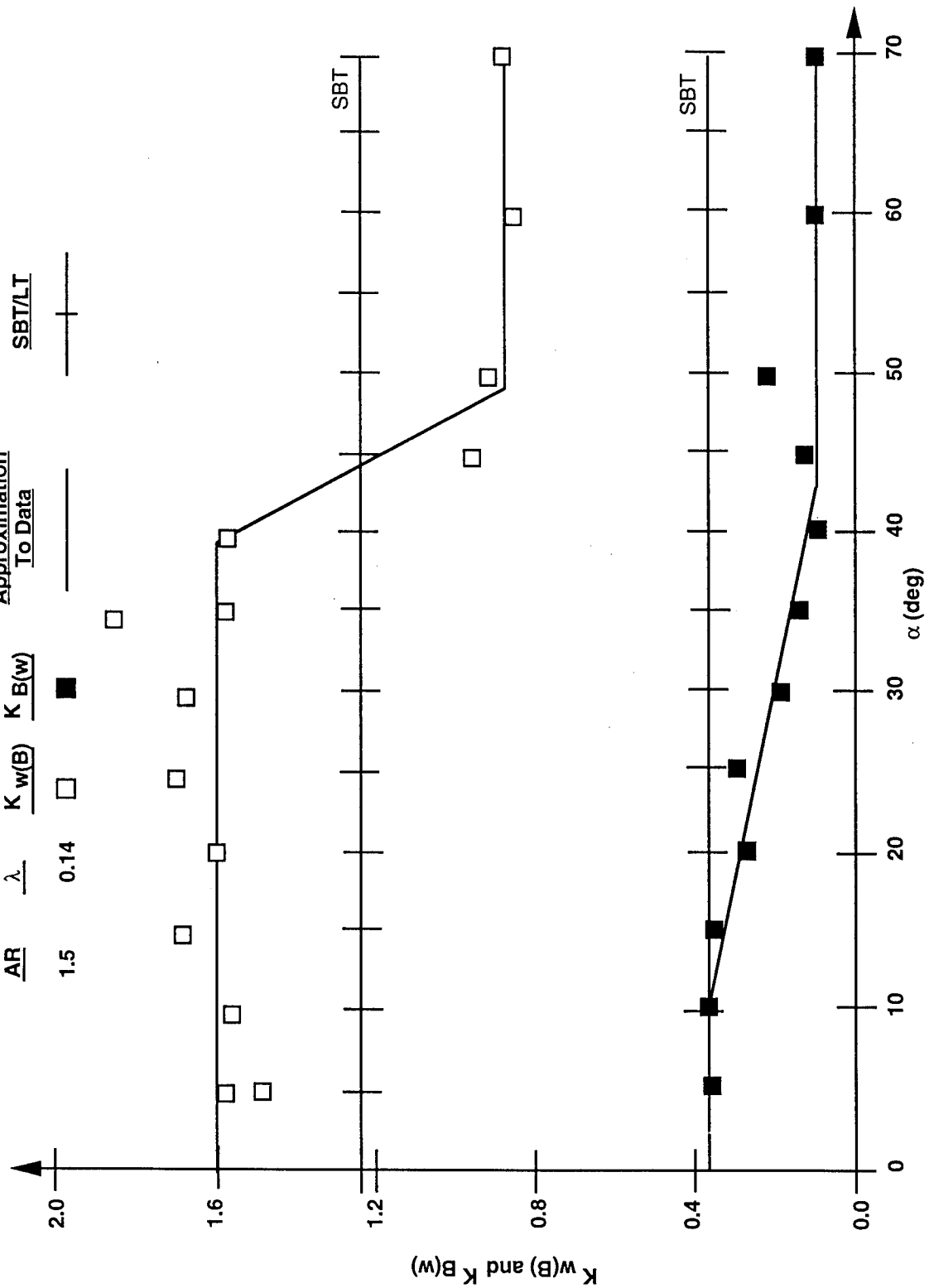

FIGURE 3. WING-BODY AND BODY-WING INTERFERENCE FACTORS AS A FUNCTION OF AOA ($M_\infty = 0.1$, r/s = 0.25, AR = 1.5)

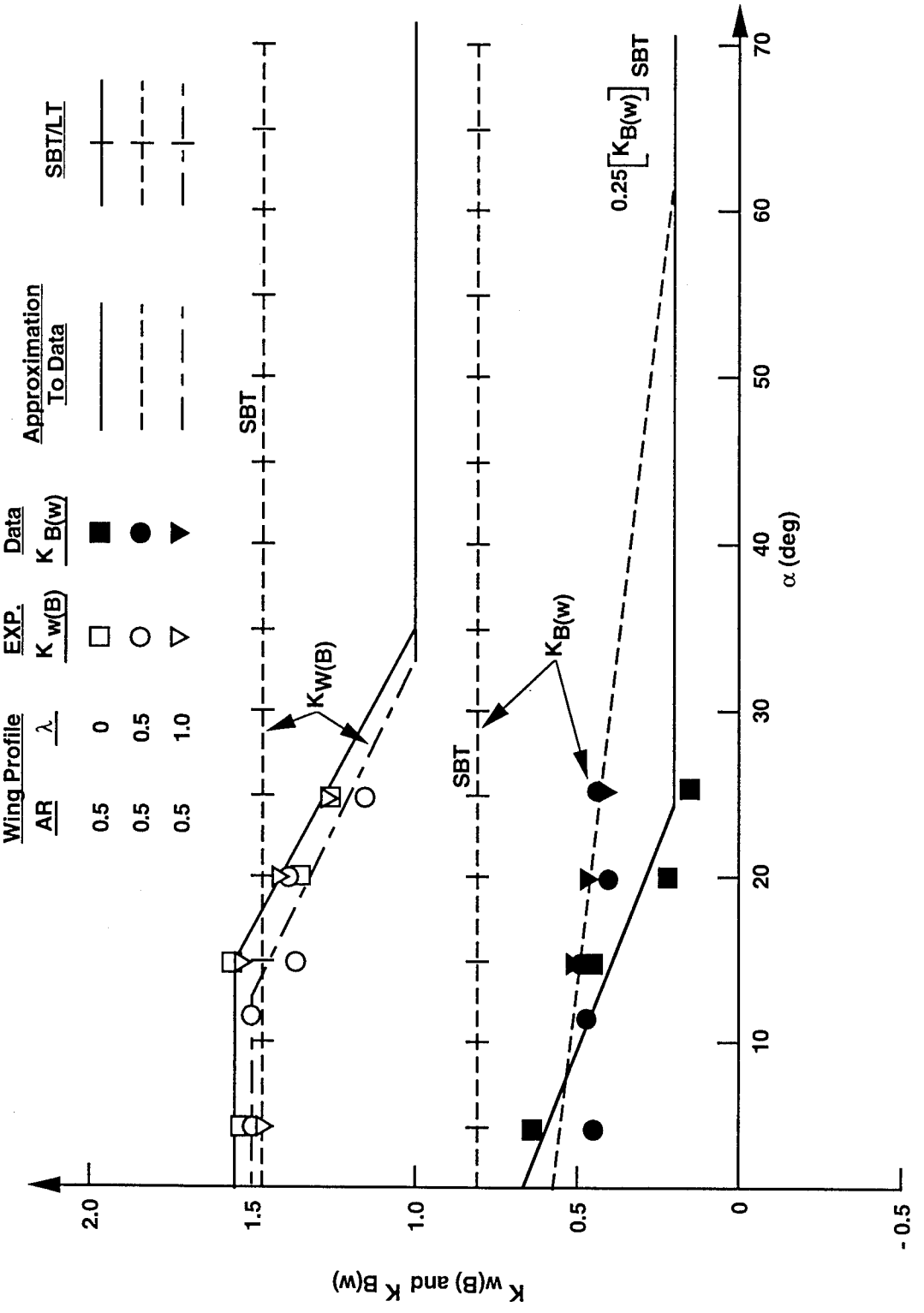

FIGURE 4. WING-BODY AND BODY-WING INTERFERENCE FACTORS AS A FUNCTION OF AOA ($M_\infty = 0.6$, $r/s = 0.5$, AR = 0.5)

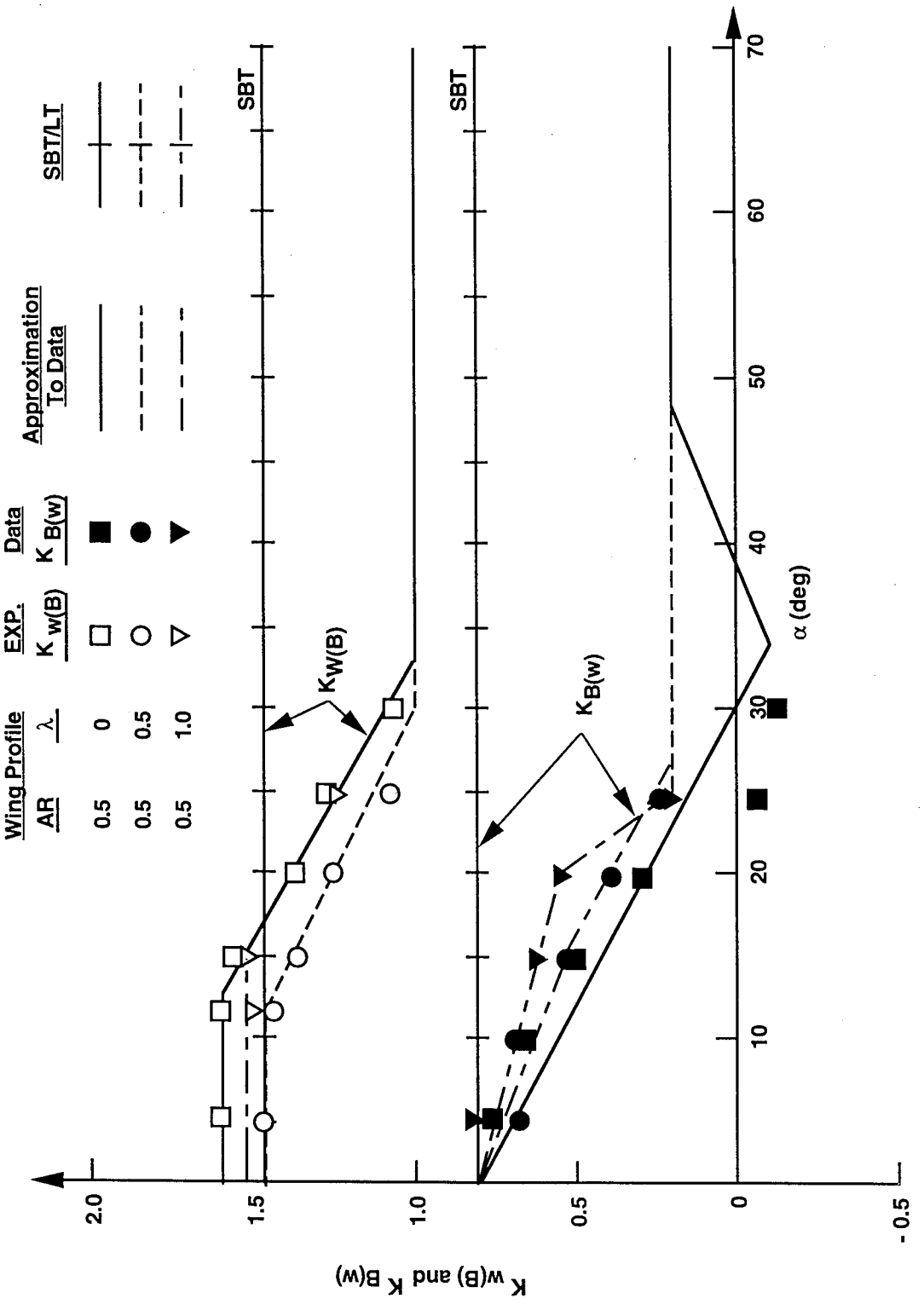

FIGURE 5. WING-BODY AND BODY-WING INTERFERENCE FACTORS AS A FUNCTION OF AOA ($M_\infty = 0.8$, r/s = 0.5, AR = 0.5)

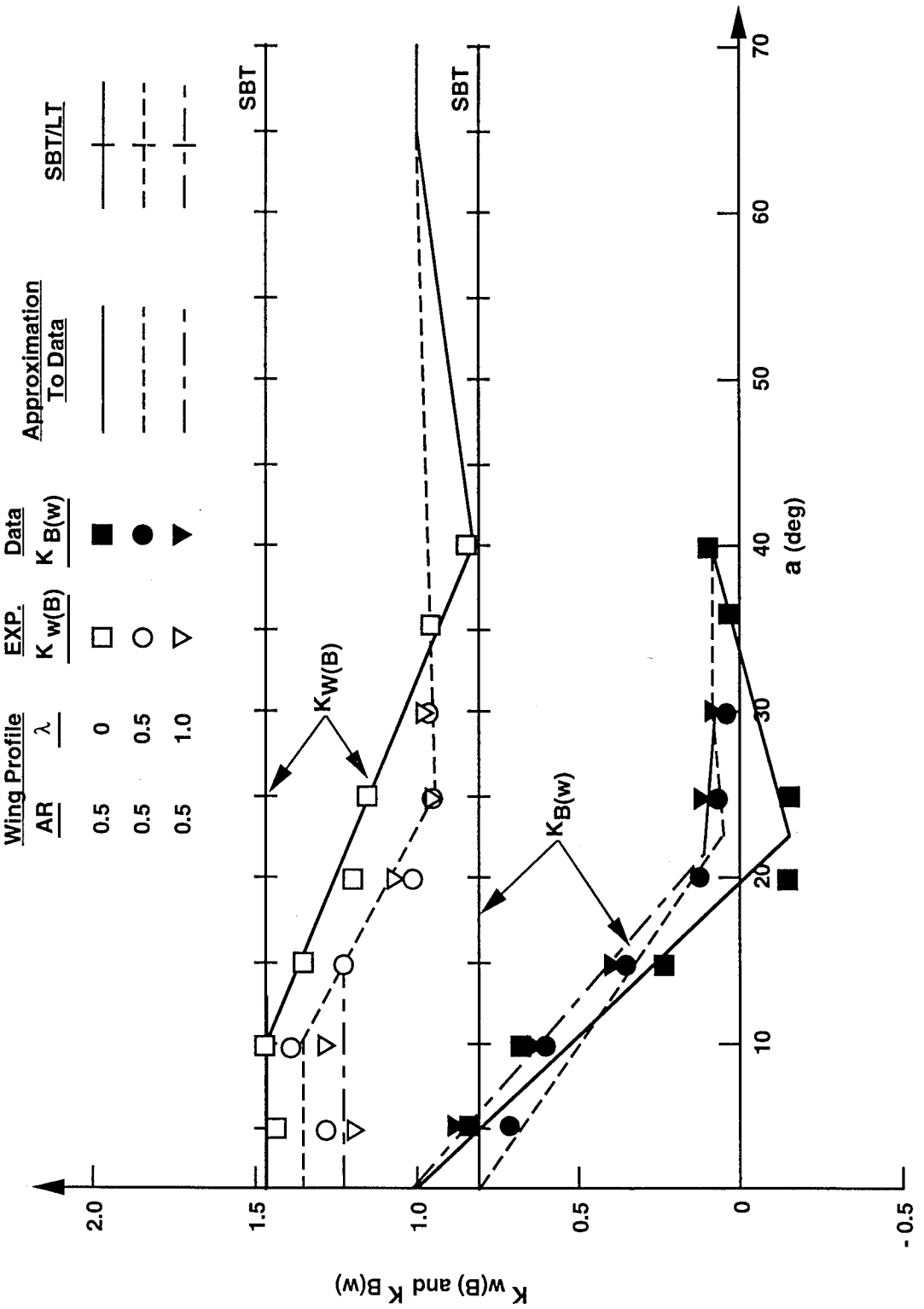

FIGURE 6. WING-BODY AND BODY-WING INTERFERENCE FACTORS AS A FUNCTION OF AOA ($M_\infty = 1.2$, $r/s = 0.5$, AR = 0.5)

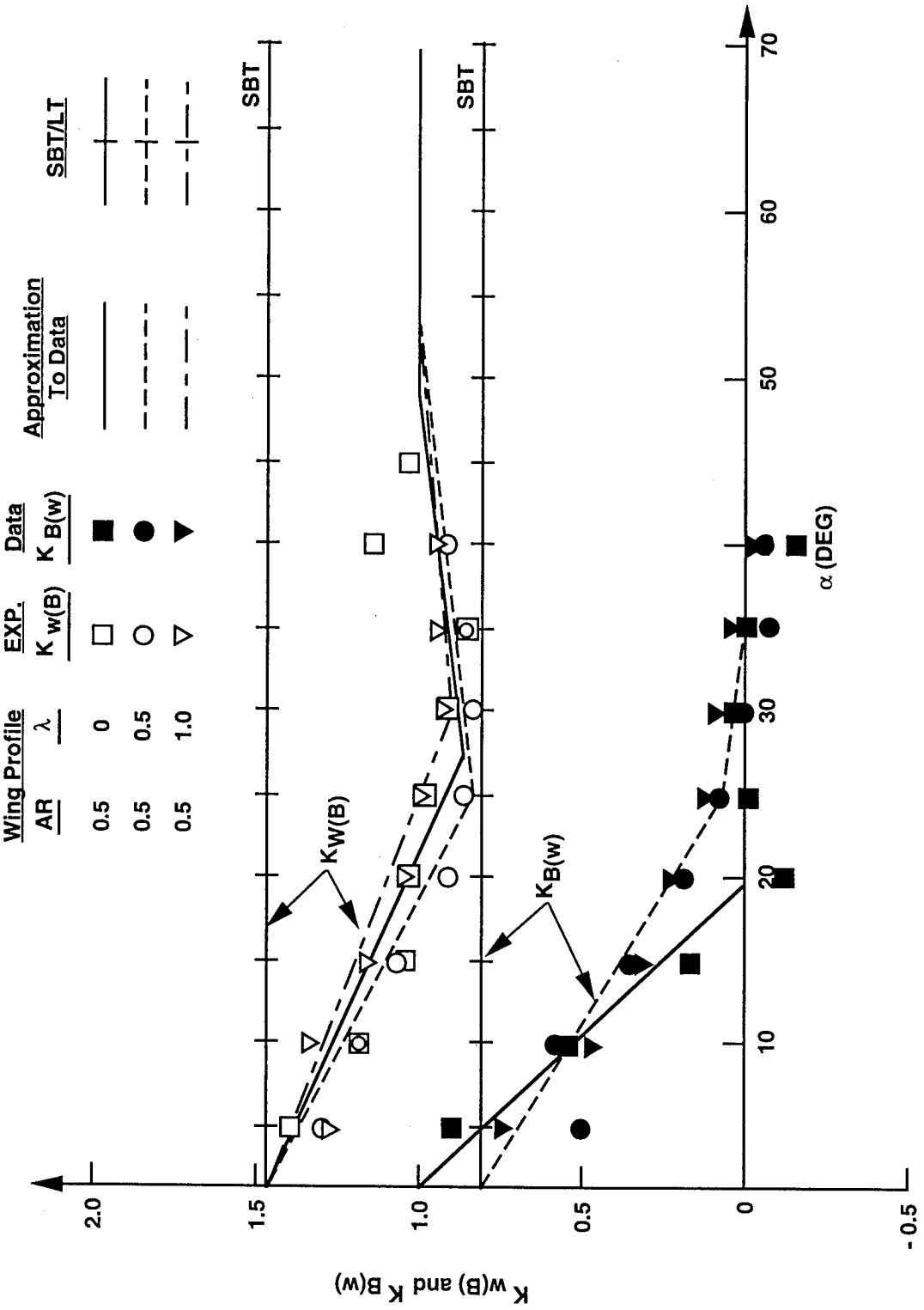

FIGURE 7. WING-BODY AND BODY-WING INTERFERENCE FACTORS AS A FUNCTION OF AOA (M_∞ = 1.5, r/s = 0.5, AR = 0.5)

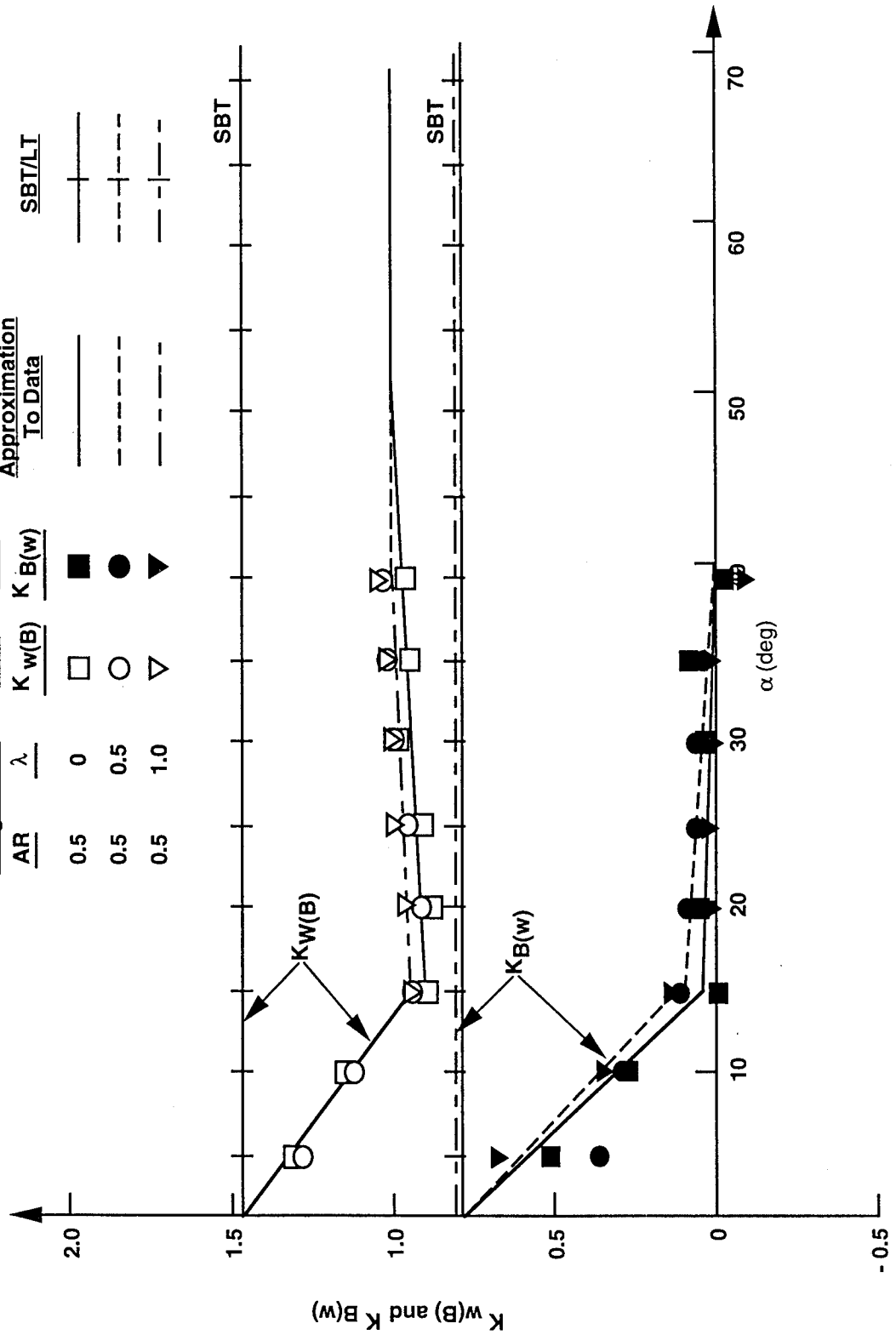

FIGURE 8. WING-BODY AND BODY-WING INTERFERENCE FACTORS AS A FUNCTION OF AOA ($M_\infty = 2.0$, r/s = 0.5, AR = 0.5)

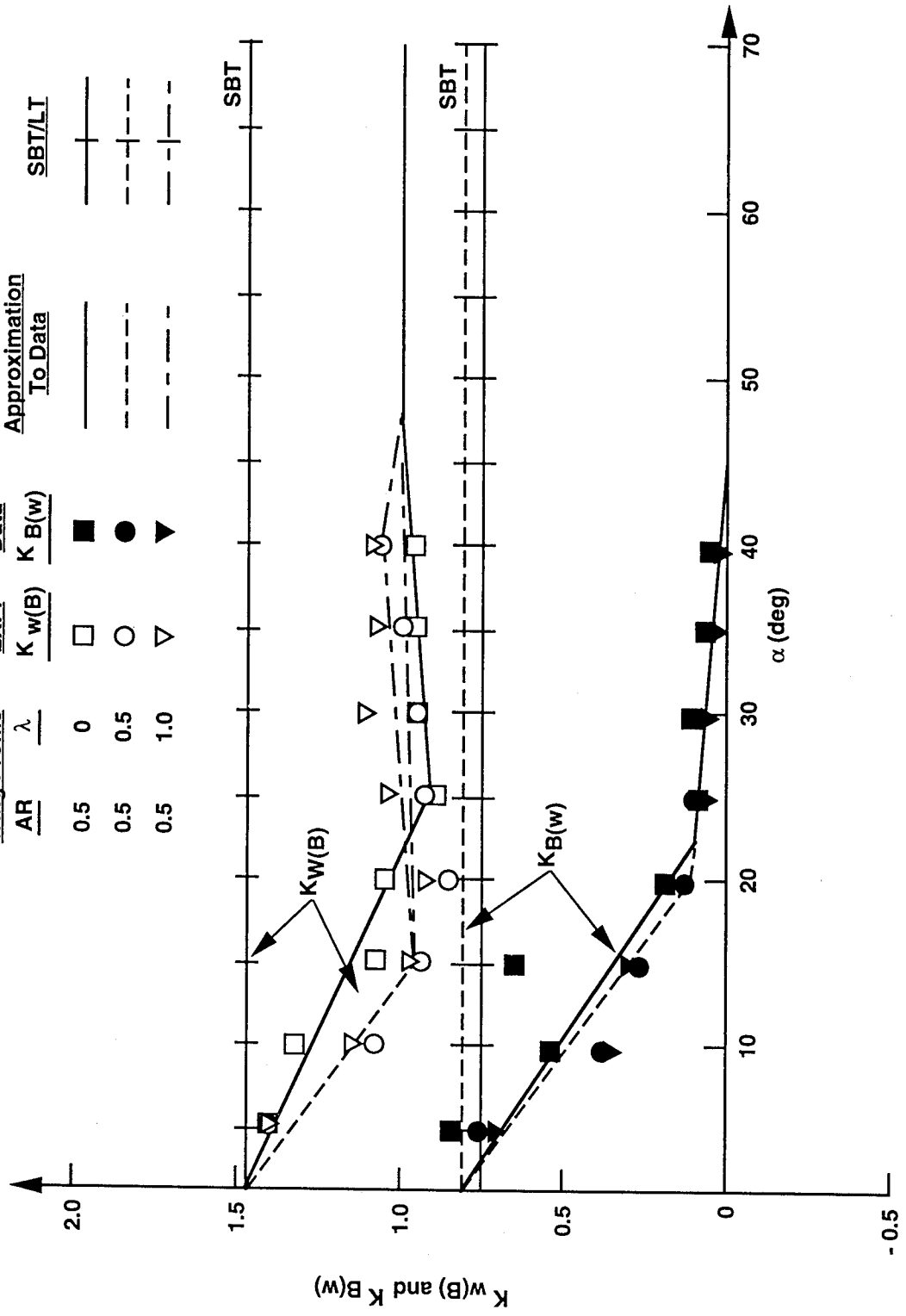

FIGURE 9. WING-BODY AND BODY-WING INTERFERENCE FACTORS AS A FUNCTION OF AOA ($M_\infty = 2.5$, $r/s = 0.5$, AR = 0.5)

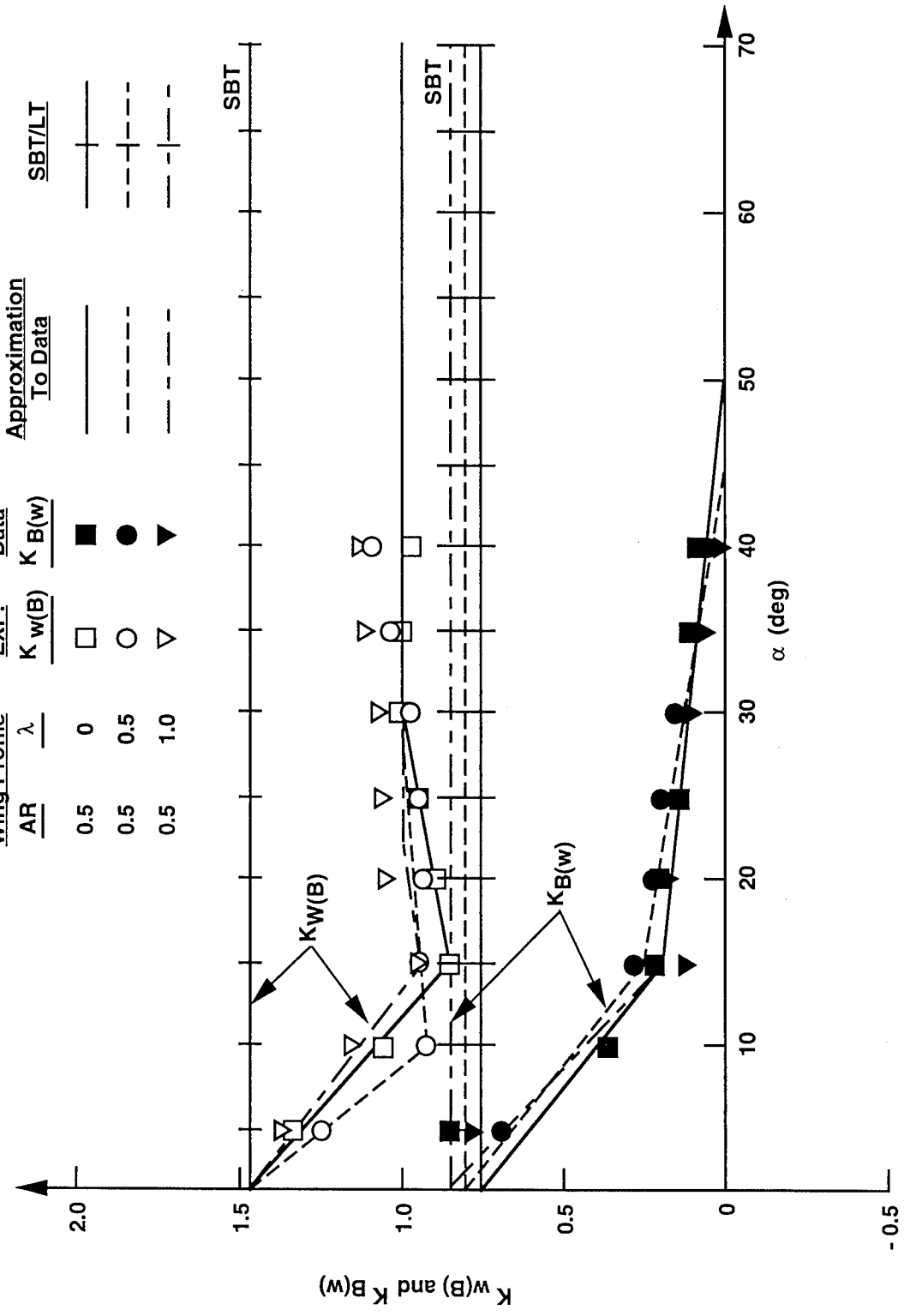

FIGURE 10. WING-BODY AND BODY-WING INTERFERENCE FACTORS AS A FUNCTION OF AOA ($M_\infty = 3.0$, r/s = 0.5, AR = 0.5)

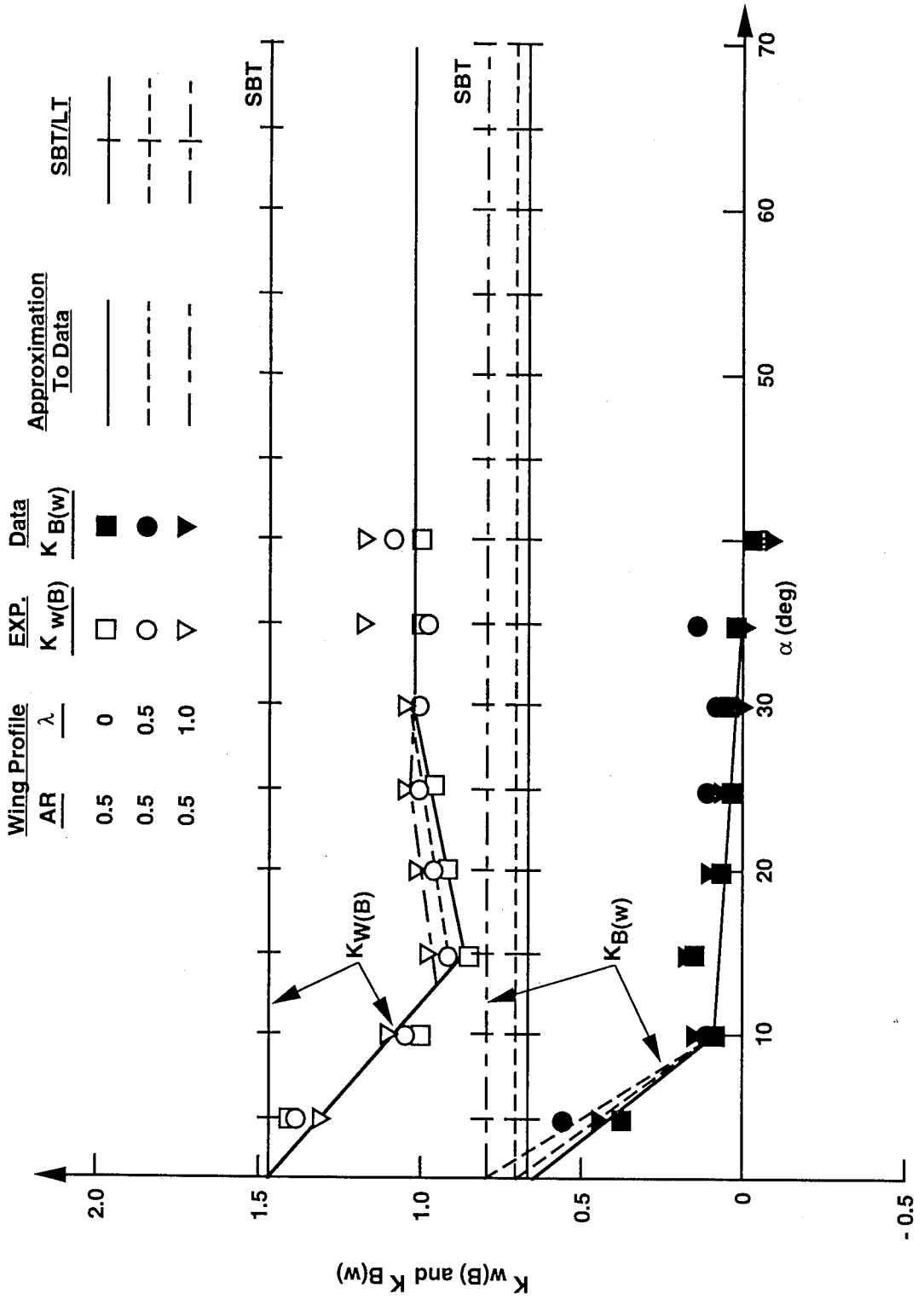

FIGURE 11. WING-BODY AND BODY-WING INTERFERENCE FACTORS AS A FUNCTION OF AOA ($M_\infty = 3.5$, r/s = 0.5, AR = 0.5)

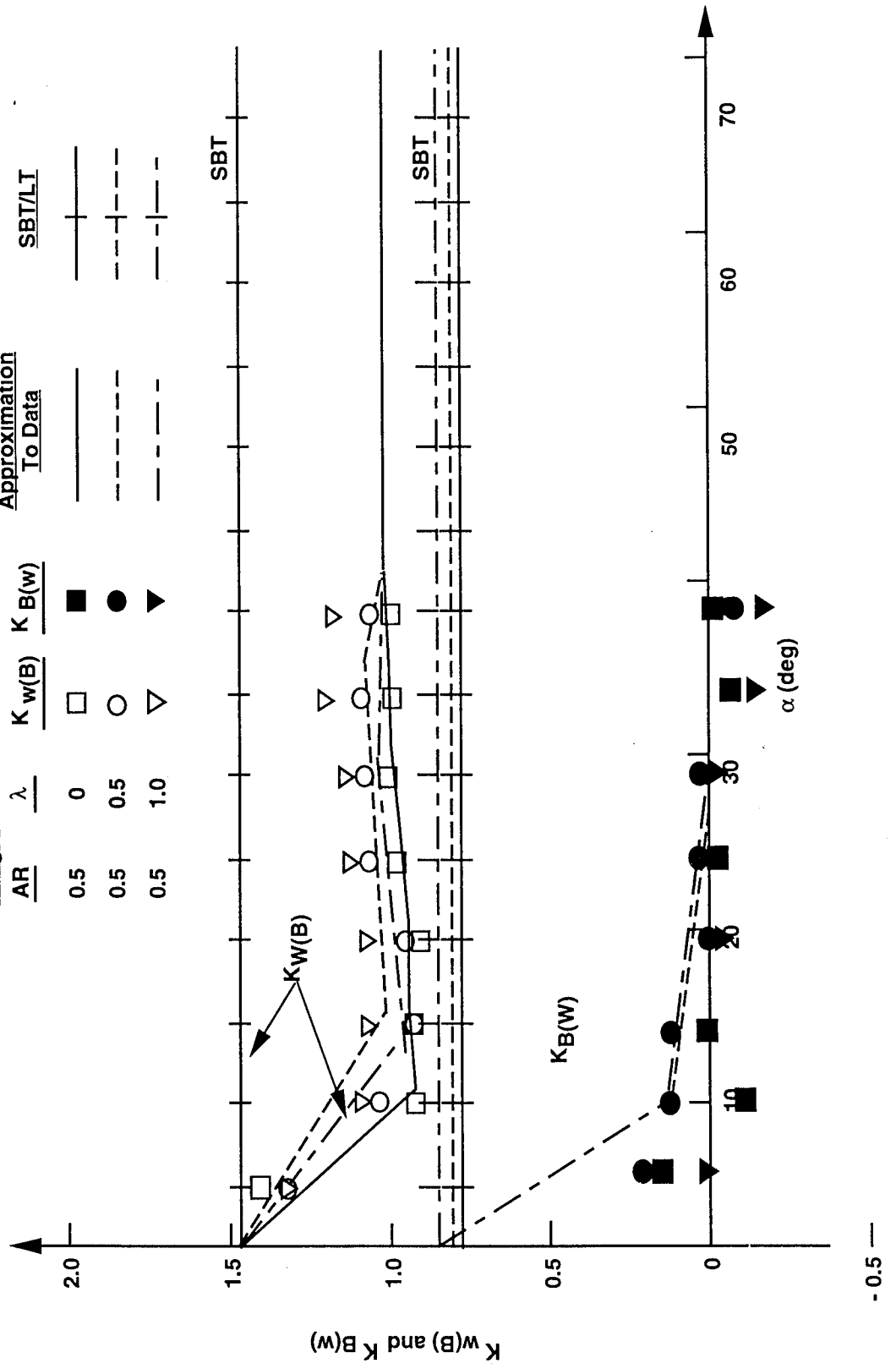

FIGURE 12. WING-BODY AND BODY-WING INTERFERENCE FACTORS AS A FUNCTION OF AOA (M_∞ = 4.5, r/s = 0.5, AR = 0.5)

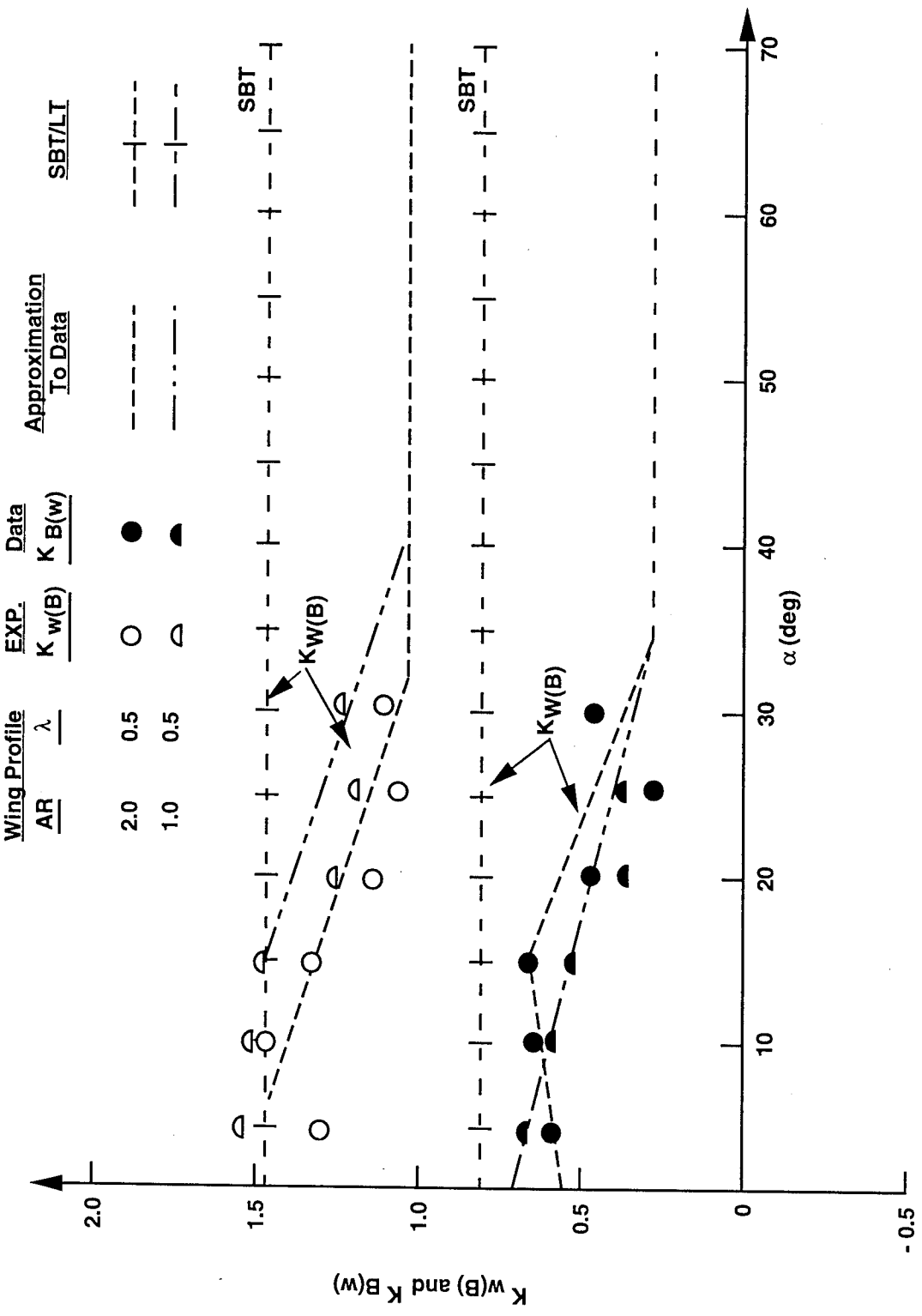

FIGURE 13. WING-BODY AND BODY-WING INTERFERENCE FACTORS AS A FUNCTION OF AOA ($M_\infty = 0.6$, r/s = 0.5, AR = 1,2)

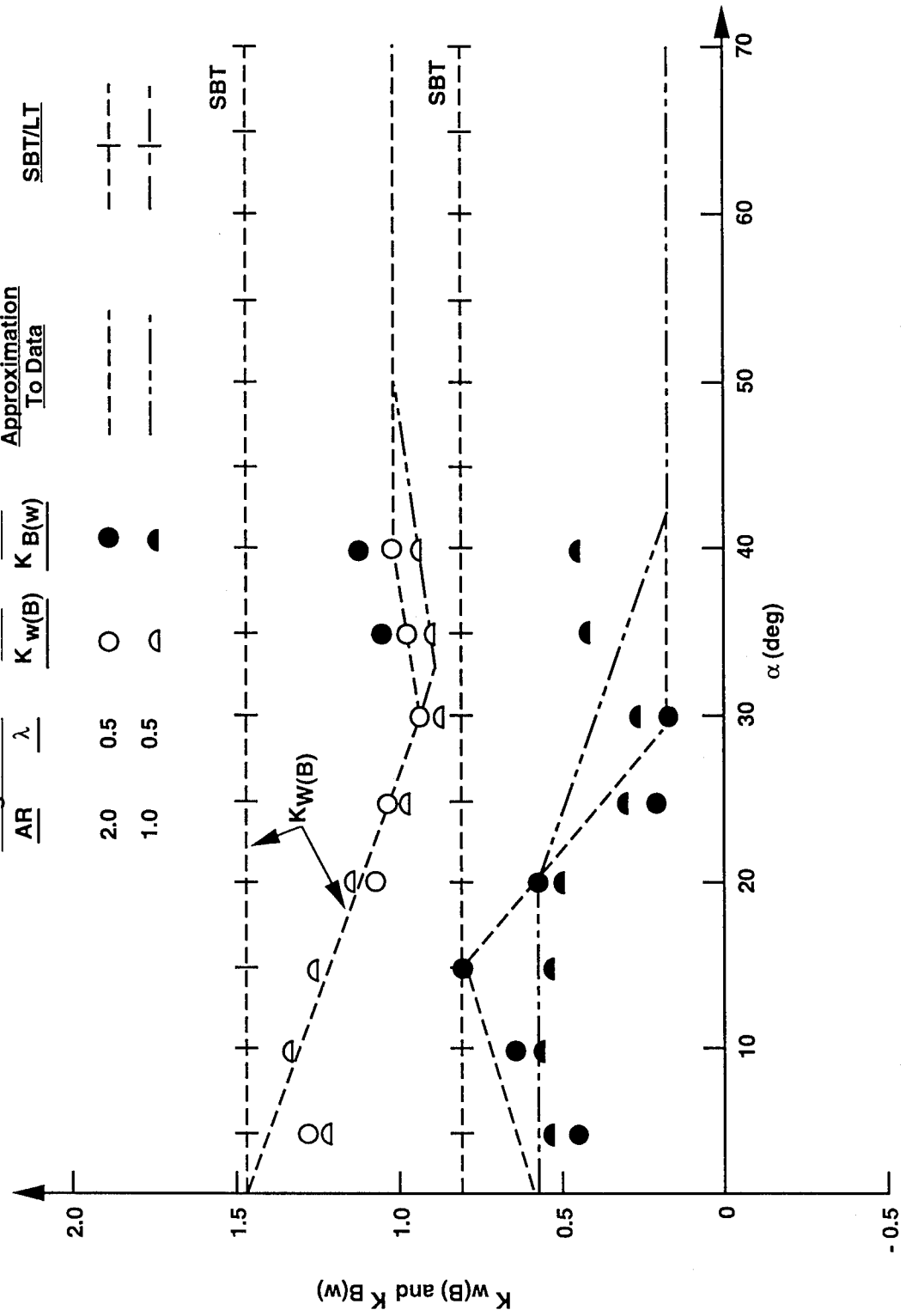

FIGURE 14. WING-BODY AND BODY-WING INTERFERENCE FACTORS AS A FUNCTION OF AOA ($M_\infty = 0.8$, $r/s = 0.5$, AR = 1,2)

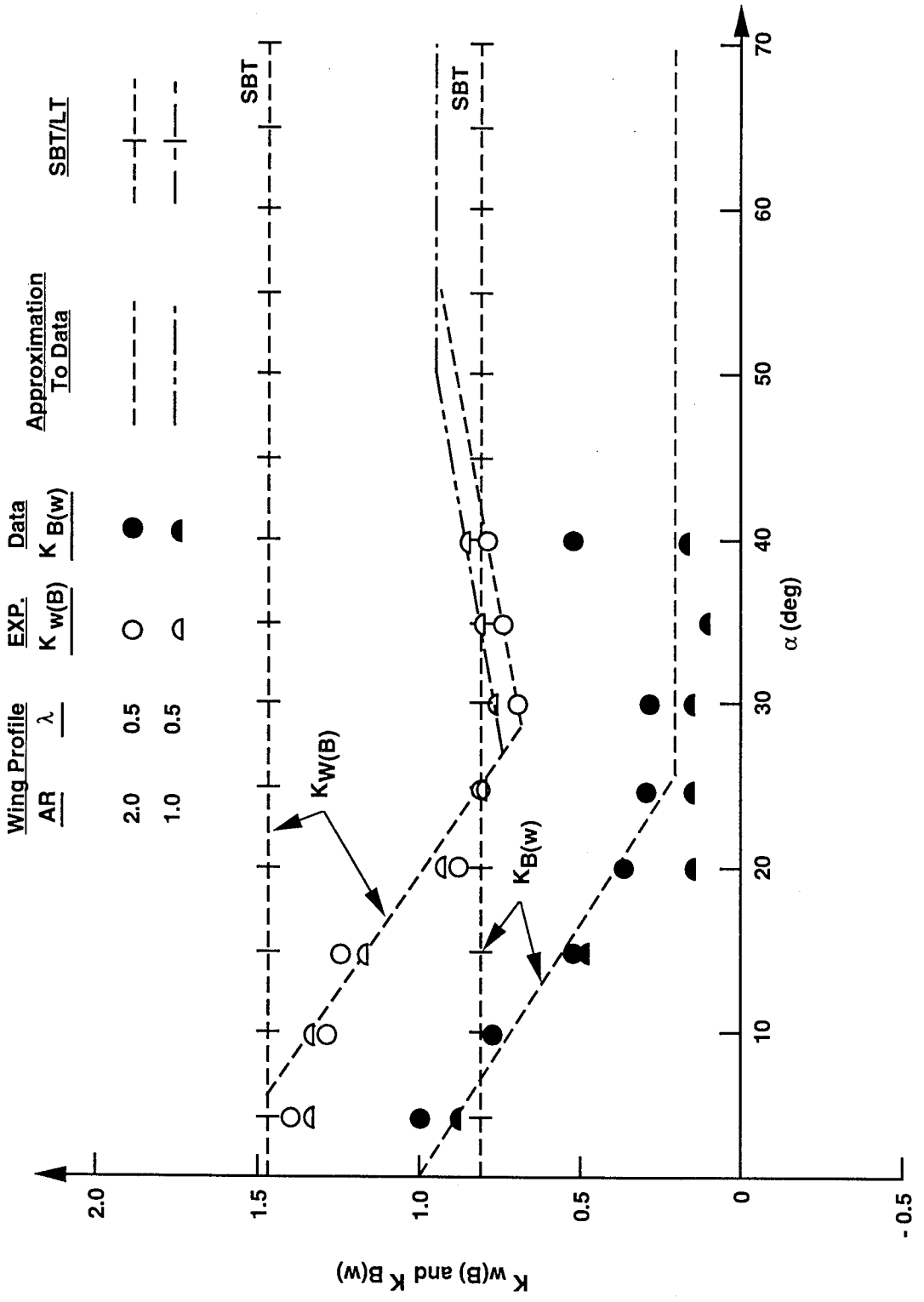

FIGURE 15. WING-BODY AND BODY-WING INTERFERENCE FACTORS AS A FUNCTION OF AOA (M_∞ = 1.2, r/s = 0.5, AR = 1,2)

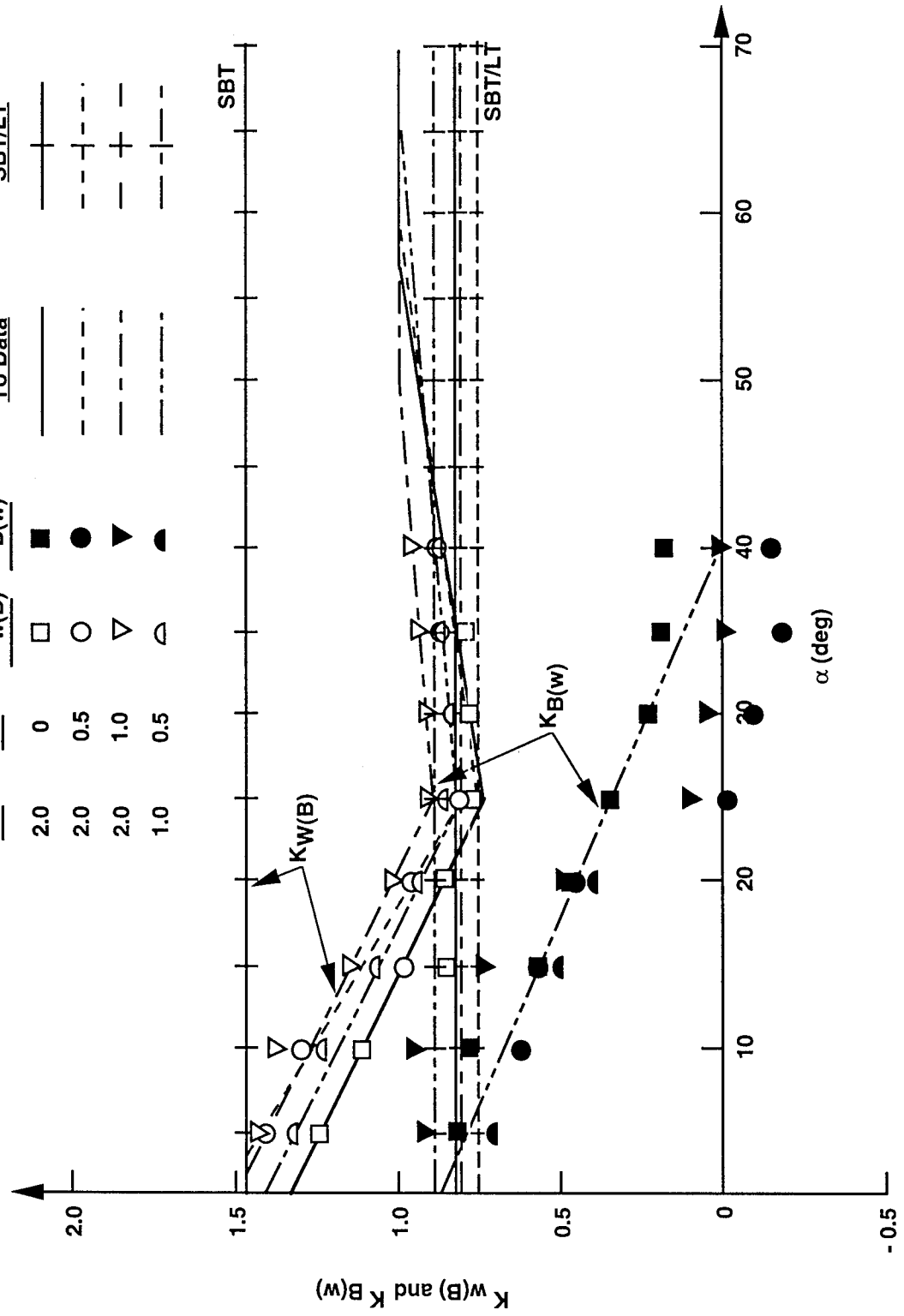

FIGURE 16. WING-BODY AND BODY-WING INTERFERENCE FACTORS AS A FUNCTION OF AOA (M_∞ = 1.5, r/s = 0.5, AR = 1,2)

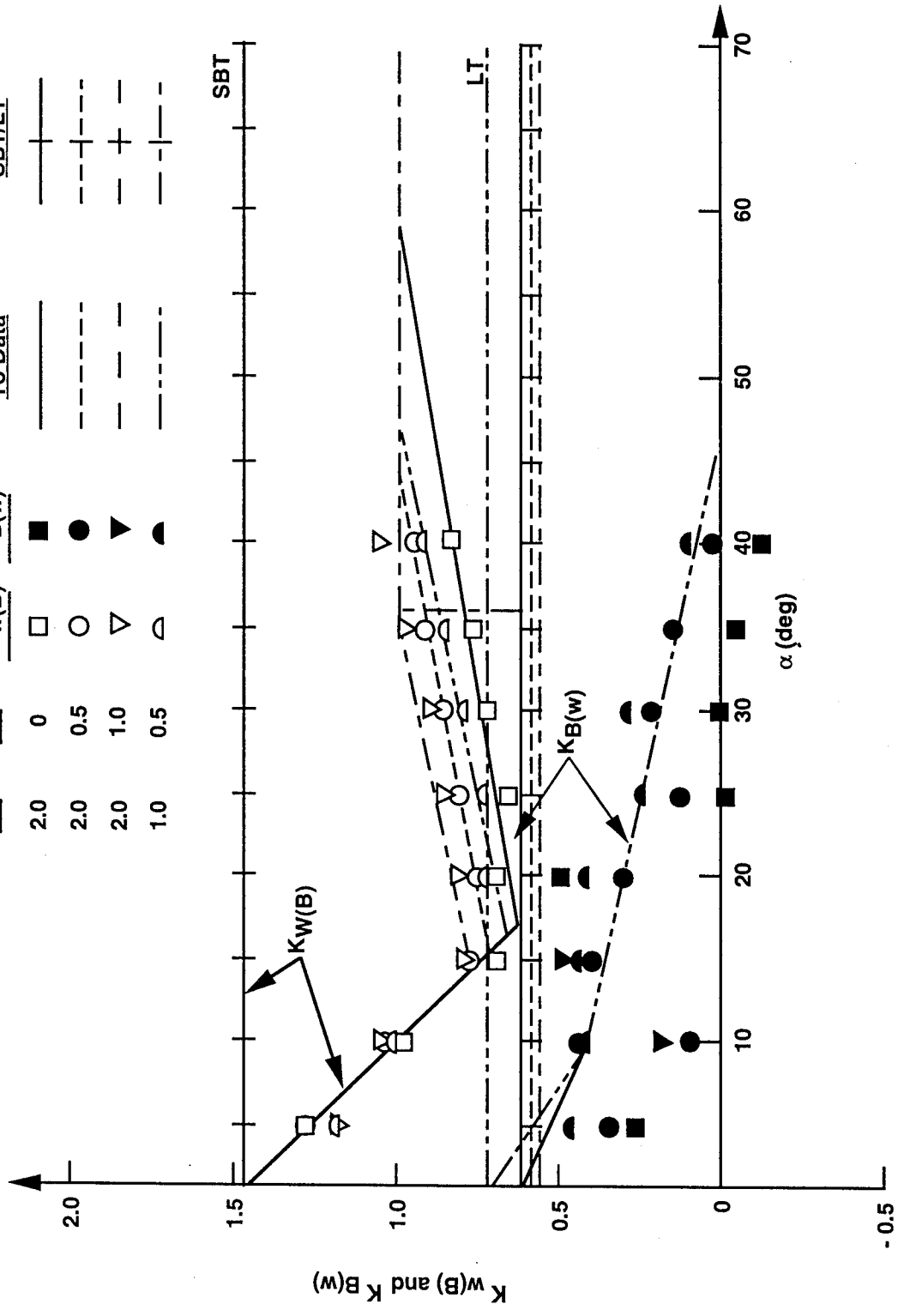

FIGURE 17. WING-BODY AND BODY-WING INTERFERENCE FACTORS AS A FUNCTION OF AOA (M_∞ = 2.0, r/s = 0.5, AR = 1,2)

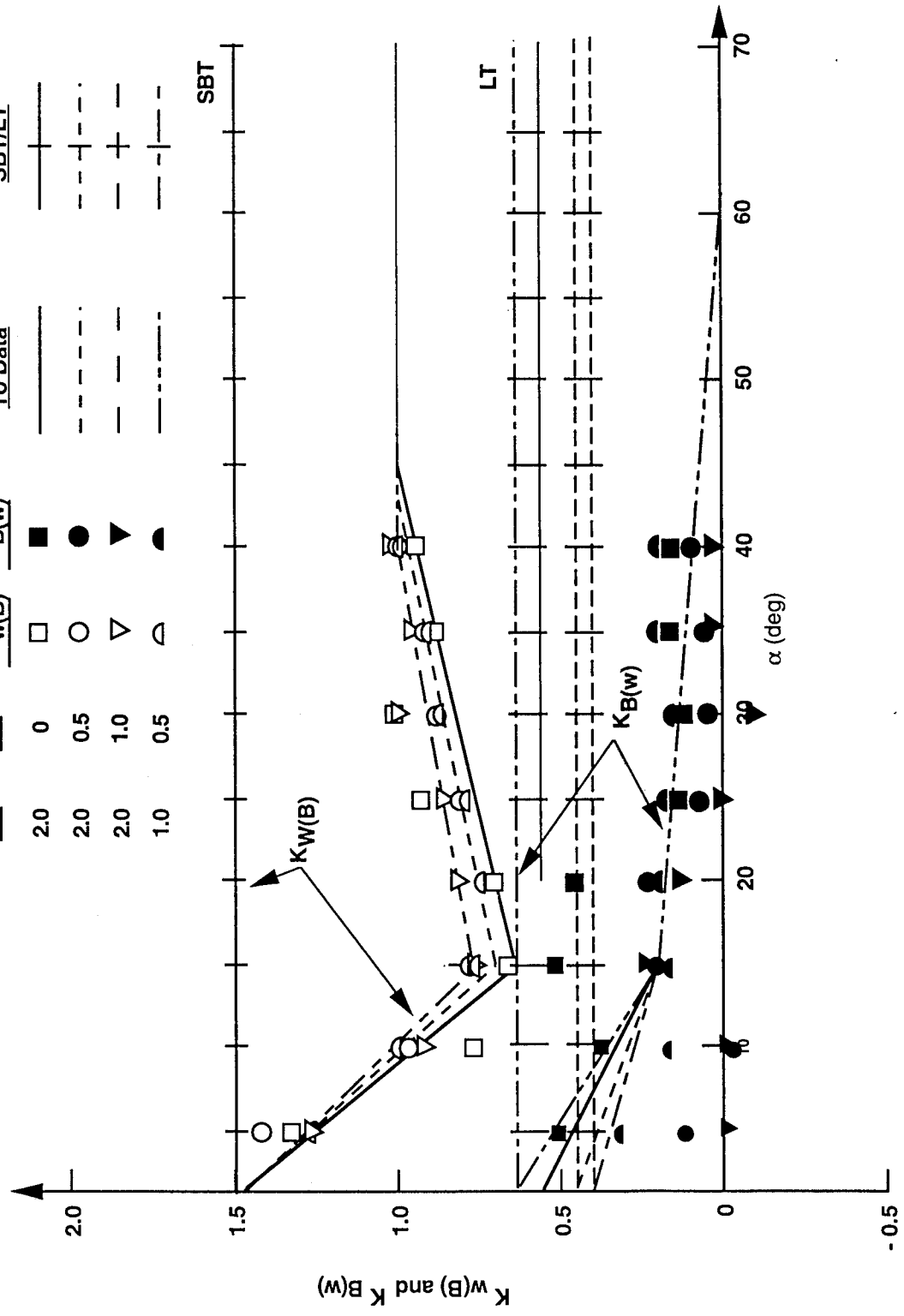

FIGURE 18. WING-BODY AND BODY-WING INTERFERENCE FACTORS AS A FUNCTION OF AOA (M_∞ = 2.5, r/s = 0.5, AR = 1,2)

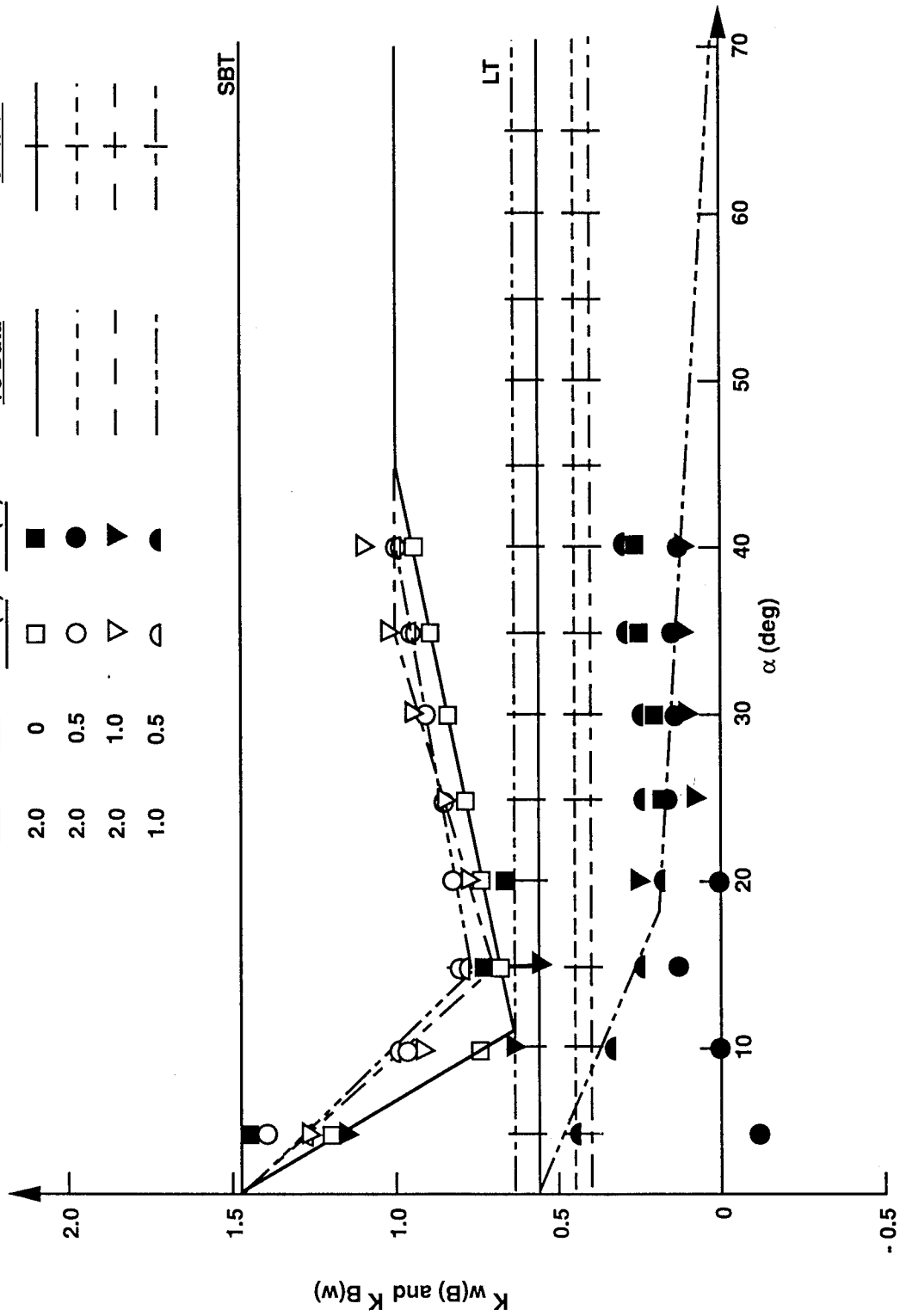

FIGURE 19. WING-BODY AND BODY-WING INTERFERENCE FACTORS AS A FUNCTION OF AOA ($M_\infty = 3.0$, r/s = 0.5, AR = 1,2)

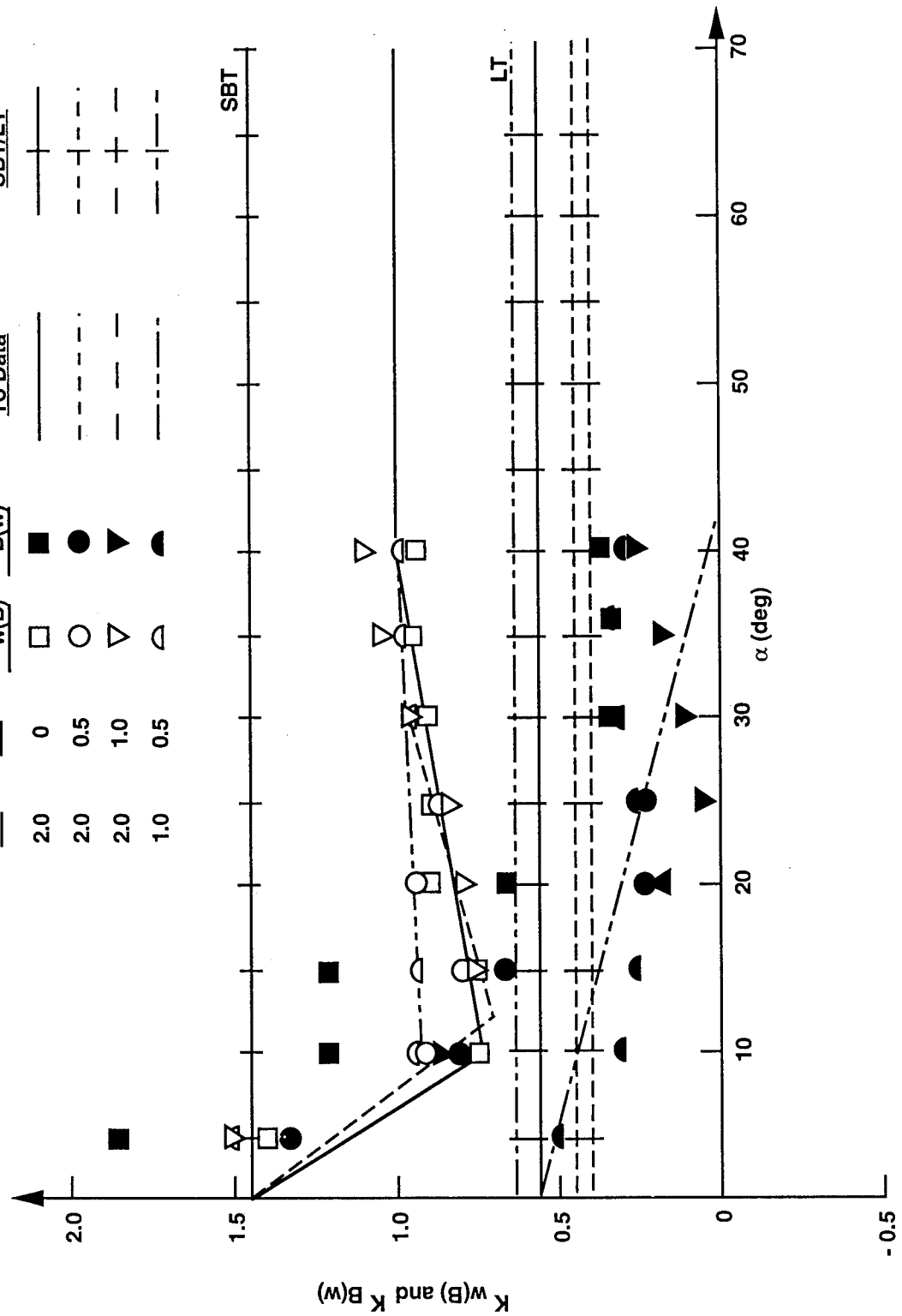

FIGURE 20. WING-BODY AND BODY-WING INTERFERENCE FACTORS AS A FUNCTION OF AOA ($M_\infty = 3.5$, r/s = 0.5, AR = 1,2)

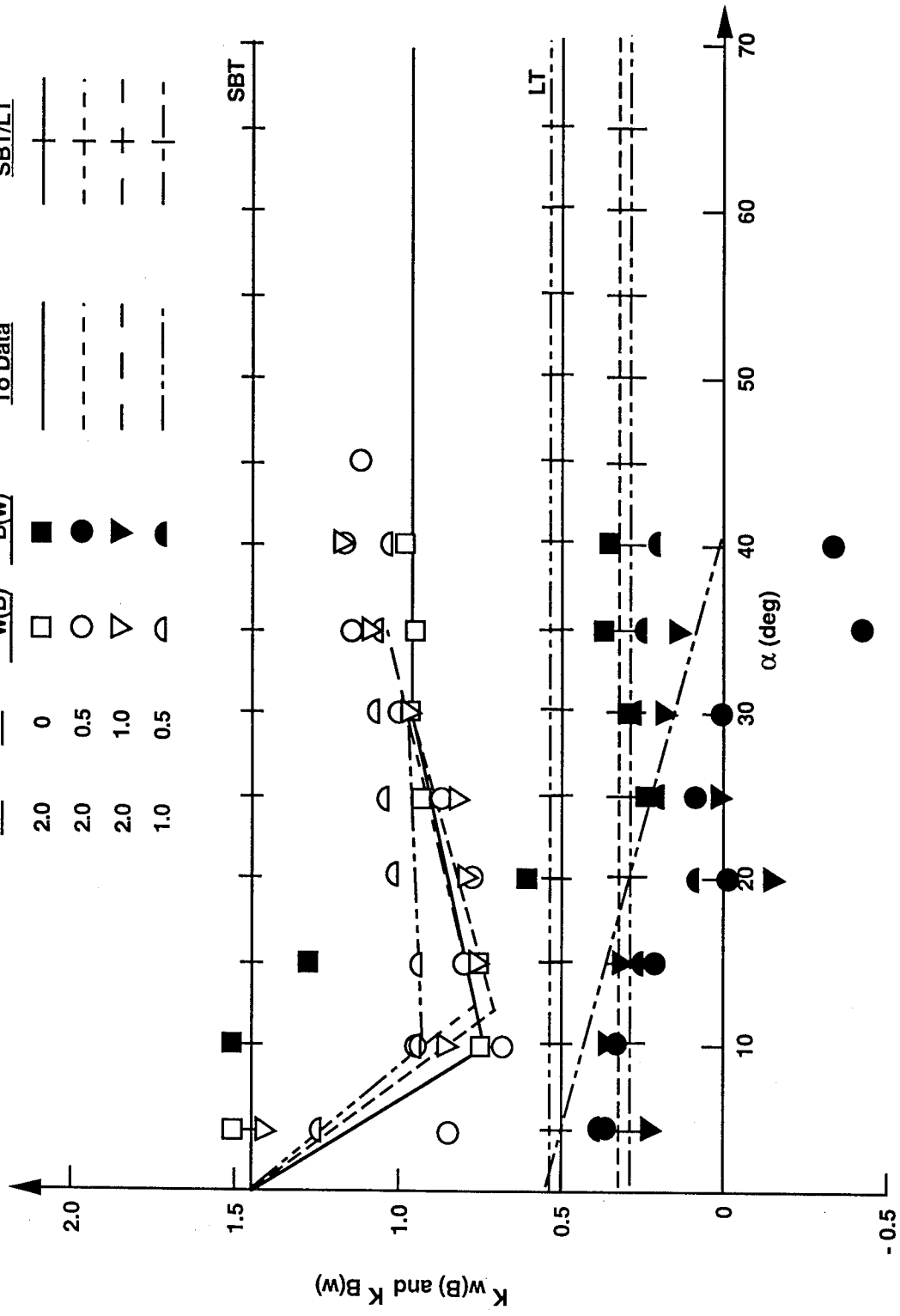

FIGURE 21. WING-BODY AND BODY-WING INTERFERENCE FACTORS AS A FUNCTION OF AOA (M_∞ = 4.5, r/s = 0.5, AR = 1,2)

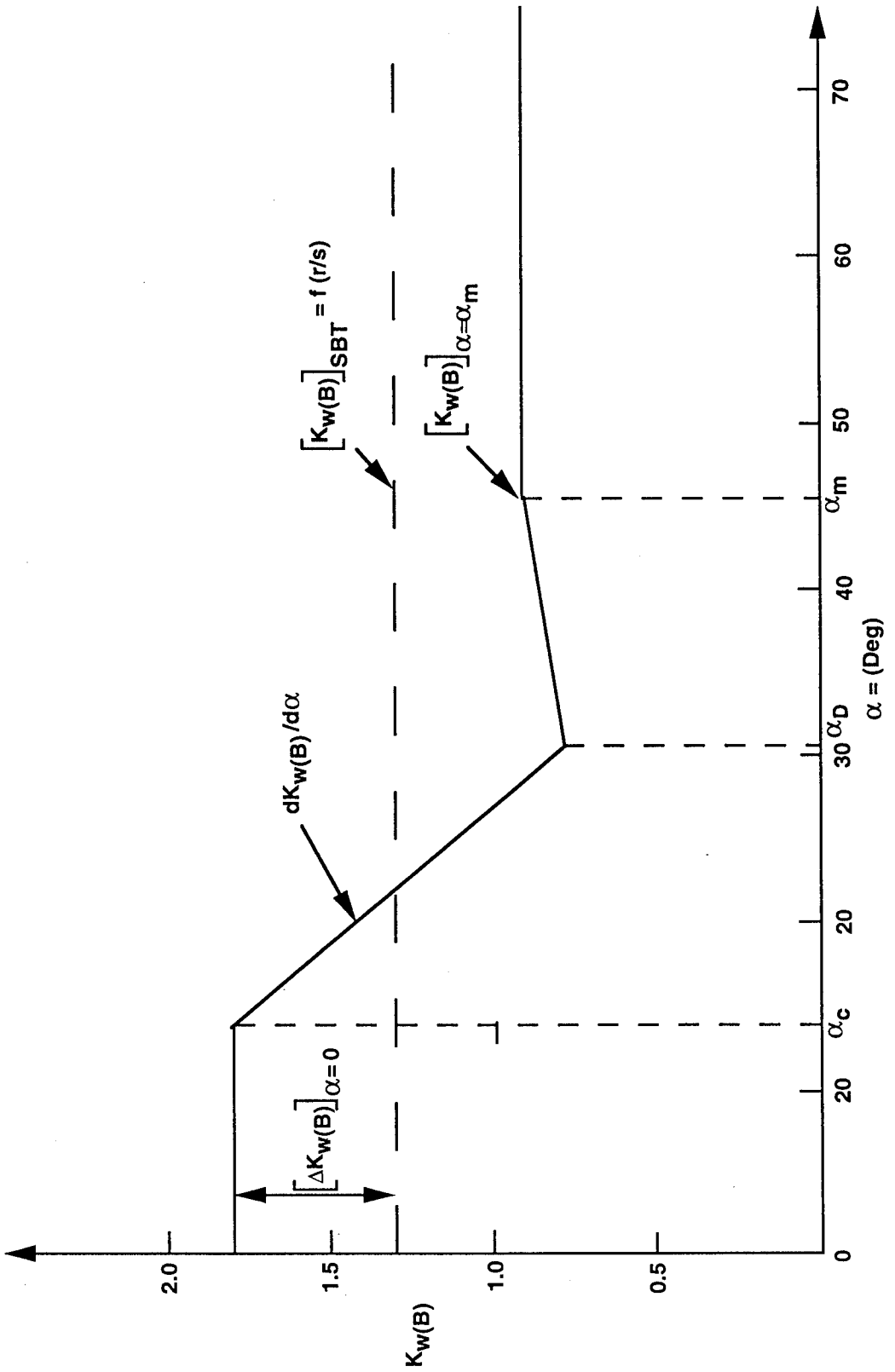

FIGURE 22. GENERIC REPRESENTATION OF WING-BODY INTERFERENCE FACTOR AT Φ = 45 DEG

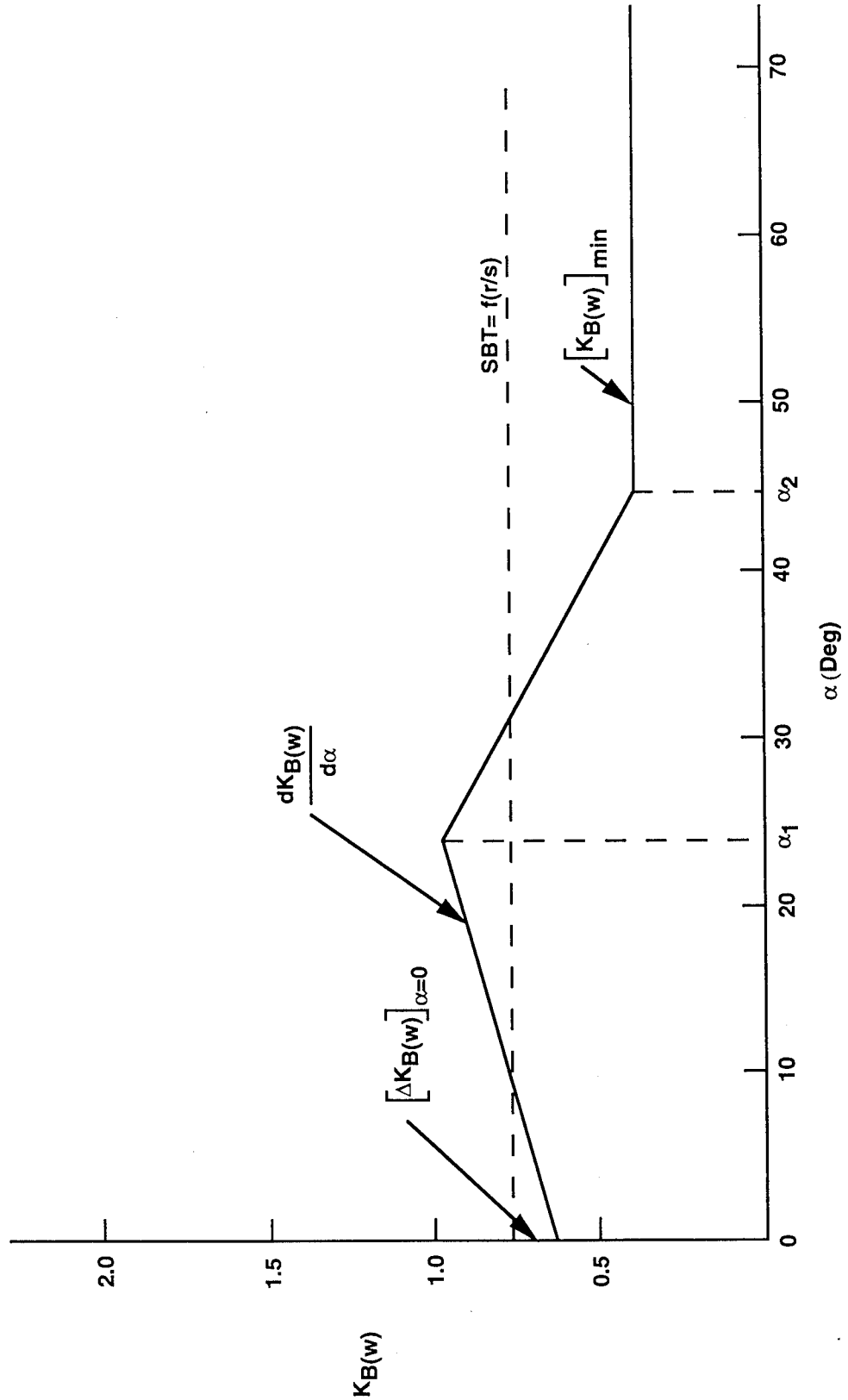

FIGURE 23. GENERIC REPRESENTATION OF BODY-WING INTERFERENCE FACTOR AT $\Phi = 45$ DEG

$\frac{d\ K_{W(B)}}{d\alpha}$ = rate of decrease of $K_{W(B)}$ between $\alpha = \alpha_C$ and $\alpha = \alpha_D$

α_D = angle of attack where $K_{W(B)}$ reaches an initial minimum

α_M = angle of attack where $K_{W(B)}$ reaches a constant value

$\left[K_{W(B)}\right]_{\alpha=\alpha_M}$ = value of $K_{W(B)}$ where a constant value with angle of attack has been attained

Tables 1-6 give values of these parameters based on the approximations in Figures 3-21.

Figure 23 shows that $K_{B(W)}$ can be approximated by five parameters. These are defined as follows:

$\left[\Delta K_{B(W)}\right]_{\alpha=0}$ = difference between SBT/LT and data at $\alpha = 0$

$\frac{dK_{B(W)}}{d\alpha}$ = rate of change of $K_{B(W)}$ between $\alpha = 0$ and $\alpha = \alpha_1$

α_1 = angle of attack where $dK_{B(W)}/d\alpha$ changes sign

α_2 = angle of attack where $K_{B(W)}$ reaches a constant

$\left[K_{B(W)}\right]_{MIN}$ = constant value of $K_{B(W)}$ above $\alpha = \alpha_2$ as a percent of linear theory or slender body theory (see Figure 24)

Tables 7-11 give values of these parameters as a function of M_∞ and the fin planform parameters.

The mathematical models for $K_{W(B)}$ and $K_{B(W)}$ are once again defined based on SBT/LT and using the data in Tables 1-11. The specific equations for $K_{W(B)}$ are

$$K_{W(B)} = \left[K_{W(B)}\right]_{SBT} + \left[\Delta K_{W(B)}\right]_{\alpha=0} \; ; \; \alpha \leq \alpha_C$$

$$= \left[K_{W(B)}\right]_{SBT} + \left[\Delta K_{W(B)}\right]_{\alpha=0} + \left|\left(|\alpha| - \alpha_C\right)\right| \frac{dK_{W(B)}}{d\alpha} \; ; \; \alpha_C < \alpha \leq \alpha_D$$

$$= 1 - \left(\frac{\alpha_M - |\alpha|}{\alpha_M - \alpha_D}\right)\left(1 - \left[K_{W(B)}\right]_{\alpha=\alpha_D}\right) \; ; \; \alpha_D < \alpha \leq \alpha_M$$

$$K_{W(B)} = \left[K_{W(B)}\right]_{\alpha=\alpha_M} \; ; \; \alpha > \alpha_M \qquad (11)$$

TABLE 1. DATA FOR $\left[\Delta K_{W(B)}\right]_{\alpha=0}$ AT Φ = 45 DEG

MACH NUMBER												
ASPECT RATIO	TAPER RATIO	≤0.1	0.6	0.8	1.2	1.5	2.0	2.5	3.0	3.5	4.5	≥5.0
≤0.25	0, 0.5, 1.0	−0.20	0.00	0.00	0.00	0.00	0	0	0	0	0	0
0.5	0.5	0.00	0.05	0.00	−0.13	0.00	0	0	0	0	0	0
1.0	0.5	0.13	0.05	0.00	0.00	−0.10	0	0	0	0	0	0
≥2.0	0.5	0.00	0.00	0.00	0.00	0.00	0	0	0	0	0	0
0.5	0	0.00	0.10	0.14	0.00	−0.22	0	0	0	0	0	0
≥2.0	0	0.00	0.00	0.00	0.00	−0.18	0	0	0	0	0	0
0.5	1.0	0.00	0.10	0.05	−0.23	0.00	0	0	0	0	0	0
≥2.0	1.0	0.00	0.00	0.00	0.00	0.00	0	0	0	0	0	0

TABLE 2. DATA FOR α_c AT Φ = 45 DEG

MACH NUMBER												
ASPECT RATIO	TAPER RATIO	≤0.1	0.6	0.8	1.2	1.5	2.0	2.5	3.0	3.5	4.5	≥5.0
≤0.25	0, 0.5, 1.0	10.0	22.0	22.0	0.0	0.0	0	0	0	0	0	0
0.5	0.5	45.0	11.5	11.0	10.0	0.0	0	0	0	0	0	0
1.0	0.5	45.0	13.3	0.0	6.5	0.0	0	0	0	0	0	0
≥2.0	0.5	20.0	10.0	0.0	6.5	2.2	0	0	0	0	0	0
0.5	0	39.0	15.0	11.5	10.0	0.0	0	0	0	0	0	0
≥2.0	0	20.0	10.0	0.0	6.5	0.0	0	0	0	0	0	0
0.5	1.0	45.0	15.0	15.0	15.0	0.0	0	0	0	0	0	0
≥2.0	1.0	20.0	10.0	0.0	6.5	1.5	0	0	0	0	0	0

TABLE 3. DATA FOR $\left[K_{W(B)}\right]_{\alpha=\alpha_D}$ AT Φ = 45 DEG

MACH NUMBER												
ASPECT RATIO	TAPER RATIO	≤0.1	0.6	0.8	1.2	1.5	2.0	2.5	3.0	3.5	4.5	≥6.0
≤0.25	0, 0.5, 1.0	1.0	1.0	1.00	1.00	1.00	1.00	1.00	1.00	1.00	1.00	1.0
0.5	0.5	1.0	1.0	1.00	0.90	0.90	1.00	0.95	1.00	0.97	1.00	1.0
1.0	0.5	1.0	1.0	1.00	0.95	1.00	1.00	1.00	1.00	1.00	1.00	1.0
≥2.0	0.5	1.0	1.0	0.95	0.95	1.00	1.00	1.00	1.00	1.00	1.00	1.0
0.5	0	1.0	1.0	1.00	1.00	0.90	0.90	0.90	0.90	0.90	0.90	1.0
≥2.0	0	1.0	1.0	0.95	1.00	1.00	1.00	1.00	1.00	1.00	1.00	1.0
0.5	1.0	1.0	1.0	1.00	1.00	1.00	1.00	1.00	1.00	1.00	1.00	1.0
≥2.0	1.0	1.0	1.0	1.00	1.00	1.00	1.00	1.00	0.93	0.90	0.95	1.0

TABLE 4. DATA FOR α_D AT Φ = 45 DEG

MACH NUMBER												
ASPECT RATIO	TAPER RATIO	≤0.1	0.6	0.8	1.2	1.5	2.0	2.5	3.0	3.5	4.5	≥6.0
≤0.25	0,0 .5, 1.0	20.0	40.0	38.0	35.0	30.0	25.0	16.3	15.1	13.9	13.1	10.0
0.5	0.5	59.0	33.0	30.0	25.6	25.0	15.0	15.0	10.0	15.0	12.0	10.0
1.0	0.5	59.0	38.0	32.0	26.0	24.0	17.0	15.0	14.4	10.0	10.0	10.0
≥2.0	0.5	39.0	31.5	30.0	28.0	25.0	16.5	15.0	14.4	10.0	13.0	10.0
0.5	0	39.0	35.5	33.0	39.5	29.5	15.0	25.0	15.0	15.0	10.0	10.0
≥2.0	0	39.0	31.5	30.0	28.0	24.7	17.0	13.5	11.4	10.0	10.0	10.0
0.5	1.0	59.0	35.5	33.0	25.6	29.5	15.0	15.0	15.0	12.0	13.0	10.0
≥2.0	1.0	39.0	31.5	30.0	28.0	23.3	14.0	16.0	15.0	11.8	12.0	10.0

TABLE 5. DATA FOR α_M AT Φ = 45 DEG

MACH NUMBER												
ASPECT RATIO	TAPER RATIO	≤0.1	0.6	0.8	1.2	1.5	2.0	2.5	3.0	3.5	4.5	≥6.0
≤0.25	0, 0.5, 1.0	40.0	45.0	45.0	40.0	44.0	43.0	38.0	28.0	25.0	29.0	20.0
0.5	0.5	65.0	33.0	30.0	49.0	52.0	40.0	40.0	30.0	25.0	25.0	20.0
1.0	0.5	65.0	38.0	47.0	49.5	66.0	48.5	45.0	41.0	40.0	10.0	20.0
≥2.0	0.5	40.0	31.5	40.0	56.0	57.0	45.0	45.0	41.0	40.0	28.0	20.0
0.5	0	40.0	35.5	33.0	65.0	48.0	50.0	46.0	30.0	30.0	50.0	20.0
≥2.0	0	40.0	31.5	40.0	56.0	55.0	58.5	49.8	44.2	41.5	28.5	20.0
0.5	1.0	65.0	35.5	33.0	49.0	52.0	40.0	28.0	24.0	21.0	13.0	20.0
≥2.0	1.0	40.0	31.5	40.0	56.0	49.5	44.0	40.0	33.0	32.0	28.0	20.0

TABLE 6. DATA FOR $\left[K_{W(B)}\right]_{\alpha=\alpha_M}$ AT Φ = 45 DEG

MACH NUMBER												
ASPECT RATIO	TAPER RATIO	≤0.1	0.6	0.8	1.2	1.5	2.0	2.5	3.0	3.5	4.5	≥6.0
≤0.25	0, 0.5, 1.0	0.80	0.95	1.0	1.0	1.0	1.0	1.0	1.0	1.0	1.0	1.0
0.5	.5	0.80	0.95	1.0	1.0	1.0	1.0	1.0	1.0	1.0	1.0	1.0
1.0	.5	0.80	0.90	1.0	1.0	1.0	1.0	1.0	1.0	1.0	1.0	1.0
≥2.0	.5	0.80	0.90	1.0	1.0	1.0	1.0	1.0	1.0	1.0	1.0	1.0
0.5	0	0.85	0.95	1.0	1.0	1.0	1.0	1.0	1.0	1.0	1.0	1.0
≥2.0	0	0.85	0.95	1.0	1.0	1.0	1.0	1.0	1.0	1.0	1.0	1.0
0.5	1.0	0.80	0.95	1.0	1.0	1.0	1.0	1.0	1.0	1.0	1.0	1.0
≥2.0	1.0	0.80	0.95	1.0	1.0	1.0	1.0	1.0	1.0	1.0	1.0	1.0

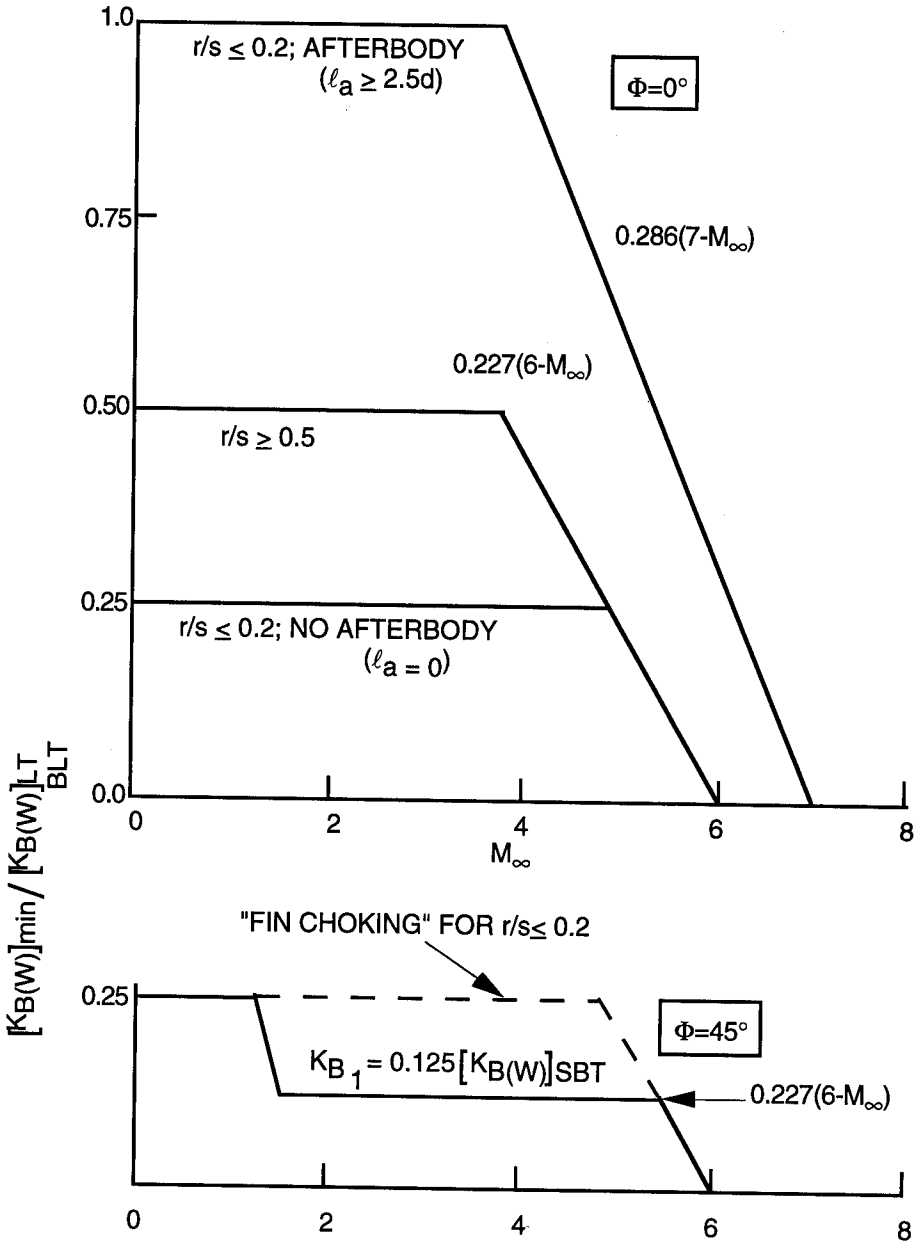

FIGURE 24. MINIMUM VALUE OF BODY-WING INTERFERENCE FACTOR AT HIGH AOA

TABLE 7. DATA FOR $\left[\Delta K_{B(W)}\right]_{\alpha=0}$

MACH NUMBER												
ASPECT RATIO	TAPER RATIO	≤0.1	0.6	0.8	1.2	1.5	2.0	2.5	3.0	3.5	4.5	≥6.0
≤0.25	0, 0.5, 1.0	−0.10	−0.18	0.00	0.00	0.0	0	0	0	0	0	0
0.5	0.5	0.0	−0.22	0.00	0.00	0.2	0.1	0.08	0	0	0	0
1.0	0.5	0.0	−0.07	−0.18	0.20	0.2	0	0	0	0	0	0
≥2.0	0.5	0.0	−0.23	−0.18	0.20	0.0	0	0	0	0	0	0
0.5	0	0.0	−0.12	0.00	0.25	0.2	0	0	0	0	0	0
≥2.0	0	0.0	−0.23	−0.18	0.20	0.0	0	0	0	0	0	0
0.5	1.0	0.0	−0.22	0.00	0.25	0.2	0.1	0.08	0	0	0	0
≥2.0	1.0	0.0	−0.23	−0.18	0.20	0.0	0	0	0	0	0	0

Here,

$$\frac{dK_{W(B)}}{d\alpha} = \left(\left[K_{W(B)}\right]_{\alpha_D} - \left[K_{W(B)}\right]_{MAX} \right) / \left(\alpha_D - \alpha_C \right)$$

where

$$\left[K_{W(B)}\right]_{MAX} = \left[K_{W(B)}\right]_{SBT} + \left[\Delta K_{W(B)}\right]_{\alpha=0}$$

The equations for the body-wing interference factor are

$$K_{B(W)} = \left[K_{B(W)}\right]_{\substack{LT \\ SBT}} + \left[\Delta K_{B(W)}\right]_{\alpha=0} + |\alpha| \frac{dK_{B(W)}}{d\alpha} \; ; \; \alpha \leq \alpha_1$$

$$K_{B(W)} = \left[K_{B(W)}\right]_{\alpha=\alpha_1} + \left(\frac{\alpha_1 - |\alpha|}{\alpha_2 - \alpha_1} \right) \left\{ \left[K_{B(W)}\right]_{\alpha=\alpha_1} - \left[K_{B(W)}\right]_{MIN} \right\} \; ; \; \alpha_1 < \alpha \leq \alpha_2$$

$$K_{B(W)} = \left[K_{B(W)}\right]_{MIN} \; ; \; \alpha \geq \alpha_2 \qquad (12)$$

TABLE 8. DATA FOR $dK_{B(W)}/d\alpha$ (PER DEG)

MACH NUMBER												
ASPECT RATIO	TAPER RATIO	≤0.1	0.6	0.8	1.2	1.5	2.0	2.5	3.0	3.5	4.5	≥6.0
≤0.25	0, 0.5, 1.0	−0.0050	−0.00557	−0.00925	−0.0215	−0.0238	−0.0450	−0.0268	−0.0650	−0.0650	−0.060	−0.06
0.5	0.5	0.0015	−0.00210	−0.00720	−0.0100	−0.0140	−0.0440	−0.0275	−0.0330	−0.0620	−0.060	−0.06
1.0	0.5	−0.0030	0.00000	0.00750	−0.0150	−0.0150	−0.020	−0.025	−0.0220	−0.0143	−0.013	−0.01
≥2.0	0.5	0.0030	0.00670	0.01330	−0.0150	−0.0170	−0.0300	−0.045	−0.054	−0.060	−0.062	−0.065
0.5	0	−0.0020	−0.00830	−0.01000	−0.0170	−0.0260	−0.005	−0.0125	−0.0100	−0.005	−0.005	−0.06
≥2.0	0	0.0030	0.00670	0.01330	−0.0150	−0.0170	−0.0300	−0.045	−0.054	−0.060	−0.062	−0.065
0.5	1.0	0.0015	−0.00120	−0.00100	−0.0140	−0.0140	−0.0425	−0.0275	−0.0400	−0.0720	−0.060	−0.06
≥2.0	1.0	0.0030	0.00670	0.01330	−0.0150	−0.0170	−0.0300	−0.045	−0.054	−0.060	−0.062	−0.065

TABLE 9. DATA FOR α_1 (DEG)

MACH NUMBER												
ASPECT RATIO	TAPER RATIO	≤0.1	0.6	0.8	1.2	1.5	2.0	2.5	3.0	3.5	4.5	≥6.0
≤.025	0, 0.5, 1.0	10.0	45.5	35.0	30.0	23.0	22.0	20.8	20.0	20.0	15.0	8.0
0.5	0.5	10.0	57.0	45.0	30.0	25.0	16.0	20.0	15.0	10.0	10.0	8.0
1.0	0.5	10.0	34.5	35.0	35.0	36.6	10.0	15.0	17.5	42.0	40.0	30.0
≥2.0	0.5	10.0	15.0	30.0	35.0	20.0	20.0	18.0	17.5	30.0	35.0	35.0
0.5	0	10.0	35.0	45.0	30.0	19.0	20.0	22.5	15.0	15.0	15.0	8.0
≥2.0	0	20.0	15.0	30.0	35.0	20.0	20.0	18.0	17.5	30.0	35.0	35.0
0.5	1.0	10.0	57.0	45.0	30.0	25.0	16.0	20.0	15.0	10.0	10.0	8.0
≥2.0	1.0	10.0	15.0	30.0	35.0	20.0	10.0	15.0	17.5	30.0	35.0	35.0

TABLE 10. DATA FOR α_2 (DEG)

MACH NUMBER												
ASPECT RATIO	TAPER RATIO	≤0.1	0.6	0.8	1.2	1.5	2.0	2.5	3.0	3.5	4.5	≥6.0
≤0.25	0, 0.5, 1.0	55.0	55.0	50.0	50.0	45.0	37.0	44.0	29.5	29.5	29.5	25.0
0.5	0.5	75.0	65.0	55.0	43.0	40.0	38.0	44.0	44.0	36.0	30.0	20.0
1.0	0.5	75.0	65.0	60.0	60.0	60.0	60.0	62.0	80.0	42.0	40.0	30.0
≥2.0	0.5	75.0	65.0	60.0	60.0	50.0	60.0	62.0	80.0	42.0	45.0	45.0
0.5	0	75.0	60.0	60.0	52.0	40.0	35.0	44.0	50.0	36.0	30.0	20.0
≥2.0	0	75.0	65.0	60.0	60.0	50.0	60.0	62.0	80.0	42.0	45.0	45.0
0.5	1.0	75.0	65.0	55.0	42.0	40.0	38.0	44.0	40.0	36.0	30.0	20.0
≥2.0	1.0	75.0	65.0	60.0	60.0	60.0	60.0	62.0	80.0	42.0	45.0	45.0

TABLE 11. DATA FOR $\left[K_{B(W)}\right]_{MIN}$ (FRACTION OF SBT/LT)

MACH NUMBER												
ASPECT RATIO	TAPER RATIO	≤0.1	0.6	0.8	1.2	1.5	2.0	2.5	3.0	3.5	4.5	≥6.0
≤0.25	0, 0.5, 1.0	0.25	0.25	0.25	0.12	0.12	0.12	0.12	0.12	0.12	0.12	0
0.5	0.5	0.25	0.25	0.25	0.12	0.12	0.12	0.12	0.12	0.12	0.12	0
1.0	0.5	0.25	0.25	0.25	0.12	0.12	0.12	0.12	0.12	0.12	0.12	0
≥2.0	0.5	0.25	0.25	0.25	0.12	0.12	0.12	0.12	0.12	0.12	0.12	0
0.5	0	0.25	0.25	0.25	0.12	0.12	0.12	0.12	0.12	0.12	0.12	0
≥2.0	0	0.25	0.25	0.25	0.12	0.12	0.12	0.12	0.12	0.12	0.12	0
0.5	1.0	0.25	0.25	0.25	0.12	0.12	0.12	0.12	0.12	0.12	0.12	0
≥2.0	1.0	0.25	0.25	0.25	0.12	0.12	0.12	0.12	0.12	0.12	0.12	0

Linear interpolation is used in Tables 1-11 to define the parameters in Equations (11) and (12) other than $\left[K_{W(B)}\right]_{SBT}$ and $\left[K_{B(W)}\right]_{LT}^{SBT}$, as a function of M_∞, $\propto$, AR, and λ. These two terms are calculated analytically using SBT or LT as done before in the previous versions of the Aeroprediction Code.

The methodology of the Φ = 45 deg technology is similar to that for Φ = 0 deg (see Reference 1); the difference is in all the constants of Tables 1-11. Exceptions to this are "fin choking," r/s effects, and center of pressure shifts. These will be discussed in the following three sections.

2.2.4 Nonlinearities Due to Internal Shocks

Three nonlinearities are difficult to account for with available data. These phenomena occur at moderate (M>2.0) and higher supersonic Mach numbers and higher values of AOA (typically ≥ 25 deg). The first nonlinearity is sometimes referred to as "fin choking"; the second is when the bow shock intersects the fins; and the third is shocks from forward-located fins intersecting aft-mounted fins. Each of these phenomena will be discussed individually. "Fin choking" is a phenomenon similar to that which occurs when an inlet becomes unstarted or a wind tunnel achieves its maximum rate of flow (an increase in power produces no more mass flow through the inlet). As the body increases in angle of attack with the fins oriented in the X or cross orientation, the flow between the fins will eventually "choke" at some angle of attack and at moderate to large supersonic Mach numbers. When this happens, a strong shock is formed just in front of the fin,[18,19] producing a high pressure region on the fins and body. This high pressure region is shifted forward from where it would be if supersonic flow occurred through the fins. While the absolute value of pressure

on the body is higher than for the unchoked flow, it occurs over a much smaller region and hence gives only slightly higher body-wing interference lift.

Modified Newtonian Theory (MNT) can be used to help approximate the combination of M and $\propto$ that will cause fin choking to occur in the $\Phi = 45$ deg plane. MNT is defined by[20]

$$C_P = C_{P_o} \sin^2 (\delta_{eq}) \tag{13}$$

where

$$C_{P_o} = \frac{2}{\gamma M_\infty^2} \left\{ \left[\frac{(\gamma+1)\ M_\infty^2}{2} \right]^{\frac{\gamma}{\gamma-1}} \left[\frac{\gamma+1}{2\gamma M_\infty^2 - (\gamma-1)} \right]^{\frac{1}{\gamma-1}} - 1 \right\} \tag{14A}$$

$$\delta_{eq} = \sin^{-1} (\sin \theta \cos \propto - \sin \propto \cos \Phi \cos \theta) \tag{14B}$$

and θ is the local slope of the body or fin surface with respect to the body axis. The local surface Mach number can be approximated by

$$M_L = \left\{ \left(\frac{2}{\gamma-1} \right) \left[\left(\frac{P_{O_2}}{P_L} \right)^{\frac{\gamma-1}{\gamma}} - 1 \right] \right\}^{1/2} \tag{15}$$

where

$$\frac{P_{O_2}}{P_L} = \frac{\frac{\gamma M_\infty^2}{2} C_{P_o} + 1}{\frac{\gamma M_\infty^2}{2} C_P + 1} \tag{16}$$

Terms C_P and C_{P_o} of Equation (16) come from Equations (13) and (14A), respectively.

Figure 25 gives the local Mach number results just upstream of the fins using Equation (15). Three Mach numbers were considered in this figure: the Mach number of the Reference 19 data of 2.7, plus a lower value of 1.5, and an upper value of ∞.

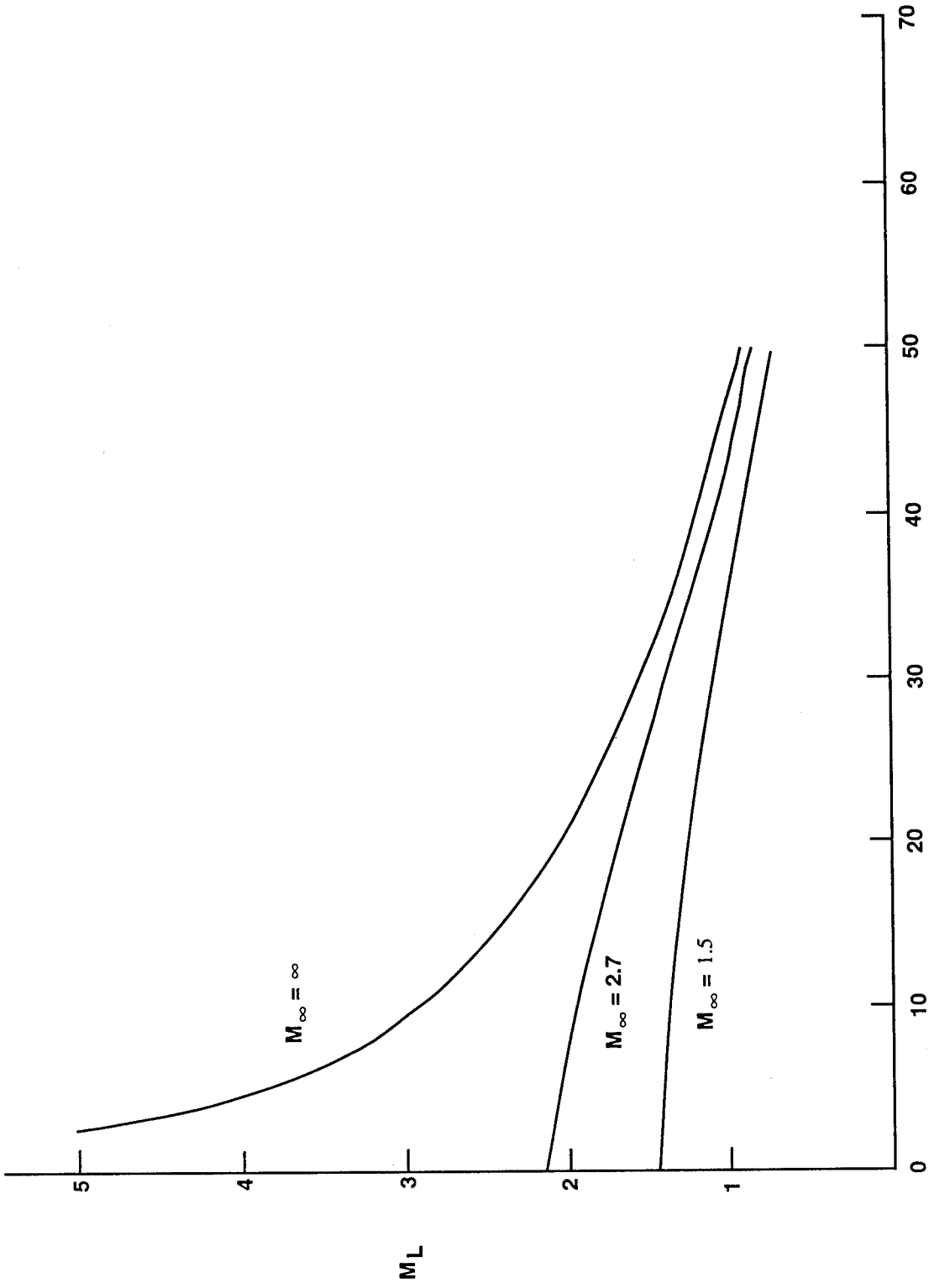

FIGURE 25. SURFACE MACH NUMBER JUST UPSTREAM OF FINS ON CYLINDRICAL AFTERBODY COMPUTED BY MNT (Φ = 180 DEG, δ_N = 2.5)

It is interesting to note that as AOA increases, freestream Mach number has less and less of an effect on local Mach number. Also note that the flow in the windward plane goes subsonic, even with no fins present, at $\propto$ = 35, 43 and 47 deg for the Mach numbers M_∞ = 1.5, 2.7 and ∞, respectively. This low Mach number flow will then intersect the fins. If the fins are in the Φ = 135 and 225 deg planes, internal shocks can reflect off opposite fins if r/s is small. This lowers the Mach number further. The larger the fins, the more reflections and more blockage that will occur and hence the lower the value of M_∞ and $\propto$ required for "fin choking." Also, the larger the fins, the harder it is for the flow in the region of the fins to escape around the fins.

Reference 18 actually showed a stagnation pressure occurring on the windward side of the fins at Φ = 135 and 225 deg at $\propto$ = 35 deg and M_∞ = 2.7. It is suspected that the flow on the body attempts to wrap around the body in the vicinity of the fins but is constrained by the fins and the flow coming in the opposite direction down the fins. These two flows then merge and cause a local stagnation region (which means zero velocity). The schlieren photograph for this condition showed a strong shock ahead of the fins merging with the bow shock. When the shock ahead of the fins merged with the bow shock, the bow shock was pushed further away from the body.

It is suspected that fin size plays a significant role, along with angle of attack and Mach number, in "fin choking." This statement is based on the fact that wings with smaller r/s values (wing-dominated configurations) seem to have more nonlinear aerodynamics in the "fin choking" range of M and $\propto$ than do those configurations that have larger values of r/s (body dominated).

Two approximations are being made to take into account some of the nonlinearities associated with high angle-of-attack aerodynamics. First, the criteria for determining when to use slender body or linear theory are strictly used only for AOA less than 15 deg. That is, if

$$\beta \, AR \, (1 + \lambda) \left(\frac{1}{m\beta} + 1 \right) > 4$$

and $\propto \leq$ 15 deg, then linear theory is used for defining $[K_{B(W)}]_{MIN}$. If the above conditions are not satisfied, $[K_{B(W)}]_{MIN}$ is determined as a fraction of slender body theory. This has the overall effect of slightly increasing the minimum value of body-wing lift for lower values of r/s.

The second change is to estimate the region of "fin choking" based on MNT and then use this region along with Reference 8 and 18 results to model the r/s effect. Figure 26 gives the approximate boundary for fin choking using MNT and the region over which it appears the nonlinear effect for $K_{B(W)}$ for r/s $\leq$ 0.2 is defined. The specific approach for implementation into the APC is discussed in the section on r/s effects (2.2.5).

The second nonlinear problem mentioned is the penetration of the bow shock by the windward plane fins. This occurs for the fin in the Φ = 180 deg plane when in the plus or Φ = 0 deg roll orientation before it does when the vehicle is rolled to a Φ = 45 deg position. The impact of this phenomenon on the aerodynamics is not clear in examining Tables 1-11. In examining fin pressure data for the two cases of Reference 18, it was found that the portion of the fin within the shock layer

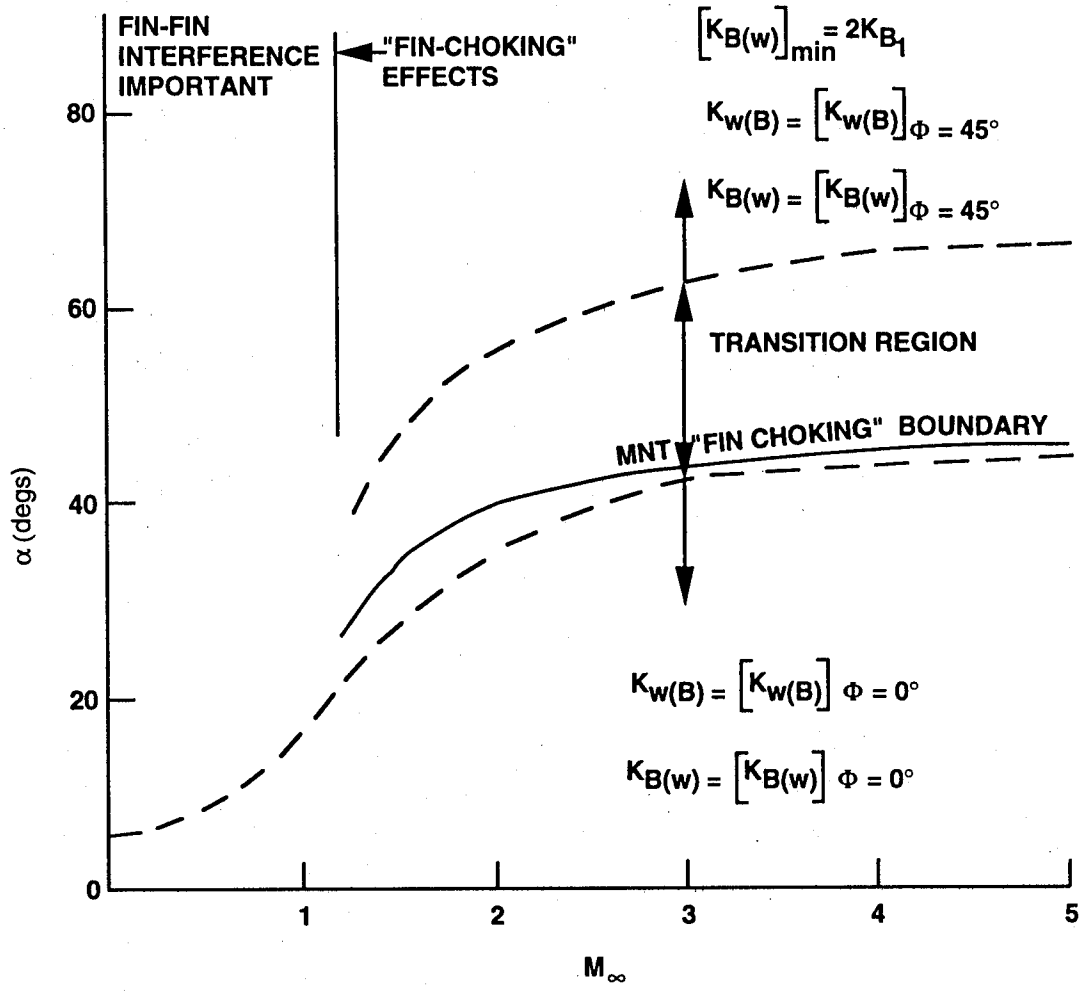

FIGURE 26. $K_{W(B)}$ AND $K_{B(W)}$ PREDICTION FOR Φ=45 DEG AND r/s ≤ 0.2

had a much higher pressure than the part outside the shock layer. This certainly would imply a difference in aerodynamics, and in fact this difference is certainly a part of Tables 1-11. However, it is not clear from the tables the contribution of this phenomenon.

The third internal shock problem is the impact that a shock from a forward located fin has on a rear mounted fin. This phenomenon, unlike the previous two, is not included in the data in Tables 1-11. This is because the data sets in both References 8 and 18 had only one set of fins present and hence this phenomenon cannot be accounted for.

In summary, it is fair to say that while the present approximate method takes into account some of the nonlinearities in missile aerodynamics due to internal shocks, it is far from complete. Additional new data, combined with numerical computations, are needed to develop an approximate engineering model to represent these nonlinearities accurately and hence completely cover the desired Mach number and angle of attack boundary of interest for all configurations of interest to weapons designers.

2.2.5 Treatment of Nonlinearities Due to r/s

Figures 3-21 and Tables 1-11 were based mostly on the data of Reference 8 that were for r/s of 0.5. This data base showed little identifiable effect from the "fin choking" and other phenomena shown by the Reference 18 data base, which was based on a r/s of 0.2. Based on this, an hypothesis is assumed that the "fin choking" phenomenon is more important for wing dominated configurations where r/s is small. To handle these situations, the following strategy was followed in treating the effects of r/s. Hopefully, this strategy will be validated or improved upon with additional wind tunnel or computational results at values of r/s less than 0.5.

$r/s \geq 0.5$. For this range of r/s, Figures 3-21 and Tables 1-11 are used directly to develop the nonlinear corrections to slender body or linear theory. The data base[8] is based on an r/s of 0.5 but will be assumed to apply for $r/s > 0.5$ as well, unless validation against cases outside the range of the data base proves unacceptable.

$r/s \leq 0.2$. When $r/s = 0.2$, the limited data base of Stallings, et al.[18] is used along with MNT to determine if "fin choking" or fin-fin interference effects are present or not. This is based on Figure 26. If these effects are present, then the $K_{W(B)}$ and $K_{B(W)}$ for $\Phi = 0$, $r/s \leq 0.2$ condition is used for $\Phi = 45$ deg up to the AOA where fin choking is important. This is based on the fact that for low r/s values, the total wing-body normal force appeared to be basically the same for $\Phi = 0$ and $\Phi = 45$ deg for the AOA below where "fin choking" or fin-fin interference occurs. While the data used are for $r/s = 0.2$, the assumption will be made that these data hold for $r/s < 0.2$ as well.

If "fin choking" does occur, the $K_{W(B)}$ and $K_{B(W)}$ for $\Phi = 0$ is used up to the lower boundary on Figure 26 where "fin choking" becomes important. For AOAs above the upper boundary on Figure 26, the $\Phi = 45$ deg, $r/s \geq 0.5$ methodology is used for $K_{W(B)}$.

The $K_{B(W)}$, $\Phi = 45$ deg, r/s $\geq$ 0.5 results are also used for r/s $\leq$ 0.2 except the $[K_{B(W)}]_{MIN}$ is lower than that for $\Phi = 0$ deg (see Figure 24). The minimum values of $K_{B(W)}$ for angles of attack above the upper boundary shown in Figure 26, where fin choking is important, are twice this minimum value for $\Phi = 45$ deg shown in Figure 24. Even though this value is twice the $\Phi = 45$ deg results, it is still much less than the $\Phi = 0$ deg results. This methodology thus says that the body-wing interference for $\Phi = 45$ deg at high angle of attack is much less than the $\Phi = 0$ deg results, but when fin choking is present, the body-wing interference is closer to the $\Phi = 0$ deg results. In other words, this is an approximate method to account for the fact that the pressures in the vicinity of the wing-body region are increased substantially when sonic flow is present. The data for the r/s = 0.5 results of course come from Tables 1-11. Between the two boundaries on Figure 26, linear interpolation is used.

The other physical phenomenon present in the Figure 26 results is an apparent "fin-fin interference" effect that occurs at $\Phi = 45$ deg and high AOA that is not present for $\Phi = 0$ deg. In examining Table 6, it is seen that $[K_{W(B)}]_{\alpha=\alpha_M}$ is less than 1.0 for low Mach numbers. This is based on the Figure 3 data and substantiated with validation against other results. Unfortunately, equivalent high AOA missile component data were not available for supersonic configurations. As a result, most of the values for $[K_{W(B)}]_{\alpha=\alpha_M}$ were assumed to be 1.0.

Recall that the way $K_{W(B)}$ was calculated was based on the wing-body data for $\Phi = 45$ deg and the wing alone data for $\Phi = 0$ deg. Hence, it is suspected that the reason the value of $[K_{W(B)}]_{\alpha=\alpha_M}$ is less than 1.0 at low Mach number is really a fin-fin interference effect for fins oriented at $\Phi = 45$ versus 0 deg roll. It is suspected that the leeward plane fins are completely in the wake of a low dynamic pressure region (M = 0.1) and hence do not have the normal force that the cruciform fins have at $\Phi = 0$ deg. In other words, it is suspected that a value of less than one would be obtained for fins at $\Phi = 45$ deg versus fins at $\Phi = 0$ deg, even if no body were present. Since fin-fin interference is not treated separately, it is included in the $K_{W(B)}$ term.

The interference factor methodology for r/s $\leq$ 0.2 is thus designed to be independent of roll for small angles of attack and to start showing the roll dependence when "fin choking" or fin-fin interference effects become important.

There is also a change in the center of pressure calculation for low r/s value configurations, which will be discussed in section 2.2.6.

<u>0.2 < r/s < 0.5</u>. For r/s values between 0.5 and 0.2, the interference factors ($K_{W(B)}$ and $K_{B(W)}$) are computed for r/s values of 0.2 and 0.5 using the approaches just outlined, and then the values at the given r/s of interest are computed based on linear interpolation. That is

$$\left[K_{W(B)}\right]_{r/s} = \left[K_{W(B)}\right]_{r/s=0.2} + \frac{r/s-0.2}{0.3}\left\{\left[K_{W(B)}\right]_{r/s=0.5} - \left[K_{W(B)}\right]_{r/s=0.2}\right\} \qquad (17A)$$

$$\left[K_{B(W)}\right]_{r/s} = \left[K_{B(W)}\right]_{r/s=0.2} + \frac{r/s-0.2}{0.3}\left\{\left[K_{B(W)}\right]_{r/s=0.5} - \left[K_{B(W)}\right]_{r/s=0.2}\right\} \quad (17B)$$

$$\left[K_{B(W)}\right]_{MIN} = K_{B_1}\left(\frac{1}{3}\right)(8 - 10r/s) \quad (17C)$$

Here K_{B_1} is the minimum value shown in Figure 24 represented by the lower curve for the results when $\Phi = 45$ deg.

This methodology inherently assumes that the "fin choking" and low r/s phenomena occur in a linear fashion as r/s gets smaller. Realistically, this is probably not the case; however, only numerical computations or wind tunnel results can specify the detailed fashion of how the interference factors vary with r/s. Until such results are available, or until computations are made on configurations outside the data base upon which this methodology is based, showing it to be incorrect, Equation (17) will be used.

2.2.6 Center of Pressure of Wing and Interference Lift Due to AOA at $\Phi = 45$ deg

There are two changes in the center of pressure prediction for the interference lift from $\Phi = 0$ deg to $\Phi = 45$ deg roll orientation. Before the changes are discussed, a brief review of the $\Phi = 0$ deg roll orientation method is appropriate.

The AOA prediction of center of pressure of the $K_{W(B)}$ term is based on linear theory of the wing-alone lift at small AOA and goes to the centroid of the wing planform area at large AOA ($\alpha_W = 60$ deg). This transition is accomplished in a quadratic fashion. If A and B are the centers of pressure of the linear and nonlinear normal force terms (in percent of mean geometric chord), and $\alpha_W = \alpha + \delta$, then the center of pressure of the wing-body or wing alone lift is

$$\left(X_{CP}\right)_{WB} = \left(X_{CP}\right)_W = A + \frac{1}{36}|\alpha_W|(B-A) + \frac{1}{5400}\alpha_W^2(A-B) \quad (18)$$

Equation (18) is the methodology used for roll position of 0 deg.

When the fins are rolled to a non-zero roll orientation, the center of pressure Equation (18) will change because of the geometry of the wings and an asymmetric effect on the wing loading. To visualize this effect, imagine a missile rolled to $\Phi = 45$ deg and increasing in AOA. As AOA increases, two things occur. First, the windward plane fins carry more and more of the load compared to the leeward plane fins. Second, the local Mach number in the windward plane is different and typically lower than the leeward plane. This has the effect of shifting the wing alone center of pressure forward in the windward plane. Since the load and wing centers of pressure are

different on the windward and leeward plane fins, this results in a net forward shift in the center of pressure for $\Phi = 45$ deg roll compared to the $\Phi = 0$ deg computation of Equation (18). This shift appears to occur for all Mach numbers, and is largest at moderate AOA, and goes to zero at AOA 0 and 90 deg. At 90 deg, the windward plane fins carry almost all the load compared to the leeward plane fins, but geometrically, the fins are all aligned perpendicular to the AOA plane.

Mathematically, this geometrical shift can be approximated by:

$$\left(\Delta X_{CP}\right)_{WB} \cong Y_{CP} \cos \Phi \sin(2\alpha) \frac{\Delta C_{N_{W(B)}}}{C_{N_{W(B)}}} \tag{19}$$

Y_{CP} of Equation (19) is the centroid of the planform area in the Y direction of the wing planform. If the wing is assumed to be represented by a trapezoidal shape, then

$$Y_{CP} = r + \left(\frac{b}{C_r + C_t}\right)\left(\frac{C_r}{2} - \frac{C_t}{3}\right) \tag{20}$$

The cos Φ factor rotates the ΔC_N term from being normal to the wing planform, to the plane of the normal force vector. The sin 2α term allows the COP shift to vary between 0 at AOA 0 and 90 deg to a maximum at AOA of 45 deg. $\Delta C_{N_{W(B)}} / C_{N_{W(B)}}$ represents the difference between the load of the windward and leeward plane fins as a fraction of the total wing-body load. Using the NASA data base[8], an estimate was made for several wings. An approximate linear trend with angle-of-attack was arrived at. While data are not available above α of 40 deg, it will be assumed this trend is linear between AOA of 0 and 65 deg. At $\alpha \geq 65$ deg it is assumed the windward plane fins carry 80 percent of the load of the wings and the leeward plane fins carry only 20 percent. With this assumption,

$$\frac{\Delta C_{N_{W(B)}}}{C_{N_{W(B)}}} = 0.8\left(\frac{\alpha}{65}\right) \; ; \; \alpha < 65^\circ$$

$$= 0.8 \; ; \; \alpha \geq 65^\circ \tag{21}$$

In Equation (21), α is in degrees. Combining Equations (19), (20), (21), there is obtained

$$\left(\Delta X_{CP}\right)_{WB} = -\left[r + \left(\frac{b}{C_r + C_t}\right)\left(\frac{C_r}{2} - \frac{C_t}{3}\right)\right] \cos(\Phi) \sin(2\alpha) \left(\frac{0.8\alpha}{65}\right) \; ; \; \alpha \leq 65$$

$$= - 0.8 \left[r + \left(\frac{b}{C_r + C_t} \right) \left(\frac{C_r}{2} - \frac{C_t}{3} \right) \right] \cos\Phi \sin(2\alpha) \; ; \; \alpha > 65° \tag{22}$$

Equation (22) is added to Equation (18) for the roll orientation of 45 deg.

The other change being made in the center of pressure for $\Phi = 45$ deg is to use the local Mach number as AOA is increased (versus the freestream Mach number) to compute the body carryover COP. The local Mach number can be computed by Equation (15) using MNT. The local Mach angle is then

$$\mu_L = \sin^{-1} \left(\frac{1}{M_L} \right) \tag{23}$$

Using the local Mach angle to determine the angle over which linear theory impacts the body carryover lift has the effect of shifting this component forward. That is because M_L decreases with increasing AOA causing μ_L to approach 90 deg. At 90 deg Mach angle, the center of pressure of linear theory is at the same location of slender body theory, that is, at the centroid of the wing root chord.

2.2.7 Wing-Body and Body-Wing Interference Due to Control Deflection

The same general approach, with slight modifications, to the nonlinear model of Reference 1 for $\Phi = 0$ deg roll will be used here for the $\Phi = 45$ deg roll position. In the Reference 1 method, $k_{W(B)}$ and $k_{B(W)}$ were approximated by

$$k_{W(B)} = C_1(M) \left[k_{W(B)} \right]_{SBT} + C_2(|\alpha_W|, M) \tag{24}$$

$$k_{B(W)} = \left[k_{B(W)} \right]_{SBT} \tag{25}$$

The parameters C_1 and C_2 were derived based on numerical experiments of the AP95 compared to data. This was because many of the fins in the Reference 8 data base were too small to allow accurate estimates of $k_{W(B)}$ as a function of parameters of interest. As a result, total missile load data were used and empirical values of C_1 and C_2 estimated as a function of combined local angle of

attack of the wing $|\alpha + \delta|$, and Mach number. Figure 27 gives the values of the parameters C_1 and C_2 for $\Phi = 0$, and Figure 28 gives the complementary set for $\Phi = 45$ deg.

In examining the constants and model of Figure 27, several physical phenomena occur that are modeled in a semiempirical sense by Equations (24) and (25). These phenomena are qualitatively shown in Figure 29A. At low Mach number, Figure 29A indicates the SBT gives a low value of $k_{W(B)}$ for small values of α_W. At a value of α_W of about 25 deg, the controls lose effectiveness as a result of a combination of stall and blow-by effects due to the separation between the wing and body. At an α_W of about 55 deg, the controls have lost all effectiveness. At Mach numbers greater than about 4, the controls initially generate less effectiveness than is generated by SBT for values of α_W up to about 20 or 25 deg. The controls then become more effective because of nonlinear compressibility effects. On the other hand, at an α_W of around 45 to 50 deg, the controls once again begin to lose effectiveness, presumably because of shock interactions and blow-by effects. For Mach numbers in between subsonic and high supersonic, $k_{W(B)}$ has behavior in between the two extremes illustrated in Figure 29A.

In comparing the nonlinear control deflection models for $\Phi = 0$ and 45 deg roll in Figures 27 and 28, a lot of similarity is seen. The constants for the $\Phi = 45$ deg are slightly different than those for $\Phi = 0$ deg and the values of α_W where the nonlinearities begin are somewhat different. However, by and large, Equation (24) holds for both the $\Phi = 0$ and 45 deg roll cases. It should be pointed out that in Reference 1, mostly linear variations of $k_{W(B)}$ with α_w were used. However, these have been improved upon for the $\Phi = 45$ deg case with cubic fits of control deflection data as seen in Figure 28. As such, all nonlinear effects are included in the variations of $k_{W(B)}$ as a function of Mach number and $|\alpha + \delta|$.

Figure 29B assumes that $k_{B(W)}$ can be represented by SBT up to some value of $|\alpha_W|$, at which point it decays to a percent of SBT. For $\Phi = 0$ deg, these values are $|\alpha_W| = 70$ deg and 50 percent of SBT as a minimum. For $\Phi = 45$ deg roll, the model for $k_{B(W)}$ is based on $|\delta|$ only and begins decaying at $|\delta| = 0$. It reaches a minimum of $k_{B(W)}$ of 25 percent of SBT analogous to the $[K_{B(W)}]_{min}$ of Figure 24.

It should also be noted that $k_{W(B)}$ and $k_{B(W)}$ of Figure 28 are multiplied by 1.414 to indicate that all four fins are assumed to be deflected by an equal amount in the $\Phi = 45$ deg roll position. Finally, for Mach numbers in between the values on Figures 27 and 28, linear interpolation is used.

2.2.8 Nonlinear Wing-Tail Interference Model for $\Phi = 0$ deg

The nonlinear wing-tail interference model used for the $\Phi = 0$ roll is defined by

$$C_{N_{T(V)}} = \frac{\left(C_{N\alpha}\right)_W \left(C_{N\alpha}\right)_T \left[K_{W(B)}{}^{\alpha} + F\, k_{W(B)}\, \delta_W\right] i \left(s_T - r_T\right) A_W}{2\pi (AR)_T \left(f_W - r_W\right) A_{ref}} \qquad (26)$$

MACH	NONLINEAR MODEL
$M \le 0.8$	If $\lvert\alpha_W\rvert \le 24.0 \rightarrow k_{W(B)} = 1.1[k_{W(B)}]_{SB}$ If $\lvert\alpha_W\rvert > 24.0 \rightarrow k_{W(B)} = 1.1[0.000794\lvert\alpha_W\rvert^2 - 0.0933\lvert\alpha_W\rvert + 2.71]$ $F = 1.1$
$M = 1.1$	If $\lvert\alpha_W\rvert \le 15.0 \rightarrow k_{W(B)} = 1.0[k_{W(B)}]_{SB}$ If $\lvert\alpha_W\rvert > 15.0 \rightarrow k_{W(B)} = 1.0[0.00087\lvert\alpha_W\rvert^2 - 0.0825\lvert\alpha_W\rvert + 1.98]$ $F = 1.1$
$M = 1.5$	If $\lvert\alpha_W\rvert \le 10.0 \rightarrow k_{W(B)} = 1.0[k_{W(B)}]_{SB}$ If $\lvert\alpha_W\rvert > 10.0 \rightarrow k_{W(B)} = 1.0[k_{W(B)}]_{SB} - 0.005[\lvert\alpha_W\rvert - 10.0]$ If $\lvert\alpha_W\rvert \le 20.0 \rightarrow F = 0.8$ If $\lvert\alpha_W\rvert > 20.0 \rightarrow F = 0.8 + 0.10[\lvert\alpha_W\rvert - 20.0]$
$M = 2.0$	If $\lvert\alpha_W\rvert \le 10.0 \rightarrow k_{W(B)} = 0.9[k_{W(B)}]_{SB}$ If $\lvert\alpha_W\rvert > 10.0 \rightarrow k_{W(B)} = 0.9[k_{W(B)}]_{SB} - 0.003[\lvert\alpha_W\rvert - 10.0]$ If $\lvert\alpha_W\rvert \le 20.0 \rightarrow F = 0.8$ If $\lvert\alpha_W\rvert > 20.0 \rightarrow F = 0.8 + 0.17[\lvert\alpha_W\rvert - 20.0]$
$M = 2.3$	If $\lvert\alpha_W\rvert \le 40.0 \rightarrow k_{W(B)} = 0.9[k_{W(B)}]_{SB}$ If $\lvert\alpha_W\rvert > 40.0 \rightarrow k_{W(B)} = 0.9[k_{W(B)}]_{SB} + 0.005[\lvert\alpha_W\rvert - 40.0]$ If $\lvert\alpha_W\rvert \le 30.0 \rightarrow F = 0.9$ If $\lvert\alpha_W\rvert > 30.0 \rightarrow F = 0.9 + 0.15[\lvert\alpha_W\rvert - 30.0]$
$M = 2.87$	If $\lvert\alpha_W\rvert \le 40.0 \rightarrow k_{W(B)} = 0.9[k_{W(B)}]_{SB}$ If $\lvert\alpha_W\rvert > 40.0 \rightarrow k_{W(B)} = 0.9[k_{W(B)}]_{SB} + 0.005[\lvert\alpha_W\rvert - 40.0]$ If $\lvert\alpha_W\rvert \le 30.0 \rightarrow F = 0.9$ If $\lvert\alpha_W\rvert > 30.0 \rightarrow F = 0.9 + 0.17[\lvert\alpha_W\rvert - 30.0]$
$M = 3.95$	If $\lvert\alpha_W\rvert \le 20.0 \rightarrow k_{W(B)} = 0.8[k_{W(B)}]_{SB}$ If $\lvert\alpha_W\rvert > 20.0 \rightarrow k_{W(B)} = 0.8[k_{W(B)}]_{SB} + 0.007[\lvert\alpha_W\rvert - 20.0]$ If $\lvert\alpha_W\rvert \le 30.0 \rightarrow F = 0.9$ If $\lvert\alpha_W\rvert > 30.0 \rightarrow F = 0.9 + 0.2[\lvert\alpha_W\rvert - 30.0]$
$M \ge 4.6$	If $\lvert\alpha_W\rvert \le 20.0 \rightarrow k_{W(B)} = 0.75[k_{W(B)}]_{SB}$ If $\lvert\alpha_W\rvert > 20.0 \rightarrow k_{W(B)} = 0.75[k_{W(B)}]_{SB} + 0.013[\lvert\alpha_W\rvert - 20.0]$ If $\lvert\alpha_W\rvert \le 35.0 \rightarrow F = 0.9$ If $\lvert\alpha_W\rvert > 35.0 \rightarrow F = 0.9 + 0.2[\lvert\alpha_W\rvert - 35.0]$

Where $\alpha_W = \alpha + \delta$ and for large α_W

$$k_{B(W)} = [k_{B(W)}]_{SB} \text{ for } \lvert\alpha_W\rvert \le 70 \text{ deg}$$

$$k_{B(W)} = [k_{B(W)}]_{SB}\left[1 - \left(\frac{\lvert\alpha_W\rvert - 70}{20}\right)\right] \text{ for } 70 < \lvert\alpha_W\rvert \le 90$$

$$k_{W(B)} = [k_{W(B)}]_{\lvert\alpha_W\rvert=70}\left[1 - \left(\frac{\lvert\alpha_W\rvert - 70}{20}\right)\right] \text{ for } 70 < \lvert\alpha_W\rvert \le 90$$

$$k_{B(W)} = k_{W(B)} = 0 \text{ for } \lvert\alpha_W\rvert > 90 \text{ deg}$$

FIGURE 27. SEMIEMPIRICAL NONLINEAR CONTROL DEFLECTION MODEL ($\Phi = 0$ DEG)

MACH	NONLINEAR MODEL
$M \leq 0.8$	If $\lvert\alpha_W\rvert \leq 40.0$ deg$\rightarrow k_{W(B)} = 1.15[k_{W(B)}]_{SB}$ If $\lvert\alpha_W\rvert > 40.0$ deg$\rightarrow k_{W(B)} = 1.15[0.000794\lvert\alpha_W\rvert^2 - 0.0933\lvert\alpha_W\rvert + 2.71]$ $F = 1.1$
$M = 1.1$	If $\lvert\alpha_W\rvert \leq 15.0\rightarrow k_{W(B)} = 0.95[k_{W(B)}]_{SB}$ If $\lvert\alpha_W\rvert > 15.0\rightarrow k_{W(B)} = 0.95[0.00087\lvert\alpha_W\rvert^2 - 0.0825\lvert\alpha_W\rvert + 1.98]$ $F = 1.1$
$M = 1.5$	If $\lvert\alpha_W\rvert \leq 35.0\rightarrow k_{W(B)} = 0.95[k_{W(B)}]_{SB}$ If $35.0 < \lvert\alpha_W\rvert \leq 55.0\rightarrow k_{W(B)} = [8.067 \times 10^{-5}(\lvert\alpha_W\rvert - 35.0)^3 + 0.00201(\lvert\alpha_W\rvert - 35.0)^2 - 0.0295(\lvert\alpha_W\rvert - 35.0) + 0.939][k_{W(B)}]_{SB}$ If $55.0 < \lvert\alpha_W\rvert \leq 62.0\rightarrow k_{W(B)} = 1.02\left[1.0 - \frac{\lvert\alpha_W\rvert - 55.0}{7.284}\right][k_{W(B)}]_{SB}$ If $\lvert\alpha_W\rvert > 62.0\rightarrow k_{W(B)} = 0.04[k_{W(B)}]_{SB}$ If $\lvert\alpha_W\rvert \leq 20.0\rightarrow F = 0.8$ If $\lvert\alpha_W\rvert > 20.0\rightarrow F = 0.8 + 0.17[\lvert\alpha_W\rvert - 20.0]$
$M = 2.0$	If $\lvert\alpha_W\rvert \leq 20.0\rightarrow k_{W(B)} = 0.95[k_{W(B)}]_{SB}$ If $20.0 < \lvert\alpha_W\rvert \leq 55.0\rightarrow k_{W(B)} = [5.699 \times 10^{-5}(\lvert\alpha_W\rvert - 20.0)^3 + 0.00420(\lvert\alpha_W\rvert - 30.0)^2 + 0.00583(\lvert\alpha_W\rvert - 20.0) + 0.980][k_{W(B)}]_{SB}$ If $55.0 < \lvert\alpha_W\rvert \leq 62.0\rightarrow k_{W(B)} = 0.89\left[1.0 - \frac{\lvert\alpha_W\rvert - 55.0}{7.3279}\right][k_{W(B)}]_{SB}$ If $\lvert\alpha_W\rvert > 62.0\rightarrow k_{W(B)} = 0.04[k_{W(B)}]_{SB}$ If $\lvert\alpha_W\rvert \leq 20.0\rightarrow F = 0.8$ If $\lvert\alpha_W\rvert > 20.0\rightarrow F = 0.8 + 0.17[\lvert\alpha_W\rvert - 20.0]$
$M = 2.35$	If $\lvert\alpha_W\rvert \leq 30.0\rightarrow k_{W(B)} = 0.95[k_{W(B)}]_{SB}$ If $30.0 < \lvert\alpha_W\rvert \leq 55.0\rightarrow k_{W(B)} = [4.257 \times 10^{-5}(\lvert\alpha_W\rvert - 30.0)^3 + 0.00291(\lvert\alpha_W\rvert - 30.0)^2 + 0.0388(\lvert\alpha_W\rvert - 30.0) + 0.976][k_{W(B)}]_{SB}$ If $55.0 < \lvert\alpha_W\rvert \leq 90.0\rightarrow k_{W(B)} = [k_{W(B)}]_{\alpha=55} - \left(\frac{\lvert\alpha_W\rvert - 55.0}{35.0}\right)([k_{W(B)}]_{\alpha=55} - 0.04[k_{W(B)}]_{SB})$ If $\lvert\alpha_W\rvert \leq 30.0\rightarrow F = 0.9$ If $\lvert\alpha_W\rvert > 30.0\rightarrow F = 0.9 + 0.15[\lvert\alpha_W\rvert - 30.0]$
$M = 2.87$	If $\lvert\alpha_W\rvert \leq 30.0\rightarrow k_{W(B)} = 0.95[k_{W(B)}]_{SB}$ If $30.0 < \lvert\alpha_W\rvert \leq 55.0\rightarrow k_{W(B)} = [6.526 \times 10^{-5}(\lvert\alpha_W\rvert - 30.0)^3 - 0.00405(\lvert\alpha_W\rvert - 30.0)^2 + 0.0575(\lvert\alpha_W\rvert - 30.0) + 0.947][k_{W(B)}]_{SB}$ If $55.0 < \lvert\alpha_W\rvert \leq 90.0\rightarrow k_{W(B)} = [k_{W(B)}]_{\alpha=55} - \left(\frac{\lvert\alpha_W\rvert - 55.0}{35.0}\right)([k_{W(B)}]_{\alpha=55} - 0.04[k_{W(B)}]_{SB})$ If $\lvert\alpha_W\rvert \leq 30.0\rightarrow F = 0.9$ If $\lvert\alpha_W\rvert > 30.0\rightarrow F = 0.9 + 0.17[\lvert\alpha_W\rvert - 30.0]$

FIGURE 28. SEMIEMPIRICAL NONLINEAR CONTROL DEFLECTION MODEL (Φ = 45 DEG)

MACH	NONLINEAR MODEL
M = 3.95	If $\lvert\alpha_W\rvert \le 35.0 \rightarrow k_{W(B)} = 0.88[k_{W(B)}]_{SB}$ If $35.0 \le \lvert\alpha_W\rvert \le 55.0 \rightarrow k_{W(B)} = [-8.84 \times 10^{-5} (\lvert\alpha_W\rvert - 35.0)^3 + 0.000173 (\lvert\alpha_W\rvert - 35.0)^2 + 0.0397 (\lvert\alpha_W\rvert - 35.0) + 0.884] [k_{W(B)}]_{SB}$ If $55.0 \le \lvert\alpha_W\rvert \le 90.0 \rightarrow k_{W(B)} = [k_{W(B)}]_{\alpha=55} - \left(\frac{\lvert\alpha_W\rvert - 55.0}{35.0}\right) ([k_{W(B)}]_{\alpha=55} - 0.04[k_{W(B)}]_{SB})$ If $\lvert\alpha_W\rvert \le 30.0 \rightarrow F = 0.9$ If $\lvert\alpha_W\rvert > 30.0 \rightarrow F = 0.9 + 0.2[\lvert\alpha_W\rvert - 30.0]$
M ≥ 4.6	If $\lvert\alpha_W\rvert \le 35.0 \rightarrow k_{W(B)} = 0.83[k_{W(B)}]_{SB}$ If $35.0 \le \lvert\alpha_W\rvert \le 55.0 \rightarrow k_{W(B)} = [4.697 \times 10^{-5} (\lvert\alpha_W\rvert - 35.0)^3 - 0.00463 (\lvert\alpha_W\rvert - 35.0)^2 + 0.0739 (\lvert\alpha_W\rvert - 35.0) + 0.8310] [k_{W(B)}]_{SB}$ If $55.0 \le \lvert\alpha_W\rvert \le 90.0 \rightarrow k_{W(B)} = [k_{W(B)}]_{\alpha=55} - \left(\frac{\lvert\alpha_W\rvert - 55.0}{35.0}\right) ([k_{W(B)}]_{\alpha=55} - 0.04[k_{W(B)}]_{SB})$ If $\lvert\alpha_W\rvert \le 35.0 \rightarrow F = 0.9$ If $\lvert\alpha_W\rvert > 35.0 \rightarrow F = 0.9 + 0.2[\lvert\alpha_W\rvert - 35.0]$
$0 \le M \le \infty$	$k_{B(W)} = [k_{B(W)}]_{SB} - \frac{\lvert\delta_W\rvert}{30.0} (0.75\ [k_{B(W)}]_{SB})$ for $\lvert\delta_W\rvert \le 30.0$ $k_{B(W)} = 0.25\ [k_{B(W)}]_{SB}$ for $\lvert\delta_W\rvert > 30.0$

FIGURE 28. SEMIEMPIRICAL NONLINEAR CONTROL DEFLECTION MODEL (Φ = 45 DEG) (CONTINUED)

where $k_{W(B)}$ and F were defined in Figure 27. Also C_{N_α} of both the wing and tail were nonlinear values. The interference factor *i* was defined by the traditional SBT/LT[21] approach.

While Equation (26) was helpful in defining some of the nonlinearities of missile aerodynamics not predicted by SBT or LT, it still had two major weaknesses. First of all, the tail interference factor methodology was independent of Mach number, and second, there was no parameter for the first term of Equation (26), similar to the parameter F of the second term, to help control the quasilinear character of the equation. These two problems were partially accounted for in the AP95[1] by placing upper limits on the $C_{N_{T(V)}}$ term as a percent of total tail lift and as a function of Mach number. However, these upper limits mainly affected large wing configurations where the wing-tail interference could exceed the tail lift.

In an effort to improve upon the present semiempirical wing-tail methodology, the literature was searched for wing-tail interference data. References 22 and 23 were found in this process. These references documented wind tunnel tests on two different missile configurations in which actual wing-tail normal force measurements were made. Reference 22 measured these results on individual fins as a function of roll position at Mach numbers of 2, 3 and 4. Reference 23 gave results for only the Φ = 0 deg roll position at M_∞ = 1.1. Figure 30 shows the configuration tested

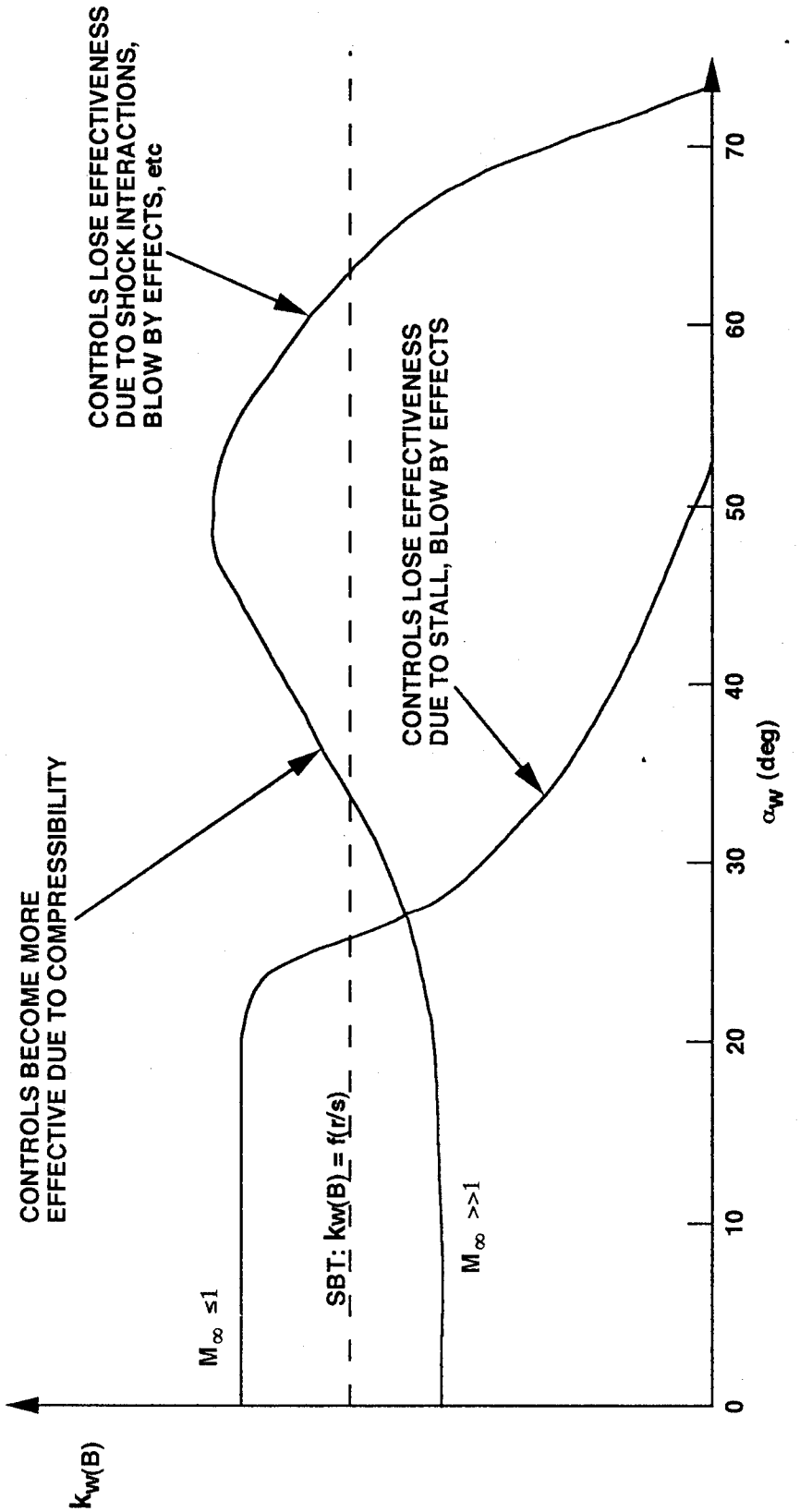

FIGURE 29A. QUALITATIVE TREND OF WING-BODY INTERFERENCE DUE TO CONTROL DEFLECTION AS FUNCTION OF M_∞, α_w

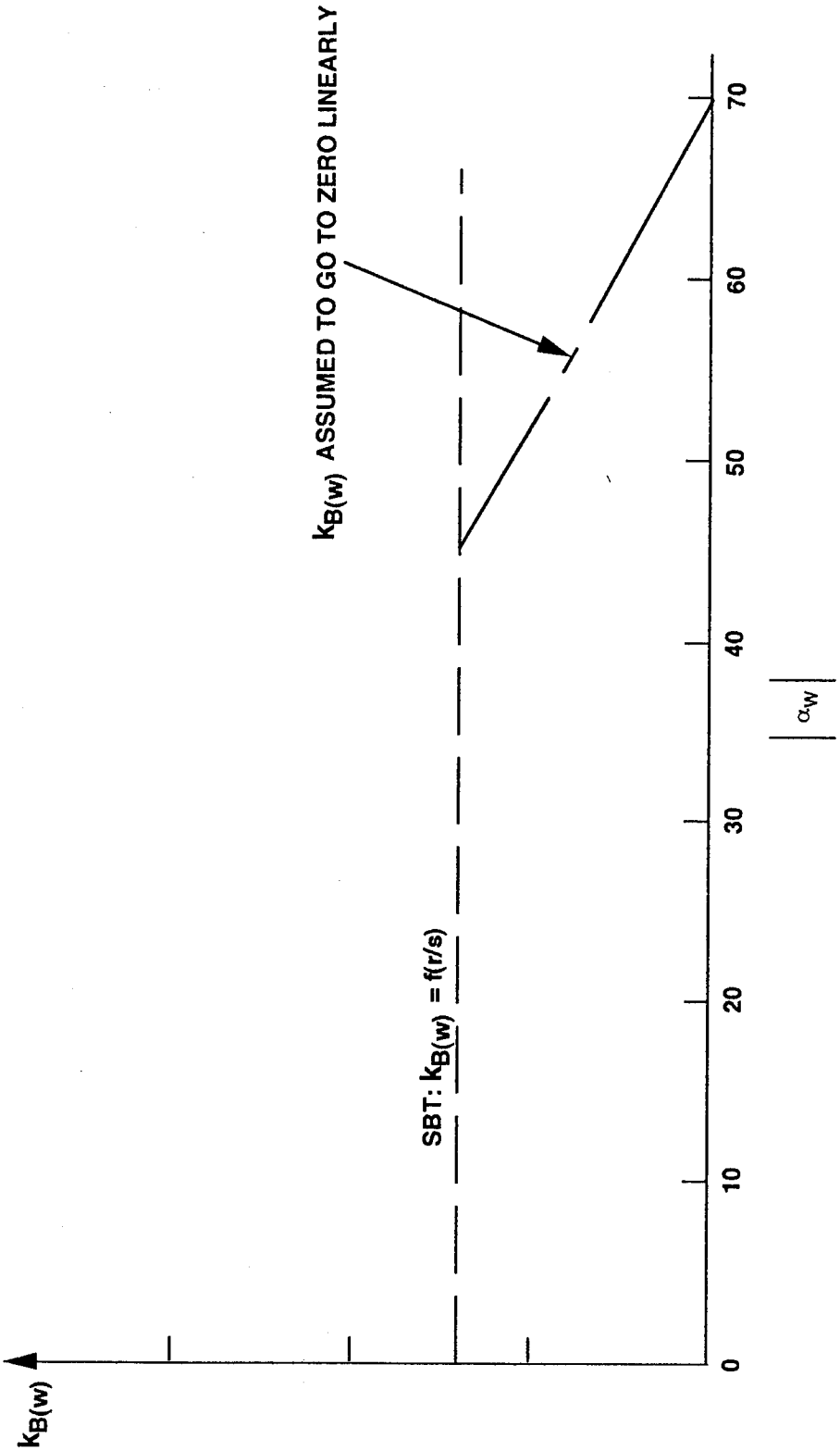

FIGURE 29B. QUALITATIVE TREND OF BODY-WING INTERFERENCE DUE TO CONTROL DEFLECTION AS FUNCTION OF α_w

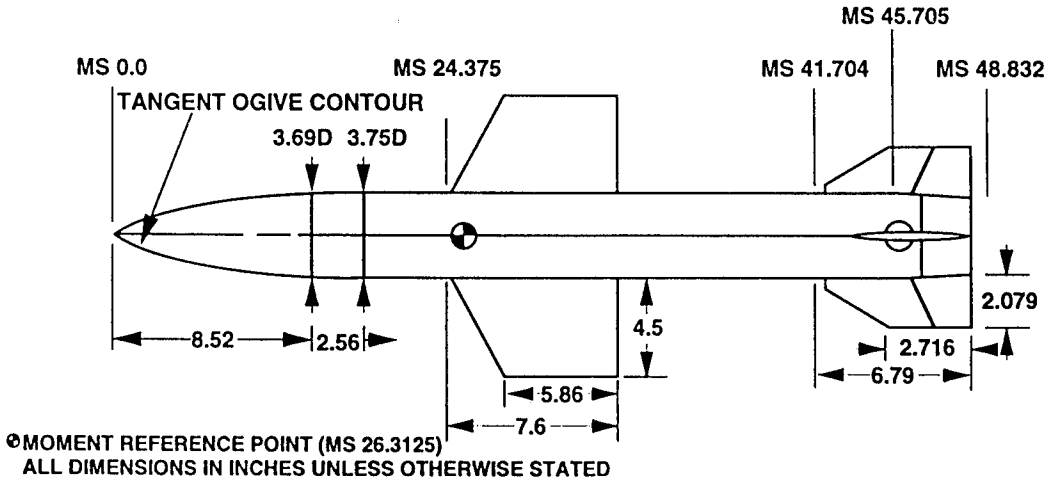

A. CONFIGURATION TESTED IN REFERENCE 22

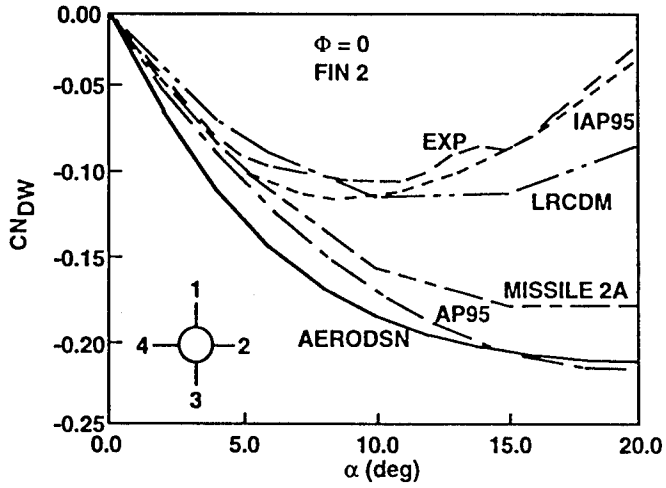

B. SINGLE FIN WING-TAIL INTERFERENCE (M=1.96)

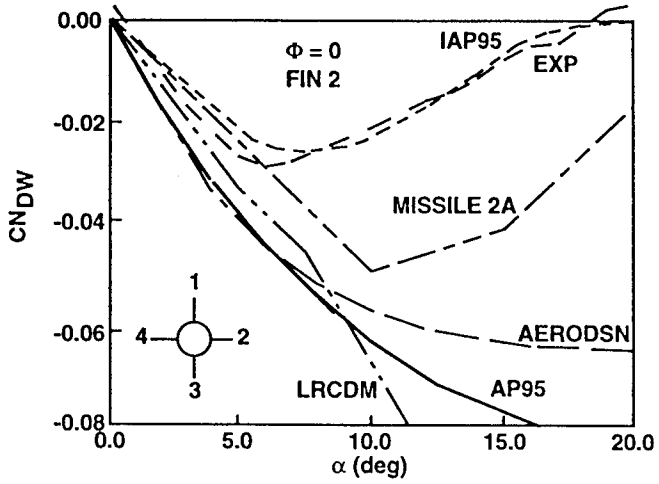

C. SINGLE FIN WING-TAIL INTERFENCENCE (M=4.02)

FIGURE 30. CONFIGURATION AND SINGLE FIN DATA FROM REFERENCE 22 FOR WING-TAIL INTERFERENCE NORMAL FORCE

in Reference 22 along with results at $M_\infty = 1.96$ and 4.02 at roll position of 0 deg. Also reported in Reference 22 were the theoretical computations from analytical codes referred to as AERODSN,[24] MISSILE 2A,[25] and LRCDM.[26] According to Reference 22, the AERODSN code has the same wing-tail interference model as the older version of the Aeroprediction Code and is based on SBT from Reference 21. The MISSILE 2A program is based on theory and experiment and therefore should contain some of the nonlinearity associated with the wing-tail interference. The LRCDM code is based on paneling methods and data bases and therefore should also contain some of the nonlinearities of the wing-tail interference. For comparison purposes, $C_{N_{T(V)}}$ computed by the AP95 for a single fin is also shown on Figures 30B and 30C. The AP95, although it contains some nonlinearities, still resembles the SBT, as seen from the close proximity to the AERODSN results. It is fair to say, in viewing the comparison of the various theoretical approaches for predicting wing-tail interference in Figure 29, that improvements in the theory are needed.

One might argue that the value of $C_{N_{T(V)}}$ is so small that it can be neglected. However, in most cases the moment arm is fairly large so even a small loss of lift on the tail is magnified in the pitching moment. As a result of this and the fact the $C_{N_{T(V)}}$ term is not predicted well by any of the theoretical approaches, it was decided to try to develop a new semiempirical approach to predict $C_{N_{T(V)}}$. The new approach will still be anchored by the traditional SBT[21] but will be modified according to the data from References 22 and 23.

A model for no control deflection, based on a third order equation in AOA is postulated to fit the data from both References 22 and 23. This model is defined by

$$\left[C_{N_{T(V)}}\right]_\alpha = A + B\alpha + C\alpha^2 + D\alpha^3 \tag{27}$$

The four constants of Equation (27) require four conditions to define them. These conditions are as follows:

(1) Slope of SBT value for $C_{N_{T(V)}}$ near $\alpha = 0$ (Using this value and a value of the real slope from data, a modified value of this slope can be obtained.)
(2) AOA where $C_{N_{T(V)}}$ goes to zero based on data
(3) AOA where $C_{N_{T(V)}}$ reaches a maximum based on data
(4) Maximum value of $C_{N_{T(V)}}$ as a percent of SBT at AOA where $C_{N_{T(V)}}$ is a maximum

Note in the four conditions chosen, SBT is used twice. Based on these conditions the four constants of Equation (27) become

$$A = 0$$

$$B = \left[\left(\frac{dC_{N_{T(V)}}}{d\alpha}\right)_{\alpha=0}\right]_{SBT} E_1$$

$$C = \frac{-B - D \alpha_N^2}{\alpha_N}$$

$$D = \frac{E_2 \alpha_N - B\alpha_N\alpha_F + B\alpha_F^2}{\alpha_N\alpha_F^3 - \alpha_F^2\alpha_N^2}$$

The parameters in the constants B, C, D are defined as follows:

α_{N_o} = Value from Figure 31A

α_F = (Value from Figure 31B) $\times \frac{\alpha_N}{100}$

E_1 = Value from Figure 31C

E_2 = (Value from Figure 31D) $\times \left(\left[C_{N_{T(V)}} \right]_{SBT} / _{\alpha = \alpha_F} \right)$

Referring back to Equation (26), if we break this equation down into the part due to AOA and the part due to control deflection, we have

$$C_{N_{T(V)}} = \left[C_{N_{T(V)}} \right]_{\alpha} + \left[C_{N_{T(V)}} \right]_{\delta} \tag{28}$$

Equation (27) is used to estimate the term due to α, and the section 2.2.4 methodology is used to predict the methodology for the second part of Equation (28). We now have independent controls on both portions of Equation (26), which is based on SBT, but the controls allow the SBT to be adjusted to data.

The question arises regarding how to account for fins that are different sizes and locations than those tested in References 22 and 23. Fortunately, both fins tested in these references were significantly larger than the tail surfaces and were located in a wing versus a canard location. Hence, the present approach will be to use these results directly for wings or canards of less area to body reference area than those tested. For wings of greater area, it is assumed that the AOA, α_N, where the $C_{N_{T(V)}}$ becomes negligible is increased according to

$$\alpha_N = \alpha_{N_o} \text{ for } A_W/A_{REF} \leq 5.5$$

$$\alpha_N = \alpha_{N_o} \left(\frac{A_W/A_{REF}}{5.5} \right) \text{ for } A_W/A_{REF} > 5.5 \tag{29}$$

with an upper limit on α_N of 2.5 α_{N_o}.

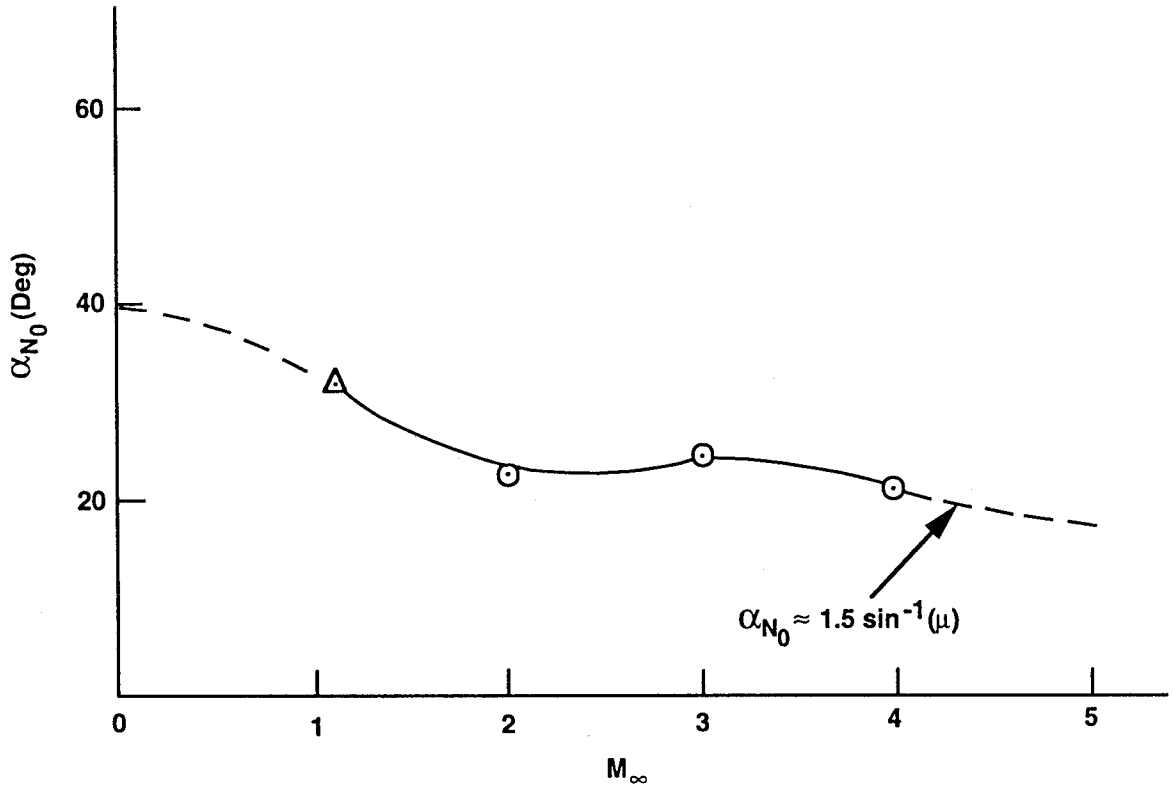

FIGURE 31A. AOA WHERE WING-TAIL INTERFERENCE IS NEGLIGIBLE

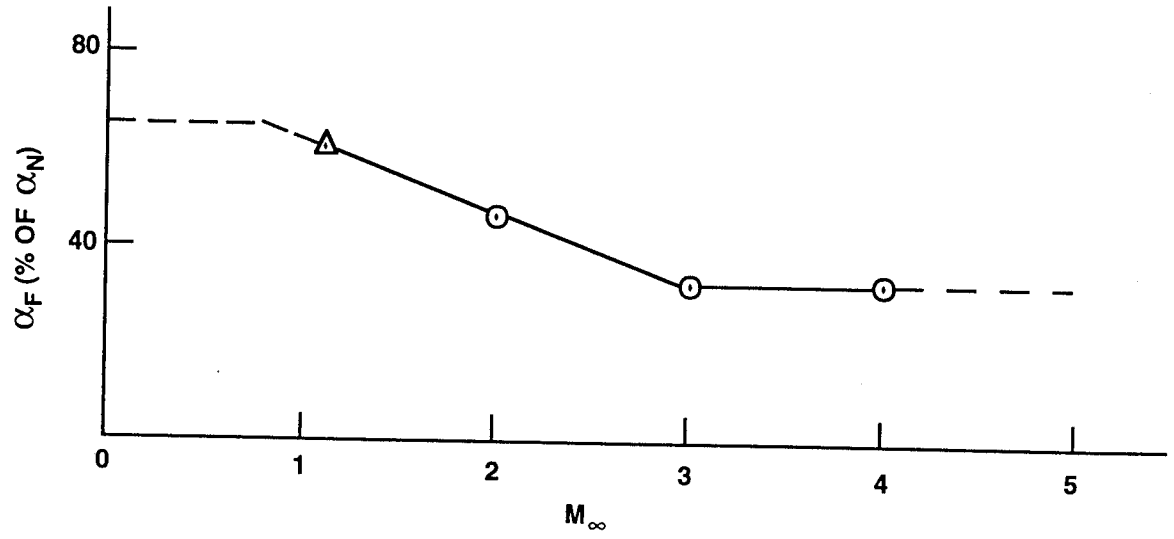

FIGURE 31B. AOA WHERE WING-TAIL INTERFERENCE
IS A MAXIMUM (PERCENT OF α_N)

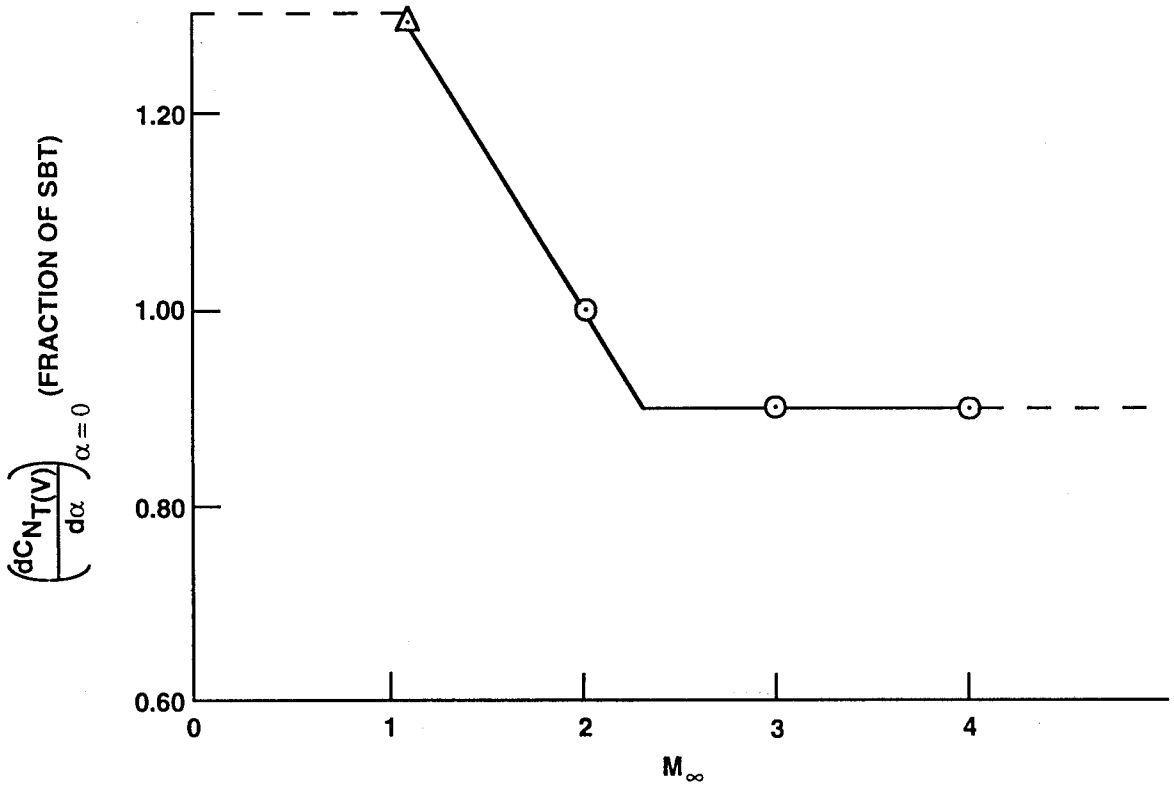

FIGURE 31C. INITIAL SLOPE AT $\alpha = 0$ OF WING-TAIL INTERFERENCE AS A FUNCTION OF M_∞

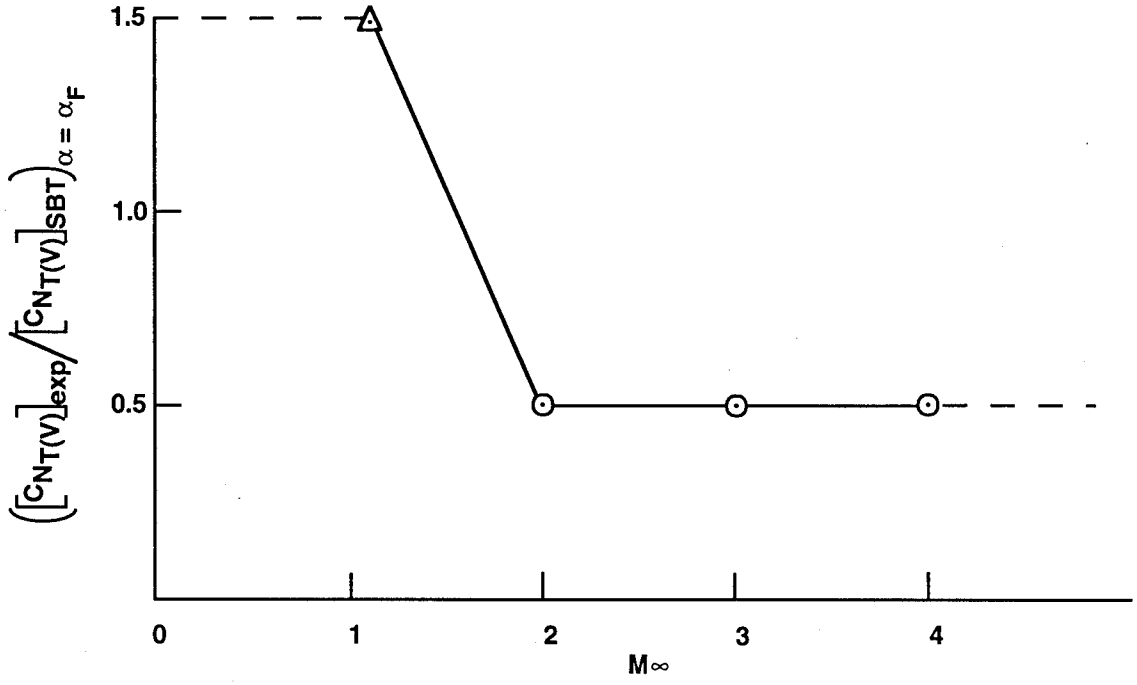

FIGURE 31D. SLENDER BODY THEORY PREDICTION OF WING-TAIL INTERFERENCE AT AOA WHERE $\left[C_{N_{T(V)}}\right]_{EXP}$ REACHES A MAXIMUM AS A FRACTION OF EXPERIMENTAL DATA

The value of A_W/A_{REF} of 5.5 corresponds to the wing area ratio of Reference 22. Also, for wings larger than those of Reference 22, an upper limit on the amount of lift loss on the tail will remain in effect. This upper limit is defined by the following methodology:

For $M \leq 1.5$

$$\frac{\left|C_{N_{T(V)}}\right|}{C_{N_T}} = 1.0 \; ; \; \alpha \leq 5$$

$$\frac{\left|C_{N_{T(V)}}\right|}{C_{N_T}} = 1.0 - 0.04125\,(\alpha - 5) \; ; \; \alpha > 5 \qquad (29A)$$

For $1.5 < M \leq 2.5$

$$\frac{\left|C_{N_{T(V)}}\right|}{C_{N_T}} = 0.9 - 0.025\alpha \; ; \; \alpha \leq 10$$

$$\frac{\left|C_{N_{T(V)}}\right|}{C_{N_T}} = 0.65 - 0.0235\,(\alpha - 10) \; ; \; \alpha > 10 \qquad (29B)$$

For $M > 2.5$

$$\frac{\left|C_{N_{T(V)}}\right|}{C_{N_T}} = 0.8 - 0.025\alpha \qquad (29C)$$

where α is AOA in degrees. Equation (29A) says that at $\alpha = 0$ deg, the maximum lift loss on the tail is limited to 100 percent of the tail lift, regardless of the size of the wings. The percent lift loss then decreases linearly with AOA as defined by Equations (29A) - (29C).

Admittedly, this is conservative (overpredicts $C_{N_{T(V)}}$) for values of $A_W/A_{REF} < 5.5$ and is simply a judgement based on numerical experiments for values of $A_W/A_{REF} > 5.5$. It does accomplish the objective of making the wing-tail interference with no control deflection more closely approximate data than available approaches, including the AP95. This is illustrated by the results shown in Figures 30B and 30C for Improved Aeroprediction Code 1995 (IAP95).

Before moving to the wing-tail interference methodology for the $\Phi = 45$ deg roll position, a comment would be valuable on the Figure 31 results, which basically compare SBT to data. First of all, it is clear that at low AOA, SBT underpredicts $C_{N_{T(V)}}$ for low Mach number and overpredicts it at high Mach number, for the Reference 22 configuration. The point of optimum prediction appears to be around Mach 2 (see Figure 31C). Second, the $C_{N_{T(V)}}$ term decays much faster at high AOA than does SBT. This is increasingly true as Mach number increases. This again highlights the Newtonian Impact assumptions at high Mach number where any vortices in the leeward plane are completely dominated by the dynamic pressure in the windward plane. Figures 31A and 31B

illustrate this fact, showing that the AOA where $C_{N_{T(V)}}$ is negligible gets smaller as M_∞ increases; also, the maximum magnitude as a percent of SBT gets smaller with increasing M_∞.

2.2.9 Nonlinear Wing-Tail Interference Model for Φ = 45 deg

The SBT representation of the wing-tail interference for Φ = 45 deg roll is outlined in Appendix A. As pointed out in the appendix, the assumption is made that the strength of the vortex shed from the windward plane fins is equal in magnitude and opposite in direction to the leeward plane fins. At small AOA, this assumption is quite reasonable and is partially what leads to the fact that cruciform wing-body-tail missile aerodynamics are independent of roll position. As AOA increases, this assumption becomes less and less valid. In fact, the lift of the windward plane fin is much larger than the leeward plane fin as AOA increases. This was modeled approximately in the center of pressure shift discussed earlier by approximating a linear variation in the shift of normal force to the windward plane fin from the leeward plane fin up to AOA 65 deg. At that point, the ratio of the windward to leeward plane load remained constant.

If we define the factors,

$$P_W = \left(1.0 + 0.6\frac{\alpha}{65}\right),\ P_\ell = \left(1.0 - 0.6\frac{\alpha}{65}\right)\ ;\ \alpha \le 65$$

$$P_W = 1.6\ ,\ P_\ell = 0.4\ ;\ \alpha > 65 \qquad (30)$$

then the interference factors can be weighted by Equation (30) depending on where the vortex is shed. If it is shed in the windward plane, then the P_W factor is appropriate; whereas if it is shed from the leeward plane, then the P_ℓ factor in Equation (30) is appropriate. This is an approximate way to represent the nonlinear nature of the load in the windward to leeward plane fin, and the strength of the vorticity shed from each fin.

Using Equation (30) along with Equations (A-42) and (A-43) of the appendix, an approximate nonlinear representation of the wing-tail interference factors for the Φ = 45 deg roll position is

$$i_1 = \left(\frac{2\cos\Phi}{1+\lambda_T}\right)\left\{P_W\left[L\left(\lambda_T, \frac{r_T}{s_T}, \frac{Y_1}{s_T}, \frac{Z_1}{s_T}\right) - L\left(\lambda_T, \frac{r_T}{s_T}, \frac{Y_2}{s_T}, \frac{Z_2}{s_T}\right)\right.\right.$$

$$- L\left(\lambda_T, \frac{r_T}{s_T}, \frac{Y_5}{s_T}, \frac{Z_5}{s_T}\right) + L\left(\lambda_T, \frac{r_T}{s_T}, \frac{Y_6}{s_T}, \frac{Z_6}{s_T}\right)\Bigg]$$

$$+ P_\ell \Bigg[- L\left(\lambda_T, \frac{r_T}{s_T}, \frac{Y_3}{s_T}, \frac{Z_3}{s_T}\right) + L\left(\lambda_T, \frac{r_T}{s_T}, \frac{Y_4}{s_T}, \frac{Z_4}{s_T}\right)$$

$$+ L\left(\lambda_T, \frac{r_T}{s_T}, \frac{Y_7}{s_T}, \frac{Z_7}{s_T}\right) - L\left(\lambda_T, \frac{r_T}{s_T}, \frac{Y_8}{s_T}, \frac{Z_8}{s_T}\right)\Bigg]\Bigg\} \tag{31}$$

$$I_4 = \left(\frac{2\sin\Phi}{1 + \lambda_T}\right)\Bigg\{P_W\Bigg[L\left(\lambda_T, \frac{r_T}{s_T}, \frac{Y_1}{s_T}, \frac{Z_1 - f_W\cos\Phi}{s_T}\right)$$

$$- L\left(\lambda_T, \frac{r_T}{s_T}, \frac{Y_2}{s_T}, \frac{Z_1 - f_W\cos\Phi}{s_T}\right)$$

$$- L\left(\lambda_T, \frac{r_T}{s_T}, \frac{Y_5}{s_T}, \frac{Z_5}{s_T}\right) + L\left(\lambda_T, \frac{r_T}{s_T}, \frac{Y_6}{s_T}, \frac{Z_6}{s_T}\right)\Bigg]$$

$$+ P_L\Bigg[-L\left(\lambda_T, \frac{r_T}{s_T}, \frac{Y_3}{s_T}, \frac{Z_3}{s_T}\right) + L\left(\lambda_T, \frac{r_T}{s_T}, \frac{Y_4}{s_T}, \frac{Z_4}{s_T}\right)$$

$$+ L\left(\lambda_T, \frac{r_T}{s_T}, \frac{Y_7}{s_T}, \frac{Z_7}{s_T}\right) - L\left(\lambda_T, r_T, \frac{Y_8}{s_T}\frac{Z_8}{s_T}\right)\Bigg]\Bigg\} \tag{32}$$

All the nomenclature in Equations (31) and (32) are defined in the Appendix A. The wing-tail interference normal force is then

$$C_{N_{T(V)}} = \frac{A_W (C_{N\alpha})_W (C_{N\alpha})_T \left[K_{W(B)}\alpha + Fk_{W(B)}\delta_W\right]}{2\pi\ (AR)_T\ (f_W - r_w)\ A_{REF}} (s_T - r_T)\left[i_1 \cos\Phi + i_4 \sin\Phi\right] \qquad (33)$$

For small AOA and no control deflection, Equation (33) reverts back to SBT.

The final modification for inclusion of nonlinearities into the wing-tail interference model for the $\Phi = 45$ deg roll position is to adjust Equation (33) based on experimental data analogous to the $\Phi = 0$ deg methodology of Figure 31. For the 45 deg roll position, the only data found on individual fins were from Reference 22. Figure 32 gives the $C_{N_{T(V)}}$ values for M_∞ values of 1.96, 3.01 and 4.02. In developing an analogous model to Figure 31 for $\Phi = 45$ deg, qualitative use will be made of the $\Phi = 0$ deg results at lower Mach number since at least one set of data[23] existed for $M_\infty = 1.1$. These results will be used to compare trends of data as a function of Mach number and AOA, not their absolute values.

Note the curves of Figure 32 show a point of inflection in the experimental data between 10 and 15 deg AOA. This is because at very low AOA, the windward and leeward plane vortices shed from the wings adversely impact the tail normal force. However, at a slightly higher AOA, the windward plane wing-shed vortex has a positive effect on the leeward plane tail because of the counterclockwise vortex hitting the windward side of the leeward tail surface. As the AOA is increased higher, the wing-shed windward plane vortex rises above the leeward plane tail fin, at which point both wing-shed vortices again have an adverse impact on the tail normal force.

While a model such as that derived for the $\Phi = 0$ roll position could be derived for the $\Phi = 45$ deg plane, it is more difficult because of a lack of data below $M_\infty = 2.0$ and the shape of the curves in Figure 32. As a result, modified SBT was used to calculate $C_{N_{T(V)}}$ at various AOAs and at the three Mach numbers where data were available. The results were compared to the experimental data of Figure 32, and the semiempirical model of Figure 33 was defined for no control deflection.

Referring to Equation (28), the first part of the equation for $\Phi = 45$ deg, $\delta_W = 0$ is

$$\left[C_{N_{T(V)}}\right]_\alpha = G_1 \left[C_{N_{T(V)}}\right]_{SBT} \qquad (34)$$

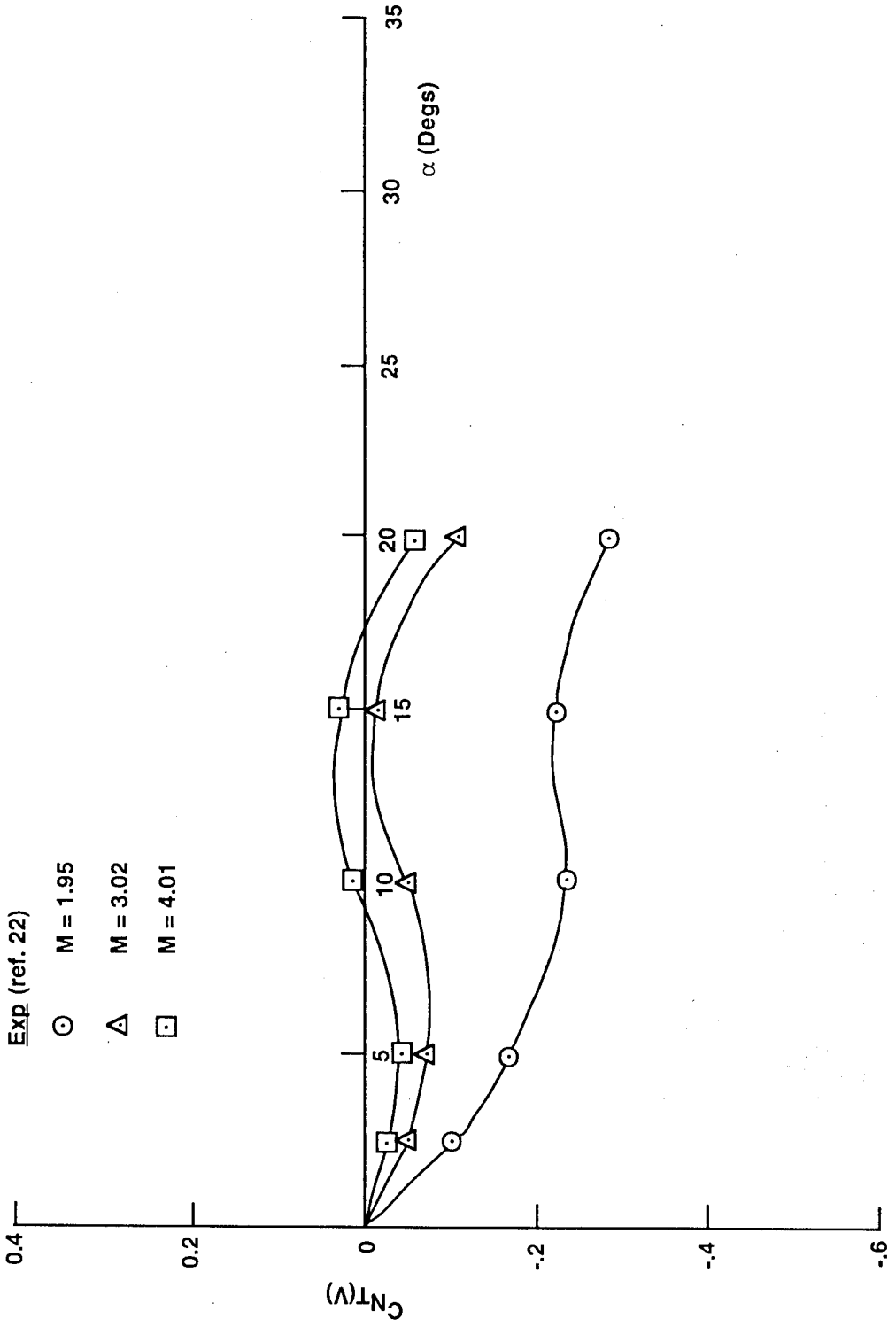

FIGURE 32. WING-TAIL INTERFERENCE (0 = 45 DEG, δ_w = 0 DEG)

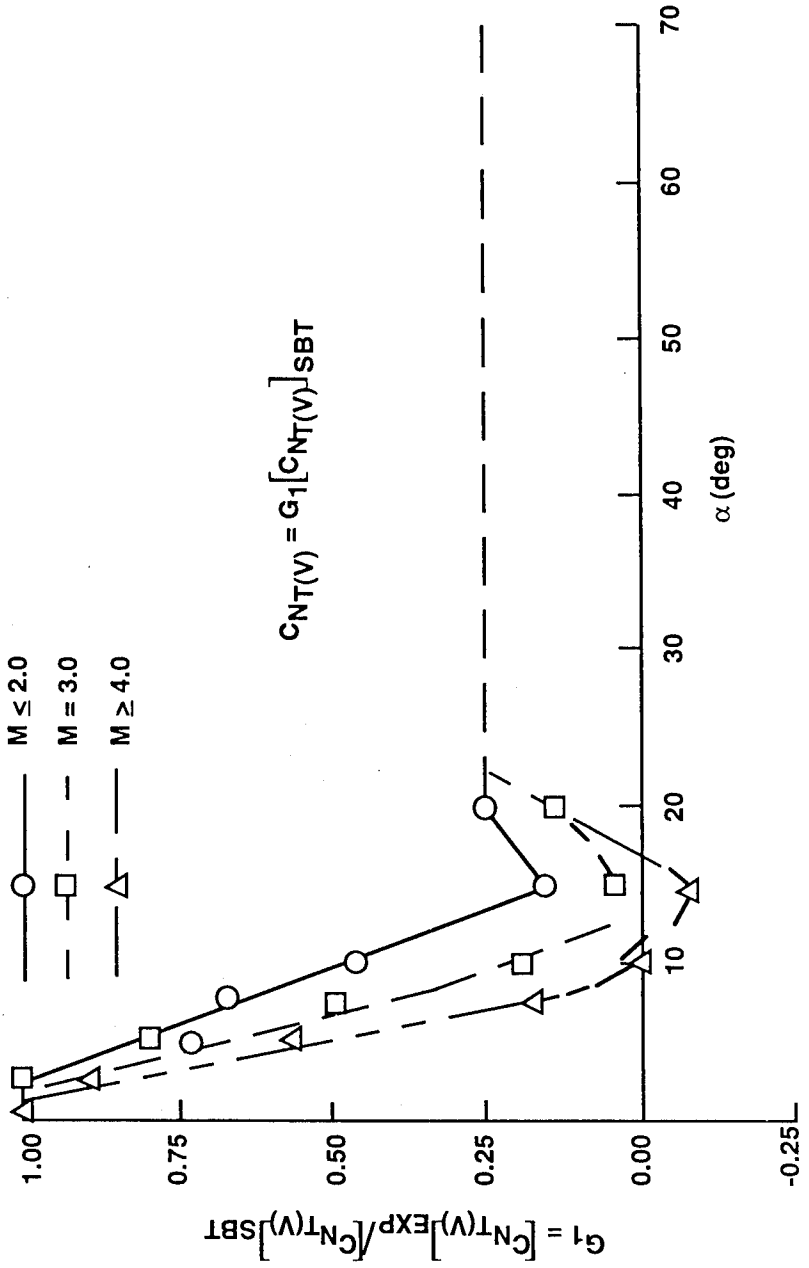

FIGURE 33. WING-TAIL INTERFERENCE MODEL FOR NO CONTROL DEFLECTION AT $\Phi = 45$ DEG

with the same maximum constraints placed on Equation (34) as for the Φ = 0 deg roll methodology. This constraint was given by Equation (29). Equation (29A) basically allows the negative tail normal force to not exceed a certain percent of the normal force of the tail regardless of SBT predictions. Equations (34) and (29), in conjunction with G_1 from Figure 33, and modified SBT [Equations (31) - (33)] defines the wing-tail interference model used for Φ = 45 deg.

3.0 RESULTS AND DISCUSSION

The new nonlinear aeroprediction methodology for the Φ = 45 deg roll position has been validated against many configurations within and outside the data bases upon which it was developed. The primary data bases upon which the methodology was based was given by References 6-8. If data points are taken at angles of attack of 10, 15, 20, 25, 30, 35, and 40 deg; at Mach numbers of 0.6, 0.8, 1.2, 1.5, 2.0, 2.5, 3.0, 3.5, and 4.5; at aspect ratios of 0.5 (λ=0, 0.5, 1.0) and 1.0; a total of 227 points are available to average. This is much lower than in previous data bases due to omission of the AR = 2.0 and 4.0 data. These data were omitted due to the very small wings used. Figure 34 compares the new Φ = 45 deg theory to the data base in terms of average C_N and X_{CP} accuracy. The average accuracy is defined as:

$$\frac{1}{227}\sum_{1}^{227}\frac{|\text{Theory} - \text{Exp}|}{\text{Exp}} \qquad (35)$$

As seen in Figure 34, the average accuracy of the Φ = 45 deg methodology compared to the data is somewhat worse than the Φ = 0 deg methodology. However, this is somewhat misleading. This is because the Φ = 0 deg results were taken directly from Reference 1 without recomputing the results with the revised "drag bucket" discussed in section 2.2.2. Since the revised "drag bucket" is not optimized to the Reference 8 database, it gave errors at the lower Mach numbers substantially larger than those in Reference 1. This was the main reason for the 2.2 percent and 0.003ℓ higher average error on C_N and X_{CP}, respectively, in Figure 34. Even with these increases in average errors, the overall average of 6.2 percent on C_N and 1.2 percent of body length for X_{CP} are well within the average error goals of ±10 percent for C_N and ± 4 percent of body length for center of pressure. It is expected that comparisons on configurations outside the Reference 8 data base at Φ = 45 deg will be as good as or better than those in Reference 1 at Φ = 0 deg.

Configurations considered in the validation process include those with both one and two sets of lifting surfaces. Those with only one set are either body-wing or body-tail configurations. Those with two sets are either canard-body-tail or wing-body-tail. The configurations with two sets of lifting surfaces will be useful in validating all the new methodology including the wing-tail interference with and without control deflections.

DATA BASE PARAMETERS

$0.6 \le M_\infty \le 4.6$
$0.25 \le AR \le 4$
$0 \le \lambda \le 1.0$
r/s = 0.5

BODY: 12.33 CALIBER OGIVE CYLINDER
3 CALIBER TAN OGIVE NOSE

COMPUTATIONAL RESULTS FOR 227 BODY-TAIL CASES

α = 10, 15, 20, 25, 30, (35, 40)

	C_N		$\overline{X}_{CP}$	
	Φ = 0 DEG AP95	Φ = 45 DEG IAP95	Φ = 0 DEG AP95	Φ = 45 DEG IAP95
AVG ERROR	4.1%	6.3%	.009ℓ	.012ℓ
MAX ERROR	11.8%	16.0%	.041ℓ	.030ℓ

FIGURE 34. COMPARISON WITH EXPERIMENTAL RESULTS OF REFERENCE 8 DATA BASE

3.1 WING-BODY OR BODY-TAIL CONFIGURATIONS

Seven configurations with one set of lifting surfaces are considered to validate the new methodology over a range of angles of attack, Mach numbers and at both the Φ = 0 and 45 deg roll orientation. Some of the Φ = 0 deg results were given previously in Reference 1, but are shown in conjunction with the Φ = 45 deg results for comparison purposes. This allows the reader to view the theoretical comparisons of the roll orientations simultaneously, as well as the impact of roll on the static aerodynamics. Emphasis in all the validations will be on normal force, pitching moment and center of pressure, as it is well known that the axial force accuracy of all the various versions of the NSWC Aeroprediction Code have been very good. Some axial force comparisons will be shown later for configurations with two sets of lifting surfaces.

The first configuration is the wing B configuration of Figure 2C. This configuration is the one used to determine the $K_{W(B)}$ and $K_{B(W)}$ nonlinear interference factors at low Mach number. Normal force coefficient and center of pressure computations compared to data[9] are presented in Figure 35. Reasonable accuracy levels are obtained for this overall configuration. If one averages the normal force and center of pressure errors at each 5 deg AOA according to Equation (35), average accuracy levels of 10.2 percent on C_N and 1.4 percent of body length for X_{CP} are obtained. This accuracy level is at the high end of the ±10 percent goal on normal force, but well within the ±4 percent ℓ on X_{CP}.

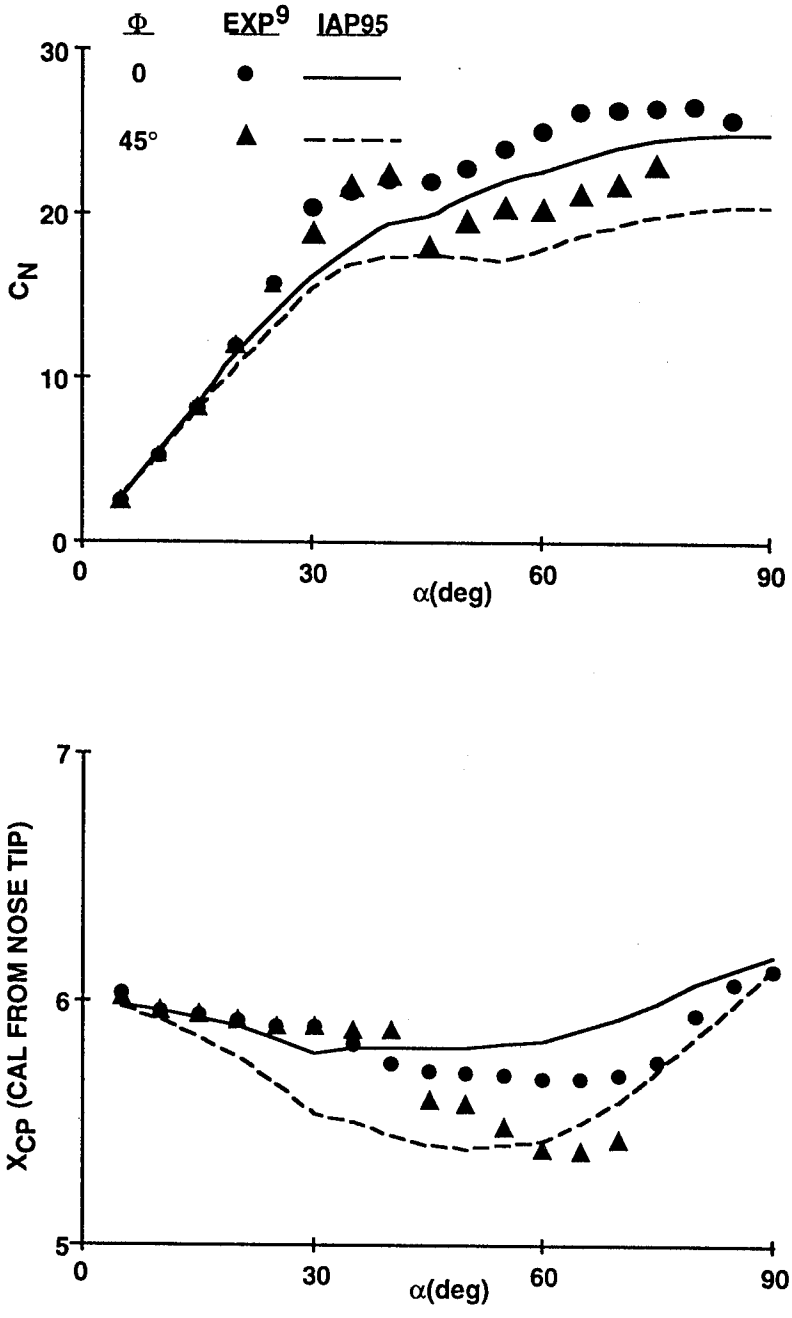

FIGURE 35. NORMAL FORCE COEFFICIENT AND CENTER OF PRESSURE COMPARISONS OF THEORY AND EXPERIMENT (CONFIGURATION OF FIGURE 2C; $M_\infty = 0.1$)

The accuracy on normal force was intentional at higher AOA. Note in Figure 35 that the predictions are consistently lower than the data above AOA approximately 25 to 30 deg. This is because this configuration was tested with a base mounted sting. Reviewing some of the wind tunnel model support interference literature (References 27-30), several conclusions were reached. These were that: a) For low Mach number, the problem of estimating interference effects of a strut or sting mount on the model aerodynamics at high AOA are not known precisely. (This is still true today). b) The preferable mount between a sting and a strut at high AOA is the sting. c) The sting tends to give positive interference (C_N too high) and the strut negative interference (C_N too low).

The affected region seems to be in the AOA range 30 to 80 deg. Sting C_N values can be high as much as 10-15 percent and strut C_N values for struts mounted in the mid-body region can be low by as much as 25-30 percent. For these reasons, the IAP95 methodology is intentionally designed to underpredict normal force on configurations at subsonic Mach numbers at high AOA where test data are from a sting mount, and therefore it is also expected the predictions will be higher than those from a strut-mounted model. The under/over prediction problem on C_N at high α appears to go away at Mach numbers slightly greater than one. This is suspected to be due to the reduction in the upstream influence of the sting on the body and the reduction of the wake effect on the body (strut mount).

The second configuration considered is a body-tail configuration (Figure 36A), also at a low Mach number of 0.15. Test results for this configuration were reported in Reference 31, but no mention was made of how the configuration was mounted in the tunnel (sting or strut). The test results are given in Figure 37. It is interesting to note that the experimental data for C_N reaches a maximum around an AOA of 55 deg and declines slightly up to 90 deg AOA. This is the typical behavior for a strut mounted configuration. The average errors for C_N and X_{CP}, between the predicted and experimental values, are 10.1 percent and 4.4 percent ℓ, respectively. Both of these are at the high end of the AP performance goal of ±10 percent on C_N and ±4 percent ℓ on X_{CP}. It is interesting to note that the C_N error in this case is positive, whereas for the case of Figure 35 it was negative. These two figures (Figures 35 and 36) illustrate the difficulty in accurately predicting static aerodynamics at subsonic Mach numbers for AOA greater than roughly 30 deg, because it is not clear what is prediction error and what is wind tunnel measurement error.

The third body-tail case even more vividly illustrates the problem of predicting aerodynamics at subsonic and transonic Mach numbers at high AOA. The configuration is shown in Figure 36B and was tested at Arnold Engineering and Development Center (AEDC) with a strut mounted to the leeward part of the configuration about in the middle of the body. According to Reference 27, this type of model support has the most severe adverse impact on the vehicle aerodynamics. Aerodynamic measurements are lower for normal force than they should be because the strut mount adversely impacts the pressure in the leeward plane of the body, causing the body to lose normal force. Figures 38A, 38B, and 38C present the experimental and predicted values of C_N and X_{CP} for M_∞ = 0.6, 0.9, and 1.3, respectively, for both the Φ = 0 and 45 deg roll positions. Note that center of pressure is reasonably well predicted at all Mach numbers and at both Φ = 0 and 45 deg. However, normal force is predicted accurately on average only at M = 1.3. The average errors on normal force for the three Mach numbers of 0.6, 0.9, and 1.3 are 19.3, 16.7, and 4 percent,

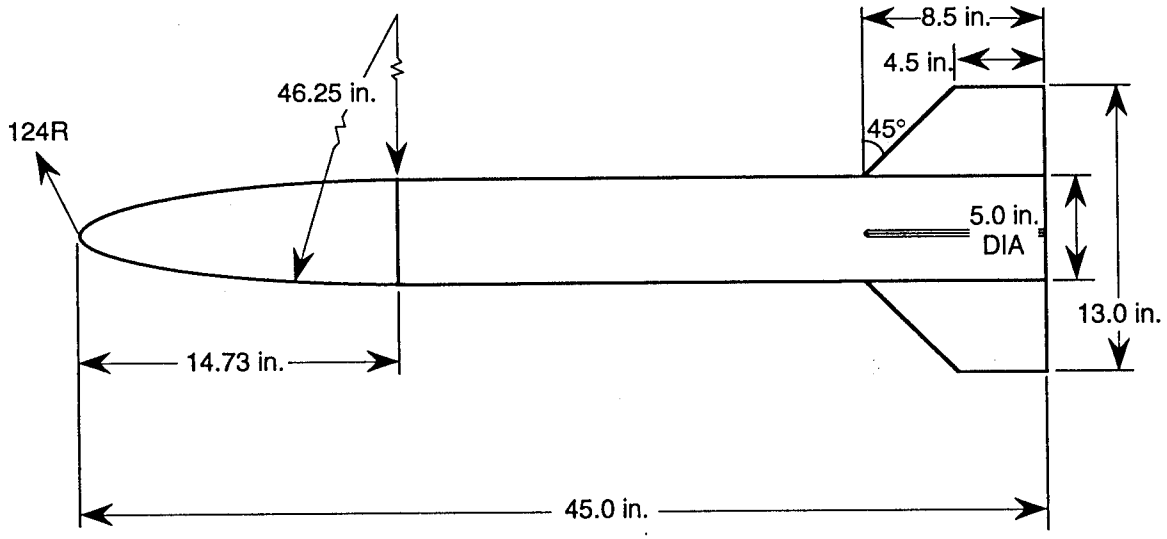

FIGURE 36A. SCHEMATIC OF REFERENCE 31 BODY-TAIL CONFIGURATION

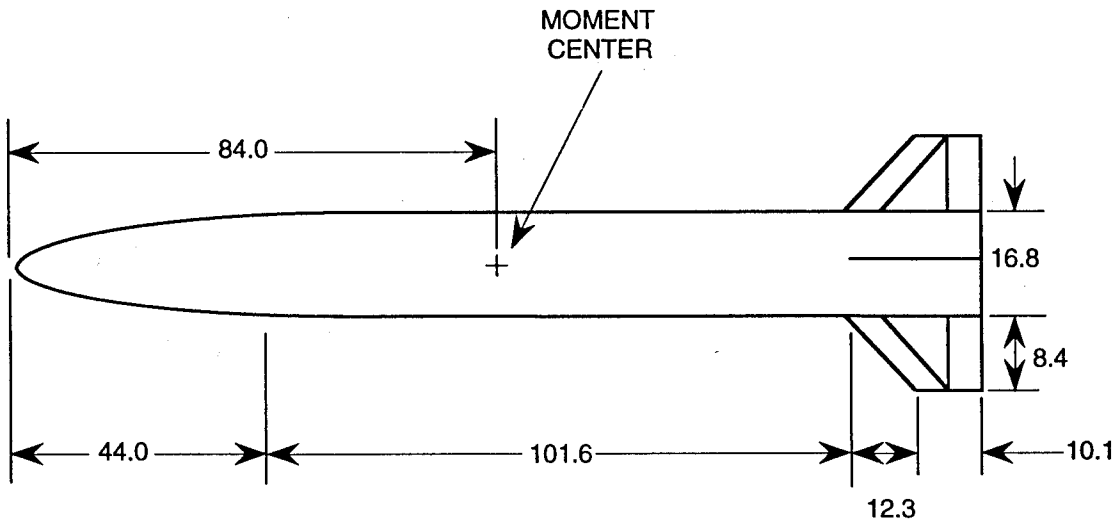

FIGURE 36B. SCHEMATIC OF REFERENCE 32 BODY-TAIL CONFIGURATION

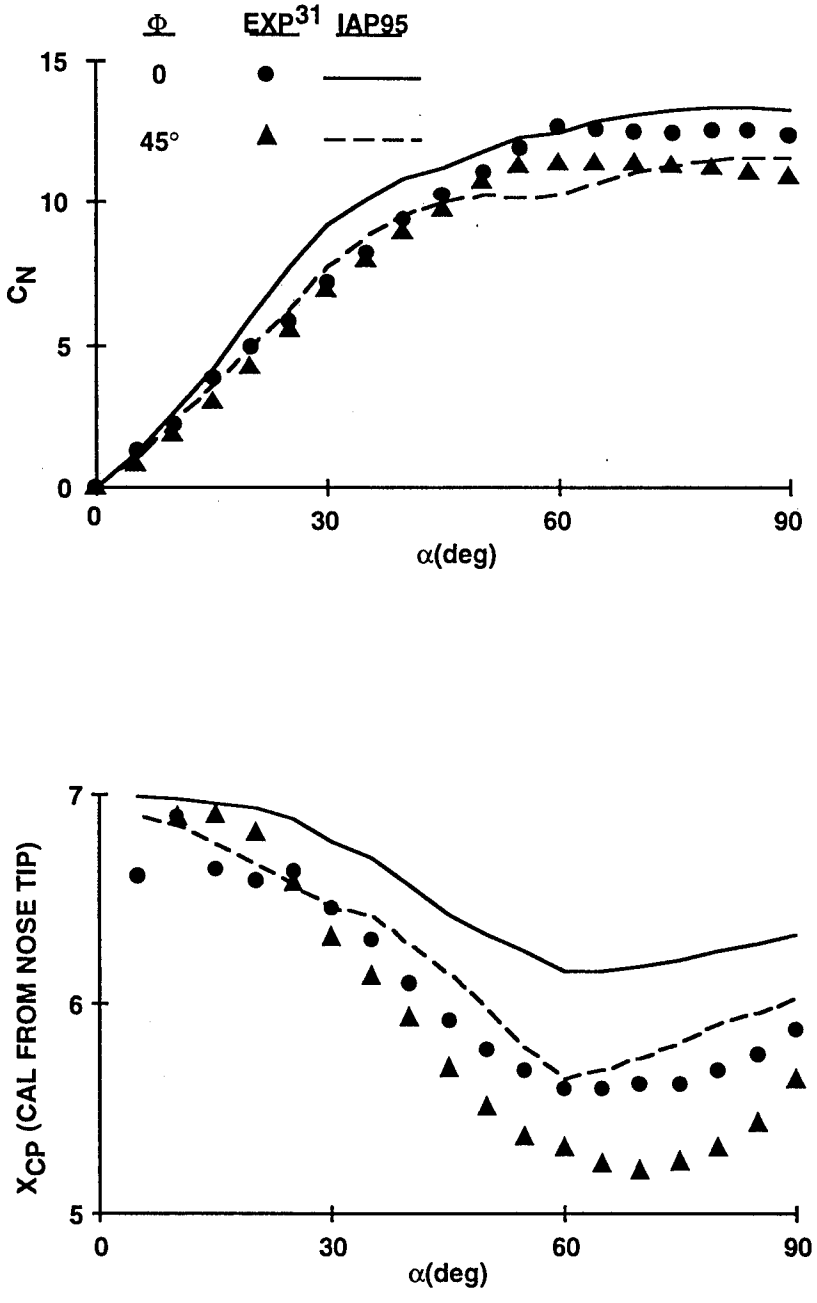

FIGURE 37. NORMAL FORCE COEFFICIENT AND CENTER OF PRESSURE COMPARISONS OF THEORY AND EXPERIMENT (CONFIGURATION OF FIGURE 36A; $M_\infty = 0.15$)

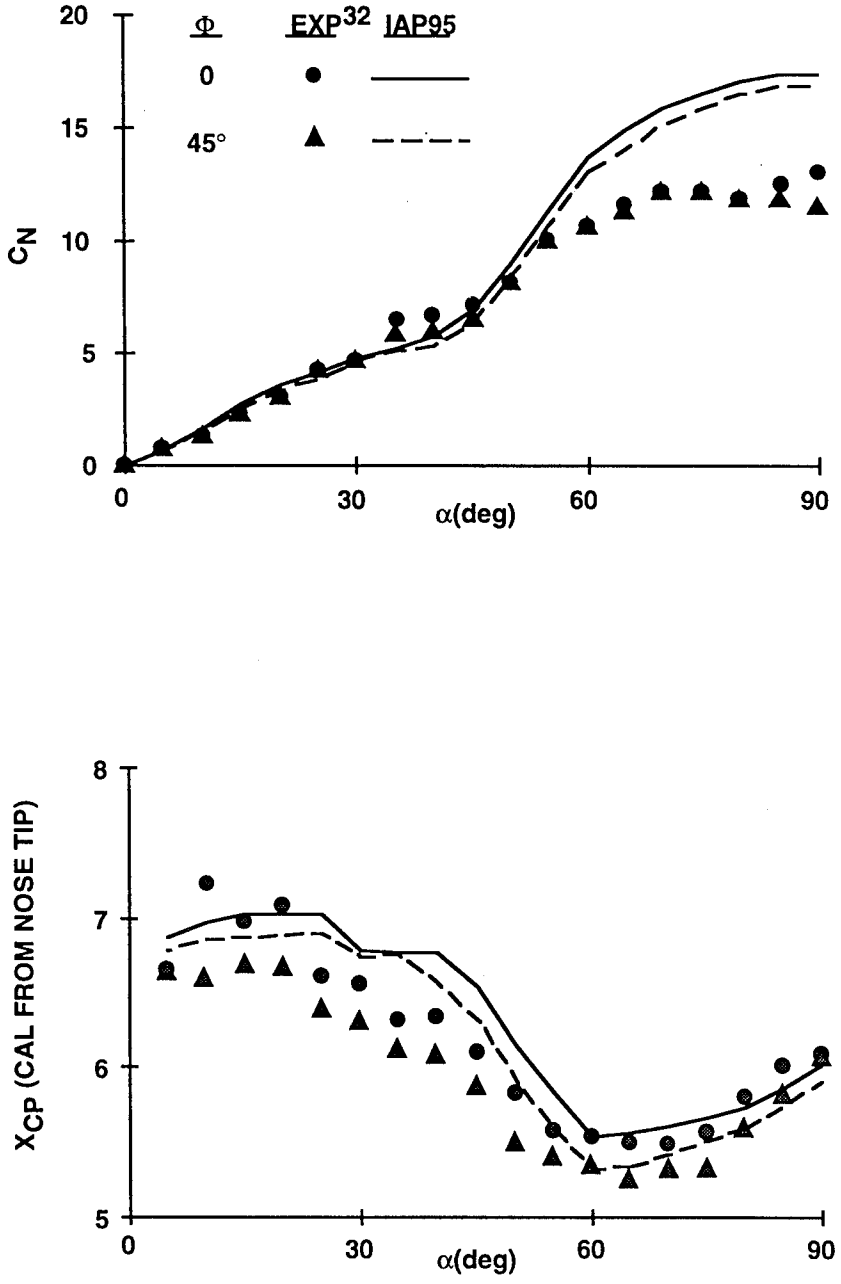

FIGURE 38A. NORMAL FORCE AND CENTER OF PRESSURE COMPARISONS OF THEORY AND EXPERIMENT (CONFIGURATION OF FIGURE 36B; $M_\infty = 0.6$)

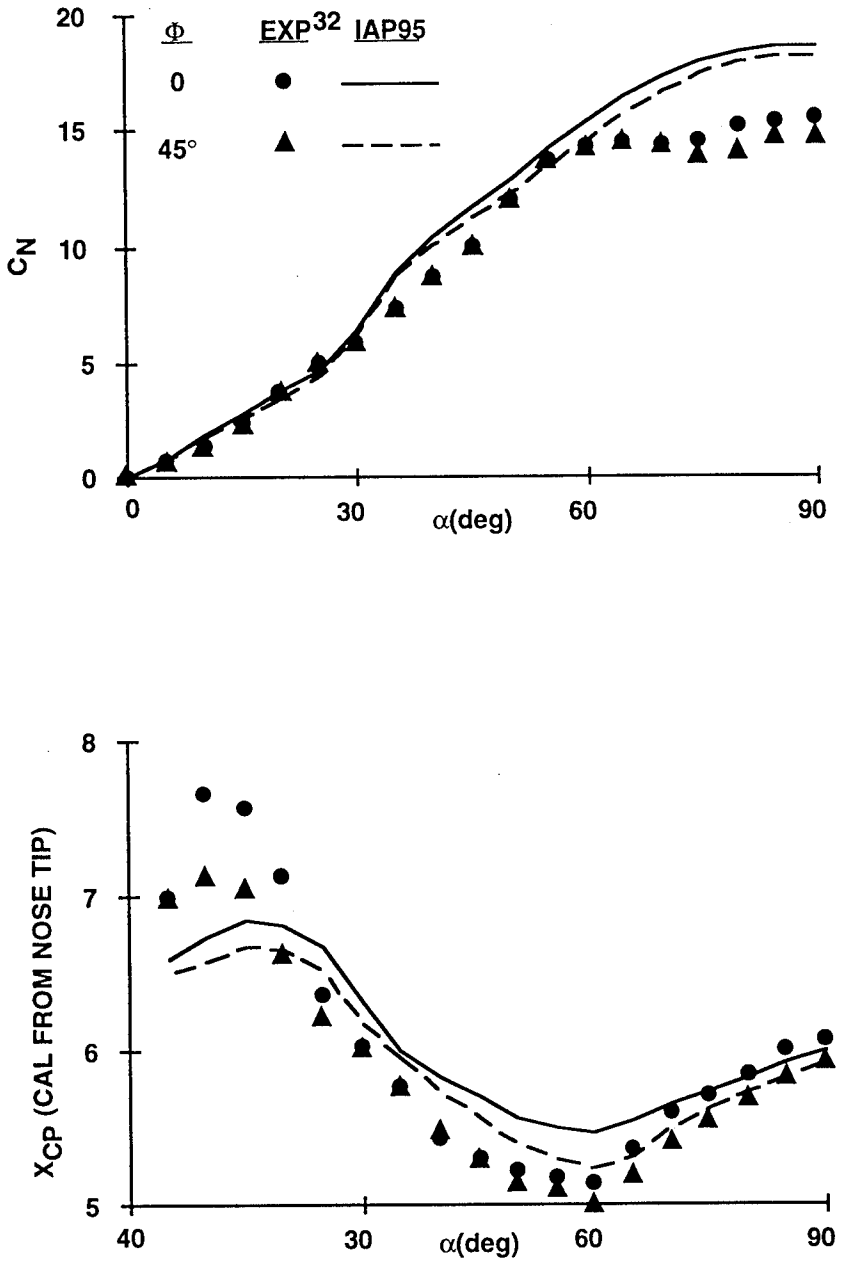

FIGURE 38B. NORMAL FORCE AND CENTER OF PRESSURE COMPARISONS OF THEORY AND EXPERIMENT (CONFIGURATION OF FIGURE 36B; $M_\infty = 0.9$)

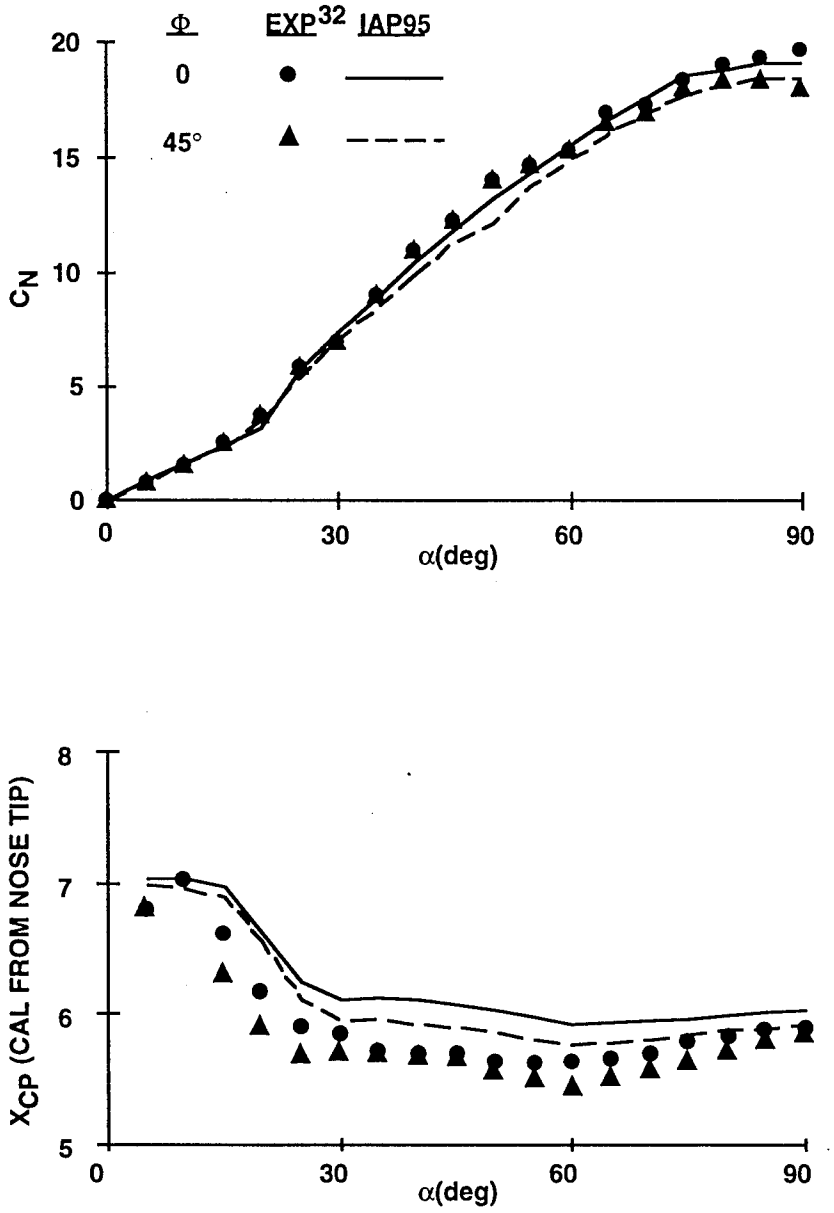

FIGURE 38C. NORMAL FORCE AND CENTER OF PRESSURE COMPARISONS OF THEORY AND EXPERIMENT (CONFIGURATION OF FIGURE 36B; $M_\infty = 1.3$)

respectively, for an overall average for these three Mach numbers of 13.3 percent. The average center of pressure errors at all three Mach numbers is a quite acceptable 2.6 percent of body length and is fairly consistent. This indicates any loss in normal force on the body due to the strut at high AOA must be somewhat evenly distributed along the body. It is interesting to note that if the subsonic, high AOA ($\alpha > 55$ deg) normal force data are eliminated from the averages, the overall normal force error is 9 percent, which is within the ±10 percent tolerance level.

The fourth configuration (Figure 39A) is a wing-body tested at both NASA/LRC[18] and New York University.[19] A sting mount was used and maximum AOA was 50 deg. Only $M_\infty = 1.6$ and 2.7 data were available. However, oil flow, pressure distribution and schlieren data were also taken. These data are very useful in showing the shock structure of the flow field and in particular the interaction of the bow shock wave with the windward plane wings. It was this data that helped the author to attempt to quantify the effects of "fin choking" at the $\Phi = 45$ deg roll position. Figures 39B and 39C present the comparison of predicted normal force coefficients and centers of pressure at $M_\infty = 1.6$ and 2.7 respectively. As seen in the figures, excellent agreement with the data is shown for both the $\Phi = 0$ and 45 deg roll positions. Average errors are 3.7 percent and 0.6 percent ℓ for C_N and X_{CP} respectively. It is also interesting to note that there is very little difference in the aerodynamics for the $\Phi = 0$ and 45 deg plane up to the point where "fin choking" starts to occur, at which point the $\Phi = 45$ deg C_N data are slightly lower than $\Phi = 0$, and the X_{CP} is slightly less stable for $\Phi = 45$ deg.

The configuration of Figure 39A had an r/s of 0.2, which meant it was wing-dominated. For wing-dominated configurations, the difference in aerodynamics between the $\Phi = 0$ and 45 deg planes is much smaller than for configurations that have large values of r/s. It is believed that is in large part due to the lower minimum value of $K_{B(W)}$ at high AOA for $\Phi = 45$ deg versus $\Phi = 0$ deg, as illustrated in Figure 24.

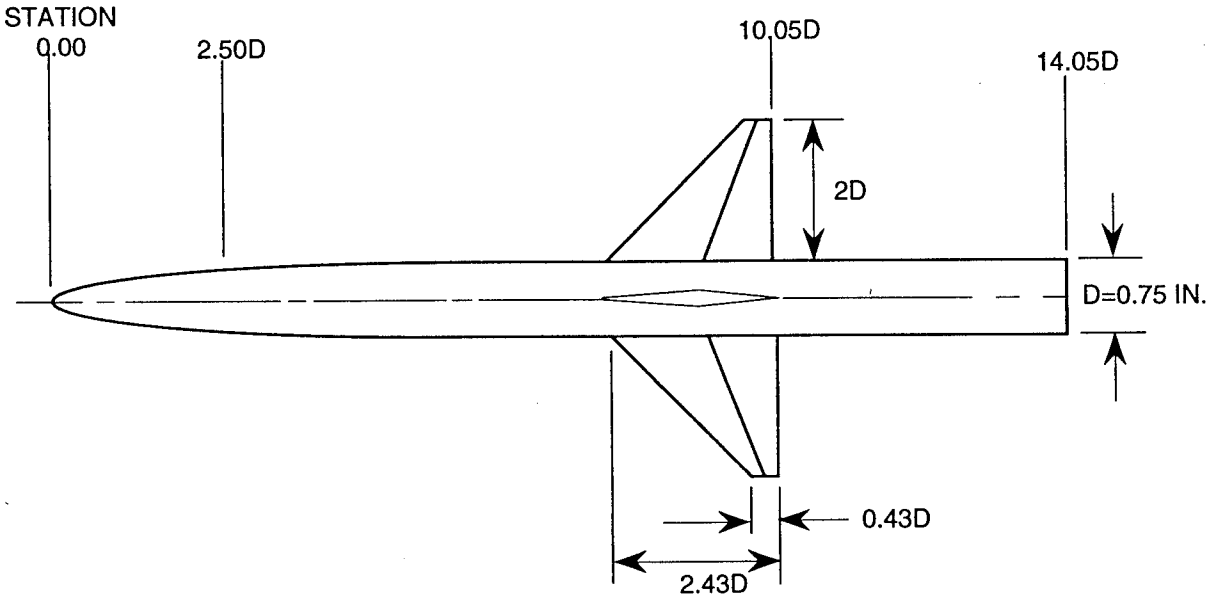

FIGURE 39A. WING-BODY CONFIGURATION USED IN VALIDATION PROCESS

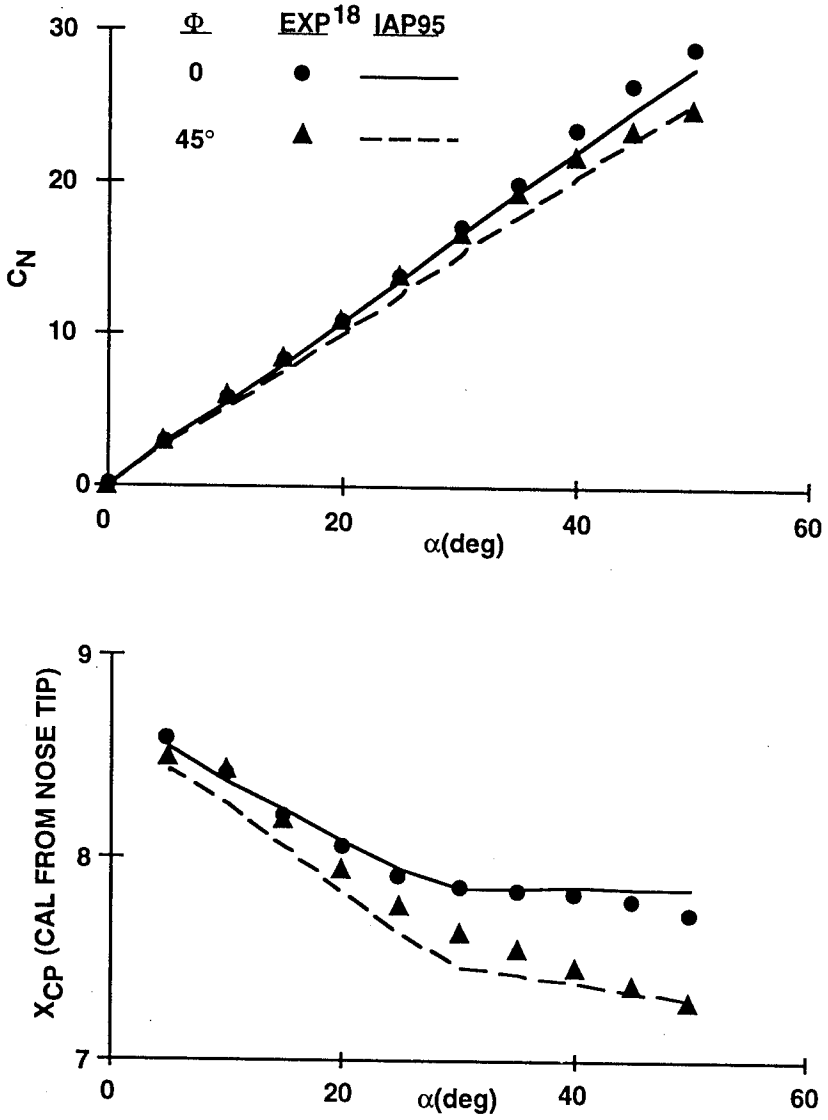

FIGURE 39B. NORMAL FORCE AND CENTER OF PRESSURE COMPARISONS OF THEORY AND EXPERIMENT ($M_\infty = 1.6$)

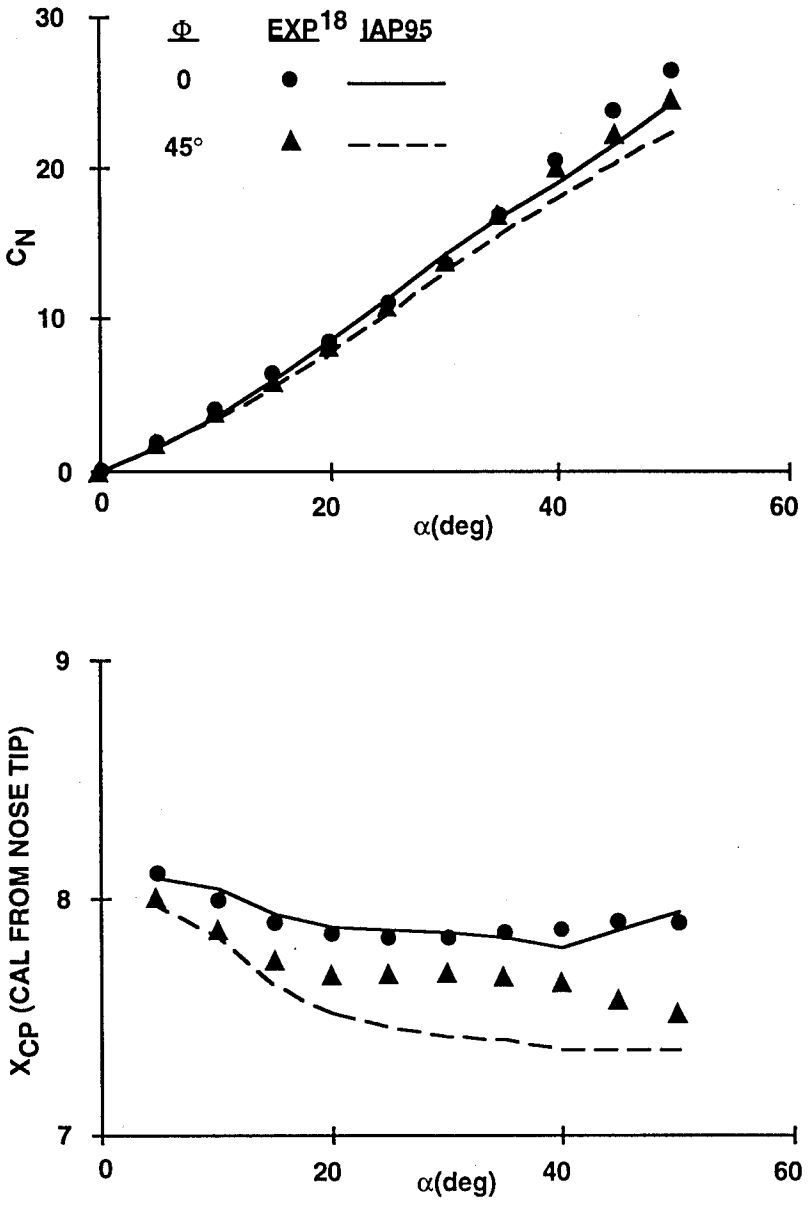

FIGURE 39C. NORMAL FORCE AND CENTER OF PRESSURE COMPARISONS OF THEORY AND EXPERIMENT ($M_\infty = 2.7$)

The last three single-fin configurations are shown in Figure 40A and consist of a 10-caliber body with a 3.5-caliber tangent-ogive nose followed by a 6.5-caliber afterbody. Six tail planforms were tested in Reference 33 and three of those are illustrated in Figure 40A. The three tail planforms allow a variation in aspect ratio of 0.31 to 1.24 with r/s varying from 0.6 to 0.27 respectively. The normal force coefficient for the configurations of Figure 40A are shown in Figure 40B for both $\Phi = 0$ and 45 deg roll at AOA 12 and 20 deg and as a function of Mach number. As noted in the Figure 40B, good agreement of the theory and experiment is shown for both AOAs, at both roll positions and for the Mach number range of 1.5 to 4.6 where data were available. It is also worthy of note that the $\Phi = 0$ and $\Phi = 45$ deg roll results differ primarily for the higher r/s and lower Mach number. This is due primarily to the lower minimum body carryover lift for $\Phi = 45$ deg compared to $\Phi = 0$ deg at high AOA. Higher AOA data than 20 deg were not available for this configuration.

3.2 WING OR CANARD-BODY-TAIL CONFIGURATIONS

Several configurations with two sets of lifting surfaces, with and without control deflections are also considered for the validation process. The first of these is an old version of the standard missile configuration tested at M = 0.1 by Dunn, et al.[34] at the Naval Postgraduate School. Reference 34 showed only normal force coefficient data, but data were given to AOA 90 deg at both the $\Phi = 0$ and 45 deg roll orientations. Figure 41 shows the configuration tested in the wind tunnel and the configuration modeled in the IAP95. Experience has shown that when a wing planform does not fit the specifications of the IAP95 logic, then the parameters to hold constant are wing area, span, aspect ratio, centroid of planform area and taper ratio. Other parameters (chord length and sweep angles) can be varied slightly to meet the constraints. Comparison of theoretical and experimental values of normal force coefficient as a function of AOA and at $\Phi = 0$ and 45 deg roll are shown at the bottom of Figure 41. Once again the comparisons are quite good up to AOA of 40 to 50 deg where the theory begins to be lower than the data suggest. However, since the model was sting-mounted, it is suspected that sting interference effects contribute to some of this difference between data and theory at the high AOA.

It is also interesting to note the fairly large difference between the $\Phi = 0$ and 45 deg normal force coefficients at high AOA. This difference can be as much as 40 to 50 percent and is attributed primarily to the dorsal body carryover lift, which gives a much higher value at $\Phi = 0$ versus $\Phi = 45$ deg. Figure 24, for large r/s values, illustrates this qualitatively.

A second wing-body-tail case is shown in Figure 42. Data from this configuration were available[35] only for $\Phi = 0$, but the case was a good candidate to compare the aerodynamics of the AP95 to the IAP95, due to its having fairly large wings and tails that were fairly close together axially. The wing-tail model primarily affects pitching moments, as the actual normal-force losses on the tail due to presence of the forward lifting surface can be fairly small in percentage except at small AOA. As a result, only pitching moments are shown. These are given in the lower portion of Figure 42 for M_∞ of 1.41, 2.0, 2.5, and 3.08. These Mach numbers bracketed the data from Reference 35 that were taken to AOA of 25 deg. As seen in Figure 42, the new wing-tail model gives some improvement over the AP95 model, with the improvements being the most noticeable

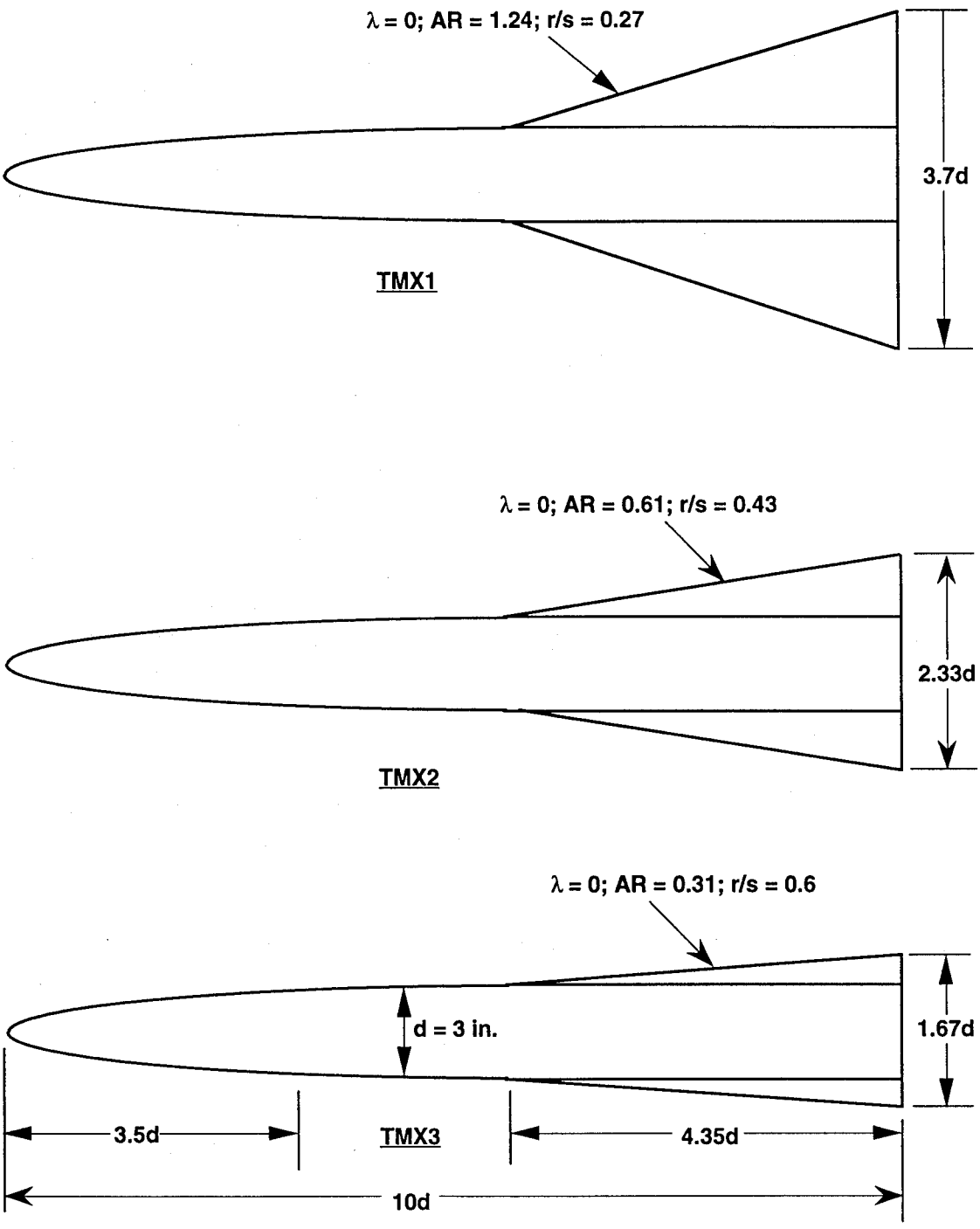

FIGURE 40A. THREE BODY-TAIL CONFIGURATIONS FROM REFERENCE 33

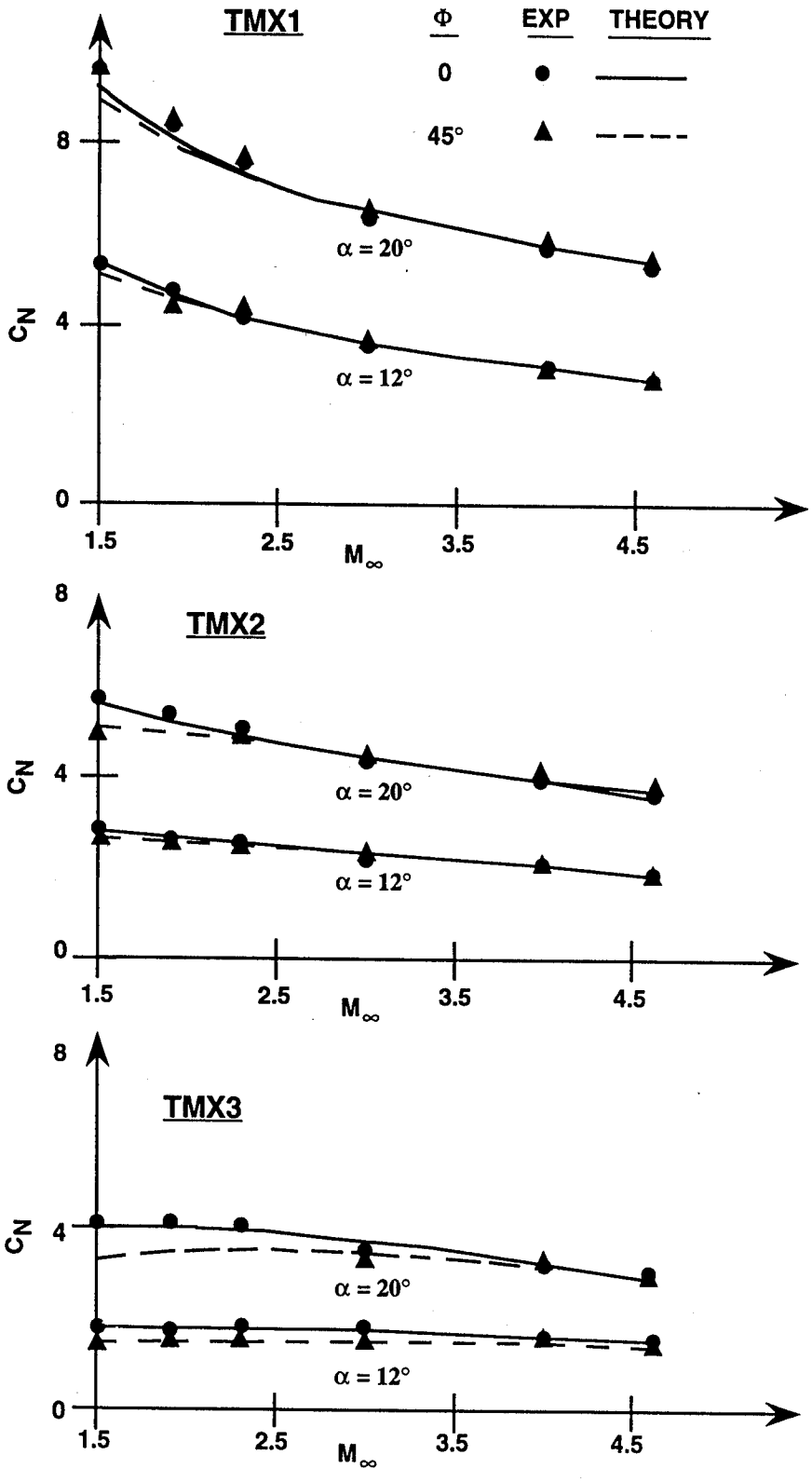

FIGURE 40B. NORMAL FORCE COEFFICIENT VS. MACH NUMBER FOR CONFIGURATION OF FIGURE 40A

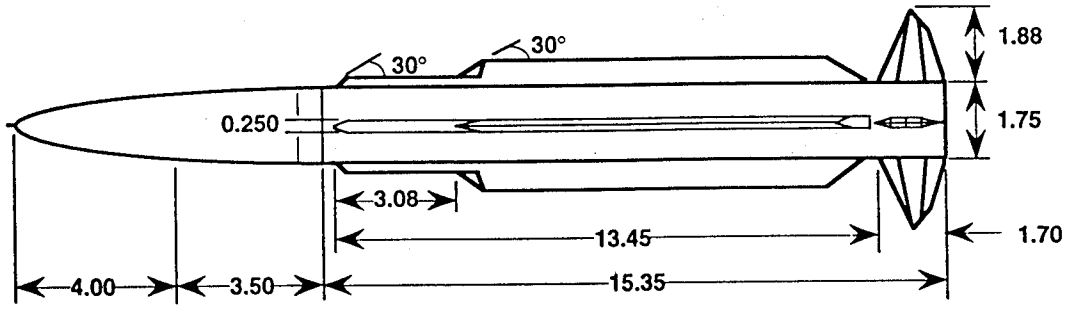

CONFIGURATION TESTED IN WIND TUNNEL
(FROM REFERENCE 34 WHERE DIMENSIONS ARE IN INCHES)

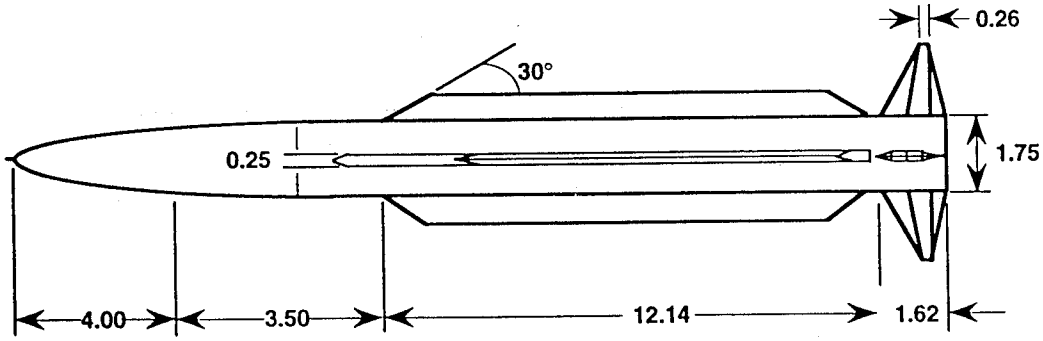

MODIFIED CONFIGURATION USED IN AEROPREDICTION COMPUTATIONS

PARAMETERS FOR BOTH MODELS

$(AR)_T = 4.0$	$b_t = 3.76$ in.	$\lambda_T = 0.16$	$(\Lambda_{LE})_T = 24°$	$A_T = 3.54$ in.^{2}
$(AR)_D = 0.12$	$b_D = 1.32$ in..	$\lambda_D = 0.77$	$(\Lambda_{LE})_D = 60°$	$A_D = 14.2$ in.^{2}

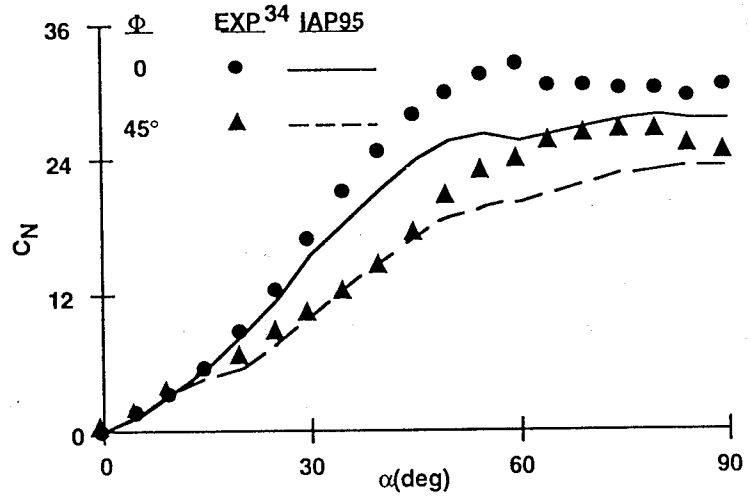

FIGURE 41. NORMAL FORCE COEFFICIENT COMPARISON OF THEORY AND EXPERIMENT ($M_\infty = 0.1$)

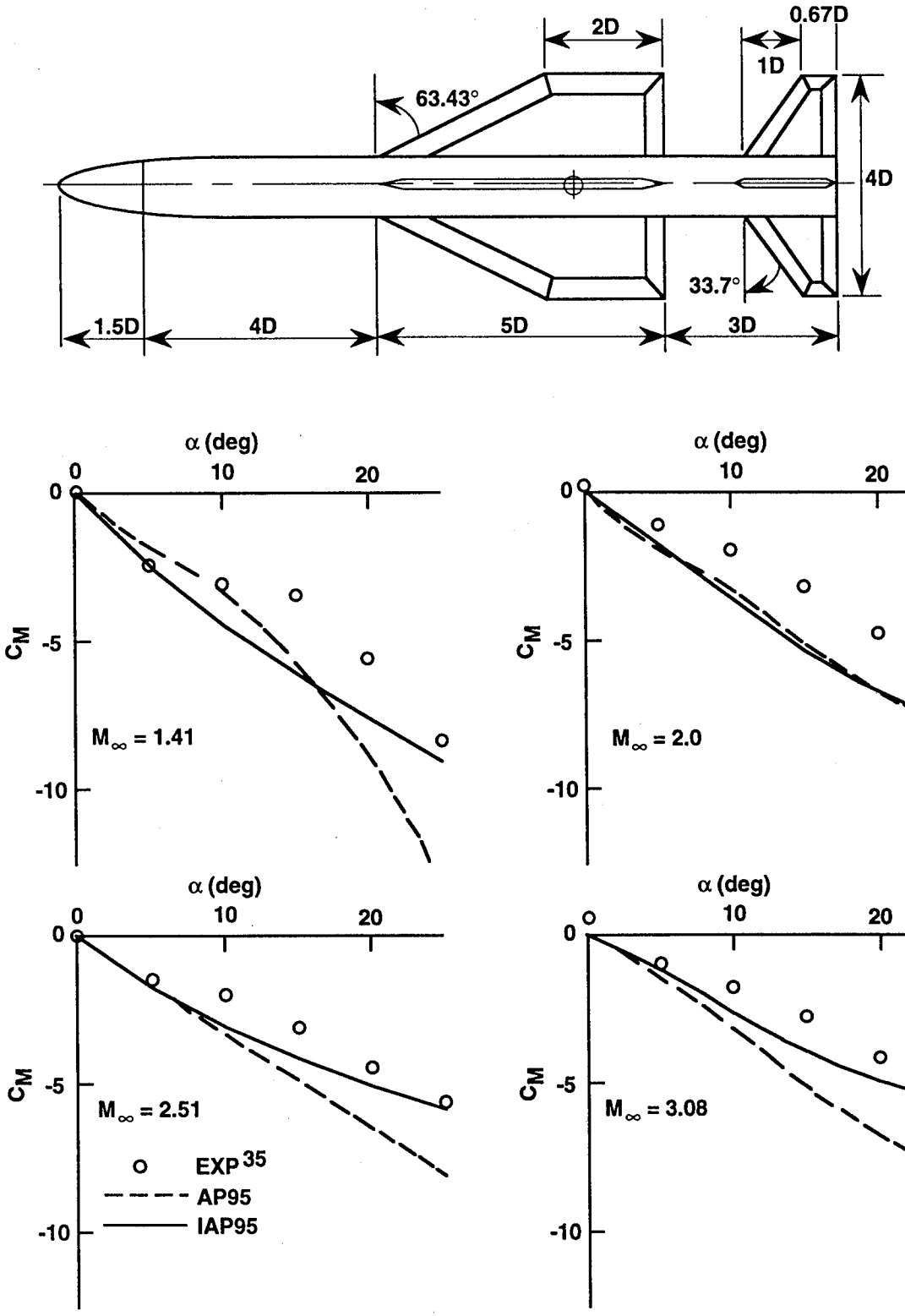

FIGURE 42. COMPARISON OF THEORY AND EXPERIMENT FOR PITCHING MOMENT COEFFICIENT (Φ = 0 DEG)

as AOA increases above 20 deg. This is because the improved model discussed in section 2.2.8 requires the wing-tail interference term due to AOA to go to zero much faster than the model in the AP95. This was based on the data of Reference 22, which is seen to hold for the configuration of Reference 35 as well.

The next two configurations are shown in Figure 43 with the wind tunnel data given in Reference 36. Both of these configurations have a fairly large lifting surface of aspect ratio close to one. The configuration in Figure 43A has a fairly large aspect ratio tail for control whereas the configuration in Figure 43B has a moderate aspect ratio canard for control. Note that the canard modelled in the IAP95 is slightly different than that tested in the wind tunnel due to the allowable variables in the IAP95. This canard has the same area, aspect ratio, span, and centroid of presented area as that tested in the wind tunnel.

The comparison of predicted lift and pitching moment coefficients with data[36] for the configuration of Figure 43A is given in Figure 44. Figure 44A gives the Mach 1.6 and 2.0 results at AOA of 10 deg; Figure 44B, the Mach 2.36 and 2.86 results at AOA of 20 deg; and Figure 44C, the Mach 3.95 and 4.63 results also at AOA 20 deg. The results are shown as a function of control deflection, since data were available for control deflections up to 30 deg for all conditions tested, whereas data were available only up to AOA of 10 deg at lower Mach numbers and slightly over 20 deg at higher AOA. Hence, both Figure 43 configurations serve to test the nonlinear control deflection prediction model with some AOA nonlinearities also included (due to an upper AOA of only 20 deg). As seen in Figure 44, at all Mach numbers, AOAs and δs, both C_L and C_M are predicted well within the accuracy goal of ±10 percent on normal force and ±4 percent of body length on center of pressure. While the pitching moment comparisons in the figures do not look quite as good as normal force, when one translates this to center of pressure, results are quite adequate. The worst-case center of pressure prediction in Figure 44 is the $\delta = 30$ deg, $\Phi = 0$ deg, M = 2.36, and AOA = 20 deg case shown in Figure 44B. For this case, the X_{CP} error is only 2.8 percent of body length. Since the body length of both configurations in Figure 43 is 14.55 calibers, the worst case error for X_{CP} is 0.4 caliber.

The other point worthy of note in Figure 44 is the comparison of the $\Phi = 45$ deg aerodynamics with those of $\Phi = 0$ deg. In general, the lift coefficient is lower for $\Phi = 45$ deg than for $\Phi = 0$ deg. The lower the Mach number, the greater the difference between the two roll orientations. This is due to a combination of: lower minimum values of body carryover lift for $\Phi = 45$ deg than for $\Phi = 0$ (see Figure 24); lower values of wing-tail interference at high Mach number and AOA; and large control surfaces. In essence, the physical mechanisms that cause differences in aerodynamics between $\Phi = 0$ and 45 deg seem to dissipate as Mach number gets into the hypersonic flow regime, where the Newtonian Impact Flow assumption appears to be reasonable. Note also the lower stability of the $\Phi = 45$ roll aerodynamics compared to the $\Phi = 0$ case at all Mach numbers in Figure 44.

The comparisons of theory with experiment for the canard-control configuration of Figure 43B are given in Figure 45. This figure is similar to Figure 44 in that results of lift and pitching moment coefficients are given for Mach 1.6, 2.0, 2.36, 2.06, 3.95, and 4.63 for the $\Phi = 0$ and 45 deg roll orientations, then compared to data. Here the control deflection is positive (leading

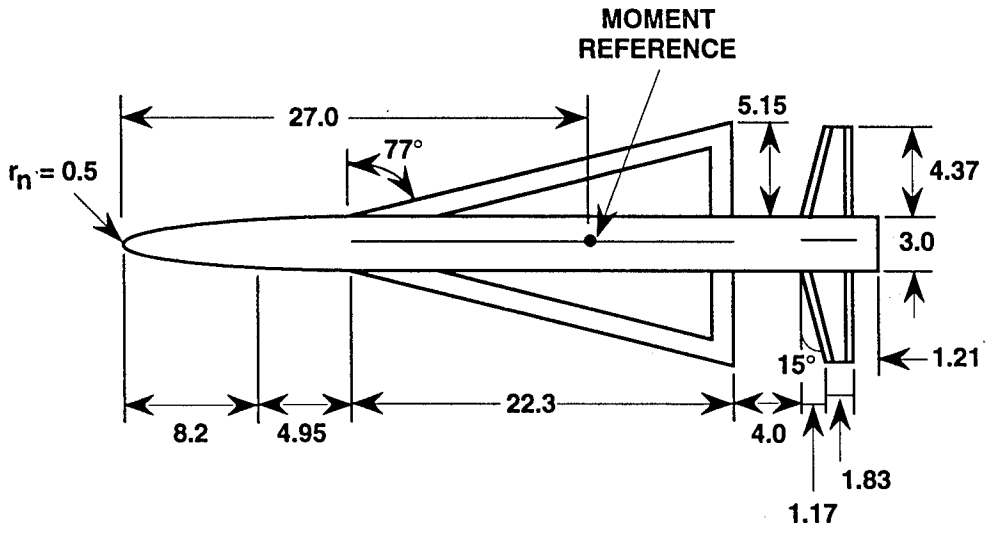

FIGURE 43A. WING-BODY-TAIL CONFIGURATION USED IN VALIDATION PROCESS[36] (DIMENSIONS IN INCHES)

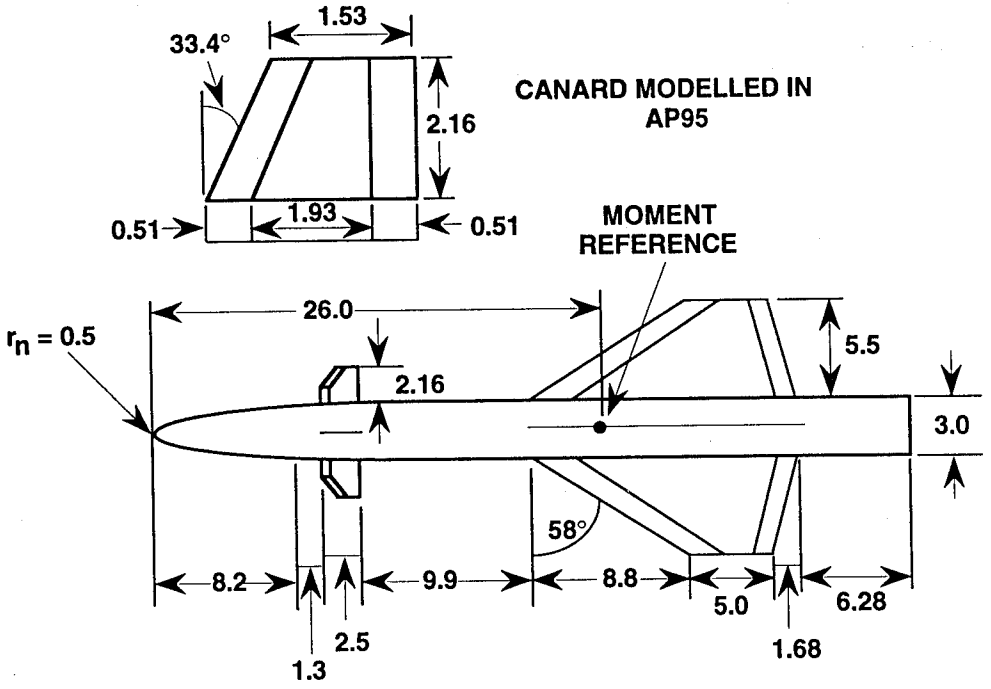

FIGURE 43B. CANARD-WING-BODY CONFIGURATION USED IN VALIDATION PROCESS[36] (DIMENSIONS IN INCHES)

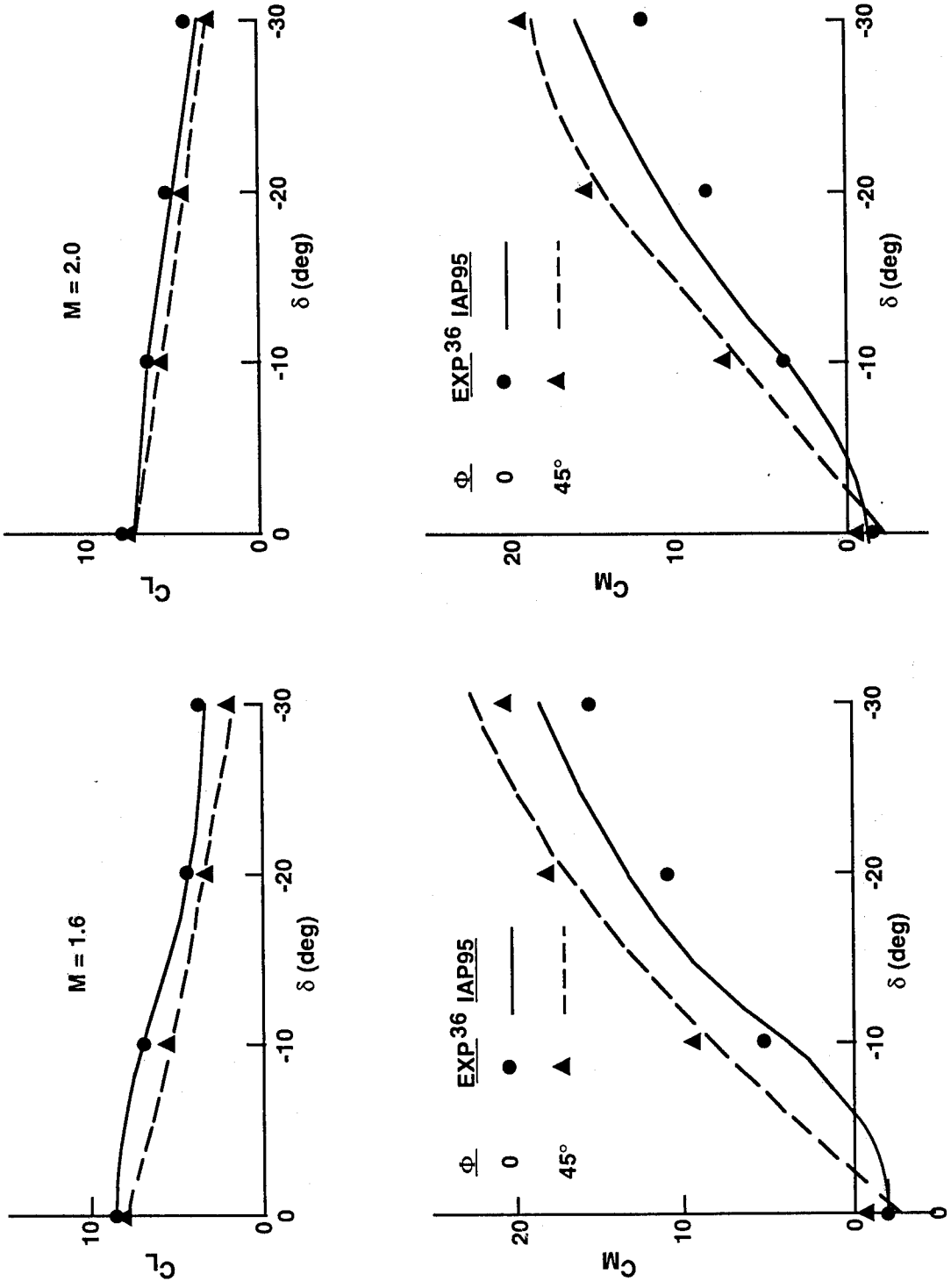

FIGURE 44A. LIFT AND PITCHING MOMENT COEFFICIENTS FOR FIGURE 43A CONFIGURATION AT AOA = 10 DEG

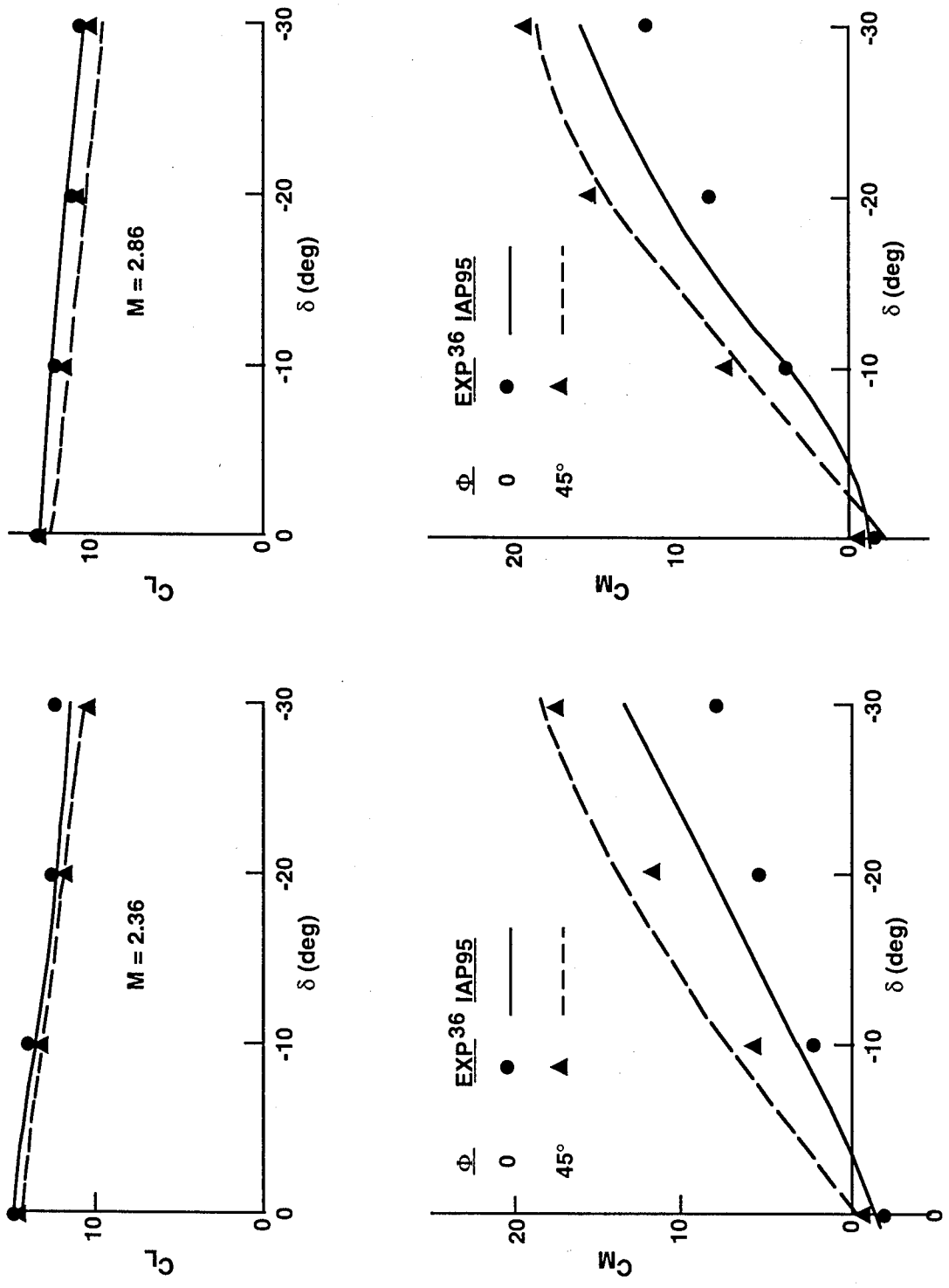

FIGURE 44B. LIFT AND PITCHING MOMENT COEFFICIENTS FOR FIGURE 43A CONFIGURATION AT AOA = 20 DEG

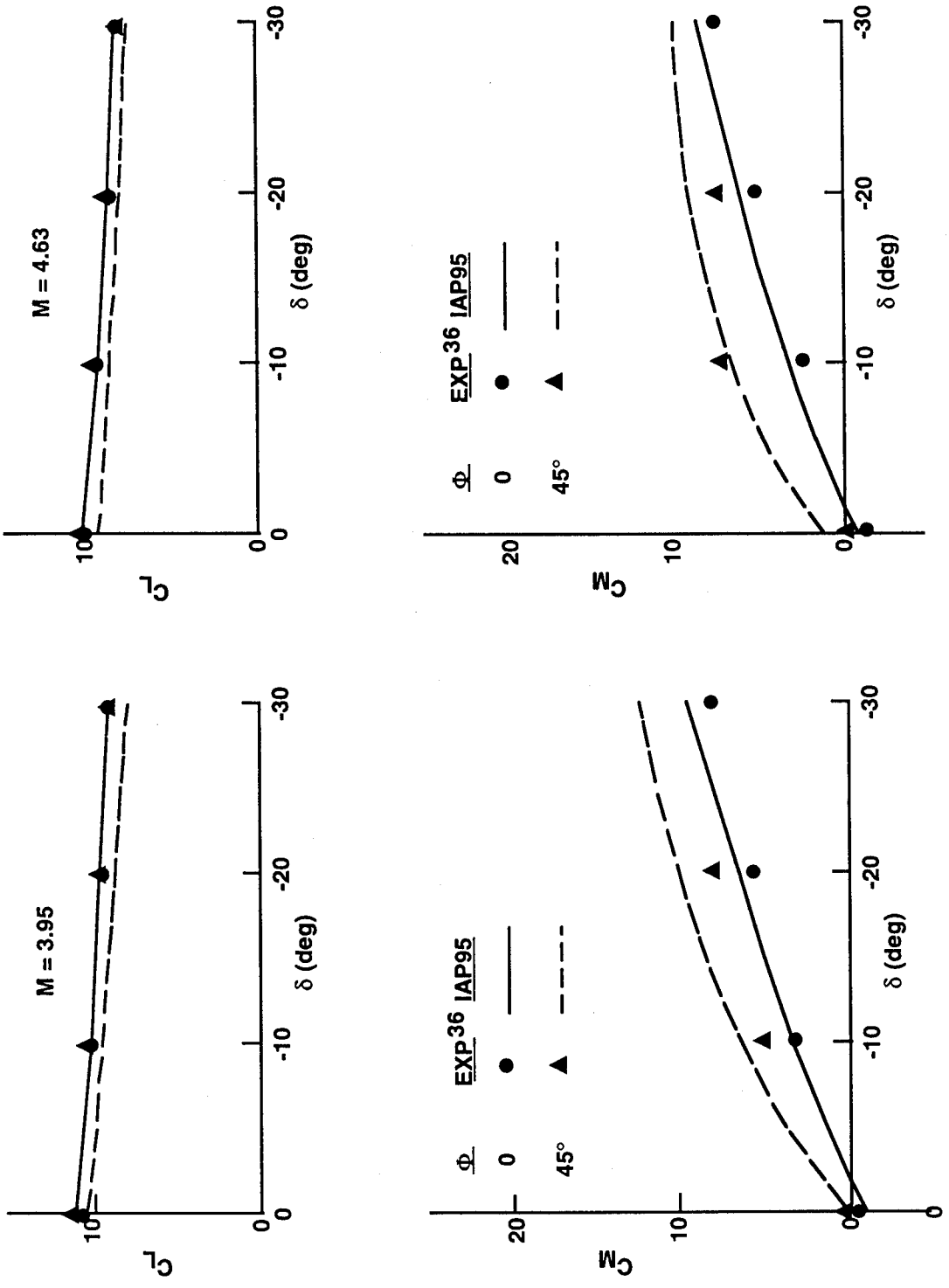

FIGURE 44C. LIFT AND PITCHING MOMENT COEFFICIENTS FOR FIGURE 43A CONFIGURATION AT AOA = 20 DEG

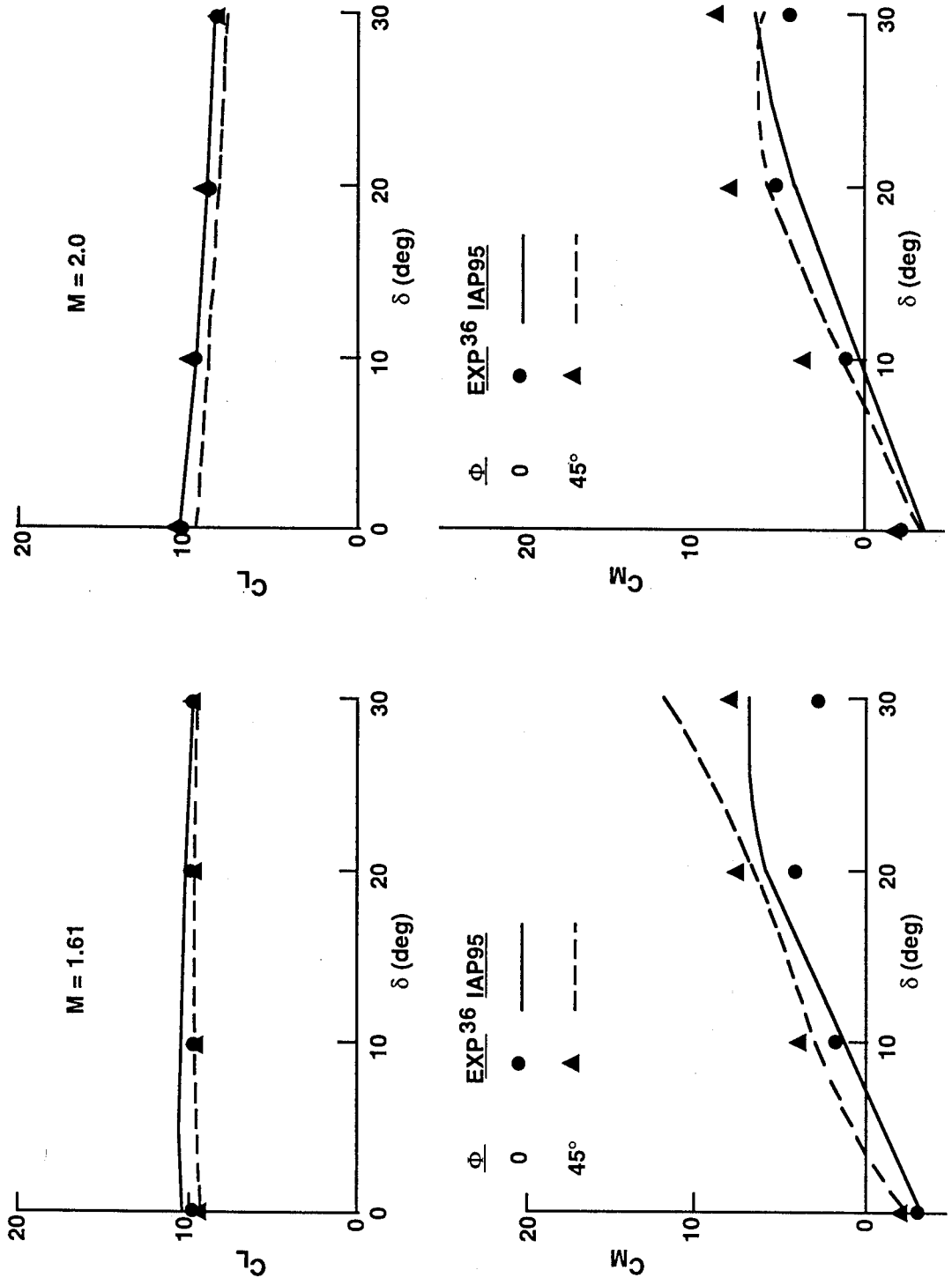

FIGURE 45A. LIFT AND PITCHING MOMENT COEFFICIENTS FOR FIGURE 43B CONFIGURATION AT AOA = 10 DEG

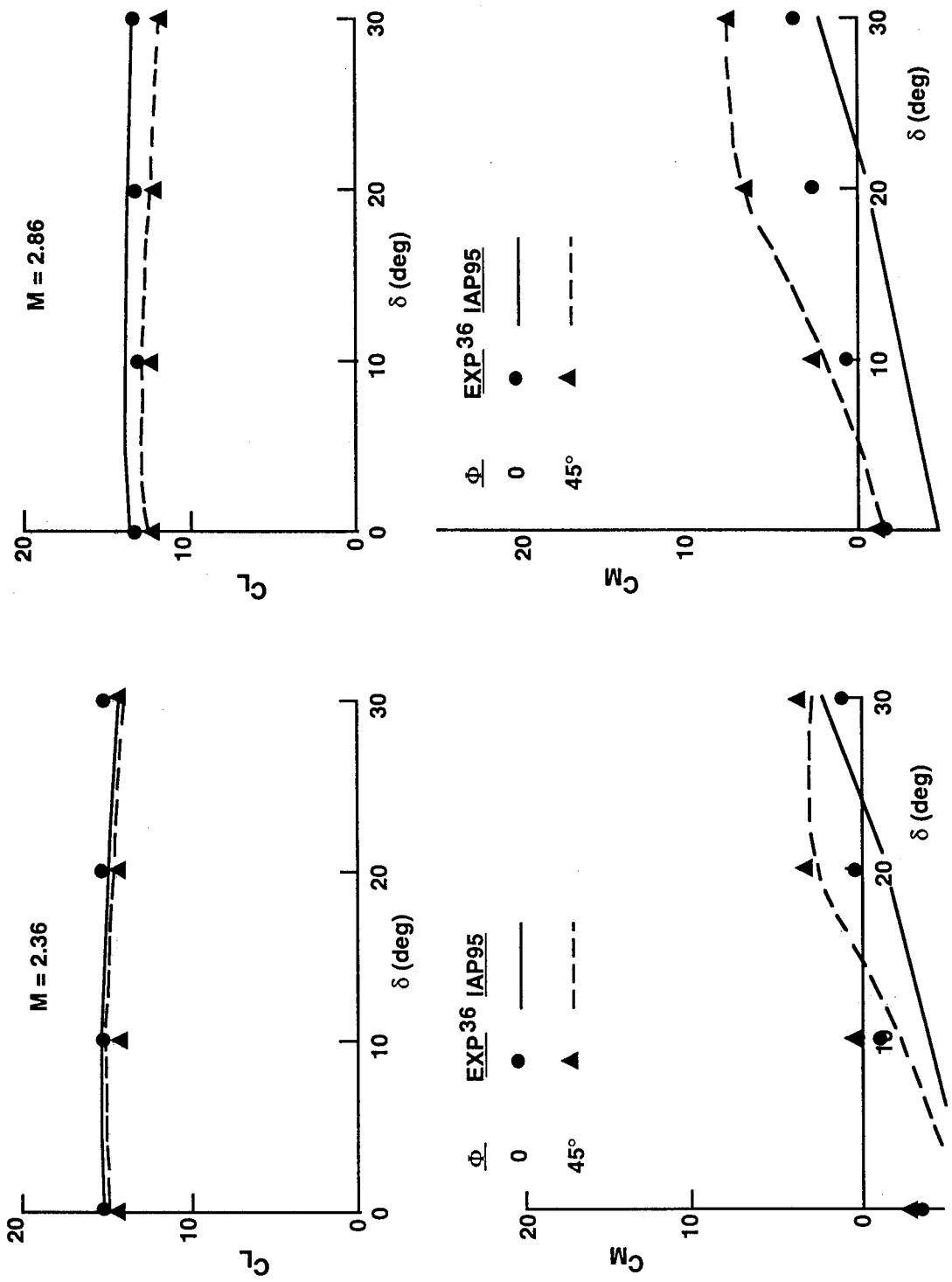

FIGURE 45B. LIFT AND PITCHING MOMENT COEFFICIENTS FOR FIGURE 43B CONFIGURATION AT AOA = 20 DEG

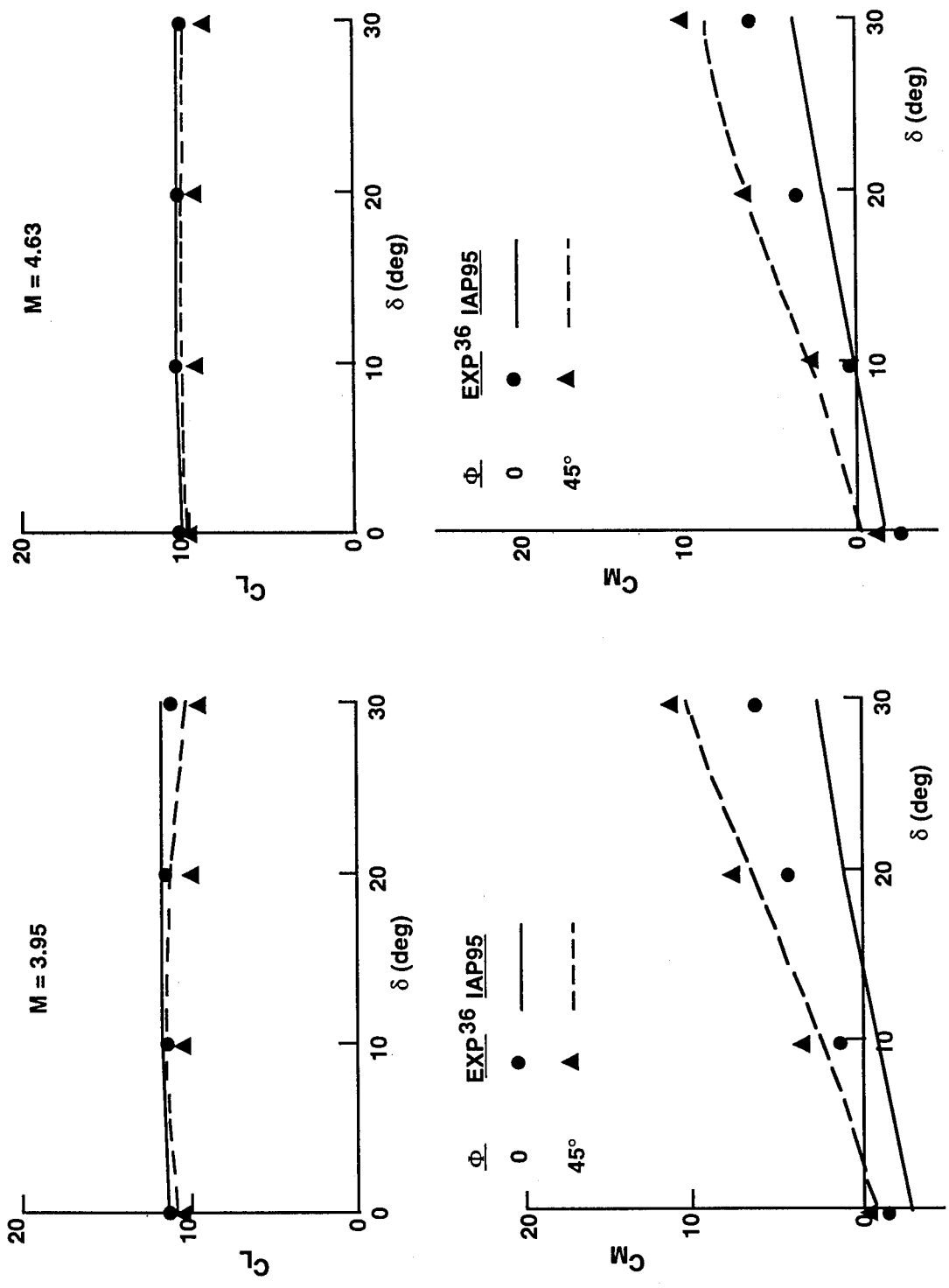

FIGURE 45C. LIFT AND PITCHING MOMENT COEFFICIENTS FOR FIGURE 43B CONFIGURATION AT AOA = 20 DEG

edge up) rather than negative as in Figure 44. Also, the control surfaces have a much smaller area than the tail surfaces of Figure 43A. These slightly smaller control surfaces also tend to decrease the difference between the Φ = 45 deg and Φ = 0 deg aerodynamics due to lower wing tail interference as well as lower forces from control deflections. Comparisons of theory and data once again are quite adequate and within the desired accuracy bounds. The worst case comparisons are for the higher Mach number lift coefficient predictions and large δ's. Notice in Figure 45C that experimental data show C_L actually decreasing with increasing δ at Φ = 45 deg. This gives errors in predictions of up to 10 percent in C_L. It is believed the reason for this phenomena is shock interference from the forward deflected control surfaces onto the fairly large aft wings. This phenomena is not accounted for in the IAP95.

The final configuration shown is the SEASPARROW configuration as shown in Figure 46A with wind tunnel results taken from Reference 37. This configuration has fairly large wings and tails, with the wings used as the control. Data were taken at Mach numbers of 1.5, 2.0, 2.35, 2.87, 3.95 and 4.63. Figures 46B, 46C, and 46D give comparisons of the IAP95 with the data at M = 1.5, 2.87, and 4.63 respectively: Results are shown for control deflections of 0 and 10 deg in Figure 46B and for 0 and 20 deg deflection in Figures 46C and 46D. Also, all results for both the Φ = 0 and 45 deg roll positions are shown. Several comments are in order with respect to the overall comparisons. First of all, the IAP model achieves its goal of predicting average accuracy of C_A, C_N of $\pm$10 percent and X_{CP} of $\pm$4 percent ℓ_B on this configuration at both the Φ = 0 and 45 deg roll positions. Secondly, C_N is predicted equally well at Φ = 0 and 45 deg. However, C_M is predicted better at Φ = 45 deg than at Φ = 0 deg due to the center of pressure shift derived in section 2.2.6. No such shift has been applied at Φ = 0 deg. Apparently one is needed, but it is not clear what the physical justification is. As seen in the pitching moment predictions for the Φ = 0 deg roll orientation, the IAP95 in general is slightly too stable. The third point is that C_A prediction is slightly better for the Φ = 0 deg roll orientation than the Φ = 45 deg position. Apparently, the factor of 1.414 applied to the fins for control deflection component of axial force is quite adequate at low angle of attack at all Mach numbers as seen in the figures. However, at high angle of attack, this factor appears to be too high at the lower supersonic Mach numbers and too low at the higher supersonic Mach numbers. It is suspected that at the lower supersonic Mach numbers, only the fins in the windward plane should have the full factor of $\sqrt{2}$, whereas those in the leeward plane should have a lower factor. For high supersonic conditions, it is suspected the bow shock and internal shock interactions actually add to the factor of $\sqrt{2}$. An empirical model for C_A to account for this physics would improve the C_A comparison, but time does not permit this effort at present.

The final point to be made is concerning the high Mach number, high AOA conditions in Figure 46D. Notice that the pitching moment suddenly loses stability above AOA of 30 deg and Φ = 0 deg roll. The normal force also decreases somewhat as well. It is believed this is due to internal shock waves from the bow shock and wing shock intersecting the tail, causing a loss of tail lift and a sudden decrease in stability. No accounting of these internal shocks from a forward mounted fin to an aft mounted fin is made in the IAP95. It is also interesting to note that above AOA 70 deg, while the results are not shown, the IAP95 predictions for pitching moment agree quite well with the data. Apparently the internal shock interactions are important between AOA of about 30 to 60 deg.

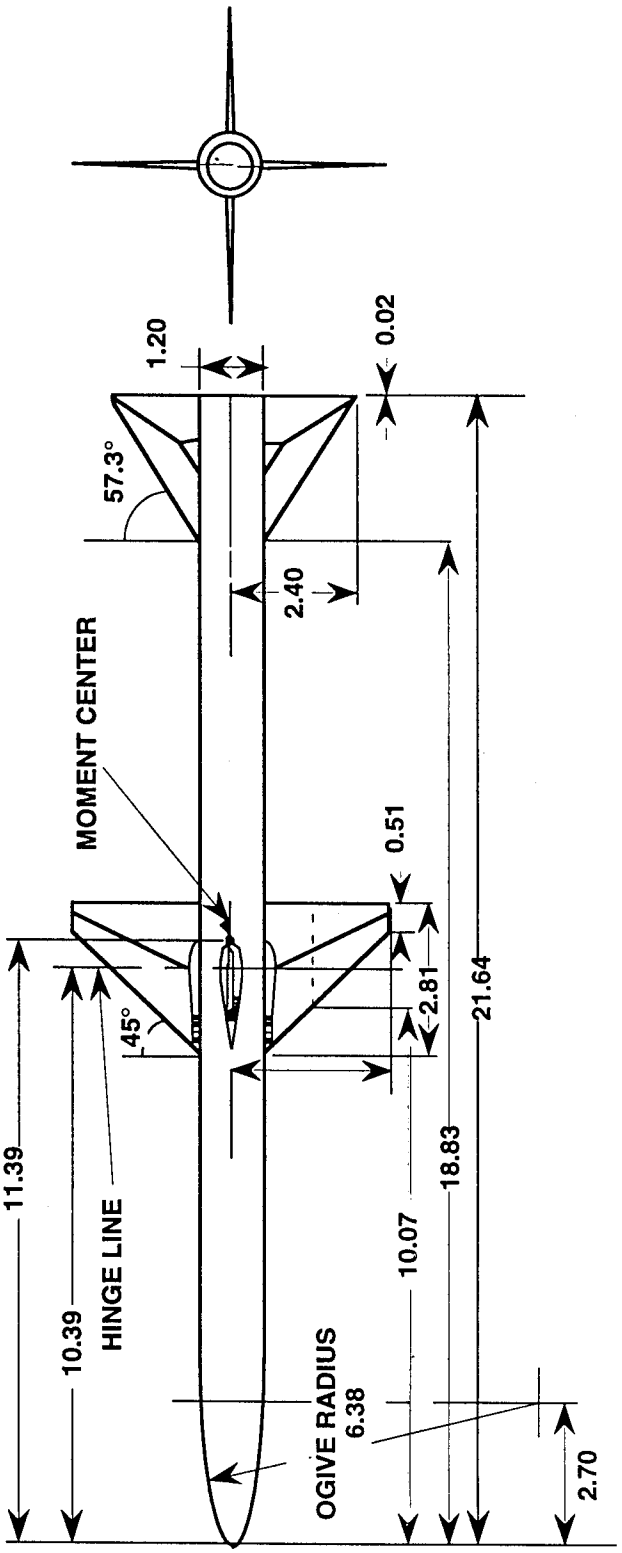

FIGURE 46A. AIR-TO-AIR MISSILE CONFIGURATION USED IN VALIDATION PROCESS[37]

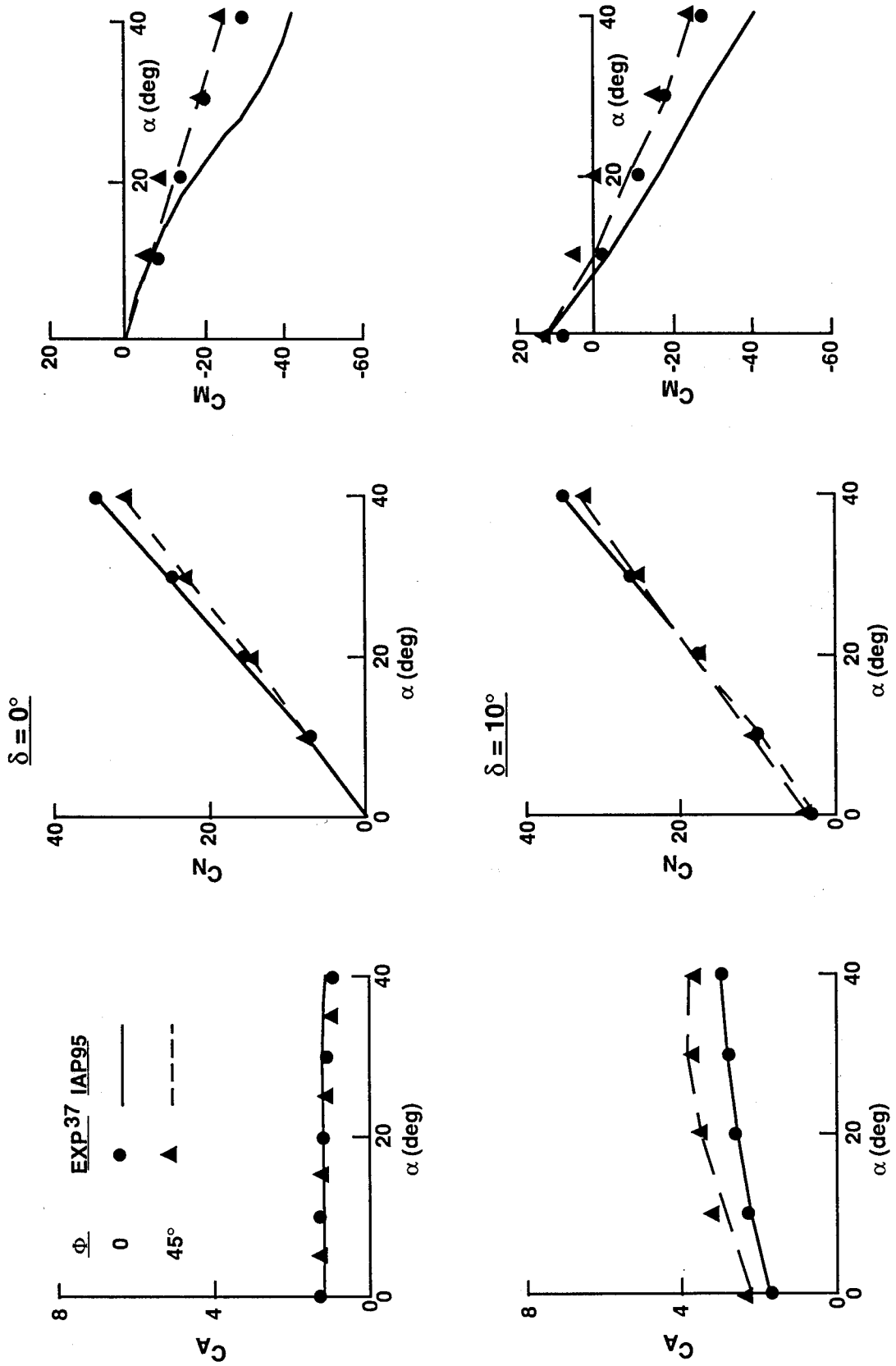

FIGURE 46B. AXIAL, NORMAL, AND PITCHING MOMENT COEFFICIENT COMPARISONS OF THEORY AND EXPERIMENT ($M_\infty = 1.5$)

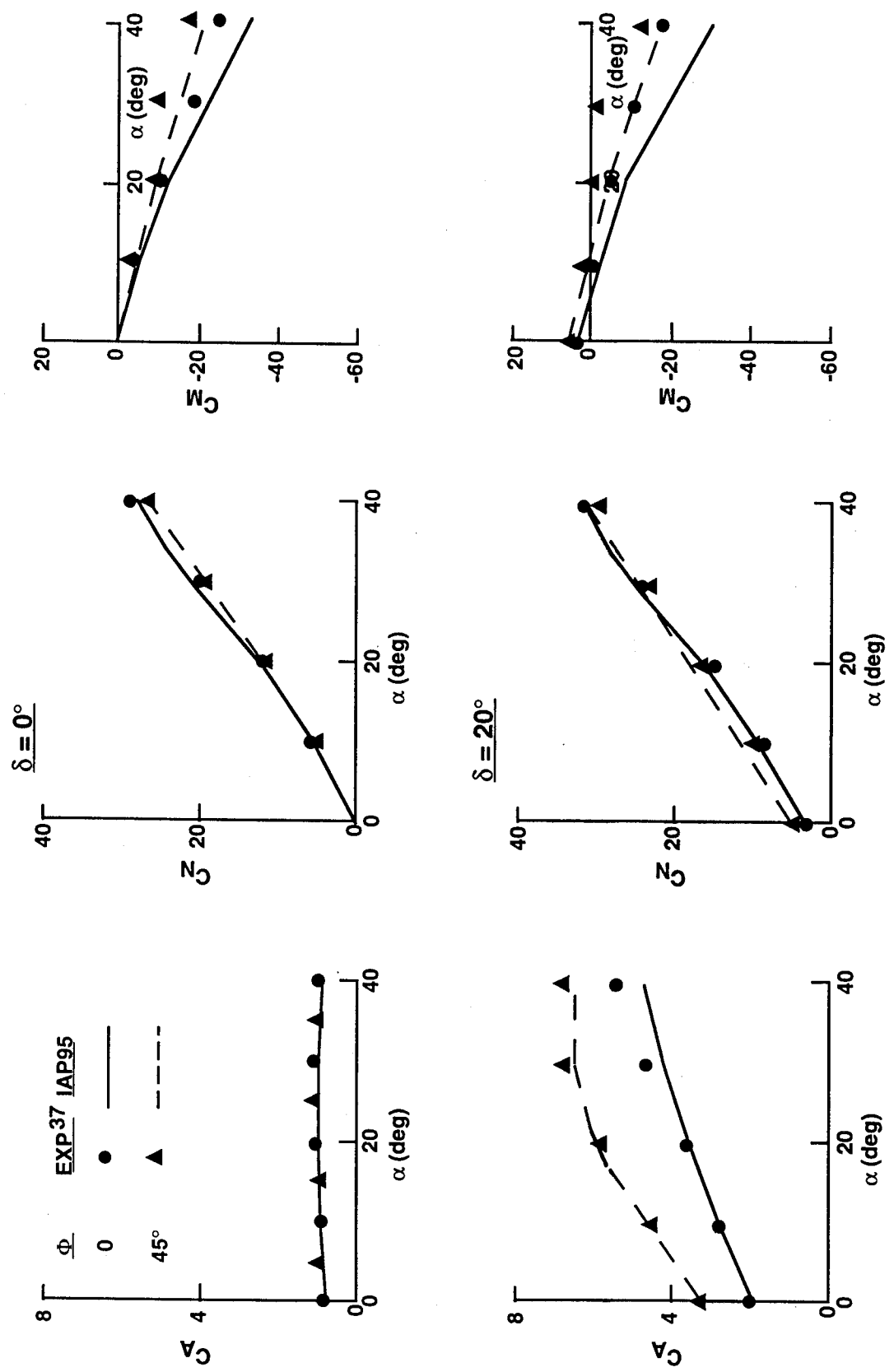

FIGURE 46C. AXIAL, NORMAL, AND PITCHING MOMENT COEFFICIENT COMPARISONS OF THEORY AND EXPERIMENT ($M_\infty = 2.87$)

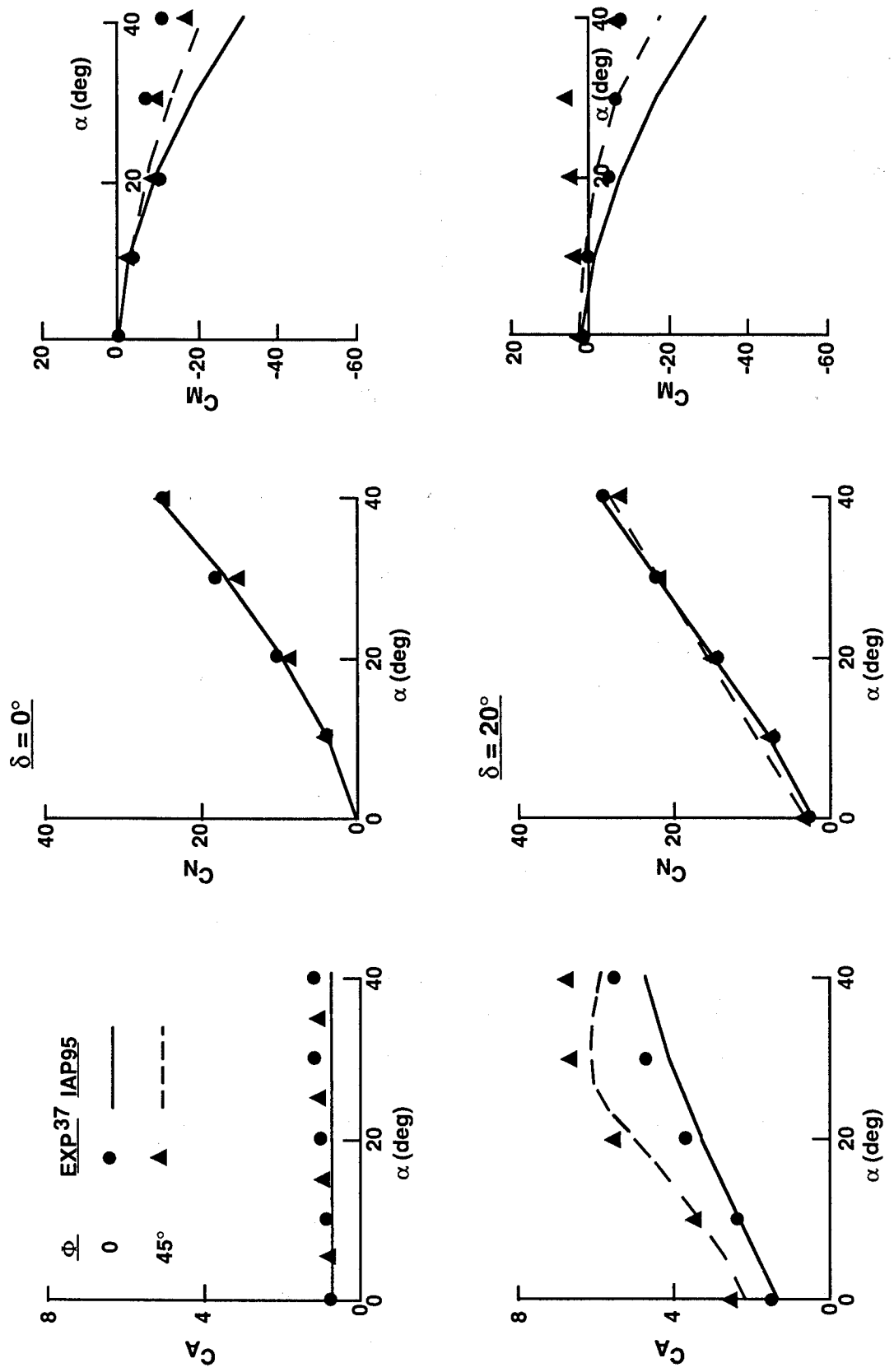

FIGURE 46D. AXIAL, NORMAL, AND PITCHING MOMENT COEFFICIENT COMPARISONS OF THEORY AND EXPERIMENT ($M_\infty = 4.63$)

4.0 SUMMARY, CONCLUSIONS AND RECOMMENDATIONS

New technology has been developed to allow engineering estimates of aerodynamics of most tactical weapon concepts for the Φ = 45 deg roll position (fins oriented in "x" or cross-fin arrangement). New technology developed for the Φ = 45 deg roll position includes:

a) Nonlinear wing-body and body-wing interference factor methodology due to AOA and control deflection.

b) A new semiempirical wing-tail interference model for both the Φ = 0 and Φ = 45 deg roll positions.

c) An approximate method to estimate wing alone shift in center of pressure at Φ = 45 deg and high AOA.

d) An approximate method to estimate "fin choking" at high M and AOA based on Newtonian impact theory

This new technology, along with the Φ = 0 methodology of Reference 1, now allows trim aerodynamics to be computed in the two roll-stabilized planes that most of the world's missiles fly. The data bases upon which the methodology was based was limited in Mach number to 4.5 and AOA of 40 deg. However, engineering judgement and other data were used to allow calculations to be performed to AOA 90 deg, Mach numbers up to 20, for axisymmetric solid rocket weapons with up to two sets of lifting surfaces.

Based on the new methodology and computations to date, the following conclusions are made.

a) The two primary reasons missile normal forces are lower at Φ = 45 deg than at Φ = 0 deg is that the minimum value of body carryover lift at high AOA is lower for Φ = 45 than Φ = 0. The larger the value of r/s, the more difference between these minimum values. If the configuration has two sets of lifting surfaces, the wing-tail interference is higher for AOA > 20 deg for the Φ = 45 deg plane than for the Φ = 0 deg plane, also contributing to a lower normal force for Φ = 45 deg and a less stable configuration.

b) At high AOA: $K_{W(B)}$ approaches 1.0 for most Mach numbers; $K_{B(W)}$ approaches some minimum value that is a function of r/s and Mach number; $k_{W(B)}$ and $\mathbf{k_{B(W)}}$ are nonlinear in total local AOA on the wing and are functions of Mach number and total AOA on the wing.

c) The actual values of wing-tail interference are much smaller than those predicted by SBT at AOA greater than about 20 deg, particularly for Mach numbers greater than about 2.0

d) "Fin choking" appears to be more of a problem on larger fin (small r/s) configurations at $\Phi = 45$ deg than on smaller fin cases (large r/s).

e) For Mach numbers less than one and AOA > 30 deg, it is not clear what the correct values of experimental normal force are for a given configuration, based on wind tunnel results available in the literature.

f) Internal shock interaction between forward-mounted and aft-mounted fins becomes increasingly important as both AOA and Mach number increase. The current methodology does not account for these effects.

g) In general, ±10 percent average accuracy has been maintained for both normal and axial force coefficients and 4 percent of body length for center of pressure in the $\Phi = 45$ deg roll position. Exceptions to this are at subsonic Mach number and high AOA where data accuracy is in question, and at high Mach number and high AOA for configurations that have two sets of lifting surfaces, where internal shock interactions may be a problem.

h) The current overall approach of using linear theory, slender body theory, or second order theory for low angle of attack aerodynamics, and estimating the nonlinear aerodynamic terms individually and directly from wind tunnel data bases, appears to be the key to the above mentioned average accuracy levels.

Based on this and previous research (References 1, 5, 12, and 16), the following recommendations are made for additional work:

a) Additional wind tunnel measurements or computational fluid dynamics cases need to be made to help define nonlinearities of the interference effects as a function of r/s.

b) A method is needed to correct wind tunnel data at subsonic Mach number and high AOA for sting or strut mounting effects.

c) An engineering method is needed to estimate internal shock interaction effects for high AOA and Mach number.

d) Any future wind tunnel test for measuring component aerodynamics should be done with lifting surfaces large enough to separate out body and wing lift accurately, with wings mounted in the middle of the body and, preferably, with simultaneous measurements of body forces in conjunction with the wing and wing forces in conjunction with the body. This would allow more accurate determination of the interference terms directly, without subtraction of two large numbers to obtain a small term.

5.0 REFERENCES

1. Moore, F. G.; McInville, R. M.; Hymer, J. C.; *The 1995 Version of the NSWC Aeroprediction Code: Part I - Summary of New Theoretical Methodology*, NSWCDD/TR-94/379, Feb 1995.

2. Nielsen, J. N.; Hemsch, M. J.; Smith, C. A.; *A Preliminary Method for Calculating the Aerodynamic Characteristics of Cruciform Missiles to High Angles of Attack Including Effects of Roll Angle and Control Deflections*, ONR-CR215-226-4F, 800 N. Qunicy St., Arlington, VA 22217.

3. Williams, J. E. and Vukelich, S. R.; *USAF Stability and Control DATCOM*, AFFDL-TR-75-45, Wright Patterson Air Force Base, Dayton, OH.

4. Wardlaw, A. B. and Davis, S.; *A Second-Order Gudonov Method for Supersonic Tactical Missiles*, NSWC TR-86-506, 1986, NSWC, Dahlgren, VA.

5. Moore, F. G.; Hymer, T.; and Devan, L.; *New Methods for Predicting Nonlinear Lift, Center of Pressure, and Pitching Moment on Missile Configurations*, NSWCDD/TR-92/217, Jul 1992, Dahlgren, VA.

6. Stallings, R. L., Jr.; and Lamb, Milton; *Wing-Alone Aerodynamic Characteristics for High Angles of Attack at Supersonic Speeds*, NASA Technical Paper 1889, Jul 1981.

7. Baker, W. B., Jr.; *Static Aerodynamic Characteristics of a Series of Generalized Slender Bodies With and Without Fins at Mach Numbers from 0.6 to 3.0 and Angles of Attack from 0 to 180°*, AEDC-TR-75-124, Vol I and II, May 1976, Tullahoma, TN.

8. NASA Langley Research Center Tri-Service Missile Data Base, Transmitted from NASA/LRC Jerry M. Allen to NAVSWC on 5 Nov 1991 (formal documentation in process)

9. Meyer, J.; *Effects of the Roll Angle on Cruciform Wing-Body Configurations at High Incidences*, Journal of Spacecraft and Rockets, Vol 31, No. 1, Jan-Feb 1994, pp 113-122.

10. Devan, L.; Mason, L; and Moore, F. G.; *Aerodynamics of Tactical Weapons to Mach Number 8 and Angle of Attack 180°*, AIAA paper 82-0250, 20th Aerospace Sciences Meeting, Orlando, FL, Jan 1982.

REFERENCES (Continued)

11. Moore, F. G., Hymer, T. C.; McInville, R. M.; *Improved Aeroprediction Code: Part I - Summary of New Methods and Comparison with Experiment*, NSWCDD/TR-93/91, May 1993.

12. Moore, F. G.; Hymer, T.; McInville, R.; *A Planar Nonlinear Missile Aeroprediction Code for All Mach Numbers*, AIAA Paper No. 94-0026, AIAA 32 Aerospace Sciences Conference, Reno, NV, Jan 10-14, 1994.

13. Jorgenson, L. H.; *Predictions of Static Aerodynamic Characteristics for Slender Bodies Alone and With Lifting Surfaces to Very High Angles of Attack*, NASA TR R-474, Sep 1977.

14. Ashley, Holt, Landahl, Martin; Aerodynamics of Wings and Bodies, Addison - Wesley Publishing Company, Inc., Reading, MA, Copyright 1965.

15. Nielsen, J. N.; Missile Aerodynamics, NEAR, Inc., Mountain View, CA, 1988.

16. Moore, F. G.; McInville, R. M.; *A New Method for Calculating Wing Alone Aerodynamics to Angle of Attack 180°*, NSWCDD/TR-94/3, Mar 1994.

17. Allen, J. H., and Perkins, E. W.; *Characteristics of Flow Over Inclined Bodies of Revolution*, NACA RM A 50L07, Mar 1951.

18. Stallings, R. L., Jr.; Lamb, Milton; Watson, C. B.; *Effect of Reynolds Number on Stability Characteristics of a Cruciform Wing-Body at Supersonic Speeds*, NASA TP 1683, Jul 1980.

19. Agnone, A. M.; Zakkay, V.; Tory, E.; Stallings, R.; *Aerodynamics of Slender Finned Bodies at Large Angles of Attack*, AIAA Paper 77-0666, 10th Fluid and Plasma Dynamics Conference, Albuquerque, NM, Jun 27-29, 1977.

20. Lees, Lester; Hypersonic Flow, Inst. Aero. Science, Preprint No. 554, 1955.

21. Pitts, W. C.; Nielsen, J. N.; and Kaaturi, G. E.; *Lift and Center of Pressure of Wing-Body-Tail Combinations at Subsonic, Transonic, and Supersonic Speeds*, NACA TR 1307, 1957.

22. Washington, W. D. and Spring, D. J.; *An Experimental Investigation of Wing-Tail Interference for a Typical Supersonic Missile*, AIAA paper 82-1339, AIAA 9th Atmospheric Flight Mechanics Conference, Aug 9-11, 1982, San Diego, CA.

23. Aiello, G. F.; Bateman, M. C.; *Aerodynamic Stability Technology for Maneuverable Missiles, Vol I Configuration Aerodynamic Characteristics*, AFFDL-TR-76-55, Vol I (Contractor Martin Marietta Corporation), Mar 1979.

REFERENCES (Continued)

24. Washington, W. D., *Computer Program for Estimating Stability Derivatives of Missile Configurations*, Technical Report RD-76-25, US Army Missile Command, Redstone Arsenal, AL, May 1976.

25. Hemsch, M. J.; and Mullen, J., Jr.; *Analytical Extension of the MISSILE1 and MISSILE2 Computer Programs*, Near TR-272, Nielsen Engineering and Research, Inc., Mar 1982.

26. Dillenius, M. F. E.; and Hemsch, M. J.; Nielsen Engineering and Research, Inc., Mountain View, CA; and Sawyer, W. C., Allen, J. M.; and Blair, A. B., Jr.; NASA Langley Research Center, Hampton, VA, *Comprehensive Missile Aerodynamics Programs for Preliminary Design*, AIAA-82-0375, AIAA 20th Aerospace Science Meeting, Jan 1982.

27. Dietz, Jr.; and Altstatt, M. C.; *Experimental Investigation of Support Interference on an Ogive Cylinder at High Incidence*, Journal of Spacecraft and Rockets paper Vol. 16, No. 2, Mar-Apr 1979, pp. 67-68.

28. Canning, T. N.; and Nielsen, J. N.; *Experimental Study of the Interference of Supports on the Aerodynamic Loads on an Ogive Cylinder at High Angles of Attack*, AIAA paper 81-0007, 19th Aerospace Sciences Meeting, Jan 12-15, St. Louis, Missouri.

29. Nelson, R. C.; and Mouch, T. N.; *Cylinder/Splitter-Plate Data Illustrating High α Support Interference*, Journal of Spacecraft and Rockets Note, Vol. 16, No. 2, Mar-Apr 1979, pp. 126-127.

30. Ericsson, L. E.; and Reding, J. P.; Review of Support Interference in Dynamic Tests, AIAA Journal, Dec 1983, pp. 1652-1662.

31. Daniels, P.; *Minimization of Lock-In Roll Moment on Missiles Via Slots*, NSWC/DL TR-3250, Jan 1975, Dahlgren, VA.

32. Whoric, J. M.; and Washington, E. S.; *Aerodynamic Characteristics of the Air Slew Demonstrator Models at Mach Numbers 0.6 to 1.3*, AEDC TR-76-92, Aug 1976.

33. Spearman, L. M.; and Triscott, C. D., Jr.; *Effects of Wing Planform on the Static Aerodynamics of a Cruciform Wing-Body Missile for Mach Numbers up to 4.63*, NASA TMX-1839, Jul 1969.

34. Howard, R. M.; and Dunn, A.; *Missile Loads at High Angles of Attack, Engineering Note in Journal of Spacecraft and Rockets*, Vol. 28, No. 1, Jan-Feb 1991, pp. 124-125.

REFERENCES (Continued)

35. Gudmundson, S. E.; Torngren, L.; *Supersonic and Transonic Wind Tunnel Tests of Slender Ogive-Cylinder Body Single and in Combination with Cruciform Wings and Tails of Different Sizes*, Technical Note FFA AU-772, Aeronautical Research Institute of Sweden, Stockholm, Sweden, 1972.

36. Corlett, W. A.; and Howell, D. T.; *Aerodynamic Characteristics of Mach 0.6 to 4.63 of Two Cruciform Missile models, One Having Trapezoidal Wings with Canard Controls and the Other Having Delta Wings with Tail Controls*, NASA TM X-2780, Jul 1973.

37. Monta, W. J.; *Supersonic Aerodynamic Characteristics of a Sparrow III Type Missile Model with Wing Controls and Comparison with Existing Tail Control Results*, NASA TP 1078, Nov 1977.

6.0 SYMBOLS AND DEFINITIONS

AOA	Angle of Attack
APC	Aeroprediction Code
AP81	Aeroprediction 1981
AP93	Aeroprediction 1993
AP95	Aeroprediction 1995
AR	Aspect Ratio = b^2/A_W
COP	Center of pressure
DOF	Degrees of freedom
IAP95	Improved Aeroprediction Code 1995
LT	Linear Theory
MNT	Modified Newtonian Theory
NASA/LRC	National Aeronautics and Space Administration/Langley Research Center
NSWCDD	Naval Surface Warfare Center, Dahlgren Division
NW	Number of wings
SB, SBT	Slender Body, Slender-body Theory
SW	Single wing
a	Speed of Sound (ft/sec)
a_0, a_1, a_2, a_3, a_4	Constants used in nonlinear wing-alone model
A_P	Planform area of the body in the crossflow plane (ft^2)

A_{REF}	Reference area (maximum cross-sectional area of body, if a body is present, or planform area of wing, if wing alone)(ft^2)
A_W, S_W	Planform area of wing in crossflow plane (ft^2)
A_{WETTED}	Area of body or wing which flow touches
b	Wing span (not including body)(ft)
C_A	Axial force coefficient
C_{A_B},C_{A_F},C_{A_W}	Base, skin-friction, and wave components, respectively, of axial force coefficient
C_{D_C}	Crossflow drag coefficient
C_{F_l}, C_{F_T}	Laminar and turbulent skin friction coefficients respectively
C_{ℓ_p}	Roll damping moment coefficient
C_M	Pitching moment coefficient (based on reference area and body diameter, if body present, or mean aerodynamic chord, if wing alone)
C_N	Normal force coefficient
C_{N_B}	Normal force coefficient of body alone
$C_{N_{B(V)}}$	Negative afterbody normal-force coefficient due to canard or wing-shed vortices
$C_{N_{B(W)}}$, $C_{N_{B(T)}}$	Normal-force coefficient on body in presence of wing or tail
$\Delta C_{N_{B(W)}}$	Additional normal-force coefficient on body due to presence of the wing
C_{N_L}	Linear component of normal-force coefficient
$C_{N_{NL}}$	Nonlinear component of normal-force coefficient
$C_{N_{T(V)}}$	Negative normal-force coefficient component on tail due to wing or canard-shed vortex
C_{N_W}	Normal force coefficient of wing alone
$C_{N_{W(B)}}$	Normal-force coefficient of wing in presence of body

C_{N_α}	Normal-force coefficient derivative
C_P	Pressure coefficient $\left(\frac{p - p_\infty}{1/2 \rho_\infty V_\infty^2}\right)$
C_{P_o}	Stagnation pressure coefficient
C_Y	Side force coefficient
c_r	Root chord (ft)
c_t	Tip chord (ft)
cal	Caliber(s) (one body diameter)
d	Body diameter (ft)
d_{ref}	Reference body diameter (ft)
$\frac{dK_{W(B)}}{d\alpha}, \frac{dK_{B(W)}}{d\alpha}$	Rate at which $K_{W(B)}$ or $K_{B(W)}$ decreases
deg	Degree(s)
E_1, E_2	Constants used in semiempirical wing-tail interference model
F, C_1, C_2, C_3	Dimensionless empirical factors used in nonlinear models of $k_{W(B)}$ and $C_{N_{T(V)}}$ to approximate effects due to high AOA or control deflection.
f, h	Lateral and vertical position of wing vortex
f_W, f_T	Lateral location of wing or tail vortex (measured in feet from body center line)
i	Tail interference factor
$K_{B(W)}$, $K_{B(T)}$	Ratio of additional body normal-force coefficient in presence of wing, or tail to wing, or tail alone normal-force coefficient at $\delta = 0$ deg
$k_{B(W)}$, $k_{B(T)}$	Ratio of additional body normal-force coefficient due to presence of wing or tail at a control deflection to that of wing or tail alone at $\alpha = 0$ deg
$[K_{B(W)}]_{MIN}$	Minimum value of $K_{B(W)}$ as percent of slender-body theory value
k_{B_1}	Lowest value of $[K_{B(W)}]_{MIN}$ for $\Phi = 45$ deg
$K_{W(B)}$, $K_{T(B)}$	Ratio of normal-force coefficient of wing or tail in presence of body to that of wing or tail alone at $\delta = 0$ deg

$k_{W(B)}$, $k_{T(B)}$	Ratio of wing or tail normal-force coefficient in presence of body due to a control deflection to that of wing or tail alone at $\alpha = 0$ deg
$[\Delta K_{W(B)}]_{\alpha=0}$ and $[\Delta K_{B(W)}]_{\alpha=0}$	Amount that the experimental values of $K_{W(B)}$ and $K_{B(W)}$ exceed slender body theory at $\alpha = 0°$
ℓ	Length (ft)
ℓ_N	Nose Length (can be in calibers or feet)
m	Cot Λ_{LE}
M	Mach number = V/a
M_C	Normal Mach number to body axis = M sin α
M_L	Local Mach number
p	Pressure (lb/ft^2)
P_ℓ, P_W	Loading factors in leeward and windward planes respectively
p_O, p_L	Local and stagnation pressure respectively (lb/ft^2)
r	Radius of body (ft)
r_N	Radius of nose tip (ft)
r_W, r_T	Radius of body at wing or tail locations
Re	Reynolds number = $\frac{\rho V \ell}{\mu_O}$
Re_{CRIT}	Critical Reynolds number where flow transitions from separating on the forward part of a circular cylinder to the rear part
Re_D	Reynolds number based on diameter of body
Re_{EFF}	Reynolds number defined to better correlate values of C_{D_c} versus Reynolds number
s	Wing or tail semispan plus the body radius in wing-body lift methodology
t/c_r	Tail thickness to its root chord

t/d	Tail thickness to body diameter
TW	Bevel length on leading edge of wind tunnel model
u, v, w	Perturbation velocities in x, y, z directions
V	Velocity (ft/sec)
x	Distance along the axis of symmetry measured positive aft of nose tip (ft or cal)
X_{CP}	Center of pressure (in feet or calibers from some reference point that can be specified) in x direction
$(X_{CP})_L$, $(X_{CP})_{NL}$	Center of pressure of linear and nonlinear terms of normal force.
x,y,z	Axis system fixed with x along centerline of body
X^1, Y^1, Z^1	Body fixed axis system with X^1 along centerline of body
Y_{CP}	Center of pressure of wing lift in y direction
α	Angle of attack (deg)
α_C	Angle of attack where wing-body interference factor starts decreasing (deg)
α_D	Angle of attack where the wing-body interference factor reaches a minimum (deg)
α_F	Value of α (as percent of α_N) where $C_{N_{T(V)}}$ reaches a maximum magnitude
α_M	Angle of attack where $K_{W(B)}$ reaches a constant value
α_N	Value of α where $C_{N_{T(V)}}$ goes to zero
α_{N_o}	Value of α where $C_{N_{T(V)}}$ goes to zero for $A_W/A_{REF} = 5.5$
α_W, α_T	Local angle of attack of wing or tail ($\alpha_W + \delta$ or $\alpha_T + \delta$, respectively, in degrees)
α_1, α_2	Angles of attack used in nonlinear model for $K_{B(W)}$
β	$\sqrt{M^2 - 1}$
δ	Control deflection (deg), positive leading edge up

δ_{eq}	Angle between velocity vector and tangent to body surface
δ_W, δ_T	Deflection of wing or tail surfaces (deg), positive leading edge up
η	Parameter used in viscous crossflow theory for nonlinear body normal force (in this context, it is the normal force of a circular cylinder of given length-to-diameter ratio to that of a cylinder of infinite length)
γ	Specific heat ratio
Γ	Vortex circulation, positive counter clockwise facing upstream (ft^2/sec)
λ	Taper ratio of a lifting surface = c_t/c_r
Λ_{LE}	Leading edge sweep angle of wing or tail (deg)
μ	Mach angle = $\sin^{-1}$ (1/M)
μ_O	Viscosity of air (slug/ft-sec)
Φ	Circumferential position around body where $\Phi = 0$ is leeward plane (deg)
ϕ	Velocity potential
ρ	Density of air (slug/ft^3)
θ	Local surface slope of body with respect to body axis
∞	Free-stream conditions
q_∞	Dynamic pressure of freestream = $\frac{1}{2} \rho_\infty V_\infty^2$ (lb/ft^2)

APPENDIX A

SLENDER BODY AND LINEAR THEORY RESULTS FOR ROLL-DEPENDENT AERODYNAMICS

For the slender body and linear theory analysis, References A-1 and A-2 will be used. The wing-alone and wing-body theories will be examined separately.

WING-ALONE AERODYNAMICS

$(C_{N_W})_\alpha$, $(C_{N_T})_\alpha$, $(C_{N_W})_{\delta_W}$ and $(C_{N_W})_{\delta_T}$ of Equation (2) in the main text are all normal force coefficients of the wing or tail in a uniform freestream with no interference effects. Here the subscripts α and δ refer to normal force coefficient due to AOA or control deflection. These terms all have a linear and a nonlinear component. Disregarding the subscripts to distinguish wing from tail or angle of attack from control deflection, the normal force of the wing can be generically defined as consisting of a linear and a nonlinear term. That is,

$$C_N = C_{N_L} + C_{N_{NL}} \tag{A-1}$$

The linear term of Equation (A-1) is normally computed from integrating the pressure differential between the lower and upper part of the wing surface over the entire wing. It is instructive to review some of the fundamentals of thin wing theory to help understand how roll orientation influences (or does not influence) the linear term of Equation (A-1).

The mathematical model to determine C_{N_L} is based on small perturbation theory for both subsonic and supersonic flow. In subsonic flow, solutions to the perturbation equation are referred to as lifting surface theory, whereas in supersonic flow they are referred to as three-dimensional thin wing theory. The small perturbation equation of motion is

$$\left(1 - M_\infty^2\right) \phi_{xx} + \phi_{yy} + \phi_{zz} = 0 \tag{A-2}$$

The boundary conditions require the flow to be tangent to the surface,

$$\frac{w(X,Y)}{V_\infty} = \phi_z = \left(\frac{dz}{dx}\right)_{x,y} + \alpha + dg/dX \tag{A-3A}$$

and the perturbation potential and velocities to vanish at a large distance from the wing.

$$\phi = \phi_x = \phi_y = \phi_z = 0 \text{ at } x,y,z = \pm\infty \tag{A-3B}$$

The flow tangency boundary condition, Equation (A-3a), can be separated into terms due to thickness, chamber, and angle of attack. For most missiles, the airfoil is symmetric about the x-y plane so the chamber effect $\frac{dg}{dx}$ is zero. The normal approach to solution of Equation (A-2) is to solve the thickness $\left(\frac{dz}{dx}\right)$ and lift problems (α) independently, since Equation (A-2) is linear. Then, if desired, the solutions can be linearly added together.

The linearized pressure coefficient for a flat surface from Equation (A-2) is

$$C_P = -2\,\phi_x = -2u(x,y,z) \tag{A-4}$$

For the axial force problem, the boundary condition is symmetric about the plane $z = 0$. For the lift problem, the normal force is the difference between the pressure on the upper and lower surfaces of the wing. For this case

$$\Delta C_P = 4\alpha\, f\left(M_\infty,\ x,y,\Lambda\right) \tag{A-5}$$

The function $f(M_\infty, x, y, \Lambda)$ is used here to indicate that a complicated expression exists to define the differential pressure from upper to lower wing surfaces that is a function of M_∞ and the wing geometric parameters. This function is different for subsonic and supersonic leading edge wings.

The important point is that for both the axial and normal force of a wing in isolation, there is no roll orientation or sideslip dependence in the pressure coefficient. As a result, we can analyze wings in isolation directly without concern for crosscoupling effects.

Examining a wing (see Figure A-1A) at some roll orientation, it is found that in the direction normal to the planform, the velocity is $V_\infty \sin\alpha \cos\Phi$ and angle of attack is $\sin\alpha \cos\Phi$, or for the small angle approximation of $\sin\alpha \approx \alpha$, the velocity is $V_\infty \alpha \cos\Phi$. Also, to rotate the normal force vector (normal to the lifting surface area) to the vertical plane, another $\cos\Phi$ is required.

The normal force of the wing alone in the x,y plane is therefore

$$\left(C_{N_L}\right)_{XY} = \left(C_{N_L}\right)\cos^2\Phi \tag{A-6}$$

If there is a wing perpendicular to the planform in Figure A-1A, so that a cruciform arrangement is present, then for this wing (see Figure A-1B)

$$\left(C_{N_L}\right)_{XY} = \left(C_{N_L}\right)\sin^2\Phi \tag{A-7}$$

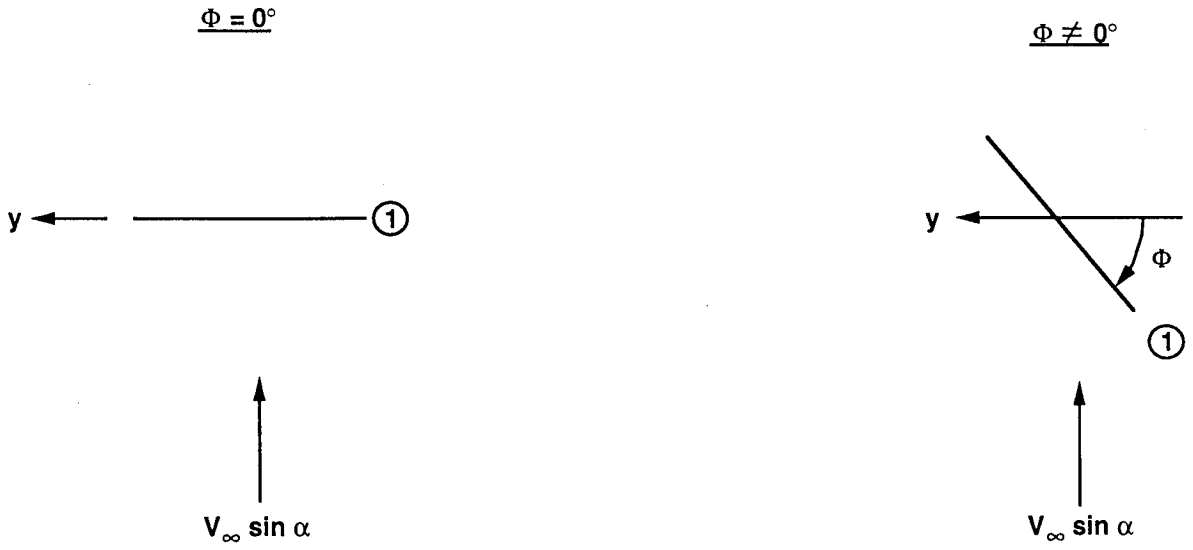

$$\left(C_{N_w}\right)_{\Phi = 0} \neq 0 \qquad \left(C_{N_w}\right)_{\Phi \neq 0} = \left(C_{N_w}\right)_{\Phi = 0} \cos^2 \Phi$$

$$\left(C_{A_w}\right)_{\Phi = 0} \neq 0 \qquad \left(C_{A_w}\right)_{\Phi \neq 0} = \left(C_{A_w}\right)_{\Phi = 0}$$

$$\left(X_{cp}\right)_{\Phi = 0} \neq 0 \qquad \left(X_{cp}\right)_{\Phi \neq 0} \approx \left(X_{cp}\right)_{\Phi = 0}$$

$$\left(C_y\right)_{\Phi = 0} = 0 \qquad \left(C_y\right)_{\Phi \neq 0} = -\left(C_{N_w}\right)_{\Phi = 0} \sin^2 \Phi$$

$$\left(C_{l_p}\right)_{\Phi = 0} \neq 0 \qquad \left(C_{l_p}\right)_{\Phi \neq 0} = \left(C_{l_p}\right)_{\Phi = 0}$$

FOR $\Phi = 45°$

$$\left(C_{N_w}\right)_{\Phi = 45°} = \left(C_y\right)_{\Phi = 45°} = \frac{1}{2}\left(C_{N_w}\right)_{\Phi = 0°}$$

FIGURE A-1A. LT AND SBT IMPLICATIONS FOR ROLL-DEPENDENT AERODYNAMICS, SINGLE WING OF SPAN B

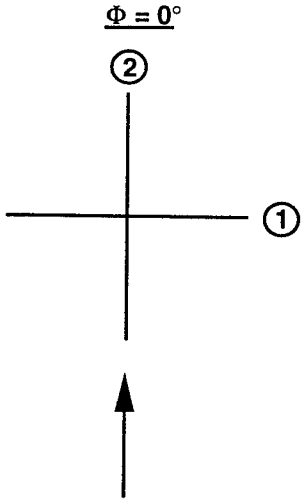

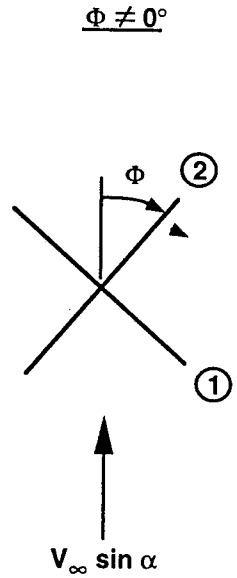

$$\left(C_{N_W}\right)_{\Phi = 0} = \left(C_{N_W}\right)_{sw}$$

$$\left(C_{N_W}\right)_{\Phi \neq 0} = \left(C_{N_W}\right)_{sw}\left[\sin^2 \Phi + \mathrm{Cos}^2 \Phi\right] = \left(C_{N_W}\right)_{sw}$$

$$\left(C_{A_W}\right)_{\Phi = 0} = 2\left(C_{A_W}\right)_{sw}$$

$$\left(C_{A_W}\right)_{\Phi = 0} = 2\left(C_{A_W}\right)_{sw}$$

$$\left(X_{cp}\right)_{\Phi = 0} = \left(X_{cp}\right)_{sw}$$

$$\left(X_{cp}\right)_{\Phi \neq 0} \cong \left(X_{cp}\right)_{sw}$$

$$\left(C_y\right)_{\Phi = 0} = 0$$

$$\left(C_y\right)_{\Phi \neq 0} = 0$$

$$\left(C_{l_p}\right)_{\Phi = 0} = 1.62\left(C_{l_p}\right)_{sw}$$

$$\left(C_{l_p}\right) = 1.62\left(C_{l_p}\right)_{sw}$$

FIGURE A-1B. LT AND SBT IMPLICATIONS OF ROLL-DEPENDENT AERODYNAMICS, CRUICIFORM WINGS OF SPAN B

For a cruciform missile, the Equations (A-6) and (A-7) are added, yielding

$$\left(C_{N_L}\right)_{XY} = C_{N_L}\left(\sin^2\Phi + \cos^2\Phi\right)$$

or

$$\left(C_{N_L}\right)_{XY} = C_{N_L} \tag{A-8}$$

This result says that for small angles of attack for a cruciform missile, the lift of the wing is independent of roll angle. This is also true of the axial force as well. This means that we can analyze the cruciform missile fins alone at roll orientation of zero and apply these results to any roll orientation.

It is also worthy to note in Figures (A-1A) and (A-1B) the implications of LT and SBT on the other aerodynamics for wings alone. Of particular note is the fact that for a single planar wing, a side force is generated for $\Phi = 0$ (Figure A-1A) whereas for a planar set of cruciform wings, no side force is generated. Also, for more than one wing, the axial force is simply the product of the value for a single wing times the number of wings present. Slender body theory also gives the result that the roll damping coefficient of a cruciform arrangement is only 1.62 times the single fin value versus twice the value.[A-1]

Figure A-1C presents the results for three sets of wings, where wing-to-wing interference has been ignored. Note once again the fact that the aerodynamics are independent of roll. Also the aerodynamics are all a function of the number of wings, NW.

The LT and SBT results of Figure A-1 are true for flowfields where perturbations in the flow due to the presence of the wing are small and where any shock waves are weak. As a result of these assumptions, it is suspected that the roll independence, roll damping and other force results of Figures A-1B and A-1C may not hold at higher angle of attack where the aerodynamics are strongly nonlinear and fin-to-fin interference effects are higher. On the other hand, this assumption will be required in the development of a semiempirical model. The reason for this goes back to the way the data bases of References A-4 to A-6 were obtained. These data bases obtained aerodynamics on a single wing alone at $\Phi = 0$ and wings in conjunction with the body at various roll orientations. The wing in conjunction with the body therefore has carryover effects from the body, nonlinear and linear angle of attack effects, body vortices, fin-to-fin interference, and any roll dependence effects. Since the data were taken in a total sense, it would be difficult, if not impossible, to accurately separate all the independent effects. As a result, a quite logical way to use the Reference 6-9 data bases is through using the wing-alone data at $\Phi = 0$ for any roll position, combined with the fin in conjunction with the body data, which has included all the effects mentioned above. The net result of this approach will be to include all the nonlinear effects mentioned into the interference factors of Equation (2) or Equation (3) of the main text.

$\Phi = 0°$

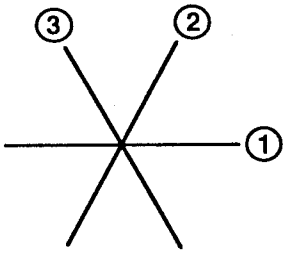

NW = 3

$\Phi \neq 0°$

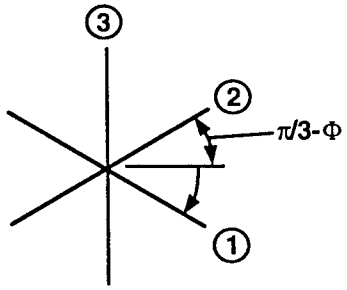

$$\left(C_{N_W}\right)_{\Phi=0} = \left(C_{N_W}\right)_{sw}\left[\frac{NW}{2}\right] \qquad \left(C_{N_W}\right)_{\Phi\neq 0} = \left(C_{N_W}\right)_{\Phi=0}$$

$$\left(C_{A_W}\right)_{\Phi=0} = \left(C_{A_W}\right)_{sw}\ (NW) \qquad \left(C_{A_W}\right)_{\Phi\neq 0} = \left(C_{A_W}\right)_{\Phi=0}$$

$$\left(X_{cp}\right)_{\Phi=0} \neq 0 \qquad \left(X_{cp}\right)_{\Phi\neq 0} \approx \left(X_{cp}\right)_{\Phi=0}$$

$$\left(C_y\right)_{\Phi=0} = 0 \qquad \left(C_y\right)_{\Phi\neq 0} = 0$$

$$\left(C_{l_p}\right)_{\Phi=0} = 2\left(C_{l_p}\right)_{sw} \qquad \left(C_{l_p}\right)_{\Phi=0} = 2\left(C_{l_p}\right)_{sw}$$

FOR MORE THAN 3 SETS OF WINGS, ALL ABOVE FORMULAS ARE STILL TRUE EXCEPT C_{l_p} . FOR NW= ∞,

$$\left(C_{l_p}\right)_{NW=\infty} = 4\left(C_{l_p}\right)_{sw}$$

FIGURE A-1C. LT AND SBT IMPLICATIONS FOR ROLL-DEPENDENT AERODYNAMICS, THREE SETS OF WINGS OF SPAN B

WING-BODY AERODYNAMICS

The implications of slender body theory on the wing-body combination will now be examined. Particular emphasis will be placed on the crossflow plane. The small perturbation equation used here is the same as Equation (A-2); however, the boundary condition (A-3A) is different. [A-2] The reason for the different boundary condition, as shown in Reference A-2, is that in the perturbation expansion of the inner and outer flow, all terms to the first order in the perturbation parameter ε vanish. Thus the perturbation velocities in the outer flow are of the order ε^2 versus ε for the 2-D and 3-D wing cases. Physically, one can interpret this as the perturbation velocities being smaller for a body of revolution in the normal force direction than for a wing planform because the body allows the flow to wrap around it in a smoother way than a wing. This process allows the perturbations in the flow at a large distance from the body to be smaller for a body than for a wing.

As a result of the perturbations being of the order ε^2 versus ε, the pressure coefficient equation is no longer linear like the wing alone. The approximate pressure coefficient equation for a wing-body combination is therefore

$$C_P = -2\phi_x - \phi_y^2 - \phi_z^2$$

$$= -2u - v^2 - w^2 \qquad \text{(A-9)}$$

Recall the boundary condition, Equation (A-3A) along with the pressure coefficient Equation (A-5), allowed us to uncouple the thickness boundary condition from the boundary condition due to angle of attack. Hence, one could compute axial force coefficients with Equation (A-4) with only the first part of Equation (A-3A) used and normal force coefficients with Equation (A-5) with the second part of Equation (A-3A) used. This can no longer be done with Equation (A-9), since terms involving the axial force and normal force boundary condition appear to the second power, coupling the axial and crossflow solutions together.

A fortunate feature of triform and cruciform missile configurations, is that when the force is integrated over the entire configuration in the lift direction, the coupling terms cancel out and the normal force is thus independent of roll position[A-1]. This means that if one is interested in calculating the normal force of a wing-body configuration with a single wing (Figure A-2A), the normal force, side force and rolling moment are all roll-dependent. However, if one is interested in calculating the aerodynamics of a cruciform wing-body combination with SBT or LT (Figure A-2B), the aerodynamics are independent of roll.

It should be re-emphasized that as long as trim aerodynamic models are of interest for missiles flying at $\Phi = 0$ or 45 deg roll orientation, and symmetrical deflections of the control surfaces are considered, the approach of neglecting the out of plane coupling aerodynamics is satisfactory. However, if one is interested in attempting to use an engineering code to generate

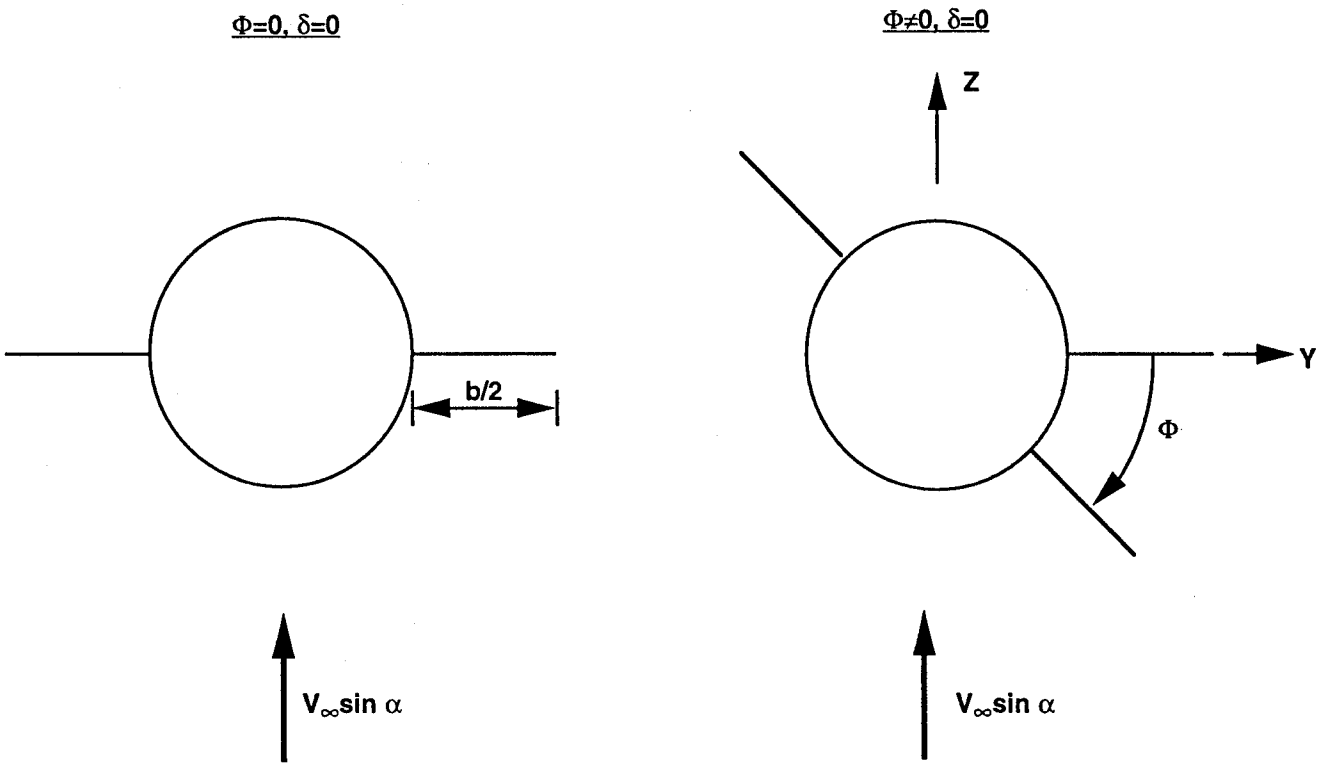

- $C_N = [K_{W(B)} + K_{B(W)}] C_{N_W} + C_{N_B}$
- $C_A = C_{A_W} + C_{A_B}$
- $C_\ell = C_Y = 0$
- LEFT AND RIGHT PANEL LOADING EQUAL

- $C_N = [K_{W(B)} + K_{B(W)}] C_{N_W} \cos^2\Phi + C_{N_B}$
- $C_A = C_{A_W} + C_{A_B}$
- $C_Y = [K_{W(B)} + K_{B(W)}] C_{N_W} \sin\Phi \cos\Phi$
- $C_\ell \equiv - K_{W(B)} C_{N_W} \bar{y}_{cp} \cos\Phi$
- LOADING ON RIGHT PANEL GREATER THAN THAT ON LEFT PANEL BY AN EQUAL AMOUNT DUE TO OUT-OF-PLANE AERODYNAMIC COUPLING

FIGURE A-2A. SBT IMPLICATIONS FOR ROLL-DEPENDENT AERODYNAMICS, WING-BODY COMBINATION (SINGLE WING OF SPAN B)

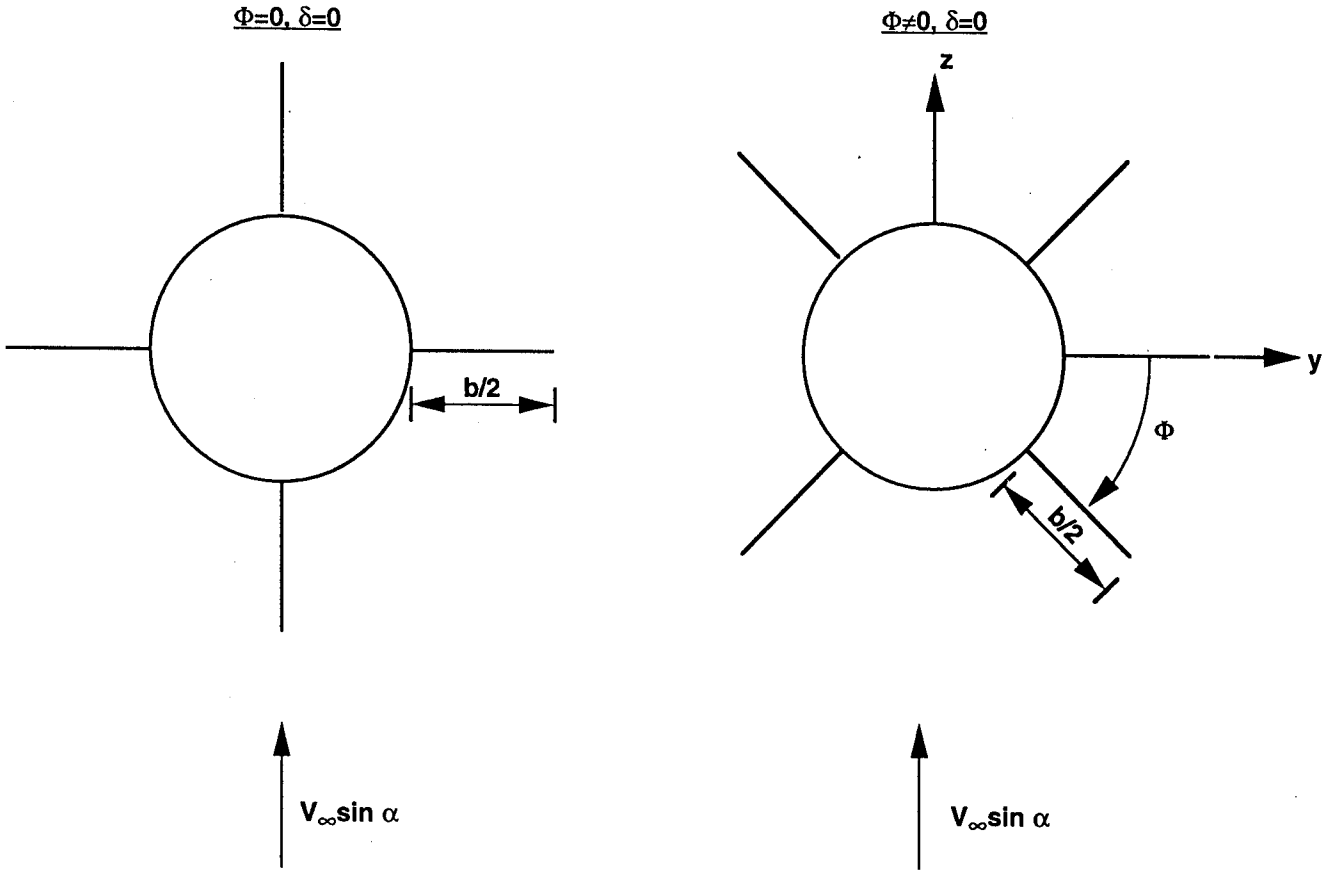

- $C_N = [K_{W(B)} + K_{B(W)}] C_{N_W} + C_{N_B}$
- $C_A = 2C_{A_W} + C_{A_B}$
- $C_\ell = C_Y = 0$
- LEFT AND RIGHT PANEL LOADING EQUAL

- $C_N = [K_{W(B)} + K_{B(W)}] C_{N_W} + C_{N_B}$
- $C_A = 2C_{A_W} + C_{A_B}$
- $C_Y = C_\ell = 0$
- LOADING ON WINDWARD PANELS GREATER BY AND EQUAL AMOUNT THAN THAT ON LEEWARD PANELS. TERMS CANCEL SO $C_Y = C_\ell = 0$
- $(C_N)_{\Phi \neq 0} = (C_N)_{\Phi=0}$

FIGURE A-2B. SBT IMPLICATIONS FOR ROLL-DEPENDENT AERODYNAMICS, WING-BODY COMBINATION (CRUCIFORM WINGS OF SPAN B)

aerodynamics for a six-degree-of-freedom trajectory simulation model, the out of plane aerodynamics cannot be neglected. An approach similar to that in Reference A-7 will be required or a more accurate aerodynamic approach where the small perturbation assumptions have not been made will most likely be required.

WING-BODY-TAIL AERODYNAMICS AT $\Phi = 0$ DEG

The major new complexity that results from adding two sets of lifting surfaces to a missile configuration (versus one) is the vortices shed from the forward surfaces impacting the rear surfaces. For this discussion, wings and canards will be used interchangeably as the forward surfaces, and tails will be the aft lifting surfaces. If the missile is at supersonic Mach numbers and at angle of attack greater than about 25 to 30 deg, shock wave interference between the forward and aft lifting surfaces or between the bow shock wave and the lifting surfaces can also occur. This problem will not be discussed in the linear theory and slender body theory discussion but is discussed in the nonlinear methods discussion of the report.

If the missile is in the $\Phi = 0$ deg roll orientation, only one wing planform will release a vortex at $\alpha > 0$ deg for fairly thin wings of zero chamber. However, at $\Phi = 45$ deg for a cruciform wing arrangement, both wings release vortices and these vortices follow different paths depending on whether they are released in the windward or leeward plane. It is instructive to examine the SBT results for both the $\Phi = 0$ and 45 deg plane in terms of the loss of lift on the tail, or $C_{N_{T(V)}}$ term of Equation (1). In reviewing the SBT results, References A-1 and A-8 will be the primary sources of material.

Figure A-3, taken from Reference A-8, is a schematic of the $\Phi = 0$ deg vortex model for a planar wing-body combination. The wing-shed vortices are shown above the tail-body cross section. It is assumed here that one is looking upstream of a wing-body-tail configuration at a positive angle of attack. The strength of the wing-shed vortices, Γ, is assumed to be positive in a counterclockwise direction looking upstream.

The term $C_{N_{T(V)}}$ of Equation (2), is defined by[A-1]

$$C_{N_{T(V)}} = \frac{\left(C_{N_\alpha}\right)_W \left(C_{N_\alpha}\right)_T \left[K_{W(B)}\, \alpha + k_{W(B)}\, \delta_W\right] i_T \left(s_T - r_T\right) A_W}{2\pi\, AR_T \left(f_W - r_W\right) A_{REF}} \qquad \text{(A-10)}$$

Some of the parameters of Equation (A-10) are shown in Figure (A-3). The parameter f_W, the point on the wing where the single vortex separates, is approximated by the centroid of the approximate elliptic circulation distribution. That is

$$f_W = r_W + (\pi/4)\ (b_W/2) \qquad \text{(A-11)}$$

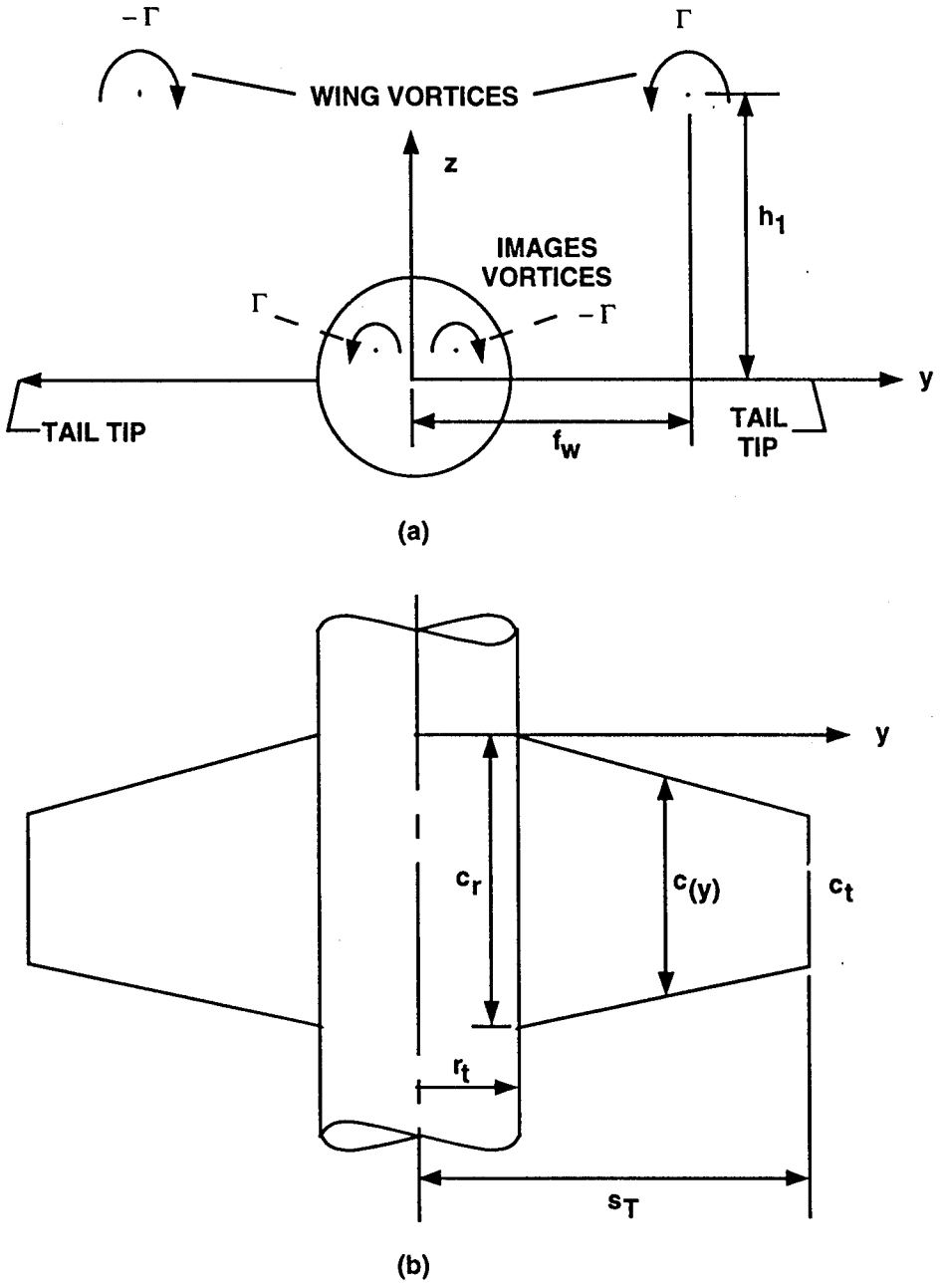

(a) WING VORTICES IN CROSSFLOW PLANE OF TAIL.
(b) TAIL PLANFORM DIMENSIONS.

FIGURE A-3. MODEL AND DIMENSIONS FOR DETERMINATION OF TAIL INTERFERENCE FACTOR BY STRIP THEORY FOR $\Phi = 0$ DEG (FROM REFERENCE A-8)

Utilizing Figure A-4, the height of the wing-shed vortex above the tail center of area is

$$h = \left\{ (X_{LE})_T - (X_{LE})_W - \frac{\pi}{4}\left(\frac{b_W}{2}\right) \tan(\Lambda_{LE})_W - C_{r_W}\left[1 - \frac{\pi}{4}(1 - \lambda_W)\right] + \overline{X}_T \right\} \tan \alpha - \sin(\delta_W) \left\{ (C_r)_W/2 + \left[\tan(\Lambda_{LE})_W + \frac{(C_r)_W}{b_W/2}(\lambda_W - 1) \right] \left(\frac{\pi}{4}\right) \left(\frac{b_W}{2}\right) \right\} \quad \text{(A-12)}$$

Equation (A-12) assumes the vortex leaves the wing at the trailing edge outboard location given by Equation (A-11). The vortex then follows the velocity vector straight back, and impacts at the tail center of pressure (here approximated along the root mid chord). To satisfy the boundary condition on the body surface of zero normal velocity requires that the vortex of equal and opposite strength to the wing vortex be placed on the radius vector along the body centroid to the wing vortex and at a distance

$$\frac{r^2}{\sqrt{f^2 + h^2}}$$

from the body centroid. Using proportionality of triangles, the coordinates of the image vortex are

$$f_i = f_W \left(\frac{r^2}{f_W^2 + h^2} \right) \quad \text{(A-13)}$$

$$h_i = h \left(\frac{r^2}{f_W^2 + h^2} \right) \quad \text{(A-14)}$$

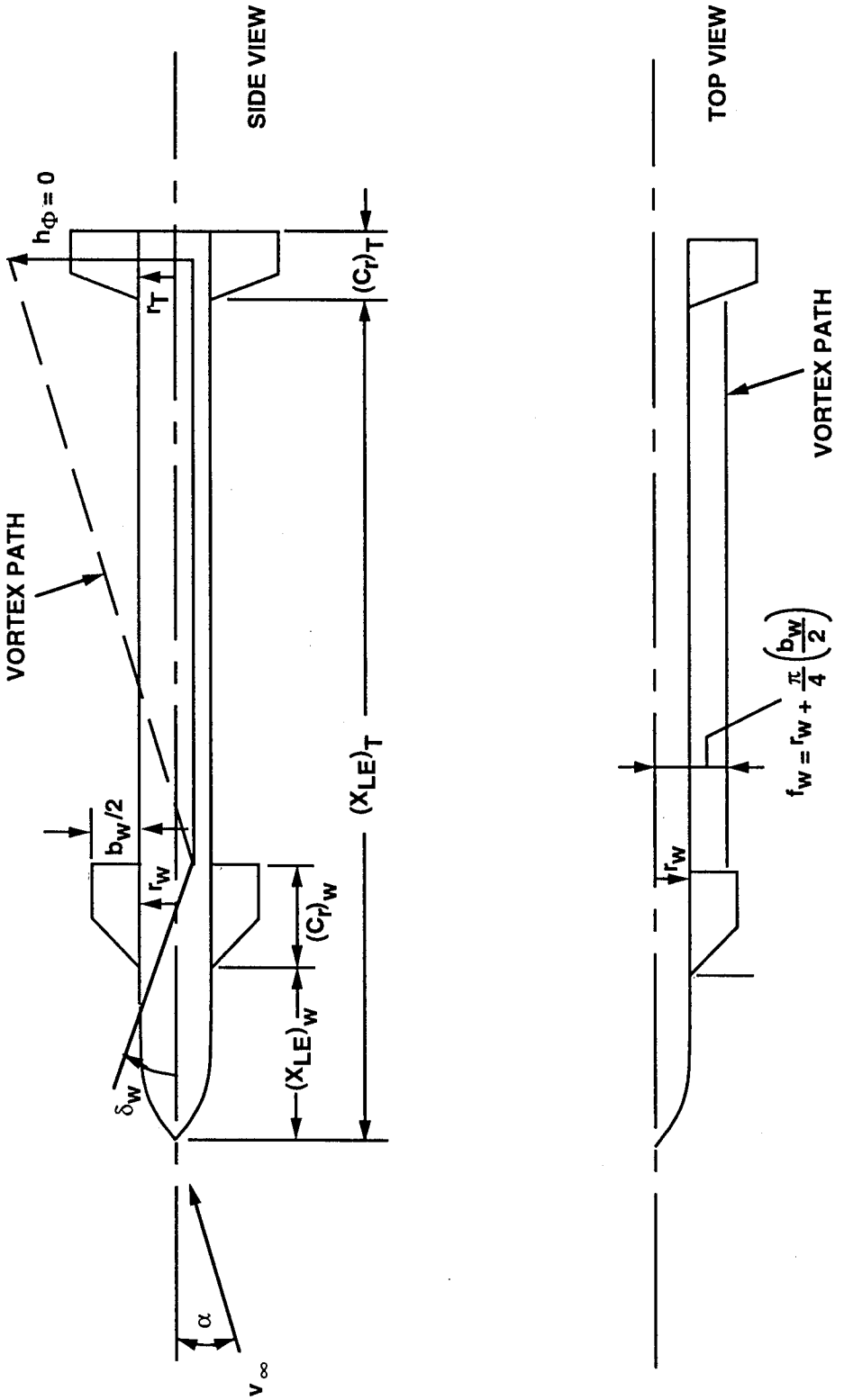

FIGURE A-4. NOMENCLATURE FOR DETERMINING HEIGHT OF WING VORTEX ABOVE TAIL MID CHORD FOR $\Phi = 0$ DEG

It should be noted that the image vortices are required to account for the body part of the configuration in the vicinity of the wing and are equal and opposite in strength to the wing-shed vortices.

The only term not defined in Equation (A-10) is the tail interference factor i_T. The tail interference factor is a nondimensional measure of the interference of a vortex on a lifting surface. In mathematical terms, this definition is

$$i_T = \left(\frac{L_{T(V)}}{L_T} \right) \left(\frac{2\pi V_O \, (s_T - r_T) \propto}{\Gamma} \right) \tag{A-15}$$

In Equation (A-15), $L_{T(V)}$ should be interpreted as the lift or normal force on the tail-body region due to a vortex shed upstream; L_T should be interpreted as the lift on the tail in isolation. Since the velocity of the vortices is counterclockwise in the tail region, this means a downward velocity, and hence, the lift on the tail due to the wing-shed vortex is negative. Hence, i_T is negative and Equation (A-10) is negative.

The general procedure to compute $L_{T(V)}$ is through the use of strip theory since this simplifies the integration of the lift over the wing surface and allows for a closed form solution. The lift due to the right external vortex on the right external tail panel (looking upstream in Figure A-3) is

$$L_1 = \frac{4 q_\infty \, \Gamma \, (c_r)_T}{2\pi \left(\sqrt{M_\infty^2 - 1} \right) V_\infty} L\left(\lambda_T, \frac{r_T}{s_T}, \frac{f_W}{s_T}, \frac{h_1}{s_T} \right) \tag{A-16}$$

The function L of Equation (A-16) is defined by

$$L\left(\lambda_T, \frac{r_T}{s_T}, \frac{f_W}{s_T}, \frac{h}{s_T} \right) = \left\{ \frac{(s_T - r_T \lambda_T) - f_W (1 - \lambda_T)}{2 (s_T - r_T)} \ell n \left[\frac{h^2 + (f_W - s_T)^2}{h^2 + (f_W - r_T)^2} \right] \right.$$

$$\left. - \frac{(1 - \lambda_T)}{(s_T - r_T)} \left[(s_T - r_T) + h \tan^{-1} \left(\frac{f_W - s_T}{h} \right) - h \tan^{-1} \left(\frac{f_W - r_T}{h} \right) \right] \right\} \tag{A-17}$$

The lift on the right panel due to the left vortex is then

$$L_2 = - \frac{4q_\infty \Gamma (c_r)_T}{2\pi \left(\sqrt{M_\infty^2 - 1}\right) V_\infty} L \left(\lambda_T, \frac{r_T}{s_T}, - \frac{f_W}{s_T}, \frac{h_2}{s_T} \right) \tag{A-18}$$

The lifts of the right and left image vortices on the right wing panel are then given by

$$L_3 = - \frac{4q_\infty \Gamma (c_r)_T}{2\pi \left(\sqrt{M_\infty^2 - 1}\right) V_\infty} L \left(\lambda_T, \frac{r_T}{s_T}, \frac{f_i}{s_T}, \frac{h_i}{s_T} \right) \tag{A-19}$$

$$L_4 = \frac{4q_\infty \Gamma (c_r)_T}{2\pi \left(\sqrt{M_\infty^2 - 1}\right) V_\infty} L \left(\lambda_T, \frac{r_T}{s_T}, - \frac{f_i}{s_T}, \frac{h_i}{s_T} \right) \tag{A-20}$$

Since the left tail panel has the same lift as the right (because of symmetry at $\Phi = 0$ deg) the total lift on the tail due to the vortices shed in the wing-body region is

$$L_{T(V)} = \frac{8q_\infty \Gamma (c_r)_W}{2\pi \left(\sqrt{M_\infty^2 - 1}\right) V_\infty} \left[L \left(\frac{f_W}{s_T} \right) - L \left(- \frac{f_W}{s_T} \right) - L \left(\frac{f_i}{s_T} \right) + L \left(- \frac{f_i}{s_T} \right) \right] \tag{A-21}$$

Equation (A-21) abbreviates the parameters in the L function Equation (A-17) given by Equations (A-16), (A-18), (A-19), (A-20) for simplicity.

The lift on the tail, again using strip theory is

$$L_T = \frac{4 \propto q_\infty (s_T - r_T) c_{r_T} (1 + \lambda_T)}{\sqrt{M_\infty^2 - 1}} \tag{A-22}$$

The nondimensional interference factor, i_T, then, becomes

$$i_T = \left(\frac{2}{1 + \lambda_T} \right) \left[L \left(\frac{f_W}{s_T} \right) - L \left(- \frac{f_W}{s_T} \right) - L \left(\frac{f_i}{s_T} \right) + L \left(- \frac{f_i}{s_T} \right) \right] \tag{A-23}$$

It should be noted that while strip theory has been used for the integration of the lift on the tail in isolation and in the presence of the vortex, these errors tend to cancel since they are nondimensionalized by one another. The same process for obtaining the interference factors $K_{W(B)}$, $K_{B(W)}$, $k_{W(B)}$ and $k_{B(W)}$ has been used with demonstrated success.

WING-BODY-TAIL AERODYNAMICS AT Φ = 45 DEG

A cruciform, in-line, wing-body-tail arrangement will be assumed for this discussion. This assumption is actually not necessary for the slender body theory, but is convenient for discussion purposes. Figure A-5 gives the geometrical arrangement for vortex placement of the eight vortices in the wing-body plane, which must be accounted for in the tail plane. It is interesting to note that even though slender body theory gives a larger lift on the windward plane fins than on the leeward plane fins (see wing-body aerodynamics discussion), the normal approach to the computation of vortex lift on the tail for small $\propto$ is to assume (referring to Figure A-5)

$$\Gamma_1 = -\Gamma_3$$

$$\Gamma_2 = -\Gamma_4 \qquad \text{(A-24)}$$

This being the case, the only difference between the Φ = 0 deg case of the previous section and the Φ = 45 deg case is the difference in trajectories due to the roll position. The physical reason that this occurs here and not with the loading computations is that the vortex strength is a function of the velocity potential difference from the upper to the lower part of the wing. Those potential differences can be added linearly together. On the other hand, the section 2.1.2 results showed the velocity to the second power, thereby coupling the axial and crossflow solutions together. It is suspected that the traditional mathematical approach of linearly adding the velocity potential differences together to obtain circulation, is one reason the work of Reference A-3 required an empirical correction to slender body theory, particularly as angle of attack increases. This is addressed further in the nonlinear methods discussion of the report.

For the Φ = 45 deg computation, the vortices will again be assumed to stream rearward along the velocity vector. In actuality, the windward plane vortices actually rise above this line because of the spin direction; the leeward plane vortices move below the velocity vector, since their spin is downward. Reference A-8 showed that the more sophisticated method of vortex tracking was not superior to the simplified approach, however.

Figure A-5B shows the vortex pattern of the eight vortices in the tail plane area based on the simplified assumption that their paths follow the velocity vector. It is of interest to calculate the effect on the tail surfaces of these eight vortices. Since the vortex pattern is symmetric about the x-z plane, only the tail surfaces in the right half plane need to be considered and these results then doubled to account for the fins in the left half plane of Figure A-5B. In the analysis, since the

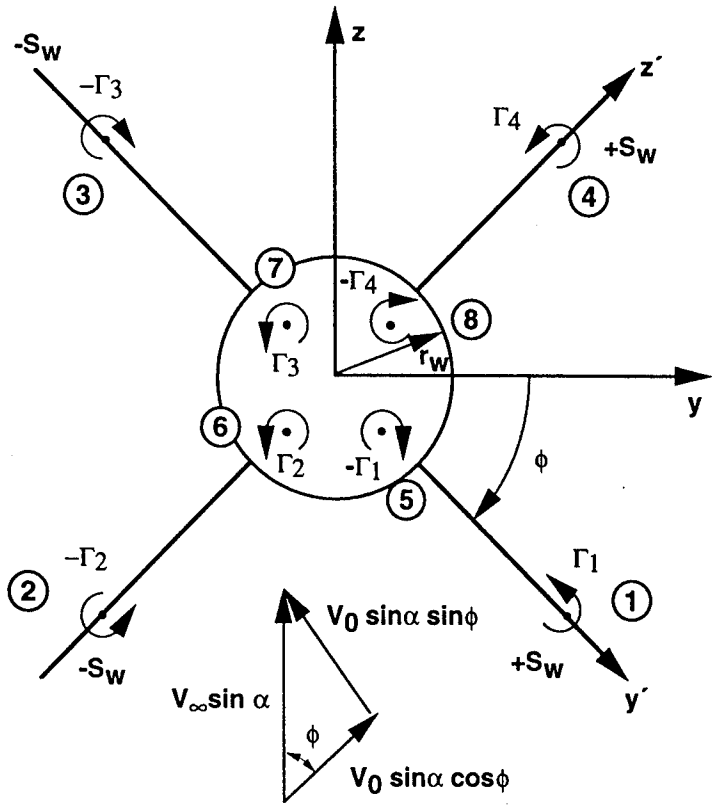

FIGURE A-5A. VORTEX MODEL OF CRUCIFORM WING-BODY ARRANGEMENT

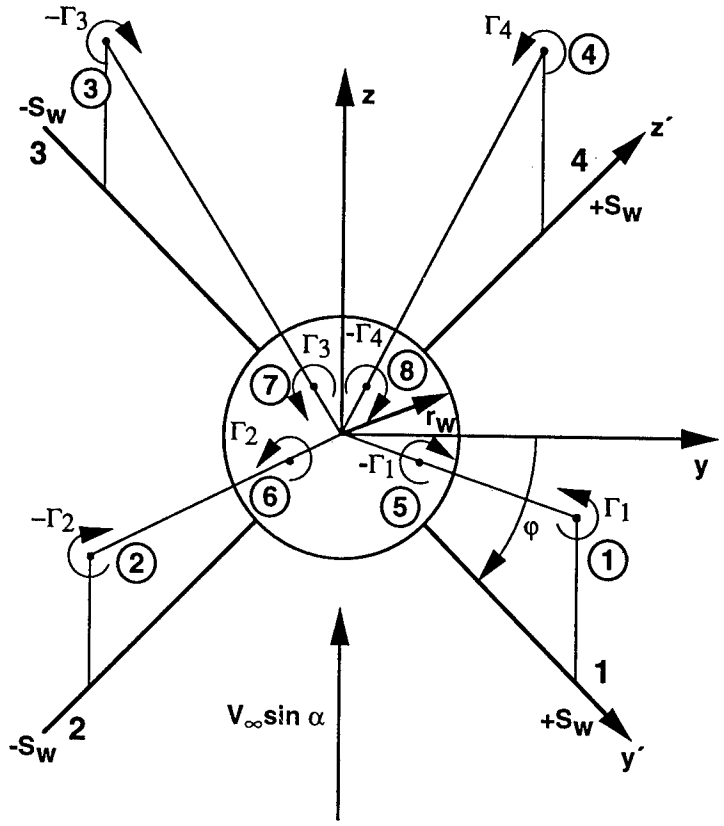

FIGURE A-5B. LOCATION OF WING-BODY VORTICES IN PLANE OF TAIL

solutions for the vortices can be added together linearly, the analysis for the $\Phi = 0$ deg plane can be utilized for the $\Phi = 45$ deg plane. Referring to Figure A-5A, the vortex strengths for the wing vortices are defined by

$$\Gamma_1 = -\Gamma_3 = 2\, V_\infty \sin \propto \cos \Phi \left(\frac{s_W^2 - r_W^2}{s_W} \right) \tag{A-25}$$

$$\Gamma_4 = -\Gamma_2 = 2\, V_\infty \sin \propto \cos \Phi \left(\frac{s_W^2 - r_W^2}{s_W} \right)$$

Of course these strengths are assumed constant from the wing (Figure A-5A) to the tail region shown in Figure A-5B. However, both *f* or *y* and *h* or *z* change for each of the vortices in going from the wings to the tail plane. For the $\Phi = 0$ deg case, only the *h*'s changed.

Referring to Figure A-5B, the numbers in circles refer to the vortex number from 1 to 8, whereas the numbers uncircled refer to the tail fin number. In analogy to the $\Phi = 0$ deg methodology, the impact of the eight vortices on tail fins 1 and 4 is required. These results can then be doubled to account for fins 2 and 3. Using subscript notation, where the subscript denotes the vortex number, the coordinates of the wing-shed vortices with respect to the y-z axis system are

$$z_1 = -f_W \sin \Phi + \tan \propto \left\{ (x_{LE})_T - (x_{LE})_W - \left(\frac{\pi}{4} \right) \left(\frac{b_W}{2} \right) \tan (\Lambda_{LE})_W \right.$$

$$\left. - c_{r_W} \left[1 - \frac{\pi}{4} (1 - \lambda_W) \right] + \bar{x}_T \right\} - \sin (\delta_W) \cos \Phi \left\{ (c_r)_W/2 \right.$$

$$\left. + \left[\tan (\Lambda_{LE})_W + \frac{(c_r)_W}{(b_W/2)} (\lambda_W - 1) \right] \left(\frac{\pi}{4} \right) \left(\frac{b_W}{2} \right) \right\} \tag{A-26}$$

$$y_1 = f_W \cos \Phi \tag{A-27}$$

$$z_2 = z_1 \tag{A-28}$$

$$y_2 = - y_1 \tag{A-29}$$

$$z_3 = z_1 + 2 f_W \cos \Phi \tag{A-30}$$

$$y_3 = - y_1 \tag{A-31}$$

$$z_4 = z_3 \tag{A-32}$$

$$y_4 = y_1 \tag{A-33}$$

Likewise, the coordinates of the body image vortices are defined by (where Equations (A-13) and (A-14) have been utilized)

$$z_5 = z_1 \left(\frac{r_W^2}{y_1^2 + z_1^2} \right) \tag{A-34}$$

$$y_5 = y_1 \left(\frac{r_W^2}{y_1^2 + z_1^2} \right) \tag{A-35}$$

$$z_6 = z_5 \tag{A-36}$$

$$y_6 = - y_5 \tag{A-37}$$

$$z_7 = z_3 \left(\frac{r_W^2}{y_1^2 + z_3^2} \right) \tag{A-38}$$

$$y_7 = - y_1 \left(\frac{r_W^2}{y_1^2 + z_3^2} \right) \tag{A-39}$$

$$z_8 = z_7 \tag{A-40}$$

$$y_8 = - y_7 \tag{A-41}$$

Referring back to Equations (A-16) through (A-23) for the $\Phi = 0$ deg roll position, note that the lift on the right tail surface was computed with the addition of four vortices. At $\Phi = 45$ deg roll, there are eight vortices that act on the two tail fins. As a result, the wing tail interference factor for tail one is (on following page)

$$i_1 = \left(\frac{2\cos\Phi}{1+\lambda_T}\right)\left[L\left(\lambda_T, \frac{r_T}{s_T}, \frac{y_1}{s_T}, \frac{z_1}{s_T}\right) - L\left(\lambda_T, \frac{r_T}{s_T}, \frac{y_2}{s_T}, \frac{z_2}{s_T}\right)\right.$$

$$- L\left(\lambda_T, \frac{r_T}{s_T}, \frac{y_3}{s_T}, \frac{z_3}{s_T}\right) + L\left(\lambda_T, \frac{r_T}{s_T}, \frac{y_4}{s_T}, \frac{z_4}{s_T}\right)$$

$$- L\left(\lambda_T, \frac{r_T}{s_T}, \frac{y_5}{s_T}, \frac{z_5}{s_T}\right) + L\left(\lambda_T, \frac{r_T}{s_T}, \frac{y_6}{s_T}, \frac{z_6}{s_T}\right)$$

$$\left. - L\left(\lambda_T, \frac{r_T}{s_T}, \frac{y_7}{s_T}, \frac{z_7}{s_T}\right) - L\left(\lambda_T, \frac{r_T}{s_T}, \frac{y_8}{s_T}, \frac{z_8}{s_T}\right)\right] \qquad \text{(A-42)}$$

Note the circulation of the vortex is positive in a counterclockwise direction. This is what determines the plus or minus signs in Equation (A-42). Likewise the interference factor for tail 4 is (on following page)

$$i_4 = \left(\frac{2 \sin \Phi}{1 + \lambda_T}\right)\left[L\left(\lambda_T, \frac{r_T}{s_T}, \frac{y_1}{s_T}, \frac{z_1 - f_W \cos \Phi}{s_T}\right)\right.$$

$$- L\left(\lambda_T, \frac{r_T}{s_T}, \frac{y_2}{s_T}, \frac{z_1 - f_W \cos \Phi}{s_T}\right)$$

$$+ L\left(\lambda_T, \frac{r_T}{s_T}, \frac{y_4}{s_T}, \frac{z_4}{s_T}\right) - L\left(\lambda_T, \frac{r_T}{s_T}, \frac{y_3}{s_T}, \frac{z_3}{s_T}\right)$$

$$- L\left(\lambda_T, \frac{r_T}{s_T}, \frac{y_5}{s_T}, \frac{z_5}{s_T}\right) + L\left(\lambda_T, \frac{r_T}{s_T}, \frac{y_6}{s_T}, \frac{z_6}{s_T}\right)$$

$$\left. + L\left(\lambda_T, \frac{r_T}{s_T}, \frac{y_7}{s_T}, \frac{z_7}{s_T}\right) - L\left(\lambda_T, \frac{r_T}{s_T}, \frac{y_8}{s_T}, \frac{z_8}{s_T}\right)\right] \qquad \text{(A-43)}$$

From Equation (10), the total interference lift on the tail surfaces is

$$C_{N_{T(V)}} = \frac{(C_{N_\alpha})_W \ (C_{N_\alpha})_T \left[K_{W(B)} \alpha + k_{W(B)} \delta_W\right]}{2\pi AR_T (f_W - r_W) A_{REF}} (s_T - r_T)\left[i_1 \cos \Phi + i_4 \sin \Phi\right] A_W \qquad \text{(A-44)}$$

It is interesting to note that for zero control deflections, the $C_{N_{T(V)}}$ term given by Equation (A-43) should be independent of roll position This means linear theory gives aerodynamics of a wing-body-tail configuration that are independent of roll position.

SUMMARY OF KEY FINDINGS FOR ROLL DEPENDENCE WITH RESPECT TO LT AND SBT

The whole purpose of a fairly thorough review of the LT and SBT was to help glean the physics involved in roll orientation at low angle of attack in order to help structure the methodology that will incorporate nonlinear effects at larger angles of attack. As such, it is worthwhile to briefly summarize these key results.

a. For cruciform wings alone or a wing-body combination, the total normal force is independent of roll.

b. For a planar wing-body combination at roll, the loading on the windward plane panel is greater by an equal amount to that on the leeward plane panel. This means that if one were trying to design a code for lateral aerodynamics, roll dependence of each fin planform must be considered. On the other hand, if longitudinal aerodynamics are of primary interest, the total normal force on the entire wing planform can be considered

c. For a cruciform wing-body-tail configuration at roll, eight vortices are shed by the wing-body region, which adversely affects the tail lift. This is as opposed to four vortices at $\Phi = 0$ deg

d. The planar theory developed for wing-tail interference can be used to approximate the loss of lift on the tails at $\Phi = 45$ deg

e. The aerodynamics of a cruciform wing-body-tail combination with zero control deflections are independent of roll position.

REFERENCES

A-1. Nielsen, J.N., *Missile Aerodynamics*, NEAR, Inc, Mountain View, CA, 1988.

A-2. Ashley, Holt and Landahl, Martin, *Aerodynamics of Wings and Bodies*, Addison-Wesley Publishing Company, Inc., Reading, MA, Copyright 1965.

A-3. Moore, F. G.; Hymer, T. G.; McInville, R. M., *Improved Aeroprediction Code: Part I-Summary of New Methods and Comparison with Experiment*, NSWCDD/TR-93/91, May 1993.

A-4. Stallings, R. L., Jr. and Lamb, Milton, *Wing-Alone Aerodynamics Characteristics for High Angles of Attack at Supersonic Speeds*, NASA Technical Paper 1889, July 1981.

A-5. Baker, W. B., Jr., *Static Aerodynamic Characteristics of a Series of Generalized Slender Bodies with and without Fins at Mach Numbers from 0.6 to 3.0 and Angles of Attack from 0 to 180°*, AEDC-TR-75-124, Vols I and II, May 1976, Tullahoma, TN.

A-6. NASA Langley Research Center Tri-Service Missile Database, Transmitted from NASA/LRC Jerry M. Allen to NAVSWC on 5 November 1991 (formal documentation in process).

A-7. Nielsen, J. N.; Hemsch, M. J.; and Smith, C.A., *A Preliminary Method for Calculating the Aerodynamics Characteristics of Cruicform Missiles to High Angles of Attack Including Effects of Roll Angle and Control Deflections*, ONR-CR215-226-4F, 800 N. Quincy Street, Arlington, VA 22217

A-8. Pitts, W.C.; Nielsen, J.N.; and Kaatari, G.E., *Lift and Center of Pressure of Wing-Body-Tail Combinations at Subsonic, Transonic, and Supersonic Speeds*, NACA TR 1307, 1957.

DISTRIBUTION

DOD ACTIVITIES (CONUS)

		Copies
ATTN	CODE 04 (BISSON)	1
	CODE 44 (ZIMET)	1
	CODE 4425 (SIEGEL)	1
	CODE 332FD (LEKOUDIS)	1
	CODE 442 (WOOD)	1
CHIEF OF NAVAL RESEARCH		
BALLSTON TOWER 1		
800 N QUINCY ST		
ARLINGTON VA 22217-5660		
ATTN	CODE CL372 (LOFTUS)	1
	CODE C2771 (SMITH)	1
	CODE C2891 (PORTER)	1
	CODE C2892 (STRUTZ)	1
	CODE C2892 (HALTER)	1
	CODE C2892 (HOUSH)	1
	CODE C2892 (GLEASON)	1
	CODE C2894 (VAN DYKEN)	1
	CODE C29B10	
	TECHNICAL LIBRARY	1
COMMANDER		
NAVAL AIR WARFARE CENTER		
WEAPONS DIVISION		
CHINA LAKE CA 93555-6001		
ATTN	TECHNICAL LIBRARY	1
COMMANDER		
NAVAL SEA SYSTEMS COMMAND		
2531 JEFFERSON DAVIS HWY		
ARLINGTON VA 22242-5160		
ATTN	AIR 53012D (JOHNSON)	1
	RM 904 JP 2	
	TECHNICAL LIBRARY	1
COMMANDER		
NAVAL AIR SYSTEMS COMMAND		
1421 JEFFERSON DAVIS HWY		
ARLINGTON VA 22243-5120		

		Copies
ATTN	C KLEIN	1
	TECHNICAL LIBRARY	1
COMMANDER		
NAVAL AIR WARFARE CENTER		
WEAPONS DIVISION		
POINT MUGU CA 93042-5000		
ATTN	T C TAI	1
	M J MALIA	1
	TECHNICAL LIBRARY	1
COMMANDER		
NAVAL SHIP RESEARCH AND		
DEVELOPMENT CENTER		
WASHINGTON DC 20034		
ATTN	R M HOWARD	1
	TECHNICAL LIBRARY	1
SUPERINTENDENT		
US NAVAL POSTGRADUATE SCHOOL		
MONTEREY CA 93943-5000		
ATTN	S GREENHALGH	1
	C REITZ	1
	TECHNICAL LIBRARY	1
COMMANDING OFFICER		
NAVAL AIR WARFARE CENTER		
AIRCRAFT DIVISION WARMINSTER		
WARMINSTER PA 18974-5000		
ATTN	HEAD WEAPONS DEPT	1
	HEAD SCIENCE DEPT	1
SUPERINTENDENT		
US NAVAL ACADEMY		
ANNAPOLIS MD 21402		
ATTN	M KRUMINS	1
	TECHNICAL LIBRARY	1
OFFICER IN CHARGE		
NAVAL INTELLIGENCE SUPPORT CENTER		
4301 SUITLAND ROAD		
WASHINGTON DC 20390 RM 810 CP5		
ALEXANDRIA VA 22217		

DISTRIBUTION (Continued)

	Copies
ATTN CODE 30 CHIEF OF NAVAL RESEARCH NAVY SDI 2211 JEFFERSON DAVIS HWY ARLINGTON VA	1
ATTN DIAG DT 4T (PAUL MURAD) DEFENSE INTELLIGENCE AGENCY WASHINGTON DC 20546	2
ATTN BRENT WAGGONER CODE 4072 BLDG 2540 NAVAL WEAPONS SUPPORT CENTER CRANE IN 47522-5000	1
ATTN CODE 5252P (KRAUSE) TECHNICAL LIBRARY COMMANDER NAVAL SURFACE WARFARE CENTER INDIAN HEAD DIVISION INDIAN HEAD MD 20640-5000	1 1
ATTN TECHNICAL LIBRARY COMMANDING GENERAL MARINE CORPS COMBAT DEVELOPMENT COMMAND QUANTICO VA 22134-5000	1
ATTN E SEARS L E LIJEWSKI C COTTRELL TECHNICAL LIBRARY AFATL (ADLRA) (DLGC) EGLIN AFB FL 32542-5000	1 1 1 1 1
ATTN TECHNICAL LIBRARY USAF ACADEMY COLORADO SPRINGS CO 80912	1
ATTN TECHNICAL LIBRARY ADVANCED RESEARCH PROJECTS AGENCY DEPARTMENT OF DEFENSE WASHINGTON DC 20305	1
ATTN B BLAKE (BLD 146) D SHEREDA (BLD 450) J JENKINS (BLD 146) R SAMUELS (BLD 856) TECHNICAL LIBRARY COMMANDING OFFICER AFSC 2210 8TH STREET WRIGHT PATTERSON AFB OH 45433	1 1 1 1 1
ATTN J USSELTON W B BAKER JR TECHNICAL LIBRARY ARNOLD ENGINEERING DEVELOPMENT CENTER USAF TULLAHOMA TN 37389	1 1 1
ATTN H HUDGINS G FRIEDMAN TECHNICAL LIBRARY COMMANDING GENERAL ARRADCOM PICATINNY ARSENAL DOVER NJ 07801	1 1 1
ATTN C H MURPHY R PUHALLA JR W STUREK C NIETUBICZ A MIKHAIL P PLOSTINS TECHNICAL LIBRARY COMMANDING GENERAL BALLISTIC RESEARCH LABORATORY ABERDEEN PROVING GROUND ABERDEEN MD 21005-5066	1 1 1 1 1 1 1
ATTN CODE TNC (BLACKLEDGE) RICH MATLOCK DIRECTOR INTERCEPTOR TECHNOLOGY BALLISTIC MISSILE DEFENSE OFFICE THE PENTAGON WASHINGTON DC 20350	1 1

DISTRIBUTION (Continued)

	Copies
ATTN SFAE SD ASP	1
SFAE SD HED	1
DEPUTY COMMANDER	
US ARMY STRATEGIC DEFENSE COMMAND	
P O BOX 1500	
HUNTSVILLE AL 35807-3801	
ATTN D WASHINGTON	1
W WALKER	1
R KRETZSCHMAR	1
COMMAND GENERAL	
US ARMY MISSILE COMMAND	
AMSMI RD SS AT	
REDSTONE ARSENAL AL 35898-5252	
DEFENSE TECHNICAL INFORMATION CENTER	
8725 JOHN J KINGMAN ROAD	
SUITE 0944	
FORT BELVOIR VA 22060-6218	2
DEFENSE PRINTING SERVICE	
WASHINGTON NAVY YARD	
WASHINGTON DC 20374	1
ATTN CODE E29L	
TECHNICAL LIBRARY	1
COMMANDING OFFICER	
CSSDD NSWC	
6703 W HIGHWAY 98	
PANAMA CITY FL 32407-7001	
ATTN DR P WEINACHT	1
AERODYNAMICS BRANCH	
PROPULSION AND FLIGHT DIV WTD	
AMSRL WT PB	
US ARMY RESEARCH LAB ABERDEEN	
PROVING GROUND MD 21005-5066	
NON-DOD ACTIVITIES (CONUS)	
ATTN NEIL WALKER	1
NICHOLAS RESEARCH CORPORATION	
MS 912	
P O BOX 400002	
4040 S MEMORIAL PKWY	
HUNTSVILLE AL 35801	

	Copies
THE CNA CORPORATION	
P O BOX 16268	
ALEXANDRIA VA 22302-0268	1
ATTN GIFT AND EXCHANGE DIVISION	4
LIBRARY OF CONGRESS	
WASHINGTON DC 20540	
GIDEP OPERATIONS OFFICE	
CORONA CA 91720	1
ATTN TECHNICAL LIBRARY	1
NASA AMES RESEARCH CENTER	
MOFFETT CA 94035-1099	
ATTN C SCOTT	1
D CURRY	1
NASA JOHNSON SPACE CENTER	
HOUSTON TX 77058	
ATTN TECHNICAL LIBRARY	1
NASA	
WASHINGTON DC 20546	
ATTN W C SAWYER	1
B HENDERSON	1
D MILLER	1
J ALLEN	1
F WILCOX	1
TECHNICAL LIBRARY	2
NASA LANGLEY RESEARCH CENTER	
HAMPTON VA 23365	
ATTN D G MILLER	1
TECHNICAL LIBRARY	1
LAWRENCE LIVERMORE NATIONAL LABORATORY	
EARTH SCIENCES DIVISION	
UNIVERSITY OF CALIFORNIA	
P O BOX 808	
LIVERMORE CA 94550	
ATTN W RUTLEDGE (1635)	1
R LAFARGE	1
R EISLER	1
TECHNICAL LIBRARY	1
SANDIA NATIONAL LABORATORY	
P O BOX 5800	
ALBUQUERQUE NM 87185-5800	

DISTRIBUTION (Continued)

	Copies
ATTN ASSISTANT DEFENSE COOPERATION ATTACHE EMBASSY OF SPAIN WASHINGTON DC 20016	1
ATTN CDR R TEMPEST BRITISH NAVY STAFF WASHINGTON DC 20008	1
ATTN ASO LO IS ISRAEL AIR FORCE LIAISON OFFICER 700 ROBBINS AVE PHILADELPHIA PA 19111	1
ATTN GERMAN MILITARY REP US OA GMR TRAFFIC AND TRANSPORTATION DIVISION 10 SERVICES ROAD DULLES INTERNATIONAL AP WASHINGTON DC 20041	1
ATTN F D DEJARNETTE NORTH CAROLINA STATE UNIVERSITY DEPT OF MECHANICAL AND AEROSPACE ENGINEERING BOX 7921 RALEIGH NC 27695	1
ATTN PROF J A SCHETZ VIRGINIA POLYTECHNIC AND STATE UNIVERSITY DEPT OF AEROSPACE ENGINEERING BLACKSBURG VA 24060	1
ATTN J M WU C BALASUBRAMAYAN TECHNICAL LIBRARY THE UNIVERSITY OF TENNESSEE SPACE INSTITUTE TULLAHOMA TN 37388	1 1 1
ATTN R NELSON TECHNICAL LIBRARY UNIVERSITY OF NOTRE DAME DEPT OF AEROSPACE AND MECHANICAL ENGINEERING BOX 537 NOTRE DAME IN 46556	1 1
ATTN PROF F NELSON DEPT OF MECH AND AERO ENG UNIVERSITY OF MISSOURI ROLLA ROLLA MO 65401	1
ATTN DR DONALD SPRING AEROSPACE ENGINEERING DEPT AUBURN UNIVERSITY AL 36849-5338	1
ATTN ROBERT ENGLAR GEORGIA TECH RESEARCH INSTITUTE AEROSPACE SCIENCE AND TECHNOLOGY LAB ATLANTA GA 30332	1
ATTN E LUCERO L TISSERAND D FROSTBUTTER L PERINI TECHNICAL LIBRARY APPLIED PHYSICS LABORATORY JOHNS HOPKINS UNIVERSITY JOHNS HOPKINS ROAD LAUREL MD 20723-6099	1 1 1 1 1
ATTN B BROOKS R STANCIL R ELKINS LORAL VOUGHT SYSTEMS P O BOX 650003 M S EM 55 DALLAS TX 75265-0003	1 1 1
ATTN TECHNICAL LIBRARY MARTIN MARIETTA AEROSPACE P O BOX 5837 ORLANDO FL 32805	1
ATTN R CAVAGE ADVANCED SYSTEMS DESIGN DEPT 113 407 (GB14) ROCKWELL NORTH AMERICAN AIRCRAFT OPERATIONS P O BOX 92098 LOS ANGELES CA 90009	1

DISTRIBUTION (Continued)

	Copies
ATTN TECHNICAL LIBRARY HUGHES AIRCRAFT COMPANY MISSILE SYSTEMS SECTOR P O BOX 7928 CANOGA PARK CA 91304-7928	1
ATTN M DILLENIUS NIELSEN ENGINEERING AND RESEARCH INC 526 CLYDE AVE MOUNTAIN VIEW CA 95043	1
ATTN J XERIKOS N CAMPBELL TECHNICAL LIBRARY MCDONNEL DOUGLAS ASTRONAUTICS CO (WEST) 5301 BOLSA AVE HUNTINGTON BEACH CA 92647	1 1 1
ATTN J WILLIAMS S VUKELICH J FIVEL R GERBSCH (CODE 1111041) TECHNICAL LIBRARY MCDONNELL DOUGLAS ASTRONAUTICS CO (EAST) BOX 516 ST LOUIS MO 63166-0516	1 1 1 1 1
ATTN TECHNICAL LIBRARY UNITED TECHNOLOGIES NORDEN SYSTEMS NORWALK CT 06856	1
ATTN T LUNDY D ANDREWS TECHNICAL LIBRARY LOCKHEED MISSILES AND SPACE CO INC P O BOX 1103 HUNTSVILLE AL 35807	1 1 1
ATTN W CHRISTENSON D WARNER ALLIANT TECHSYSTEMS INC 600 SECOND ST NE HOPKINS MN 55343	1 1
ATTN TECHNICAL LIBRARY B SALAMI J BOUDREAU RAYTHEON MISSILE SYSTEMS 50 APPLE HILL DR STOP T3TBB TEWKSBURY MA 01876-0901	1 1 1
ATTN LLOYD PRATT AEROJET TACTICAL SYSTEMS CO P O BOX 13400 SACRAMENTO CA 95813	1
ATTN JOSEPH ANDRZIJEWSKI MEVATEC CORP 1525 PERIMETER PARKWAY SUITE 500 HUNTSVILLE AL 35806	1
ATTN DR G S SCHMIDT LORAL DEFENSE SYSTEMS 1210 MASSILLAN ROAD AKRON OH 44315-0001	1
ATTN W NORDGREN 721 GOULD INC OSD 18901 EUCLID AVE CLEVELAND OH 44117	1
ATTN TECH LIBRARY AEROJET ELECTRONIC SYSTEMS P O BOX 296 III AZUSA CA 91702	1
ATTN L E ERICSSON P REDING G CHRUSCIEL TECHNICAL LIBRARY LOCKHEED MISSILES AND SPACE CO INC P O BOX 504 SUNNYVALE CA 94086	1 1 1 1
ATTN K C LEE ACCUREX CORP P O BOX 7040 520 CLYDE AVE MOUNTAIN VIEW CA 94039	1

DISTRIBUTION (Continued)

	Copies
ATTN TECH LIBRARY FMC NAVAL SYSTEMS DIV 4800 E RIVER ROAD MINNEAPOLIS MN 55421-1402	1
ATTN DORIA GLADSTONE BATTELLE MEMORIAL INSTITUTE COLUMBUS DIVISION 505 KING AVE COLUMBUS OH 43201-2693	1
ATTN JAMES SORENSON ORBITAL SCIENCES 3380 SOUTH PRICE ROAD CHANDLER AZ 85248	1
ATTN J FORKOIS KAMAN SCIENCES CORP 1500 GARDEN OF THE GODS ROAD P O BOX 7463 COLORADO SPRINGS CO 80933	1
ATTN FRED KAUTZ MIT LINCOLN LABORATORY LEXINGTON MA 02173-0073	1
ATTN D J GRIESE MAIL STOP 4C 61 BOEING DEFENSE AND SPACE GROUP P O BOX 3999 SEATTLE WA 98124-2499	1
ATTN W J CLARK DYNA EAST CORPORATION 3132 MARKET ST PHILADELPHIA PA 19104	1
ATTN BRIAN WALKUP HERCULES AEROSPACE PRODUCT CO ALLEGHANY BALLISTIC LAB ROCKET CENTER WV 26726	1
ATTN B D PRATS MARTIN MARIETTA ASTROSPACE AEROTHERMOPHYSICS 230 E GODDARD BLVD KING OF PRUSSIA PA 19406	1
ATTN DR T LIN TRW ELECTRONICS AND DEFENSE SECTOR BLDG 527 RM 706 P O BOX 1310 SAN BERNADINO CA 92402	1
ATTN G VINCENT SPARTA INC 4301 CORPORATE DR HUNTSVILLE AL 35805	1
ATTN D P FORSMO TECHNICAL LIBRARY RAYTHEON COMPANY MISSILE SYSTEMS DIVISION HARTWELL RD BEDFORD MA 01730	1 1
ATTN M S MILLER BRIAN EST DYNETICS INC P O DRAWER B HUNTSVILLE AL 35814-5050	1 1
ATTN H A MCELROY GENERAL DEFENSE CORP P O BOX 127 RED LION PA 17356	1
ATTN R SEPLAK BRUNSWICK CORP DEFENSE DIVISION 3333 HARBOR BLVD COSTA MESA CA 92628-2009	1
ATTN J W MCDONALD GENERAL RESEARCH CORP ADVANCED TECHNOLOGY INC 5383 HOLLISTER AVE P O BOX 6770 SANTA BARBARA CA 93160-6770	1
ATTN CAROL BUTLER OTI INTERNATIONAL 60 2ND ST SUITE 301 P O BOX 37 SHALIMAR FL 32579	1

DISTRIBUTION (Continued)

	Copies
ATTN ENGINEERING LIBRARY ARMAMENT SYSTEMS DEPT GENERAL ELECTRIC CO BURLINGTON VT 05401	1
ATTN TECHNICAL LIBRARY OAYNE AERONAUTICAL 2701 HARBOR DRIVE SAN DIEGO CA 92138	1
ATTN WILLIAM FACINELLI ALLIED SIGNAL P O BOX 22200 MS 1230 21E TEMPE AZ 85285	1
ATTN T LIBRARY RAYTHEON COMPANY SPENCER LABORATORY BOX SL 7162 BURLINGTON MA 01803	1
ATTN DR T P SHIVANANDA TRW BMD P O BOX 1310 SAN BERNADINO CA 92402-1313	1
ATTN T R PEPITONE AEROSPACE TECHNOLOGY INC P O BOX 1809 DAHLGREN VA 22448	1
ATTN ERIC MOORE MAILSTOP MER 24 1281 LOCKHEED SANDERS P O BOX 868 NASHUA NH 03061	1
ATTN DR BRIAN LANDRUM RI BLDG E33 PROPULSION RESEARCH CENTER UNIVERSITY OF ALABAMA HUNTSVILLE AL 35899	1
ATTN BRUCE NORTON MAIL STOP BL 1 RAYTHEON 100 VANCE TANK RD BRISTOL TN 37620	1
ATTN JIM ROBERTSON RESEARCH SOUTH INC 555 SPARKMAN DRIVE SUITE 818 HUNTSVILLE AL 35816-3423	1
ATTN BOB WHYTE ARROW TECH ASSOCIATES INC 1233 SHELBURNE ROAD D8 SO BURLINGTON VT 05403	1
ATTN JUAN AMENABAR SAIC 1700 N MOORE ST STE 1820 ARLINGTON VA 22209	1
ATTN TECHNICAL LIBRARY TELEDYNE RYAN AERONAUTICAL 2701 HARBOR DRIVE SAN DIEGO CA 92138	1
NON-DOD ACTIVITIES (EX-CONUS)	
ATTN LOUIS CHAN INSTITUTE FOR AEROSPACE RESEARCH NATIONAL RESEARCH COUNCIL MONTREAL RD OTTAWA ONTARIO CANADA K1A0R6	1
ATTN H B ASLUND SAAB MILITARY AIRCRAFT 581 88 LINKOEPING SWEDEN	1
ATTN R BARDWELL DEFENSE SYSTEMS LTD THE GROVE WARREN LANE STANMORE MIDDLESEX UNITED KINGDOM	1
ATTN A BOOTH BRITISH AEROSPACE DEFENCE LTD MILITARY AIRCRAFT DIVISION WARTON AERODROME WARTON PRESTON LANCASHIRE PR4 1AX UNITED KINGDOM	1

DISTRIBUTION (Continued)

	Copies
ATTN R CAYZAC GIAT INDUSTRIES 7 ROUTE DE GUERCY 18023 BOURGES CEDEX FRANCE	1
ATTN MAJ F DE COCK ECOLE ROYALE MILITAIRE 30 AV DE LA RENAISSANCE 1040 BRUXELLES BELGIUM	1
ATTN J EKEROOT BOFORS MISSILES 691 80 KARLSKOGA SWEDEN	1
ATTN CH FRANSSON NATIONAL DEFENCE RESEARCH ESTABLISHMENT DEPT OF WEAPON SYSTEMS EFFECTS AND PROTECTION KARLAVAGEN 106B 172 90 SUNDBYBERG SWEDEN	1
ATTN M HARPER-BOURNE DEFENCE RESEARCH AGENCY Q134 BUILDING RAE FARNBOROUGH HAMPSHIRE QU14 6TD UNITED KINGDOM	1
ATTN A H HASSELROT FFA P O BOX 11021 161 11 BROMMA SWEDEN	1
ATTN B JONSSON DEFENCE MATERIAL ADMINISTRATION MISSILE TECHNOLOGY DIVISION 115 88 STOCKHOLM SWEDEN	1
ATTN P LEZEAUD DASSAULT AVIATION 78 QUAI MARCEL DASSAULT 92214 SAINT CLOUD FRANCE	1
ATTN J LINDHOUT N L R ANTHONY FOKKERWEG 2 1059 CM AMSTERDAM THE NETHERLANDS	1
ATTN A MICKELLIDES GEC MARCONI DEFENCE SYSTEMS LTD THE GROVE WARREN LANE STANMORE MIDDLESEX UNITED KINGDOM	1
ATTN K MOELLER BODENSEEWERK GERAETETECHNIK GMBH POSTFACH 10 11 55 88641 UBERLINGEN GERMANY	1
ATTN G MOSS ROYAL MILITARY COLLEGE AEROMECHANICAL SYSTEMS GROUP SHRIVENHAM SWINDON WILTS SN6 8LA UNITED KINGDOM	1
ATTN RIBADEAU DUMAS MATRA DEFENSE 37 AV LOUIS BREGUET BP 1 78146 VELIZY VILLACOUBLAY CEDEX FRANCE	1
ATTN R ROGERS DEFENCE RESEARCH AGENCY BLDG 37 TUNNEL SITE CLAPHAM BEDS MK 41 6AE UNITED KINGDOM	1

DISTRIBUTION (Continued)

	Copies
ATTN S SMITH DEFENCE RESEARCH AGENCY Q134 BUILDING RAE FARNBOROUGH HAMPSHIRE QU14 6TD UNITED KINGDOM	1
ATTN J SOWA SAAB MISSILES AB 581 88 LINKOPING SWEDEN	1
ATTN D SPARROW HUNTING ENGINEERING LTD REDDINGS WOOD AMPTHILL BEDFORDSHIRE MK452HD UNITED KINGDOM	1
ATTN P STUDER DEFENCE TECHNOLOGY AND PROCUREMENT AGENCY SYSTEMS ANALYSIS AND INFORMATION SYSTEMS DIVISION PAPIERMUEHLESTRASSE 25 3003 BERNE SWITZERLAND	1
ATTN D WALLSTROM THE AERONAUTICAL RESEARCH INST OF SWEDEN P O BOX 11021 161 11 BROMMA SWEDEN	1
ATTN DR R G LACAU AEROSPATIALE MISSILE DEPT E ECN CENTRE DES GATINES 91370 VERRIERE LE BUISSON FRANCE	1
ATTN J M CHARBONNIER VON KARMAN INSTITUTE 72 CHAUSSEE DE WATERLOO 1640 RHODE SAINT GENESE BELGIUM	1

	Copies
ATTN P CHAMPIGNY DIRECTION DE LAERONAUTIQUE ONERA 29 AV DE LA DIVISION LECLERC 92320 CHATILLON SOUS BAGNEUX CEDEX FRANCE	1
ATTN DR P HENNIG DEUTSCHE AEROSPACE (DASA) VAS 414 ABWEHR AND SCHUTZ POSTFACH 801149 8000 MUENCHEN 80 GERMANY	1
ATTN J EVANS DREV P O BOX 8800 COURCELLETE PROVENCE OF QUEBEC CANADA GOA1RO	1
ATTN H G KNOCHE DR GREGORIOU MESSERSCHMIDT BOLKOW BLOHM GMBH UNTERNEHMENSBEREICH APPARATE MUNCHEN 80 POSTFACH 801149 BAYERN GERMANY	1 1
INTERNAL	
A	1
B	1
B05 (STATON)	1
B44	1
B44 (PRIOLO)	1
B44 (HSIEH)	1
B44 (WARDLAW)	1
B51 (ARMISTEAD)	1
C	1
D	1
D4	1
E231	3
E282 (SWANSBURG)	1
F	1
G	1
G02	1
G04	5

DISTRIBUTION (Continued)

	Copies
G05	1
G06	1
G20	1
G205	1
G23	1
G23 (CHADWICK)	1
G23 (DEVAN)	1
G23 (GRAFF)	1
G23 (HARDY)	1
G23 (HYMER)	5
G23 (MCINVILLE)	5
G23 (OHLMEYER)	1
G23 (ROWLES)	1
G23 (WEISEL)	1
G30	1
G40	1
G50	1
G60	1
G70	1
G73	1
K	1
K10	1
K20	1
K204	1
N	1